THEORETICAL MODELLING OF THE ENTRAINMENT AND THERMOMECHANICAL EFFECTS OF CONTAMINATION PARTICLES IN ELASTOHYDRODYNAMIC CONTACTS

by

GEORGE K. NIKAS

A thesis submitted to the University of London for the degree of

Doctor of Philosophy

and the

Diploma of Imperial College.

April 1999

Tribology Section
Department of Mechanical Engineering
Imperial College of Science, Technology and Medicine
London SW7 2BX, England

ABSTRACT

The basic aim of this work was the theoretical investigation of the mechanisms of entrainment and elastoplastic compression/shearing of soft/ductile contamination particles in sliding-rolling elastohydrodynamic contacts. In pursuit of this target, two models were developed to study the entrainment process of spherical particles in the inlet zone of lubricated point contacts (chapter 1) and the mechanism of thermomechanical deformation of soft/ductile spherical particles in the inlet and central (Hertzian) zone of lubricated line contacts (chapters 2-5). The models were materialized through computer simulations to analyze a large number of typical applications and to cover a broad range of operating conditions, representative of industrial Machine Elements (gears, bearings, etc.).

The simulation revealed the risks involved in the presence of soft contaminants in concentrated contacts. More specifically, contamination particles were related to surface indentation, scuffing/seizure (directly or indirectly), as well as thermomechanical wear (local high-heat tempering reactions and even melting). The models are aimed to predict clearly the onset of damage due to the presence of one or more, mainly soft/ductile and metallic, contamination particles in concentrated contacts and to predict the critical values of operational parameters like the slide/roll ratio, film thickness, thermomechanical properties of the materials involved, etc., which would produce an unsafe working environment, in the presence of specific solid contaminants. The assessment of the risk of damage was both short-term (surface indentation, abrasion and scuffing caused by lubricant starvation due to inlet blockage by debris) and long-term (fine pitting and residual stresses due to the plastic indentation of debris, which would extent to gross damage, or small thermo-cracks caused by the frictional heating of debris, which could later propagate under the action of high solid or lubricant pressures). Results are verified by comparison with experimental findings from the literature and new hypotheses (like the four last conclusions of chapter 5), are put forward to explain some reported failures or to point experimentalists to specific areas of future research.

TABLE OF CONTENTS

CHAPTER 2

MOTION AND DEFORMATION OF A SOFT PARTICLE IN AN ELASTOHYDRODYNAMIC LINE CONTACT

CHAPTER 3

THERMAL MODELLING OF THE FRICTIONAL HEATING BETWEEN A SOFT PARTICLE AND THE COUNTERFACES IN AN ELASTOHYDRODYNAMIC LINE CONTACT

CHAPTER 4

THERMOELASTIC ANALYSIS OF THE SQUASHING OF A SOFT PARTICLE IN AN ELASTOHYDRODYNAMIC LINE CONTACT

CHAPTER 5

REFINEMENT OF THE MODEL AND GENERAL APPLICATION

ACKNOWLEDGEMENTS

The following persons deserve special mention for supporting me during this lengthy research.

My parents, Kostas and Charoula, deserve by far the largest credit for all kinds of support, emotional, financial and other. Without their love and devotion, I wouldn't stand where I am today.

Special thanks are due to my supervisor, Dr Ritchie Sayles, for his kindness, calm attitude, and for treating me as equal, despite his high expertise. Ritchie has to be especially praised for giving me all the financial support and expensive computing equipment I asked for, immediately and with no questions asked. He also arranged for my Research Assistantship in the Tribology Section and gave me some of the most difficult and challenging subjects torturing Tribologists (which increased the fuel consumption of my brain dramatically, but I won't send him the bill).

I would also like to thank my unofficial supervisor, Visiting Professor, Dr Stathis Ioannides, for spending some of his limited time to share his vast experience with me, and for the numerous discussions we had in our mother language (Greek). Stathis gave some great inspiration for this research. He also arranged for sponsoring part of this research (see chapter 1) through SKF-ERC.

LIST OF FIGURES

LIST OF TABLES

LIST OF SYMBOLS

Chapter	Symbol	Description
1	a	Substitution variable (equation (1.11)).
1	a_1 - a_9	Substitution variables (equations (1.31)-(1.39)).
1	b	Substitution variable (equation (1.12)).
1	c	Substitution variable (equation 1.13)).
1	C_D	Fluid drag coefficient (equation (1.67)).
1	C_1 - C_9	Substitution variables (equations (1.15)-(1.23)).
1	d	Substitution variable (equation (1.14)).
1	D	Initial diameter of the undeformed (spherical) particle.
1	Det	Determinant (equation (1.93)).
1	D_{N_1}, D_{N_2}	Determinants (equations (1.94), (1.95)).
1	e_1, e_2, e_3	Substitution variables (equations (1.24)-(1.26)).
1	E	Effective modulus of elasticity (equation (1.57)).
1	E_1	Modulus of elasticity of the material of the ball.
1	E_2	Modulus of elasticity of the material of the flat.
1	$\underset{\sim}{f}$	Substitution vector (equation (1.42)).
1	$F_{\mathrm{fluid,x}}$	x-component of the fluid force on the particle (equation (1.90)).
1	$F_{\mathrm{fluid,y}}$	y-component of the fluid force on the particle (equation (1.91)).
1	G	The EHL material-parameter (see Hamrock, 1994, page 437).
1	h	Fluid film thickness (equation (1.61)).
1	h_{c}	Central film thickness (figure 1.1).
1	h_{in}	Oil bath thickness (figure 1.1).
1	I_z	The fixed number of k-nodes in the z-direction.
1	$\mathbf{J}$	Jacobian matrix (see equation (1.30)).
1	$\mathbf{J}^*$	Adjoint matrix (equation (1.43)).
1	J_{11} - J_{33}	Substitution variables (equations (1.44)-(1.52)).

Chapter	**Symbol**	**Description**
1	L	Length of the “reference fluid volume” (figure 1.2).
1	N	Number of the k-nodes in the z-direction.
1	N_x, N_y	Integer constants (equations (1.58), (1.59)).
1	$\underset{\sim}{N}_1, \underset{\sim}{N}_2$	Normal forces between the particle and the counterfaces (figure 1.3 and equations (1.83), (1.84)).
1	$N_{1,\mathrm{x}}$, $N_{1,\mathrm{y}}$	Magnitudes of the components of vector $\underset{\sim}{N}_1$ (direction x or y).
1	$N_{2,\mathrm{x}}$, $N_{2,\mathrm{y}}$	Magnitudes of the components of vector $\underset{\sim}{N}_2$ (direction x or y).
1	p_{H}	Maximum Hertzian pressure for the contact of the ball and the flat (equation (1.74)).
1	P	The load applied on the ball.
1	r	Distance from the centre of the Hertzian contact circle (equation (1.62)).
1	r_{a}	Radius of the imaginary circle where the particle comes in contact with both the ball and the flat, with the particle being undeformed.
1	$ran1$	Random number between 0 and 1.
	R	Radius of the ball.
1	R_{H}	Radius of the Hertzian contact circle (figure 1.2 and equation (1.56)).
1	Re_{p}	Particle Reynolds number (equation (1.68)).
1	Re_{x}	Reynolds number of the macroscopic flow, calculated for the $\underset{\sim}{u}$ velocity component.
1	Re_{y}	Reynolds number of the macroscopic flow, calculated for the $\underset{\sim}{v}$ velocity component.
1	S	Semi-width of the reference fluid volume (figure 1.2).
1	S_r	Slide/roll ratio (equation (1.107)).
1	$\underset{\sim}{T}_1, \underset{\sim}{T}_2$	Solid frictional forces on the particle on plane xz (figure 1.3).
1	$\underset{\sim}{T}_3, \underset{\sim}{T}_4$	Solid frictional forces on the particle on plane yz (figure 1.3).

Chapter	**Symbol**	**Description**
1	$\underset{\sim}{u}$	Fluid velocity component in the x-direction (figure 1.1).
1	u_a	Rolling (tangential) speed of the ball for y = 0.
1	u_{ave}	Average value of the u-speed at the position of the particle, along the diameter of the particle parallel in the x-direction.
1	U	The EHL speed-parameter (see Hamrock, 1994, page 437).
1	v_{ave}	Average value of the *v*-speed at the position of the particle, along the diameter of the particle parallel in the y-direction.
1	V_s	Sliding speed of the ball relatively to the flat.
1	$\underset{\sim}{w}$	Fluid velocity component in the z-direction (figure 1.1).
1	W	The EHL load-parameter (see Hamrock, 1994, page 437).
1	$\underset{\sim}{x}$	Vector of the fluid velocity components (equation (1.41)).
1	x_A	x-coordinate of point A (figure 1.3).
1	x_B	x-coordinate of point B (figure 1.3).
1	x_C	x-coordinate of the centre of the particle C (figure 1.3).
1	x_0	x-coordinate of the initial position of a particle in the reference volume.
1	y_A	y-coordinate of point A (figure 1.3).
1	y_B	y-coordinate of point B (figure 1.3).
1	y_C	y-coordinate of the centre of the particle C (figure 1.3).
1	y_0	y-coordinate of the initial position of the particle in the reference volume.
1	z_1	z-coordinate of the lower surface of the (elastically deformed) ball (equation (1.72)).
1	z_2	z-coordinate of the surface of the (elastically deformed) flat (equation (1.73)).
1	α	See equations (1.97) and (1.98).
1	β	See equations (1.97) and (1.99).
1	γ	See equations (1.97) and (1.100).
1	Δx, Δy, Δz	Spatial steps for the solution of the Navier-Stokes equations.
1	η	Dynamic viscosity of the fluid.

Chapter	**Symbol**	**Description**
1	λ	Constant (see equations (1.101), (1.103) and (1.104)).
1	μ_1	Friction coefficient between the particle and the ball.
1	μ_2	Friction coefficient between the particle and the flat.
1	ν	Kinematic viscosity of the lubricant at environmental conditions.
1	ν_1	Poisson ratio of the material of the ball.
1	ν_2	Poisson ratio of the material of the flat.
1	ρ	Density of the fluid.
1	υ	Sum of surface displacements (appearing in equation (1.61)).
1	φ	Angle of the tangent to the ball's wall (figure 1.1).
1	φ_1, φ_4	Angles (equations (1.75)-(1.78)).
1	ω	Rotational speed (spin) of the (spherical) particle.
2	A	Facial surface of the deformed particle (disk) (equation (2.26)).
2	b	Hertzian contact semi-width (figure 2.1 and equation (2.2)).
2	c_0	Constant (equation (2.42)).
2	C_D	Fluid drag coefficient on the particle (equation (2.28)).
2	$\mathrm{d}F_{\mathrm{stat}}$	Elemental fluid force on a sector of the deformed particle due to the elastohydrodynamic fluid pressure (figure 2.6 and equation (2.21)).
2	$\mathrm{d}F_{\mathrm{stat,x}}$	x-component of the elemental force $\mathrm{d}F_{\mathrm{stat}}$ (equation (2.22)).
2	D	Diameter of the undeformed particle.
2	E	Effective modulus of elasticity (equation (2.4)).
2	E_1, E_2	Moduli of elasticity (surface 1 or 2).
2	F_{dyn}	Fluid force on the particle, owing to the action of the dynamic fluid pressure on the particle (equations (2.25), (2.29)).
2	F_{fluid}	Overall fluid force on the particle (figure 2.7 and equation (2.39)).
2	F_{stat}	Fluid force on the particle, owing to the elastohydrodynamic-fluid-pressure gradient (equation (2.23)).

Chapter	Symbol	Description
2	h	Elastohydrodynamic film thickness (figure 2.1 and equation (2.1)).
2	h_c	Elastohydrodynamic central film thickness (figure 2.1).
2	k_p	Yield stress in simple shear of the material of the particle.
2	m	Mass of the particle.
2	$\underset{\sim}{N_1}$, $\underset{\sim}{N_2}$	Solid normal forces on the particle (figure 2.2).
2	p	Elastohydrodynamic pressure of the lubricant.
2	p_s	Solid pressure between the particle and the counterfaces.
2	R	Radius of the deformed (disk-shaped) particle.
2	R_{eq}	Effective radius of curvature of the contact (equation (2.3)).
2	R_s	Radius of the stick region between the particle and a counterface (appears in equation (2.32)).
2	R_1, R_2	Radii of curvature (surface 1 or 2).
2	Re_p	Particle Reynolds number; Reynolds number of the local fluid flow around the particle (equation (2.27)).
2	S_0	Viscosity-temperature coefficient (appears in equation (2.30)).
2	t	Time elapsed since the particle was first pinched.
2	$\underset{\sim}{T_1}$, $\underset{\sim}{T_2}$	Solid frictional forces on the particle (figure 2.2).
2	u_1, u_2	Tangential speeds of the counterfaces (figure 2.1).
2	U	Macro-speed of the lubricant relatively to the particle (see equations (2.25) and (2.27)).
2	V_{extr}	Extrusion speed of the particle (speed of the lateral expansion of the particle during its plastic compression).
2	$\underset{\sim}{V_{p1}}$	Velocity of the particle relatively to surface 1 (opposite to $\underset{\sim}{V_{1p}}$ shown in figure 2.7).
2	$\underset{\sim}{V_{p2}}$	Velocity of the particle relatively to surface 2 (figure 2.7; see also equation (2.45)).
2	$\underset{\sim}{V_{1p}}$	Velocity of surface 1 relatively to the particle (figure 2.7; see also equation (2.46)).
2	V_{12}	Sliding speed of the contact ($V_{12} = u_1 - u_2$).

Chapter	**Symbol**	**Description**
2	$\underset{\sim}{V}_{2p}$	Velocity of surface 2 relatively to the particle (opposite to $\underset{\sim}{V}_{p2}$ shown in figure 2.7).
2	V_{σ}	Volume of the particle.
2	w	Load per unit length of the contact.
2	x	Distance of the centre of particle’s disk from the centre of the contact (x = 0) (equations (2.40), (2.43)).
2	X'	Instantaneous displacement of particle’s geometrical centre (centre of the particle disk) relatively to surface 2 (figure 2.7 and equation (2.44)).
2	Y_{p}	Yield stress in uniaxial tension of the material of the particle.
2	Z_1	Viscosity-pressure coefficient (appearing in equation (2.30)).
2	a_1, a_2	Angles (figure 2.2 and equations (2.11) or (2.16) and (2.17)).
2	Δt	Time step.
2	ε	“Flow perturbation” parameter (see explanations below equation (2.23)).
2	η	Dynamic viscosity of the lubricant.
2	η_0	Dynamic viscosity of the lubricant at environmental conditions.
2	θ	Temperature of the lubricant.
2	θ_0	Environmental temperature.
2	μ_f	Friction coefficient between a particle and a counterface.
2	μ_1, μ_2	Coefficients of kinetic (sliding) friction between the particle and a counterface (counterface 1 or 2).
2	ν_1, ν_2	Poisson ratios (surface 1 or 2).
2	ρ	Density of the lubricant.
2	ρ_p	Density of the material of the particle.
2	φ_1, φ_2	Angles (see figure 2.7 and equation (2.35)).
3	a_{22}	Heat partition coefficient, giving the proportion of the emitted heat of a sector that goes to counterface 2 (equations (3.29) – (3.31)).

Chapter	**Symbol**	**Description**
3	A	Lateral wet area of a peripheral sector (equations (3.36)).
3	c	Specific heat.
3	c_{fluid}	Specific heat of the lubricant.
3	g	The gravitational acceleration (g $\cong$ 9.81 m/s^2).
3	Gr	Grashof number.
3	Gr_L	Surface-length Grashof number (equation (3.45)).
3	h	Lubricant film thickness.
3	h_L	Surface-length heat convection coefficient.
3	k_{p}	Yield stress in simple shear of the material of the particle.
3	K	Equivalent thermal conductivity (equation (3.8)).
3	K_{fluid}	Thermal conductivity of the lubricant.
3	K_{p}	Thermal conductivity of the material of the particle.
3	K_{x}, K_{y}, K_{z}	Principal thermal conductivities (direction x, y or z).
3	K_1, K_2	Thermal conductivities of the counterfaces (counterface 1 or 2).
3	L	Integration reference length (equation (3.39)).
3	N_{s}	Number of sectors on a track (equation (3.18)).
3	N_{t}	Number of tracks on the particle.
3	Nu_L	Surface-length Nusselt number (equation (3.41)).
3	p	Pressure between the particle and the counterfaces.
3	Pr	Prandtl number (equation (3.44)).
3	q	Heat produced due to friction between a sector of the particle and a counterface (equation (3.3)).
3	q_{cool}	Heat emitted from a surface rectangle (of area S) of a counterface.
3	q_{e}	Heat of a sector that is transferred back to the counterfaces during a time step Δt (equation (3.27)).
3	q_{p}	Frictional heat of a sector due to the internal shearing of the particle, owing to the particle’s plastic compression (equation (3.21)).
3	$q_{\mathrm{p,conv}}$	Heat convected from a peripheral sector of the particle to the lubricant during a time step Δt (equation (3.35)).

Chapter	Symbol	Description
3	$q_{\mathrm{p,conv,total}}$	Total heat lost along particle's periphery during a time step Δt (equation (3.49)).
3	$q_{\mathrm{p,total}}$	Heat temporarily stored to a particle during a time step Δt (equation (3.26)).
3	$q_{\mathrm{p,1}}$, $q_{\mathrm{p,2}}$	Frictional heat generated at the interface of the particle and counterface 1 or 2.
3	Q	"Strength" of a heat source (see equation (3.5)).
3	r	Distance of a sector from the centre of the particle.
3	R	Radius of the deformed (disk-shaped) particle (equation (2.20)).
3	Ra_L	Surface-length Rayleigh number (equation (3.48)).
3	Re	Reynolds number.
3	Re_L	Surface-length Reynolds number (equation (3.42)).
3	S	Area of an elemental surface rectangle of a counterface.
3	$\overline{S}$	Integration area (see equations (3.52) and (3.53)).
3	t	Time.
3	t'	Time ($t' < t$).
3	U	Local speed of the fluid relatively to a sector (equation (3.43)).
3	V	Resultant speed of a sector of the particle relatively to a counterface (equation (3.2)).
3	V_{slid}	Sliding-speed component of a sector relatively to a counterface, due to the sliding motion of the particle as a rigid body (figure 3.1).
3	V_{x}, V_{y}	x and y-components of the speed of a sector of the particle relatively to a counterface (equations (3.1)).
3	V_{12}	Relative sliding speed of the counterfaces.
3	$\overline{x}$	Distance (see equations (3.15)).
3	x_{init}	Lower x-limit of the grid for the calculation of the convective heat losses (see equation (3.53)).
3	x_{fin}	Upper x-limit of the grid for the calculation of the convective heat losses (see equation (3.53)).

Chapter	**Symbol**	**Description**
3	x_{p}	The distance of the centre of the particle from the centre of the contact (given by x in equation (2.40)).
3	x_V	x-displacement of a point of the medium from time t' to time t (see equations (3.14)).
3	X	Transformed spatial variable (see equations (3.7)).
3	y_{fin}	Upper y-limit of the grid for the calculation of the convective heat losses (see equation (3.53)).
3	y_V	y-displacement of a point of the medium from time t' to time t (see equations (3.14)).
3	Y	Transformed spatial variable (see equations (3.7)).
3	Z	Transformed spatial variable (see equations (3.7)).
3	α	Heat partition coefficient.
3	α_1, α_2	Heat partition coefficients, giving the proportion of heat that goes to counterface 1 or 2.
3	β	Parameter (equations (3.46) and (3.47)).
3	β_{p}	Parameter (equation (3.22)).
3	β_{12}	Parameter (equation (3.32)).
3	δ	Parameter (equation (3.28)).
3	$\Delta\vartheta$	Angular integration step (equation (3.17)).
3	Δr	Spatial integration step (equation (3.16)).
3	Δt	Time step.
3	η	Local dynamic viscosity of the lubricant (see equation (2.30)).
3	ϑ	Angle (figure 3.1).
3	θ	Temperature (see equation (3.4)) or local skin temperature of a counterface, excluding heat convection from the counterface to the lubricant.
3	θ_{fluid}	Reference temperature of the fluid next to a particular peripheral sector of the particle.
3	θ_{p}	Temperature of a peripheral sector of the particle (equation (3.37)).
3	θ_0	Initial temperature.

Chapter	**Symbol**	**Description**
3	θ_1, θ_2	Local skin temperatures (counterface 1 or 2).
3	λ	Thermal diffusivity (see equation (3.4)).
3	λ_p	Thermal diffusivity of the material of the particle.
3	λ_x, λ_y, λ_z	Principal thermal diffusivities (direction x, y or z) (equation (3.11)).
3	$\lambda_{z,1}$	Principal thermal diffusivity of the material of counterface 1 in the z-direction.
3	μ	Coefficient of friction between the particle and a counterface.
3	μ_{int}	Friction coefficient between two internal layers of the plastically deforming particle (see equation (3.20)).
3	ρ	Material density.
3	ρ_{fluid}	Local density of the lubricant (see equation (2.31)).
4	b	Hertzian contact semi-width.
4	$c(x, y, z)$	Integration function (see equations (4.63), (4.64)).
4	c_1, c_2	Substitution variables (equations (4.73)).
4	E	Modulus of elasticity.
4	F_1	Substitution variable (equation (4.10)).
4	G	Shear modulus.
4	G_1	Substitution variable (equation (4.11)).
4	H_1	Substitution variable (equation (4.12)).
4	L	Lamé constant (equation (4.69)).
4	m	Substitution variable (equation (4.78)).
4	n	Substitution variable (equation (4.79)).
4	N	Total number of surface nodes.
4	N_{old}	Number of “old” nodes (see figure 4.3).
4	p	Solid pressure.
4	q_x, q_y	Surface tractions (direction x or y).
4	R	Radius of the deformed (disk-shaped) particle (see equation (2.20)).
4	t	Time.

Chapter	**Symbol**	**Description**
4	T	Temperature increment above the bulk temperature (flash temperature).
4	u	Elastic displacement in the x-direction.
4	$u_{\mathrm{x}}, u_{\mathrm{y}}, u_{\mathrm{z}}$	Elastic displacements (direction x, y or z).
4	w	Elastic displacement in the z-direction.
4	W	Load per unit length of the line contact of the counterfaces.
4	x_{p}	Distance of the centre of the particle from the centre of the Hertzian zone of the line contact of the counterfaces.
4	Y	Yield stress in uniaxial tension or compression.
4	α	Coefficient of linear thermal expansion.
4	γ	Elastic shear strain.
4	$\Delta x, \Delta y, \Delta z$	Spatial steps.
4	ε	Elastic normal strain.
4	$\varepsilon_x, \varepsilon_y, \varepsilon_z$	Elastic normal strains (direction x, y or z).
4	η	Integration variable.
4	λ	Thermal diffusivity.
4	ν	Poisson ratio.
4	ξ	Integration variable.
4	ρ	Substitution variable (equation (4.14)).
4	ρ_{m}	Material density.
4	$\sigma_{\mathrm{mechanical}}$	Mechanical normal stress.
4	$\sigma_{\mathrm{overall}}$	Overall normal stress (= mechanical + thermal).
4	$\sigma_{\mathrm{thermal}}$	Thermal normal stress.
4	$\sigma_x, \sigma_y, \sigma_z$	Elastic normal stresses (direction x, y or z).
4	$\sigma_x^{(\mathrm{Hertz})}, \sigma_z^{(\mathrm{Hertz})}$	Normal stresses (direction x or z), caused by a Hertzian loading in a non-conformal line contact (equations (4.75), (4.76)).
4	$\overline{\sigma}_{z,\mathrm{thermal}}^{(\psi)}$	Surface normal thermal stress in the z-direction, “produced” by the method of the “thermoelastic displacement potential”.
4	$\tau_{\mathrm{mechanical}}$	Mechanical shear stress.
4	τ_{overall}	Overall shear stress (= mechanical + thermal).

Chapter	Symbol	Description
4	τ_{thermal}	Thermal shear stress.
4	$\tau_x,\ \tau_y,\ \tau_z$	Elastic shear stresses (direction x, y or z).
4	$\tau_{zx}^{(\text{Hertz})}$	Shear stress, caused by a Hertzian loading in a non-conformal line contact (equation (4.77)).
4	$\bar{\tau}_{zx,\text{thermal}}^{(\psi)}$	Surface shear thermal stress, “produced” by the method of the “thermoelastic displacement potential”.
4	$\bar{\tau}_{zy,\text{thermal}}^{(\psi)}$	Surface shear thermal stress, “produced” by the method of the “thermoelastic displacement potential”.
4	υ	Elastic displacement in the y-direction.
4	υ_e	Speed of dilatational waves in a solid.
4	υ_θ	Speed of motion of the temperature field.
4	ψ	“Thermoelastic displacement potential”.
4	Ω	Substitution variable (equation (4.13)).
5	b	Hertzian contact semi-width (equation (2.2) and figure 2.1).
5	D	Diameter of the undeformed spherical particle.
5	D_{critical}	Critical diameter of an undeformed spherical particle in order to cause surface damage.
5	F_{dyn}	Fluid force on the particle, owing to the action of the dynamic fluid pressure on the particle (equations (2.25), (2.29)).
5	F_{fluid}	Overall fluid force on the particle (figure 2.7 and equation (2.39)).
5	F_{stat}	Fluid force on the particle, owing to the elastohydrodynamic-fluid-pressure gradient (equation (2.23)).
5	h	Elastohydrodynamic film thickness.
5	h_{c}	Central film thickness (figure 2.1).
5	H	Height of a sector (equation (5.6)).
5	m	Mass of the particle.
5	N_{y}	Number of sectors along the radius of the particle on the y-axis.
5	p	Solid pressure on the particle (figure 5.2).
5	p_{EHL}	Elastohydrodynamic pressure (figure 5.1).

Chapter	**Symbol**	**Description**
5	p_{old}	Pressure p calculated two steps previously in the convergence iteration scheme (see equation (5.22)).
5	p_{previous}	Pressure p calculated one step previously in the convergence iteration scheme (see equation (5.22)).
5	R	Radius of the deformed (disk shaped) particle during its deformation (figure 5.5, equations (5.24) and (2.20)).
5	R_{max}	Maximum radius of the disk-shaped (deformed) particle, which appears when the particle is in the Hertzian zone of the contact (equation (5.26)).
5	R_1, R_2	Radii of curvature of the counterfaces 1 and 2.
5	t	Time elapsed since the particle gets trapped.
5	T_1, T_2	Flash temperatures on counterfaces 1 and 2.
5	u	Surface elastic displacement in the x-direction.
5	u_1, u_2	Tangential speeds of the counterfaces (figure 2.1).
5	V_{extr}	Extrusion speed of the particle (equation (2.52), figure 5.12).
5	V_{p1}, V_{p2}	Speeds of a particle relatively to surfaces 1 and 2 (see figure 5.12, equations (2.45) and (2.46). See also section 2.7).
5	V_{s}	The sliding speed of the contact.
5	V_y	Magnitude of the y-component of the velocity vector of a sector relatively to the counterfaces (see equations (5.1)).
5	V_σ	Volume of the undeformed particle (see equation (5.23)).
5	V_1, V_2	Resultant speeds of a sector relatively to counterfaces 1 and 2 (equations (5.2)).
5	$V_{1,x}$, $V_{2,x}$	Magnitudes of the x-components of the velocity vectors of a sector relatively to counterfaces 1 or 2 (equations (5.1)).
5	w	Surface elastic displacement in the z-direction.
5	$\overline{w}_1, \overline{w}_2$	Surface normal displacements of counterfaces 1 and 2 (equation (5.7)).
5	$\overline{w}_{1,\text{mechanical}}$, $\overline{w}_{2,\text{mechanical}}$	Mechanical parts of $\overline{w}_1, \overline{w}_2$.

Chapter	**Symbol**	**Description**
5	$\overline{w}_{1,\text{normal}}, \overline{w}_{2,\text{normal}}$	Parts of $\overline{w}_1^{(\text{suppress})}, \overline{w}_2^{(\text{suppress})}$, owing to normal loads (equations (5.9)).
5	$\overline{w}_{1,\text{tangential}}$, $\overline{w}_{2,\text{tangential}}$	Parts of $\overline{w}_1^{(\text{suppress})}, \overline{w}_2^{(\text{suppress})}$, owing to tangential loads (equations (5.10)).
5	$\overline{w}_{1,\text{thermal}}, \overline{w}_{2,\text{thermal}}$	Thermal parts of $\overline{w}_1, \overline{w}_2$ (equations (5.11)).
5	$\overline{w}_1^{(\text{suppress})}, \overline{w}_2^{(\text{suppress})}$	Surface normal displacements of counterfaces 1 and 2 due to the action of a suppressive surface loading $\left\langle -\overline{\sigma}_{z,\text{thermal}}^{(\psi)}, -\overline{\tau}_{zx,\text{thermal}}^{(\psi)}, -\overline{\tau}_{zy,\text{thermal}}^{(\psi)} \right\rangle$ (equations (5.8)).
5	$\overline{w}_1^{(\psi)}, \overline{w}_2^{(\psi)}$	Surface normal displacements due to the application of the method of the “thermoelastic displacement potential”.
5	x	Distance of the centre of the particle disk from the centre of the contact (x = 0) (equations (2.40) and (2.43)).
5	$x_{t=0}$	Distance x at time t = 0 (point where the particle is first pinched).
5	x_{init}	Length (see equations (5.25) and figure 5.6).
5	$x_{\text{fin}}^{(\text{t=0})}$	Length (see equations (5.25) and figure 5.6).
5	$x_{\text{init}}^{(\text{t=0})}$	Length (see equations (5.25) and figure 5.6).
5	y_{fin}	y-limit of a grid (see equations (5.25)).
5	y_{init}	y-limit of a grid (see equations (5.25)).
5	Y_{p}	Yield stress in uniaxial compression of particle’s material.
5	z_{fin}	z-limit of a grid (see equations (5.25)).
5	z_{init}	z-limit of a grid (see equations (5.25)).
5	Z_1	Viscosity-pressure coefficient of the lubricant (see equation (2.30)).
5	δ	Under-relaxation factor (see equation (5.22)).
5	Δs	Length of the edge of the (square) base of a sector (equation (5.16)).
5	Δx, Δy, Δz	Spatial steps for the thermomechanical stress calculations in directions x, y and z.

Chapter	**Symbol**	**Description**
5	ϑ	Angle between axis x and the vector of the extrusion velocity (figure 3.1).
5	θ	Temperature.
5	θ_0	Bulk (initial, environmental) temperature.
5	μ	Average friction coefficient (equation 5.20)).
5	$\mu_1,\ \mu_2$	Coefficients of dynamic (sliding) friction between the particle and counterfaces 1 and 2.
5	$\tau_1,\ \tau_2$	Surface tractions (figure 5.2).
5	$\overline{\sigma}^{(\psi)}_{z,\text{thermal}}$	Surface normal thermal stress in the z-direction, “produced” by the method of the “thermoelastic displacement potential”.
5	$\overline{\tau}^{(\psi)}_{zx,\text{thermal}}$	Surface shear thermal stress, “produced” by the method of the “thermoelastic displacement potential”.
5	$\overline{\tau}^{(\psi)}_{zy,\text{thermal}}$	Surface shear thermal stress, “produced” by the method of the “thermoelastic displacement potential”.
5	υ	Surface elastic displacement in the y-direction.
5	$\varphi_1,\ \varphi_2$	Angles (equations (5.3)).

INTRODUCTION

From the outset of this research, the author was well aware of the risks involved when solid contaminants were allowed to be present in the lubrication zone of modern, high-performance Machine Elements. Numerous studies and industrial reports were already published, which showed that solid contaminants were responsible for a large proportion of reported failures and that lubricant cleanliness is a key factor in the long-term unproblematic operation of gears and bearings. What was not very clear and required further investigation was the mechanisms in which the contaminants are acting in their destructive work and *where* lies the limit between safe and unsafe operation of a contaminated contact.

Obviously, the previous questions are vital in understanding and predicting which environments are prone to failure and to undertake preventative measures, which will minimize the risk, without maximizing the operational cost. For example, typical filters in the bearing industry block particles usually not less than 10 μm, not because filters of 3 μm are not available, but because the finer the filter is, the higher is the running cost (fine filters clog more often, need regular attention, result in higher lubricant-pressure drops, etc.). Under this perspective, the effect of debris particles on the life of Machine Elements is, like all problems in Mechanical Engineering, a problem that has to be solved with a compromise between machine reliability and operational cost.

Leonardo da Vinci was probably among the first to report on the effects of debris particles in contacts, as early as in the 15th century. However, since the industrial revolution of the 19th century and until a few decades ago, the effects of dirt and dust in the operation of machine elements like gears and bearings was not given primary attention because:

(a) there were other primary sources of concern, like the cleanliness and homogeneity of steels, and

(b) the average lubrication film thickness and machine tolerances in typical industrial applications were substantially higher than these of today

With the evolution of high-speed/load components, the average lubricant film was gradually reduced to even sub-micron levels, and this brought in the foreground the influence of even the smallest particles wandering around in a lubrication environment. Bearing companies were particularly affected by the action of contamination particles because of the tolerances and speed, load and reliability demands associated with bearings. Since bearings are the most widely used Machine Elements, it is clear that whatever reduces their performance is a cause of major concern.

Debris particles are known to be responsible for increased wear. This wear has either one of the following forms.

(1) **Abrasion**. This wear-mode is associated with scratching/grooving of hard particles on usually softer surfaces, in contacts that involve sliding (as in gears). It can also appear in rolling contacts with low slide/roll ratios (as in rolling bearings). This is the most widely acknowledged debris-related wear mode and there are numerous publications dealing with the theoretical simulation and experimental study of this field (Rabinowicz and Mutis (1965), Larsen-Badse (1968a, 1968b), Richardson (1968), Chandrasekaran *et al*. (1985), Xuan *et al*. (1989), Williams and Hyncica (1992), Dwyer-Joyce *et al*. (1994) – these are just a few selected papers).

(2) **Indentation**. Debris dents are among the most commonly observed defects on bearing surfaces. Usually associated with the existence of hard particles, dents are areas where plastic flow has occurred, and thus, are "surrounded" by residual stresses (Ko and Ioannides (1989), Xu *et al*. (1997)). The mechanisms of debris indentations are a favorite subject in the literature, in both analytical and experimental studies (Hamer *et al*. (1987), Sayles and Ioannides (1988), Hamer *et al*. (1989b), Sayles *et al*. (1990), Hamer and Hutchinson (1992), Dwyer-Joyce (1993), Sayles (1995), Ville and Nelias (1997, 1998), Hamilton *et al*. (1998)). This popularity is sparkled by a serious cause: dents (especially those that have raised sharp shoulders, produced by hard particles) are directly related with surface fatigue in both dry contacts (Sayles, 1995) and elastohydrodynamic contacts (Venner and Lubrecht, 1994). The highly stressed areas around dents are precursors of cracks and result in rolling fatigue, significantly reducing the life of Machine Elements (Sayles and Ioannides, 1988). When sharp-edged dents are repeatedly over-rolled, cyclic edge stresses at their shoulders may lead to spalling

fatigue and even scuffing (Tallian, 1992). However, even smooth dents (caused by soft/ductile particles) are dangerous in elastohydrodynamic contacts because of the sudden loss of lubricant pressure (and corresponding film thinning or collapse) when these dents (or cavities) are over-rolled. Webster *et al*. (1986) showed analytically that stress peaks during the over-rolling of dents could be as much as three times greater than the subsurface stress maximum, resulting from a corresponding ideal Hertzian loading, and reported a 7-fold reduction in the fatigue life of rolling bearings tested under 40 μm filtration as compared with the fatigue life expected when a 3 μm filtration is used, the difference being attributed to the surface indentations.

(3) **Gross (macro) scuffing.** In recent years, it has been recognized that solid particles can obstruct the lubrication of contacts by accumulating in the inlet zone and preventing the lubricant replenishment of the contact (Wan and Spikes, 1986 and 1988). This led to a new postulate for the initiation of scuffing (Enthoven and Spikes, 1995), based on the fluid starvation and film collapse in elastohydrodynamic contacts, caused by wear-particle accumulation in the inlet zone.

(4) **Local (micro) scuffing.** Another perspective was put forward by Chandrasekaran *et al*. (1985) during scuffing tests in four-ball machines (sliding contact). They observed that the contamination of oil promoted scuffing. They postulated that a possible cause for this is the desorption of the lubricant when the contact temperature exceeds a certain limit, the temperature rise being caused by the frictional heating of the contaminants in the contact (because the particles were embedding one surface and were shearing on the other surface). Later, Khonsari and Wang (1990) were probably the first to present a theoretical analysis to study the frictional heating caused by a single hard particle when sliding on a surface, and proposed that this could explain some of the scuffing failures. A recent study follows on the same steps (Khonsari *et al*., 1999).

(5) **Spalling.** This is a rather limited and unknown debris-related failure mechanism. When soft/ductile particles are compressed, they reduce to sharp platelets, which are harder than the matrix particles due to plastic strain hardening. Due to this increased hardness, such platelets are prone to cause surface damage in sliding contacts where they shear and remove surface material. Moreover, in rolling elliptical contacts, such platelets can cause spalling (removal of surface material)

due to their spinning inside the contact, owing to the Heathcote differential slip effect (Chao *et al*., 1996).

The sources of debris in Machine Element environments are numerous. They can be both external and internal.

(a) External sources of debris.

The air and the lubricant are the most common bearers of foreign particles. When sealing is poor or has failed, debris (like for example dust) may intrude through any suitable opening (broken seals, labyrinth gaps, etc.).

(b) Internal sources of debris.

Sources of debris that are internal to machines involve worn surfaces (bearings, gears, seals) that lose fragments during operation, lubricant-born debris (deposits like soot and sludge during poor combustion in internal-combustion engines, grease thickeners, etc.), as well as components that were poorly cleaned before assembly (as for example, the gears or the shell in a gearbox).

Although a significant amount of research has been devoted the last decade in understanding the mechanisms of debris particle damage in concentrated contacts (Wan and Spikes (1986, 1988), Sayles and Ioannides (1988), Hamer *et al*. (1987, 1989a, 1989b), Dwyer-Joyce *et al*. (1992, 1994), Dwyer-Joyce (1993), Sayles (1995), Enthoven and Spikes (1995), Dwyer-Joyce and Heymer (1996), Hamilton *et al*. (1998), etc.), most studies are experimental and confined to particular cases, with simplifications that limit the general applicability of their results. Such simplifications are used to bypass the significant complexity of the general problem. A satisfactory global theoretical treatment is connected with complicated mathematics and requires the simultaneous use of tools from apparently different theories and sciences: Theory of Elasticity, Theory of Plasticity, Theory of Thermoelasticity, Theory of Elastohydrodynamic Lubrication (EHL), Contact Mechanics and even Chemistry. For a reader who will study this Thesis carefully, the previous statement will soon become clear. Moreover, existing models and studies are mainly confined to hard particles and rolling contacts, whereas soft/ductile contaminants and mixed rolling-sliding contacts remain a rather neglected part in the literature, especially by the non-existence of theoretical models.

It is this gap that the present theoretical study attempts to fill. With two theoretical models to cover the behaviour and effects from (mainly soft/ductile) particles in rolling-sliding, lubricated contacts, the study has reached some very important conclusions, which confirm existing experimental findings and, additionally, suggest new/suspected mechanisms of the behaviour of particles in concentrated contacts. Such important conclusions involve the following:

(1) Soft debris particles are sometimes even more destructive than equally sized hard particles. The reason is due to a thermomechanical wear mode predicted by the models of the Thesis and associated mainly with ductile particles.

(2) Particles are clearly shown to often accumulate in the inlet zone of lubricated contacts and cause lubricant starvation, <u>film collapse and even scuffing</u>.

(3) Soft particles are shown to cause frictional heating in contacts that involve sliding. The frictional heating can sometimes be so severe that the local temperature increase in the contact may exceed 2,000 °C! Surface melting and <u>local scuffing</u> due to the presence of <u>soft/ductile</u> particles in lubricated contacts is a new/strengthened theory that emerged from this study.

Other significant conclusions are listed at the end of each of chapters 1-5 and, collectively (main and brief conclusions only) in chapter 6.

Despite the amount of analytical work spent in this study, it is still only one step forward on a difficult and challenging path. The author kindly welcomes any suggestions for improvements and would be happy to contribute in further research on this field.

CHAPTER 1

ENTRAINMENT OF SOLID PARTICLES IN ELASTOHYDRODYNAMIC POINT CONTACTS

1.1 Introduction

It is well known that contamination particles in lubricating oils directly affect the operation and life expectancy of machine elements such as bearings, gears, cams and followers, etc. Experimental studies have shown that there is often a dramatic increase in surface wear when solid particles, even soft ones, interfere between two cooperating surfaces as, for example, between two gear teeth. A partial solution to this problem is the use of improved sealing techniques. However, this usually results in complicated design and increased running costs. A fine filter can collect most of the harmful particles but may become clogged and needs additional attention and more frequent replacement than a less fine filter. On the other hand, microscopic filtration results in fluid pressure-drop and energy losses. In practice, many hydraulic systems have bypass valves to avoid interruption of lubricant supply when a filter becomes severely clogged. This means that contamination particles may be given the chance to bypass the filters and enter the lubrication zone.

There are, however, two important issues, which must be taken into account.

(a) There are particles, which, under specific operating conditions of a lubricated contact, may not cause damage. The severity of possible damage depends on the ratio of the particles' hardness over the counterface hardness, the ratio of the particles' size over the central film thickness, the sliding and rolling velocity of the contact, the mechanical and thermal properties of the particles and the surfaces, etc.

(b) Some operational parameters of a contact, like the slide/roll ratio or the oil bath thickness, play a major role in the likelihood of particle entrapment. This has been shown experimentally in, for example, Wan and Spikes (1988), and Dwyer-Joyce and Heymer (1996). In this chapter, it is shown theoretically, too. A careful selection of these parameters, following the guidelines and results of the present work, may reduce (by design) the likelihood of particle entrapment, without the necessity to introduce improved filtering.

This chapter is devoted to the development of a theoretical model to simulate the entrainment process of small, spherical, solid particles in an EHD contact of a ball, sliding-rolling on a flat surface. Assuming a random distribution of particles in front of the moving ball, a 3-dimensional fluid flow analysis reveals the paths that particles are expected to follow and, as a result, the probability that a particle will end on the ball (collide with the ball) or bypass it. In the case of a particle ending on the ball, a mechanical force analysis can show if the particle is likely to be entrapped and pass under the ball, or get expelled from the contact. The case of a particle being entrapped is associated with surface damage due to denting or scratching/grooving. Finally, the case of a particle being expelled (possibly many times) is associated with fluid starvation due to particle accumulation in the inlet zone of the contact, which, if persistent, may result in scuffing.

The motion of particles in viscous fluids at low Reynolds number has attracted much attention in the past due to its significance in physical science and the chemical industry. There are studies dated as early as the analysis of Stokes in 1851, concentrating on the translation of rigid spheres through unbounded quiescent flows at very low Reynolds number. Extended theoretical analyses can be found in Jeffery (1922), Rubinow and Keller (1961), Bretherton (1962), Safman (1965), Leal (1979, 1980 - together with extensive bibliographic research), Brunn (1976a, 1976b, 1977), Drew (1978), and Sugihara-Seki (1993). The previous studies are all very complicated and concentrate mainly on the Fluid Mechanics aspects of the problem. The studies involve Newtonian and non-Newtonian (viscoelastic) fluids, one or more particles (mainly simulated by rigid spheres), and even account for the interactions among the particles due to fluid flow disturbances as well as electric forces (Saville, 1977). Recent studies, which are more tribology-oriented, can be found in Dai and Khonsari (1993), Dwyer-Joyce and Heymer (1996), and Kumar *et al*. (1997).

The present work is a much simplified one because it assumes that the fluid containing a contamination particle is undisturbed by the presence of the particle. However, this is not unrealistic if the following are taken into account:

- In the simulation, there is always only a single particle in the flow. Interactions with other particles are, hence, absent.
- The particle is quite small (size in the order of 1-50 μm). Pressure differences upstream and downstream of the particle are very low.
- The particle Reynolds number of the flow is very low (at the order of 10^{-3} up to 1). The local flow is creeping and micro-vortices are absent.
- The particle is considered spherical and rigid.
- The flow is essentially under constant environmental pressure.

In view of the previous considerations, the mathematical problem is satisfactorily well posed. It is noted that the intention of the present study is to concentrate on easily conceivable results, which can be put into practice with minimal effort and confusion. For this reason, it is intended that the results of this study (within the frames of mathematical completeness) be used by the practitioner rather than the mathematician.

1.2 Mathematical model

1.2.1 Solution of the fluid flow problem

The model involves a ball moving on a flat surface. The ball has a rolling velocity as well as a sliding velocity relative to the stationary surface. A view of the assembly can be seen in figure 1.1. The fluid flow in the oil bath is treated as 3-dimensional, despite the relatively thin film thickness h_{in}, which can be as low as a few microns for starved contacts. The following assumptions are made.

(1) The elastohydrodynamic pressure distribution is substituted by the well-known Hertzian pressure distribution for a point contact. As a matter of fact, it is known in the literature (see, for example, Hamrock, 1994) that the fluid pressure distribution is very close to that predicted by Hertz for a dry contact, the only

deviation being at the end of the Hertzian zone, where the elastohydrodynamic pressure spike exists (a nice figure is shown in Lin and Chu, 1991 (figure 4)). The latter is not a problem here because the last half of the Hertzian zone is not included in the study. Therefore, a Hertzian pressure distribution can be used as a good approximation.

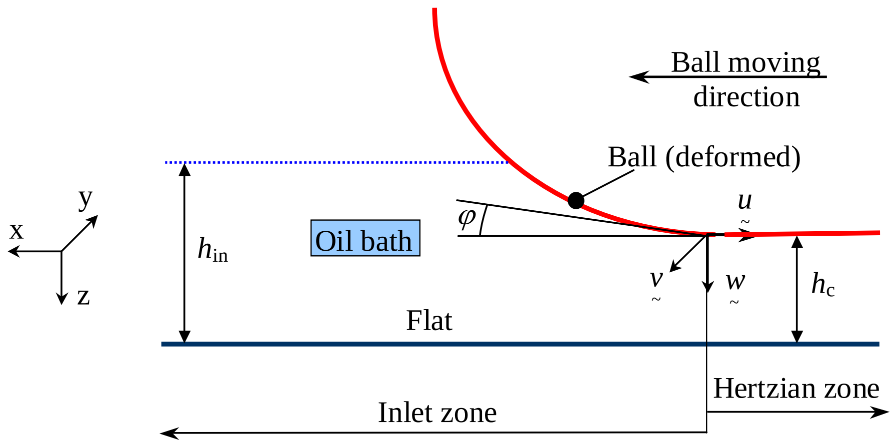

Figure 1.1 Configuration of the model; ball, flat surface and oil bath.

(2) The particles are assumed spherical. Although many shapes can be considered, the sphere is the simplest one and is the best starting point for the analysis.

(3) Particles which have a mean diameter D smaller than the central film thickness h_c of the contact (figure 1.1) are not of concern in this study. Therefore, only particles with $D > h_c$ are studied here. This means that particles cannot enter "deep" inside the inlet zone of the contact without being compressed. Thus, for the area of application of the present simulation, particles travel in an environment (oil bath) where the fluid static pressure is equal to the environmental pressure (as opposed to the elastohydrodynamic pressure, which is much higher).

(4) The fluid flow is assumed unchanged in time. The study involves one particle at a time, so that the fluid flow is minimally disturbed by particle's presence.

In the area of study (inlet zone), the fluid pressure, according to the assumption (3) above, is constant. The same is true for the temperature. Consequently, lubricant's viscosity and density in the inlet zone are both constant, since these two properties are functions of the pressure and temperature. The flow in this area is actually similar to a channel flow and, hence, is treated as incompressible.

Gathering all assumptions made previously, the flow is treated as 3-dimensional, steady state, viscous and incompressible. The Navier-Stokes equations for this type of problem are as follows.

$$u \cdot \frac{\partial u}{\partial x} + v \cdot \frac{\partial u}{\partial y} + w \cdot \frac{\partial u}{\partial z} = \nu \cdot \left(\frac{\partial^2 u}{\partial x^2} + \frac{\partial^2 u}{\partial y^2} + \frac{\partial^2 u}{\partial z^2} \right) \tag{1.1}$$

$$u \cdot \frac{\partial v}{\partial x} + v \cdot \frac{\partial v}{\partial y} + w \cdot \frac{\partial v}{\partial z} = \nu \cdot \left(\frac{\partial^2 v}{\partial x^2} + \frac{\partial^2 v}{\partial y^2} + \frac{\partial^2 v}{\partial z^2} \right) \tag{1.2}$$

$$u \cdot \frac{\partial w}{\partial x} + v \cdot \frac{\partial w}{\partial y} + w \cdot \frac{\partial w}{\partial z} = \nu \cdot \left(\frac{\partial^2 w}{\partial x^2} + \frac{\partial^2 w}{\partial y^2} + \frac{\partial^2 w}{\partial z^2} \right) \tag{1.3}$$

where ν is the kinematic viscosity of the lubricant at environmental conditions. The systems of coordinates xyz and fluid velocity components $\underset{\sim}{u}$, $\underset{\sim}{v}$ and $\underset{\sim}{w}$ are shown in figure 1.1. Equations (1.1)-(1.3) are discretized through a second order, finite difference scheme. The solution domain is shown in figure 1.2. The dimensions of the reference fluid volume are: $L \geq 10 \cdot R_H$ and $S \geq 2 \cdot R_H$, where R_H is the radius of the Hertzian contact circle. The lower boundary of the reference volume is the flat, whereas the upper boundary is the free surface of the lubricant and the wall of the ball. Thus, the reference volume has a thickness that varies from h_c to h_{in}. The grid in figure 1.2 is constructed of nodes, which are equidistant in both the x and y-direction. Thus, spatial steps Δx and Δy are constant. Step Δz along the z-axis varies depending on the (x,y) position, as is explained later.

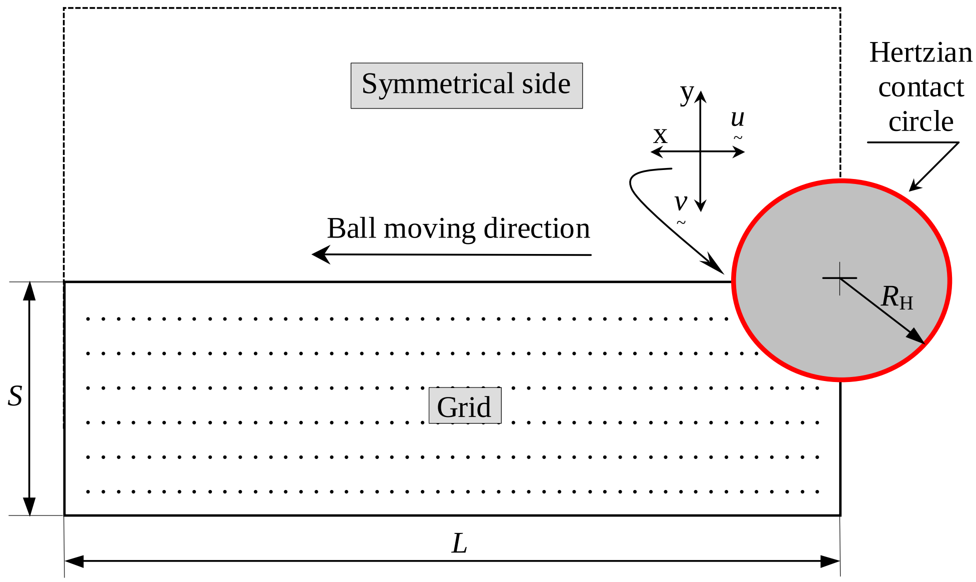

Figure 1.2 Reference volume and grid.

After discretization, equations (1.1)-(1.3) are written as follows:

$$u \cdot \frac{3 \cdot u - 4u_{i-1} + u_{i-2}}{2 \cdot \Delta x} + v \cdot \frac{3 \cdot u - 4 \cdot u_{j-1} + u_{j-2}}{2 \cdot \Delta y} + w \cdot \frac{3 \cdot u - 4 \cdot u_{k-1} + u_{k-2}}{2 \cdot \Delta z} =$$
$$= \nu \cdot \left[\frac{u - 2 \cdot u_{i-1} + u_{i-2}}{(\Delta x)^2} + \frac{u - 2 \cdot u_{j-1} + u_{j-2}}{(\Delta y)^2} + \frac{u - 2 \cdot u_{k-1} + u_{k-2}}{(\Delta z)^2} \right] \tag{1.4}$$

$$u \cdot \frac{3 \cdot v - 4v_{i-1} + v_{i-2}}{2 \cdot \Delta x} + v \cdot \frac{3 \cdot v - 4 \cdot v_{j-1} + v_{j-2}}{2 \cdot \Delta y} + w \cdot \frac{3 \cdot v - 4 \cdot v_{k-1} + v_{k-2}}{2 \cdot \Delta z} =$$
$$= \nu \cdot \left[\frac{v - 2 \cdot v_{i-1} + v_{i-2}}{(\Delta x)^2} + \frac{v - 2 \cdot v_{j-1} + v_{j-2}}{(\Delta y)^2} + \frac{v - 2 \cdot v_{k-1} + v_{k-2}}{(\Delta z)^2} \right] \tag{1.5}$$

$$u \cdot \frac{3 \cdot w - 4w_{i-1} + w_{i-2}}{2 \cdot \Delta x} + v \cdot \frac{3 \cdot w - 4 \cdot w_{j-1} + w_{j-2}}{2 \cdot \Delta y} + w \cdot \frac{3 \cdot w - 4 \cdot w_{k-1} + w_{k-2}}{2 \cdot \Delta z} =$$
$$= \nu \cdot \left[\frac{w - 2 \cdot w_{i-1} + w_{i-2}}{(\Delta x)^2} + \frac{w - 2 \cdot w_{j-1} + w_{j-2}}{(\Delta y)^2} + \frac{w - 2 \cdot w_{k-1} + w_{k-2}}{(\Delta z)^2} \right] \tag{1.6}$$

Boundary conditions

On the flat and the ball's wall, the lubricant can neither penetrate nor slip. These constraints are translated into the following equations:

$$u_{k=2} \cong u_{k=1} = \frac{u_{\mathrm{a}}}{R} \cdot \sqrt{R^2 - [(j-1) \cdot \Delta y]^2} \cdot \cos(\varphi) - u_{\mathrm{a}} - V_s \tag{1.7}$$

$$v_{i=1} = w_{i=1} = 0 \tag{1.8}$$

$$u_{k=N} = v_{k=N} = w_{k=N} = 0 \tag{1.9}$$

where:

u_{a} is the rolling velocity of the ball (position $y = 0$),

R is the radius of the ball,

Δy is the spatial step in the y-direction,

V_s is the sliding velocity of the ball relatively to the flat,

φ is the angle of the tangent to the ball's wall (figure 1.1),

N is the number of the k-nodes along axis z ($k = N$ is for the node on the flat).

The coordinate systems shown in figure 1.2 have their common origin located at position $(i,j,k) = (3,1,1)$, which is on the boundary of the Hertzian contact circle. The symmetry of the flow about plane $y = 0$ is taken into account and the solution domain is the $y < 0$ half-space (figure 1.2). Speeds u, v and w in the two half-spaces $y < 0$ and $y > 0$ are as follows:

$$u_{y<0} = u_{y>0} \quad , \quad v_{y<0} = -v_{y>0} \quad , \quad w_{y<0} = w_{y>0} \tag{1.10}$$

In order to proceed with the solution, the following substitutions are made:

$$\mathrm{a} \equiv \frac{1}{2 \cdot \Delta x} \tag{1.11}$$

$$b \equiv \frac{1}{2 \cdot \Delta y} \tag{1.12}$$

$$c \equiv \frac{1}{2 \cdot \Delta z} \tag{1.13}$$

$$d \equiv \frac{\nu}{(\Delta x)^2 + (\Delta y)^2 + (\Delta z)^2} \tag{1.14}$$

$$C_1 \equiv -4 \cdot u_{i-1} + u_{i-2} \tag{1.15}$$

$$C_2 \equiv -4 \cdot u_{j-1} + u_{j-2} \tag{1.16}$$

$$C_3 \equiv -4 \cdot u_{k-1} + u_{k-2} \tag{1.17}$$

$$C_4 \equiv -4 \cdot v_{i-1} + v_{i-2} \tag{1.18}$$

$$C_5 \equiv -4 \cdot v_{j-1} + v_{j-2} \tag{1.19}$$

$$C_6 \equiv -4 \cdot v_{k-1} + v_{k-2} \tag{1.20}$$

$$C_7 \equiv -4 \cdot w_{i-1} + w_{i-2} \tag{1.21}$$

$$C_8 \equiv -4 \cdot w_{j-1} + w_{j-2} \tag{1.22}$$

$$C_9 \equiv -4 \cdot w_{k-1} + w_{k-2} \tag{1.23}$$

$$e_1 \equiv \nu \cdot \left[\frac{-2 \cdot u_{i-1} + u_{i-2}}{(\Delta x)^2} + \frac{-2 \cdot u_{j-1} + u_{j-2}}{(\Delta y)^2} + \frac{-2 \cdot u_{k-1} + u_{k-2}}{(\Delta z)^2} \right] \tag{1.24}$$

$$e_2 \equiv \nu \cdot \left[\frac{-2 \cdot v_{i-1} + v_{i-2}}{(\Delta x)^2} + \frac{-2 \cdot v_{j-1} + v_{j-2}}{(\Delta y)^2} + \frac{-2 \cdot v_{k-1} + v_{k-2}}{(\Delta z)^2} \right] \tag{1.25}$$

$$e_3 \equiv \nu \cdot \left[\frac{-2 \cdot w_{i-1} + w_{i-2}}{(\Delta x)^2} + \frac{-2 \cdot w_{j-1} + w_{j-2}}{(\Delta y)^2} + \frac{-2 \cdot w_{k-1} + w_{k-2}}{(\Delta z)^2} \right] \tag{1.26}$$

Using substitutions (1.11)-(1.26), the system of equations (1.4)-(1.6) is transformed as follows:

$$\mathrm{a} \cdot u \cdot (3 \cdot u + C_1) + b \cdot v \cdot (3 \cdot u + C_2) + c \cdot w \cdot (3 \cdot u + C_3) = d \cdot u + e_1 \tag{1.27}$$

$$\mathrm{a} \cdot u \cdot (3 \cdot v + C_4) + b \cdot v \cdot (3 \cdot v + C_5) + c \cdot w \cdot (3 \cdot v + C_6) = d \cdot v + e_2 \tag{1.28}$$

$$\mathrm{a} \cdot u \cdot (3 \cdot w + C_7) + b \cdot v \cdot (3 \cdot w + C_8) + c \cdot w \cdot (3 \cdot w + c_9) = d \cdot w + e_3 \tag{1.29}$$

The Jacobian determinant of the previous system of equations (1.27)-(1.29) is:

$$|\mathbf{J}| = \begin{vmatrix} \mathrm{a}_1 & \mathrm{a}_2 & \mathrm{a}_3 \\ \mathrm{a}_4 & \mathrm{a}_5 & \mathrm{a}_6 \\ \mathrm{a}_7 & \mathrm{a}_8 & \mathrm{a}_9 \end{vmatrix} \tag{1.30}$$

where

$$\mathrm{a}_1 \equiv 3 \cdot (\mathrm{a} \cdot u + b \cdot v + c \cdot w) + \mathrm{a} \cdot (3 \cdot u + C_1) - d \tag{1.31}$$

$$\mathrm{a}_2 \equiv b \cdot (3 \cdot u + C_2) \tag{1.32}$$

$$\mathrm{a}_3 \equiv c \cdot (3 \cdot u + C_3) \tag{1.33}$$

$$a_4 \equiv a \cdot (3 \cdot v + C_4) \tag{1.34}$$

$$a_5 \equiv 3 \cdot (a \cdot u + b \cdot v + c \cdot w) + b \cdot (3 \cdot v + C_5) - d \tag{1.35}$$

$$a_6 \equiv c \cdot (3 \cdot v + C_6) \tag{1.36}$$

$$a_7 \equiv a \cdot (3 \cdot w + C_7) \tag{1.37}$$

$$a_8 \equiv b \cdot (3 \cdot w + C_8) \tag{1.38}$$

$$a_9 \equiv 3 \cdot (a \cdot u + b \cdot v + c \cdot w) + c \cdot (3 \cdot w + C_9) - d \tag{1.39}$$

Equations (1.27)-(1.29) form a non-linear system, which is solved here by the Newton-Raphson method. The method is expressed by the following iterative equation:

$$\underset{\sim}{x}^{(k+1)} = \underset{\sim}{x}^{(k)} - \frac{1}{|\mathbf{J}|} \cdot \mathbf{J}^* \cdot \underset{\sim}{f} \tag{1.40}$$

where

$$\underset{\sim}{x} = (u,v,w)^T \tag{1.41}$$

$$\underset{\sim}{f} = \begin{pmatrix} a \cdot u \cdot (3 \cdot u + C_1) + b \cdot v \cdot (3 \cdot u + C_2) + c \cdot w \cdot (3 \cdot u + C_3) - d \cdot u - e_1 \\ a \cdot u \cdot (3 \cdot v + C_4) + b \cdot v \cdot (3 \cdot v + C_5) + c \cdot w \cdot (3 \cdot v + C_6) - d \cdot v - e_2 \\ a \cdot u \cdot (3 \cdot w + C_7) + b \cdot v \cdot (3 \cdot w + C_8) + c \cdot w \cdot (3 \cdot w + C_9) - d \cdot w - e_3 \end{pmatrix} \tag{1.42}$$

and the adjoint matrix $\mathbf{J}^*$ is

$$\mathbf{J}^* = \begin{pmatrix} J_{11} & J_{21} & J_{31} \\ J_{12} & J_{22} & J_{32} \\ J_{13} & J_{23} & J_{33} \end{pmatrix} \tag{1.43}$$

whereas

$$J_{11} = a_5 \cdot a_9 - a_6 \cdot a_8 \tag{1.44}$$

$$J_{21} = a_3 \cdot a_8 - a_2 \cdot a_9 \tag{1.45}$$

$$J_{31} = a_2 \cdot a_6 - a_3 \cdot a_5 \tag{1.46}$$

$$J_{12} = a_6 \cdot a_7 - a_4 \cdot a_9 \tag{1.47}$$

$$J_{22} = a_1 \cdot a_9 - a_3 \cdot a_7 \tag{1.48}$$

$$J_{32} = a_3 \cdot a_4 - a_1 \cdot a_6 \tag{1.49}$$

$$J_{13} = a_4 \cdot a_8 - a_5 \cdot a_7 \tag{1.50}$$

$$J_{23} = a_2 \cdot a_7 - a_1 \cdot a_8 \tag{1.51}$$

$$J_{33} = a_1 \cdot a_5 - a_2 \cdot a_4 \tag{1.52}$$

Because of the high non-linearity of the system, the version of the Newton-Raphson method used here is a globally convergent one, with line search and backtracking to guarantee the convergence of the algorithm regardless of the initial guess (Press *et al.*, 1992, section 9.7). Moreover, the results for speeds u and v are checked and, if necessary, corrected, using the boundary conditions and especially their accurately known values at planes i = 1 and j = 1.

Particle trajectories, as is shown later, are calculated using only the $\underset{\sim}{u}$ and $\underset{\sim}{v}$ velocity components. The results for the $\underset{\sim}{w}$ component are not used further in the analysis. Therefore, although the solution obtained for the flow field is 3-dimensional, particle trajectories are calculated on the xy-plane (figure 1.1), using speeds u and v averaged along axis z, as if the problem were 2-dimensional. The omission of the $\underset{\sim}{w}$ velocity component is done for two reasons:

(a) to simplify calculations, and
(b) because the thickness of the reference volume (z-direction) is much smaller than the other two principal dimensions.

The accuracy of the calculations can be improved by checking the continuity of flow and applying appropriate corrections to intermediate results. This means that after solving the system of equations (1.4)-(1.6) in the whole grid, a check at the equation of mass conservation

$$\frac{\partial u}{\partial x}+\frac{\partial v}{\partial y}+\frac{\partial w}{\partial z}=0 \tag{1.53}$$

and proper re-adjustment of the results must be done, followed by a new solution of the equations until convergence is achieved.

1.2.2 Initial position and motion of a particle

Particles are treated as spheres throughout this study. Because of their smallness, their real shape is not crucial when considering fluid forces on them. It is definitely more important to think of their actual shape when they are pinched between the ball and the flat, but this is the subject of section 1.2.3.

The distribution of particles at time $t = 0$ when the study of the history of each particle starts, is generally random. Although the mass concentration of particles in the inlet of the contact may be more-or-less known, the number of particles in the reference volume (figure 1.2) may vary significantly, especially when considering possible turbulence and other transient phenomena. For example, it is well known that, in a set of spur gears, lubricant is trapped between two engaging teeth, resulting in a strong and noisy jet of fluid passing through the gap of the closing teeth with, sometimes, sonic or supersonic speeds. It is rather obvious that this affects the concentration of particles in the fluid in a rather unpredictable way.

The analysis following in the next pages does not account for possible interactions among neighboring particles. These interactions could be of the following origin.

(a) Particle collisions.

(b) Electromagnetic and adhesion forces when particles come very close, or touch each other.

This simplification is not a great disadvantage of the analysis because of the following reasons.

(a) Even one isolated particle gives plenty of information regarding what is expected to happen in the contact when more particles are considered simultaneously.

(b) A single particle, if large enough, is possible to initiate a cumulative process which leads to fluid starvation by, for example, remaining in the inlet zone for long enough time as to allow other particles to accumulate and obstruct the flow of the lubricant.

In the next step of the present analysis, a single particle is put at a randomly chosen position in the lower half of the reference volume (figure 1.2). Coordinates x_0 and y_0 of the initial position of the particle are defined by the following equations:

$$x_0 = \left(R_{\mathrm{H}} \cdot N_x - r_{\mathrm{a}}\right) \cdot ran1 + r_{\mathrm{a}} \tag{1.54}$$

$$y_0 = R_{\mathrm{H}} \cdot N_y \cdot ran1 \tag{1.55}$$

The radius R_{H} of the Hertzian contact circle (figure 1.2) is:

$$R_{\mathrm{H}} = \left(\frac{3 \cdot P \cdot R}{2 \cdot E}\right)^{\frac{1}{3}} \tag{1.56}$$

where P is the load on the ball, R is the radius of the ball, and E is the effective modulus of elasticity

$$E = \frac{2}{\frac{1-\nu_1^2}{E_1} + \frac{1-\nu_2^2}{E_2}} \tag{1.57}$$

where E_1, E_2 and ν_1, ν_2 are the moduli of elasticity and the Poisson ratios of the materials of the ball and the flat respectively.

"*ran*1" is a random number between 0 and 1. In order to obtain such a number, Press *et al.*, 1992 (p. 271) propose a random number generator, which is used in the present study.

N_x and N_y are integer numbers, given by the following equations:

$$N_x \equiv \frac{L}{R_\mathrm{H}} \tag{1.58}$$

$$N_y \equiv \frac{S}{R_\mathrm{H}} \tag{1.59}$$

where L and S are the length and semi-width of the reference volume, as is shown in figure 1.2.

Finally, r_a is the radius of the imaginary circle where the particle comes in contact with both the ball and the flat. This is the smallest distance from the nominal point of contact (centre of the Hertzian circle), where the particle is still undeformed; it can be calculated with very good approximation from the following equation:

$$h(r_\mathrm{a}) = D \tag{1.60}$$

where D is the particle's diameter and h is the fluid film thickness

$$h = h_\mathrm{c} + R \cdot \left[1 - \sqrt{1 - \left(\frac{r}{R}\right)^2}\,\right] + \upsilon(r) - \upsilon(0) \tag{1.61}$$

where r is the distance from the centre of the Hertzian contact circle (nominal point of "contact")

$$r = \sqrt{x^2 + y^2} \tag{1.62}$$

and $\upsilon(r)$ is the sum of the surface displacements of the ball and the flat (due to the elastohydrodynamic pressure) at a distance r from the nominal point of contact.

Equation (1.60) "says" that at the distance r_a from the centre of the Hertzian contact circle, where the particle is in contact with both the ball and the flat, the distance between the ball's wall and the flat is equal to the diameter of the particle. This is so because the deformed surfaces of the ball and the flat near the Hertzian contact circle are nearly parallel, according to the simplified EHL theory.

The central film thickness appearing in equation (1.61) can be calculated by any known semi-empirical formula for point contacts, as the following:

$$h_c = 1.9 \cdot R \cdot U^{0.67} \cdot G^{0.53} \cdot W^{-0.067} \tag{1.63}$$

where U, G and W are the usual speed, material and load dimensionless parameters respectively, found in modern literature (see for example Hamrock, 1994, page 437).

Spatial steps Δx and Δy, which define the distance of two neighboring nodes in the x and y-direction respectively (figure 1.2), are constant, as already mentioned. Step Δz along the z-axis is variable and is defined by the following equation:

$$\Delta z \triangleq \frac{\min\{h_{in}, h\}}{I_z - 1} \tag{1.64}$$

where h_{in} is the oil bath thickness (figure 1.1), I_z is the fixed number of k-nodes along the z-axis, and h is taken from equation (1.61). A variable step Δz is used in order to reduce the number of k-nodes (nodes along the z-axis) and, therefore, the overall number of grid nodes and the computer CPU (Central Processing Unit) time needed to obtain a solution, without significant loss of accuracy.

Particle motion is studied in two dimensions, namely in x and y. Weight and (fluid) lift, which are forces along the z-axis, are neglected. As has already been explained, this is done primarily because the thickness of the reference volume is very small compared with its other two dimensions, and secondly, because particle's vertical motion is not of great concern in this study. Conclusively, only inertia and fluid drag forces are taken into account. If the particle reaches the critical zone $r = r_a$, then solid frictional forces between the particle and the surrounding surfaces are taken into account as well, and this is studied in section 1.2.3.

From the force equilibrium on the particle along the x-axis, the following equation is derived:

$$C_D \cdot \frac{1}{2} \cdot \rho \cdot u_{\text{ave}}^2 \cdot \frac{\pi}{4} \cdot D^2 = m \cdot \ddot{x} \tag{1.65}$$

where ρ is the density of the fluid. Similarly, in direction y:

$$C_D \cdot \frac{1}{2} \cdot \rho \cdot v_{\text{ave}}^2 \cdot \frac{\pi}{4} \cdot D^2 = m \cdot \ddot{y} \tag{1.66}$$

The left side of equations (1.65) and (1.66) is the fluid force component on the particle. This is the fluid drag, which pushes the particle to follow the streamlines of the flow. It is thus implied that the motion of the particle is solely due to the Stokes drag force applied to it from the fluid.

In the present analysis, there is nothing to prevent the particle from having a rotational speed as it translates in the fluid. It has actually been shown that a spinning spherical particle experiences a transverse force, known as “lift” force, which is perpendicular to the drag force (see for example Rubinow and Keller (1961), and Saffman (1965)). However, the previous researchers have shown that this lift force is usually very small compared to the drag force for creeping flows – usually more than one order of magnitude lower (Saffman (1965) – page 394, Drew (1978) – page 399). Such a force accounts for the curving of a pitched baseball or golf ball (Rubinow and Keller, 1961). In order to quantify the effect of this transverse force in the present analysis, the author followed Rubinow and Keller (1961 – page 454). According to their paper, the ratio of the drag forge over the “lift” force under consideration is

$$\frac{\text{Drag force}}{\text{"Lift" force}} \cong \frac{6 \cdot \eta}{D^2 \cdot \rho \cdot \omega}$$

where η is the dynamic viscosity of the fluid, D is particle's diameter, ρ is the density of the fluid, and ω is the rotational speed of the particle. Using the results of the present study, as these are presented in section 1.3 later and in table 1.1, it is found that, in order for the lift force to be of the same order of magnitude as the drag force, the particle must have a rotational speed (spin) of the order of $67 \cdot 10^6$ rpm! Even if the spinning speed of the particle is around 10^6 rpm, the lift force is 67 times lower than the drag force. Since such a high rotational speed is unrealistic in our case, it is inferred that the transverse (lift) force on the particle is infinitesimal and, therefore, can be omitted in the calculations. (Trying to check a "worse" case scenario, the author calculated a lift force that is 875 times lower than the drag force, but it must be noted that even this example could not be encountered in reality.)

Proceeding with the analysis, the fluid drag coefficient C_D is a function of the particle Reynolds number $\mathrm{Re_p}$ of the flow. Due to the smallness of the particle, it is assumed that the flow is creeping ($\mathrm{Re_p} < 1$). For a sphere in creeping flow, the fluid drag coefficient is (see Munson *et al*. (1990), Table 9.4, page 611):

$$C_D \cong \frac{24}{\mathrm{Re_p}} \tag{1.67}$$

where

$$\mathrm{Re_p} \equiv \frac{D \cdot U}{\nu} \tag{1.68}$$

where U is the speed of the fluid relatively to the sphere (particle). The validity of equation (1.67) is actually checked at each node in the reference volume of the flow. It is indeed found that, for a typical case, $\mathrm{Re_p} < 1$, as is shown in the detailed examples in section 1.3. Therefore, the use of equation (1.67) is fully justified.

Using classical second order, central, finite, time differences, equations (1.65) and (1.66) are discretized as follows:

$$x_{t+\Delta t} \cong \frac{-3 \cdot \pi \cdot \rho \cdot \mathrm{sgn}(u_{\mathrm{ave}}) \cdot (u_{\mathrm{ave}} \cdot D \cdot \Delta t)^2}{m \cdot \mathrm{Re_x}} + 2 \cdot x_t - x_{t-\Delta t} \tag{1.69}$$

$$y_{t+\Delta t} \cong \frac{3 \cdot \pi \cdot \rho \cdot (v_{\text{ave}} \cdot D \cdot \Delta t)^2}{m \cdot \text{Re}_{\text{y}}} + 2 \cdot y_t - y_{t-\Delta t} \tag{1.70}$$

where Re_x and Re_y are the corresponding Reynolds numbers using the fluid velocity component in the x and y-direction respectively, and sgn(x) is the sign function of variable x:

$$\text{sgn}(x) \equiv \begin{cases} +1 & \text{if } x > 0 \\ -1 & \text{if } x < 0 \end{cases} \tag{1.71}$$

u_{ave} and v_{ave} are averaged values of the u and v-speeds in the x and y-direction respectively, along a length equal to the particle's diameter D. For example, if $D \cong 4 \cdot \Delta x$, then u_{ave} is the arithmetic mean value of the u-speeds at five nodes in the neighborhood of the particle.

If $u_{\text{ave}} = 0$, then of course $x_{t+\Delta t} = x_t$. Similarly, if $v_{\text{ave}} = 0$, then $y_{t+\Delta t} = y_t$. In reality, the previous two conditions are never (mathematically) met and can be considered as mathematical simplifications.

1.2.3 Modelling the way a particle is entrapped or expelled

Regarding the simple question *"Is a particle to be entrapped or expelled from the contact?"*, the answer does not come easily. This is because the shape of the particle as well as the exact shape of the elastically deformed surfaces (including surface roughness) is not accurately known. Moreover, the friction coefficient between the particle and each surrounding surface in the contact is not precisely known and can vary significantly, not only by choosing a different lubrication regime as a basis for the study, but also within the frame of a specific lubrication regime. One may argue that the solid friction coefficient between a particle and a lubricated surface at light loads can be considered approximately equal to that for boundary lubrication (roughly around 0.1 - see for example figure 1.8 in Hamrock, 1994). For hard particles with irregular shapes, it is more difficult to evaluate a representative value of the friction coefficient than in the case of particles with smooth appearance.

Thankfully, the results of this study (presented in section 1.3) suggest that the value of the solid friction coefficient used in the calculations is not as critical as it seems to be. The reason for this may be the fact that the friction coefficient for the contact of the particle and the ball, and the one for the contact of the particle and the flat, are considered to be close to each other, which is a realistic assumption. Larger discrepancies are expected when the latter is not met. The computer program written for this study can easily evaluate the effect of the operational parameters of the problem, friction coefficients included.

In the next step of the analysis, the following two assumptions are made.

(1) Particles are considered spherical. Although it is understood that many particle shapes exist in reality, there must be a starting point in the analysis and an equivalent spherical particle is not an unrealistic assumption.

(2) The unperturbed elastohydrodynamic pressure distribution between the ball and the flat is the one predicted by the Hertzian theory for dry point contacts. EHL theory has shown repeatedly with good approximation (see for example Hamrock, 1994, chapter 22, and Venner, 1991, chapter 9) that this *is* indeed the case, at least in the inlet and first-half of the Hertzian zone, including the second trailing half of the Hertzian zone if the contact is heavily loaded (which results in a decreased pressure spike). Since the reference volume and grid in this study (figure 1.2) cover the inlet zone and the first half of the Hertzian zone, assumption (2) is fully justified.

In figure 1.3, a particle is shown in touch with both the ball and the flat, in the $y < 0$ half-space. Figure 1.3 shows the particle at the critical distance r_a, in the inlet zone of the contact. Frictional forces $\underset{\sim}{T}_1$ and $\underset{\sim}{T}_2$ are on the plane where the sliding-velocity vector of the contact is lying (plane xz). On the other side, frictional forces $\underset{\sim}{T}_3$ and $\underset{\sim}{T}_4$ lie on plane yz, which is perpendicular to the direction of the sliding velocity of the contact. The latter forces arise due to the compression of the particle and the curvature of the distorted surfaces on plane yz. Normal forces $\underset{\sim}{N}_1$ and $\underset{\sim}{N}_2$ are due to the reaction of the particle to its compression between the ball and the flat.

The coordinate system shown in figure 1.3 has its origin O located at point (0,0,0), which is the centre of the Hertzian contact circle, <u>on the wall</u> of the distorted ball.

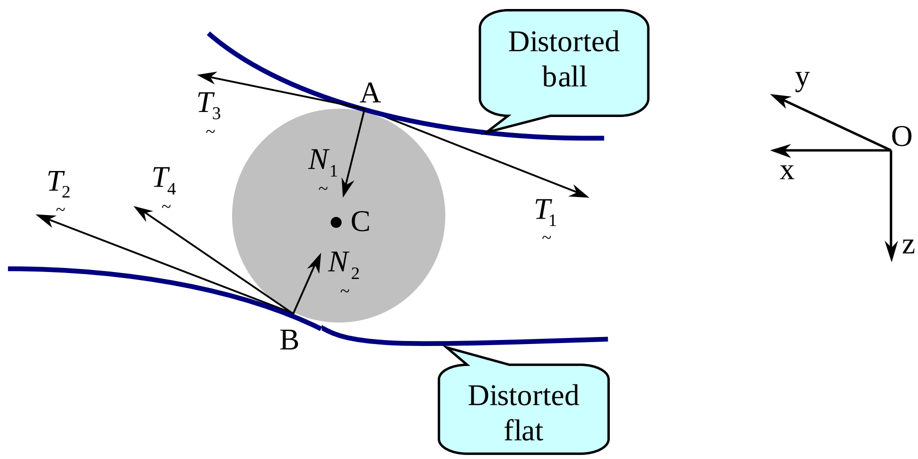

$A \leftrightarrow (x_A, y_A, z_A)$, $B \leftrightarrow (x_B, y_B, z_B)$, $C \leftrightarrow (x_C, y_C, z_C)$, $O \leftrightarrow (0,0,0)$

Figure 1.3 Solid frictional forces ($\underset{\sim}{T}_1$ and $\underset{\sim}{T}_2$ on plane xz, $\underset{\sim}{T}_3$ and $\underset{\sim}{T}_4$ on plane yz) and normal forces ($\underset{\sim}{N}_1$ and $\underset{\sim}{N}_2$) on the particle.

From the geometry of the contact and after a lot of algebraic manipulation, the distorted surface profiles of the ball (z_1) and the flat (z_2) outside circle $r = r_a$, due to the Hertzian pressure field, are described by the following equations:

$$z_1 = \frac{1-\nu_1^2}{E_1} \cdot \frac{p_H \cdot R_H}{2} \cdot \left\{ \left[2 - \left(\frac{r}{R_H} \right)^2 \right] \cdot \arcsin\left(\frac{R_H}{r} \right) + \sqrt{\left(\frac{r}{R_H} \right)^2 - 1} - \frac{\pi}{2} \right\} + \tag{1.72}$$

$$R \cdot \left[\sqrt{1 - \left(\frac{r}{R} \right)^2} - \sqrt{1 - \left(\frac{R_H}{R} \right)^2} \right]$$

$$z_2 = h_c + \frac{1-\nu_2^2}{E_2} \cdot \frac{p_H \cdot R_H}{2} \cdot \left\{ \left[2 - \left(\frac{r}{R_H} \right)^2 \right] \cdot \arcsin\left(\frac{R_H}{r} \right) + \sqrt{\left(\frac{r}{R_H} \right)^2 - 1} - \frac{\pi}{2} \right\} \tag{1.73}$$

where p_H is the maximum Hertzian pressure:

$$p_H = \frac{3 \cdot P}{2 \cdot \pi \cdot R_H^2} \tag{1.74}$$

The following angles are now defined:

$$\varphi_1 \mathrel{\hat{=}} \angle\left(\underset{\sim}{T_1}, Ox \right) = \arctan\left(\left| \left[\frac{\partial z_1}{\partial x} \right]_{(x=x_A, y=y_A)} \right| \right) \tag{1.75}$$

$$\varphi_2 \mathrel{\hat{=}} \angle\left(\underset{\sim}{T_2}, Ox \right) = \arctan\left(\left| \left[\frac{\partial z_2}{\partial x} \right]_{(x=x_B, y=y_B)} \right| \right) \tag{1.76}$$

$$\varphi_3 \mathrel{\hat{=}} \angle\left(\underset{\sim}{T_3}, Oy \right) = \arctan\left(\left| \left[\frac{\partial z_1}{\partial y} \right]_{(x=x_A, y=y_A)} \right| \right) \tag{1.77}$$

$$\varphi_4 \mathrel{\hat{=}} \angle\left(\underset{\sim}{T_4}, Oy \right) = \arctan\left(\left| \left[\frac{\partial z_2}{\partial y} \right]_{(x=x_B, y=y_B)} \right| \right) \tag{1.78}$$

where the partial derivatives in equations (1.75)-(1.78) are given by the following equations:

$$\frac{\partial z_1}{\partial q} = q \cdot \left\{ \frac{-1}{\sqrt{R^2 - r^2}} - \frac{1-\nu_1^2}{E_1} \cdot \frac{p_H}{R_H} \cdot \left[\arctan\left(\frac{R_H}{\sqrt{r^2 - R_H^2}} \right) + R_H \cdot \frac{\sqrt{r^2 - R_H^2}}{r^2} \right] \right\} \quad , q \leftrightarrow x, y \tag{1.79}$$

$$\frac{\partial z_2}{\partial q} = q \cdot \frac{1-\nu_2^2}{E_2} \cdot \frac{p_{\mathrm{H}}}{R_{\mathrm{H}}} \cdot \left[R_{\mathrm{H}} \cdot \frac{\sqrt{r^2 - R_{\mathrm{H}}^2}}{r^2} - \arctan\left(\frac{R_{\mathrm{H}}}{\sqrt{r^2 - R_{\mathrm{H}}^2}} \right) \right] \ , q \leftrightarrow x, y \tag{1.80}$$

Solid frictional forces can be calculated by the following equations:

$$T_1 = T_3 = \mu_1 \cdot N_1 \tag{1.81}$$

$$T_2 = T_4 = \mu_2 \cdot N_2 \tag{1.82}$$

where μ_1 and μ_2 are the friction coefficients for surface 1 (ball) and 2 (flat), respectively. The friction between the particle and the surrounding surfaces is expected to be of the sliding type (or "dynamic" friction) along direction Ox and of the sticking type (or "static" friction) along direction Oy, for the critical time the particle stays at distance $r = r_a$ away from the Hertzian circle centre. The notion of static friction (instead of the usual dynamic friction) has no particular importance here as far as the end results are concerned, because, as it is known, a static-friction coefficient and the corresponding dynamic-friction coefficient have magnitudes very close to each other. Moreover, it is assumed that there is no significant difference in surface roughness along Ox and Oy, which would otherwise infer slightly different friction coefficients. Such effects are of secondary importance in the study and, as is shown in section 1.3, are of limited value since slight variations of the friction coefficients do not yield significantly different results. Therefore, only two solid-friction coefficients are used in the calculations instead of four.

Normal forces $\underset{\sim}{N_1}$ and $\underset{\sim}{N_2}$ are calculated as follows:

$$\underset{\sim}{N_1} = -\frac{\nabla z_1}{\left\| \nabla z_1 \right\|} \cdot N_1 \tag{1.83}$$

$$\underset{\sim}{N_2} = \frac{\nabla z_2}{\left\| \nabla z_2 \right\|} \cdot N_2 \tag{1.84}$$

where

$$\nabla z_i = \left(\frac{\partial z_i}{\partial x}, \frac{\partial z_i}{\partial y}, -1 \right) \quad , (i = 1, 2) \tag{1.85}$$

The norms appearing in equations (1.83) and (1.84) are calculated from the following equation:

$$\left\| \nabla z_i \right\| = \sqrt{\left(\frac{\partial z_i}{\partial x} \right)^2 + \left(\frac{\partial z_i}{\partial y} \right)^2 + 1} \quad , (i = 1, 2) \tag{1.86}$$

From the force equilibrium in axis x, it is derived that

$$-T_1 \cdot \cos(\varphi_1) + T_2 \cdot \cos(\varphi_2) + N_{1,\mathrm{x}} + N_{2,\mathrm{x}} + F_{\mathrm{fluid,x}} = 0 \tag{1.87}$$

and similarly for axis y

$$-\operatorname{sgn}(y) \cdot [T_3 \cdot \cos(\varphi_3) + T_4 \cdot \cos(\varphi_4)] + N_{1,\mathrm{y}} + N_{2,\mathrm{y}} + F_{\mathrm{fluid,y}} = 0 \tag{1.88}$$

where $N_{1,\mathrm{x}}$, $N_{2,\mathrm{x}}$, $N_{1,\mathrm{y}}$, $N_{2,\mathrm{y}}$, are the magnitudes of the components of vectors $\underset{\sim}{N}$ in axes x and y, given by the following general equation:

$$N_{i,q} = \frac{(-1)^i}{\left\| \nabla z_i \right\|} \cdot \frac{\partial z_i}{\partial q} \cdot N_i \quad , \quad i = 1, 2 \quad \text{and} \quad q \leftrightarrow x, y \tag{1.89}$$

$F_{\mathrm{fluid,x}}$ and $F_{\mathrm{fluid,y}}$ are the components of the fluid force on the particle in axes x and y, respectively. Using equations (1.67) and (1.68), it is found that

$$F_{\mathrm{fluid,x}} = C_D \cdot \frac{1}{2} \cdot \rho \cdot u_{\mathrm{ave}}^2 \cdot \frac{\pi}{4} \cdot D^2 = -3 \cdot \pi \cdot \eta \cdot D \cdot u_{\mathrm{ave}} \tag{1.90}$$

$$F_{\mathrm{fluid,y}} = C_D \cdot \frac{1}{2} \cdot \rho \cdot v_{\mathrm{ave}}^2 \cdot \frac{\pi}{4} \cdot D^2 = -3 \cdot \pi \cdot \eta \cdot D \cdot v_{\mathrm{ave}} \tag{1.91}$$

where η is the dynamic (or absolute) viscosity of the fluid.

It must be noted that the force equilibrium in the z-axis is obviously guaranteed by the combined force equilibrium in axes x and y. It must also be noted that the direction of vector $\underset{\sim}{T_2}$ is opposite to the direction of vector $\underset{\sim}{T_1}$ (as shown in figure 1.3) because what is mainly of concern in this analysis is what will happen <u>just after</u> the particle is dragged towards the Hertzian zone. The latter is a critical stage because it results in either the entrapment of the particle or a (possibly temporary) rejection from the contact.

From the linear system of equations (1.87) and (1.88), forces N_1 and N_2 are calculated as follows:

$$N_1 = \frac{\mathrm{D}_{N_1}}{\mathrm{Det}} \quad \text{and} \quad N_2 = \frac{\mathrm{D}_{N_2}}{\mathrm{Det}} \quad (\mathrm{Det} \neq 0) \tag{1.92}$$

where the determinants are given by the following equations:

$$\begin{aligned}\mathrm{Det} = &\left[\mu_1 \cdot \cos(\varphi_1) + \frac{1}{\|\nabla z_1\|} \cdot \frac{\partial z_1}{\partial x}\right] \cdot \left[\mathrm{sgn}(y) \cdot \mu_2 \cdot \cos(\varphi_4) - \frac{1}{\|\nabla z_2\|} \cdot \frac{\partial z_2}{\partial y}\right] + \\ &\left[\mu_2 \cdot \cos(\varphi_2) + \frac{1}{\|\nabla z_2\|} \cdot \frac{\partial z_2}{\partial x}\right] \cdot \left[\mathrm{sgn}(y) \cdot \mu_1 \cdot \cos(\varphi_3) + \frac{1}{\|\nabla z_1\|} \cdot \frac{\partial z_1}{\partial y}\right]\end{aligned} \tag{1.93}$$

$$\begin{aligned}\mathrm{D}_{N_1} = F_{\mathrm{fluid,x}} \cdot &\left[\mathrm{sgn}(y) \cdot \mu_2 \cdot \cos(\varphi_4) - \frac{1}{\|\nabla z_2\|} \cdot \frac{\partial z_2}{\partial y}\right] + \\ F_{\mathrm{fluid,y}} \cdot &\left[\mu_2 \cdot \cos(\varphi_2) + \frac{1}{\|\nabla z_2\|} \cdot \frac{\partial z_2}{\partial x}\right]\end{aligned} \tag{1.94}$$

$$\mathrm{D}_{N_2} = F_{\text{fluid,y}} \cdot \left[\mu_1 \cdot \cos(\varphi_1) + \frac{1}{\|\nabla z_1\|} \cdot \frac{\partial z_1}{\partial x} \right] -$$
$$F_{\text{fluid,x}} \cdot \left[\operatorname{sgn}(y) \cdot \mu_1 \cdot \cos(\varphi_3) + \frac{1}{\|\nabla z_1\|} \cdot \frac{\partial z_1}{\partial y} \right] \tag{1.95}$$

If both N_1 and N_2 are calculated to have positive values, the particle is to be squeezed and its "thickness" reduced. Following this, the deformed (thinner) particle will be able to enter deeper in the EHD gap. This is an indication of entrapment and this observation is more realistic for particles softer than the counterfaces (ball and flat). In the case of particles harder than the counterfaces, surface denting will result in a similar effect. In the latter case, it should also be taken into account the fact that the ball has a rolling velocity, which helps it to overcome the obstacle (particle). If either N_1 or N_2 is calculated to have a negative value, the particle will be expelled from the contact, because the only possible kind of interaction between the particle and one of the counterfaces is repulsion and not attraction, provided that the possibility of some degree of adhesion is ignored. These thoughts lead to the following assumption:

> <u>Assumption:</u>
> If (calculated) $N_1 > 0$ and $N_2 > 0$
> then the particle will be pinched (and possibly trapped),
> otherwise it will be expelled from the contact.

It is necessary at this point to mention that the above assumption gives only an *indication* of entrapment. The assumption uses the word "pinched" instead of "entrapped" because final and irreversible entrapment cannot be absolutely ensured by checking the force equilibrium on the particle only at the position it is first pinched. This is shown in the analysis of chapter 2, where the force equilibrium on the particle is checked during the motion of the particle inside the elastohydro-dynamic gap. On the other hand, the trajectory of a trapped particle inside an elastohydrodynamic gap is almost entirely governed by the frictional forces on it (see chapter 2). However, in the case of elliptical contacts or contacts with variable local sliding, the length of the trajectory of a particle depends mainly on the local sliding (or tangential) speeds of the counterfaces. In the case of a cylinder sliding on one direction on a flat surface, a trapped particle may have to travel all the way along a straight line from the point it is pinched to the outlet zone of the contact, where it is finally rejected (as is shown in chapter 2). In the case of a sphere sliding and spinning on a flat surface, a trapped particle may have to travel a very short distance along a curved trajectory before being rejected. The previous two examples indicate that the severity and duration of particle entrapment depends largely on the geometry and kinematic conditions of a contact. The author has compiled a computer program to study this interesting issue, which, in elliptical contacts, is associated with spalling due to the (known as) Heathcote differential slip effect (see for information in Chao *et al.*, 1996).

The analysis of the present section is completed with the method of calculation of the coordinates x_A, y_A, x_B, y_B of points A and B (figure 1.3). The equations of line ε that comes through points A(x_A,y_A,z_A) and C(x_C,y_C,z_C) are as follows:

$$\varepsilon \;\therefore\; \frac{x - x_A}{x_C - x_A} = \frac{y - y_A}{y_C - y_A} = \frac{z - z_A}{z_C - z_A} \tag{1.96}$$

The equations of line ε' that comes through point A(x_A,y_A,z_A) and is parallel to vector $\underset{\sim}{N_1} = (\alpha, \beta, \gamma)$ are as follows:

$$\varepsilon' \;\therefore\; \frac{x - x_A}{\alpha} = \frac{y - y_A}{\beta} = \frac{z - z_A}{\gamma} \tag{1.97}$$

where (using equations (1.83) and (1.85))

$$\alpha \equiv \left[\frac{-\dfrac{\partial z_1}{\partial x}}{\left\| \nabla z_1 \right\|} \right]_{(x=x_A,\, y=y_A)} \tag{1.98}$$

$$\beta \equiv \left[\frac{-\frac{\partial z_1}{\partial y}}{\left\| \nabla z_1 \right\|} \right]_{(x=x_A, y=y_A)} \tag{1.99}$$

$$\gamma \equiv \frac{1}{\left\| \nabla z_1 \right\|_{(x=x_A, y=y_A)}} \tag{1.100}$$

whereas it has been assumed, without loss of generality, that $N_1 = 1$. Lines ε and ε' must be identical:

$$\varepsilon \equiv \varepsilon' \Leftrightarrow \left(x_C - x_A = \lambda \cdot \alpha \text{ and } y_C - y_A = \lambda \cdot \beta \text{ and } z_C - z_A = \lambda \cdot \gamma \ , \lambda \neq 0 \right) \tag{1.101}$$

where λ is a constant to be determined. Point A(x_A,y_A,z_A) belongs to the particle, which is a sphere with diameter D and centre C(x_C,y_C,z_C). Therefore, the coordinates of point A must satisfy the equation of the sphere:

$$(x_A - x_C)^2 + (y_A - y_C)^2 + (z_A - z_C)^2 = \frac{D^2}{4} \tag{1.102}$$

Using equations (1.101), the previous equation (1.102) gives:

$$\lambda = \pm \frac{D}{2 \cdot \sqrt{\alpha^2 + \beta^2 + \gamma^2}} \tag{1.103}$$

From equation (1.100), it is easily seen that $\gamma > 0$. Also, $z_C > z_A$. Therefore, using the last of equations (1.101), it is derived that $\lambda > 0$. Moreover, it is easily proven that $\alpha^2 + \beta^2 + \gamma^2 = 1$. Conclusively, equation (1.103) gives finally:

$$\lambda = \frac{D}{2} \tag{1.104}$$

Using the first two of equations (1.101) (those inside the parentheses), as well as equations (1.79), (1.98) and (1.99), the following equation is derived:

$$y_A = \frac{y_C}{x_C} \cdot x_A \tag{1.105}$$

Finally, the following system results:

$$\begin{Bmatrix} y_A = \dfrac{y_C}{x_C} \cdot x_A \\ x_C - x_A = \dfrac{D}{2} \cdot \alpha \end{Bmatrix} \tag{1.106}$$

where α is a function of x_A and y_A, and coordinates x_C and y_C as well as diameter D are known quantities. The system of equations (1.106) is non-linear and is solved by a trial-and-error method, which comprises the following steps:

(1) x_A is given a trial value in the range $(x_C - \delta, x_C + \delta)$, where δ is an appropriately chosen constant (it is expected from the geometry of the problem that x_A must have a value very close to that for x_C).

(2) y_A is calculated from the first of equations (1.106).

(3) The following quantity is calculated: $error = \left| x_C - x_A - \dfrac{D}{2} \cdot \alpha \right|$.

(4) Steps (1)-(3) above are repeated to cover the whole range $x_C - \delta < x_A < x_C + \delta$.

(5) Final values of x_A and y_A are those which give the minimum error, as defined in step (3).

Following the above procedure, x_B and y_B are also calculated. Thus, points A and B are located. This is followed by a force calculation on the particle, according to the analysis presented previously, in order to check if the particle is pinched or expelled. There are two possibilities:

(a) The particle is expelled. In this case, the particle's new position is set to be close to its last position, such that $\sqrt{x_C^2 + y_C^2} \geq r_a$ (in other words, the particle is left just outside the critical circle where it comes into contact with both the ball and the flat). Following this, the particle continues its voyage in the fluid, and the whole analysis is repeated. This part of the study is very crucial, because, if particles are expelled relatively many times, they may start accumulating in the inlet zone of the contact, with a tendency to cause fluid starvation and, possibly, result in scuffing.

(b) The particle is pinched. In this case, the story of the particular particle ends. If there are other particles or, more precisely, different initial positions to be studied, then the analysis of this chapter is repeated for them as well.

The analysis presented thus far is outlined in the flowchart of figure 1.4.

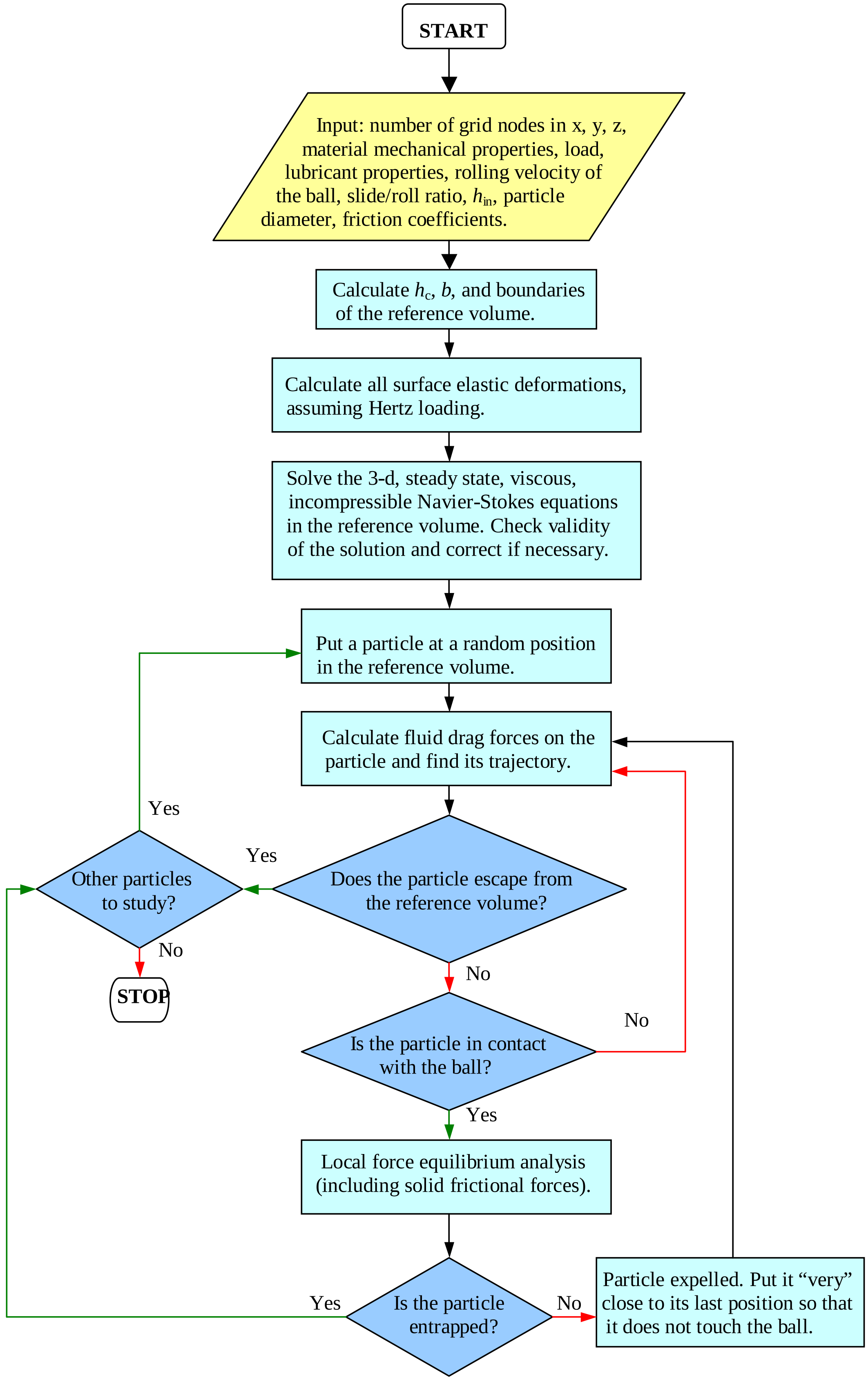

Figure 1.4 Flowchart of the model of particle entrainment in a point EHD contact.

1.3 Examples

The mathematical analysis outlined in section 1.2 has been transferred into computer code. A brief description of the computer program is presented in section 1.5. In the present section, a variety of results is presented through detailed diagrams, which show the effects of the slide/roll ratio, the oil-bath thickness and the size of the contamination particles on the lubrication of an elastohydrodynamic point contact of a ball sliding-rolling on a flat surface. The aims of this section, and of the present chapter in general, are as follows.

(a) Study of the likelihood of oil starvation, caused by the accumulation of contamination particles in the inlet zone of the elastohydrodynamic contact. In the cases where oil starvation is more likely, scuffing may follow shortly after the conditions for oil starvation are met.

(b) Study of the likelihood of surface damage (denting or scratching/grooving). This is equivalent to the study of the likelihood for a particle to become entrapped and be squashed in the elastohydrodynamic gap.

The values of the parameters held constant throughout this investigation are shown in table 1.1.

Table 1.1

Values of the parameters held constant in the example	
Ball radius	R = 4 mm
Modulus of elasticity	$E_1 = E_2$ = 200 GPa
Poisson ratio	$\nu_1 = \nu_2 = 0.3$
Ball's load	50 N
Dynamic viscosity of the lubricant	η = 0.1 Pa·s
Pressure-viscosity coefficient of the lubricant	$2 \cdot 10^{-8}$ m^2/N
Density of the lubricant	ρ = 870 kg/m^3
Rolling velocity of the ball	u_a = 1 m/s
Material density of a particle	7000 kg/m^3
Solid-friction coefficient	$\mu_1 = \mu_2 = 0.1$
Number of initial positions of a particle in the reference volume	100
Number of grid nodes (i,j,k)	400×100×10

The slide/roll ratio S_r is defined as the ratio of the sliding velocity of the ball relatively to the stationary flat, over the ball's rolling velocity:

$$S_r \equiv \frac{V_s}{u_\mathrm{a}} \tag{1.107}$$

The slide/roll ratio is varied (in steps of 0.1) between 0.1 and 2.0, to cover the range of values met in most engineering applications. Also, three oil-bath thicknesses h_in are used in the study, namely 50 μm, 100 μm and 500 μm, in order to cover the cases of starved and flooded elastohydrodynamic contacts. The size of the contamination particles used for the study is represented by their diameter, which takes three values, namely 5 μm, 10 μm and 20 μm, in order to cover the cases of small, medium and relatively large particles. In summary, the values of the parameters varied during this example are presented in table 1.2.

Table 1.2

Values of the parameters that vary in the example	
Particle diameter	D = 5, 10, 20 μm
Oil bath thickness	h_in = 50, 100, 500 μm
Slide/roll ratio	S_r = 0.1-2.0 (in steps of 0.1)

The figures presented in the following eight sub-sections (six figures for each sub-section) have a horizontal axis representing the slide/roll ratio, whereas the vertical axis represents quantities (explained in each sub-section), which test the likelihood of particle entrapment and the likelihood of particle accumulation in the inlet zone of the test contact. The curves shown in the figures are 3$^{\mathrm{rd}}$ degree polynomial fits, which give a good qualitative view in order to collect useful results and draw meaningful conclusions. Important general conclusions are summarized in section 1.4.

1.3.1 The likelihood of particle accumulation – risk of lubricant starvation

The likelihood of particle accumulation is checked by calculating the percentage of particles expelled at least fifty times from the contact, based on the number of particles studied. The number of “fifty” rejections was chosen arbitrarily as an indication of prolonged presence of a particle just outside the critical radius r_a, where a particle comes in contact with both the ball and the flat. Obviously, the more times a particle is expelled from the contact, the higher is the likelihood of other particles to gather around the first one, which stands as an obstruction in front of the ball, and thus, the higher is the likelihood of particle accumulation in the inlet zone of the contact. Particle accumulation results in obstruction of the lubricant flow and thus poor lubricant replenishment of the contact. The end effect could be oil starvation and increased wear, or, even worse, film breakdown and scuffing.

In the series of the following six figures, the effects of the oil bath thickness, particle size and slide/roll ratio on the probability of particle accumulation are examined.

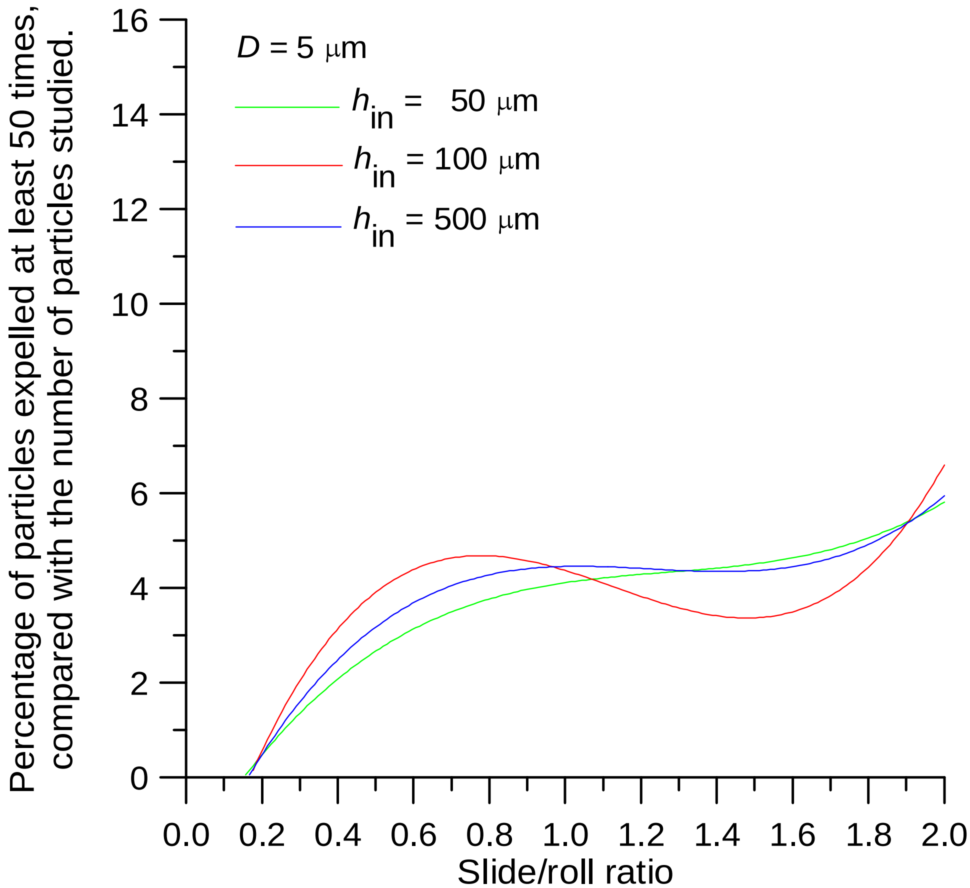

Figure 1.5

Figure 1.5 shows that the likelihood of small-particle rejection from the contact increases generally following an increase of the slide/roll ratio. The greatest increase is located in the area $0.1 < S_r < 0.6$, as well as for high sliding conditions ($S_r > 1.8$). Particle accumulation and oil starvation are more likely for thicker films and smaller particles. The likelihood of small-particle rejection is diminished for very low slide/roll ratios.

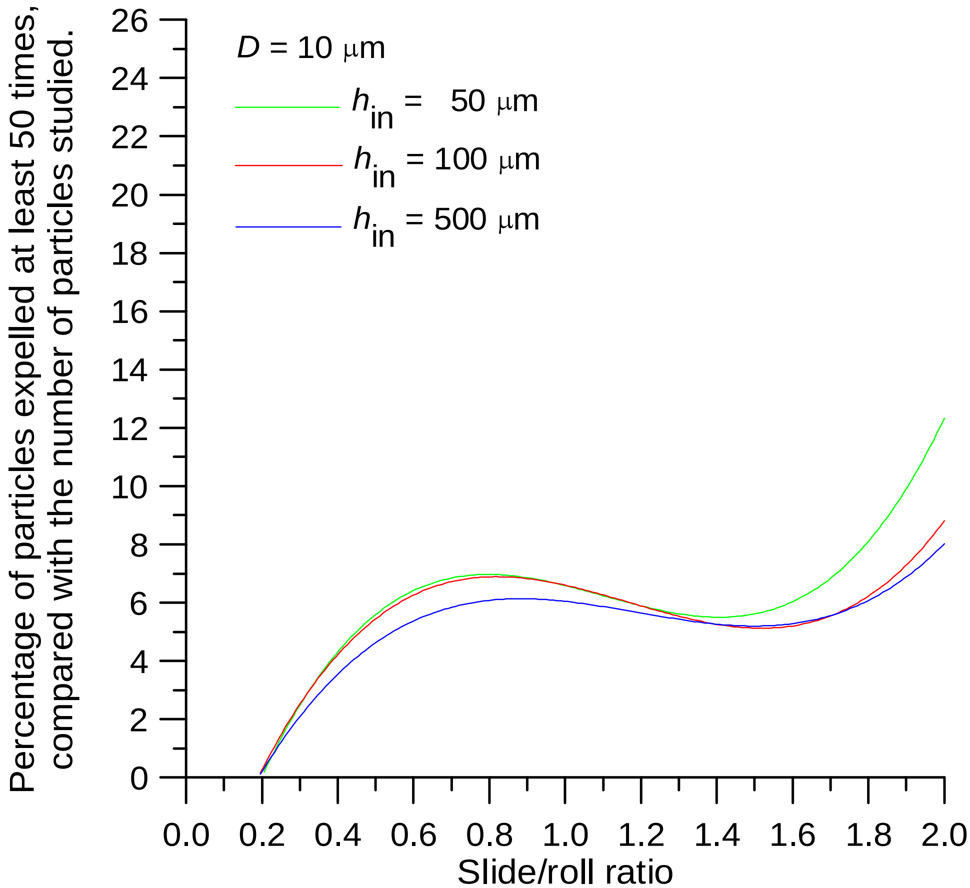

Figure 1.6

According to figure 1.6, the effect of the oil-bath thickness on the rejection of medium sized particles is rather small. In agreement with figure 1.5, the likelihood of particle rejection from the contact is diminished for low slide/roll ratios, whereas it stays approximately constant for $0.7 < S_r < 1.6$, and increases steeply for $S_r > 1.6$ and up to the maximum slide/roll ratio studied ($S_r = 2$). Therefore, it is shown again that high-sliding conditions are in favor of particle rejection from the contact (and thus in favor of particle accumulation).

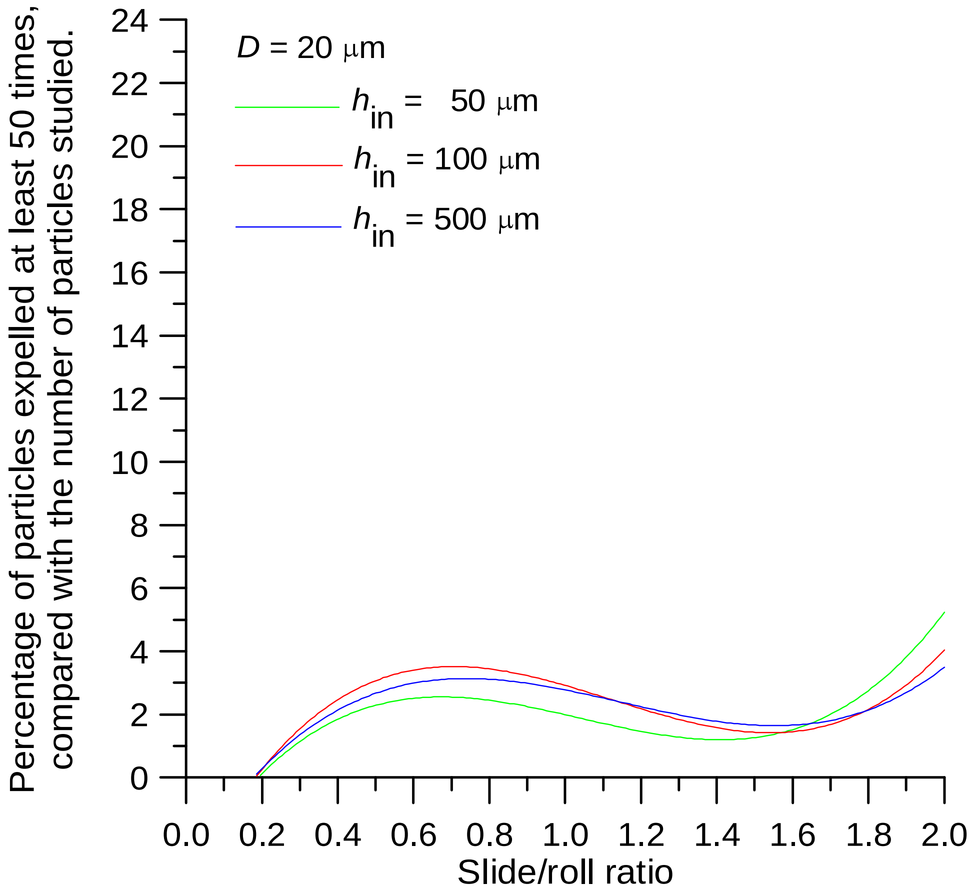

Figure 1.7

Figure 1.7 shows that larger (20 μm) particles are less likely to be repetitively expelled from the contact, compared with smaller particles (5 μm and 10 μm - figures 1.5 and 1.6). Qualitatively, the curves are similar to those in figures 1.5 and 1.6, and the same general conclusions apply here as well.

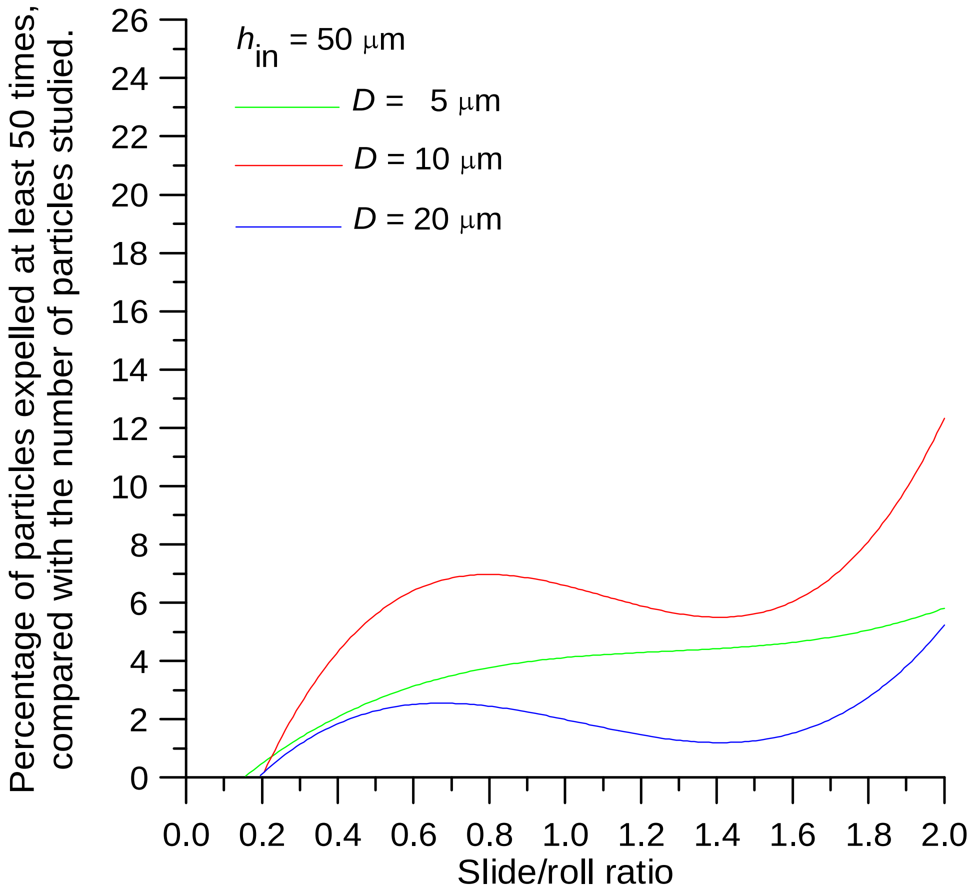

Figure 1.8

Figure 1.8 shows that, for thin oil bath films, medium sized (10 μm) particles have a greater likelihood of repetitive rejection compared with small (5 μm) and large (20 μm) particles. Rejection is increased for high-sliding conditions.

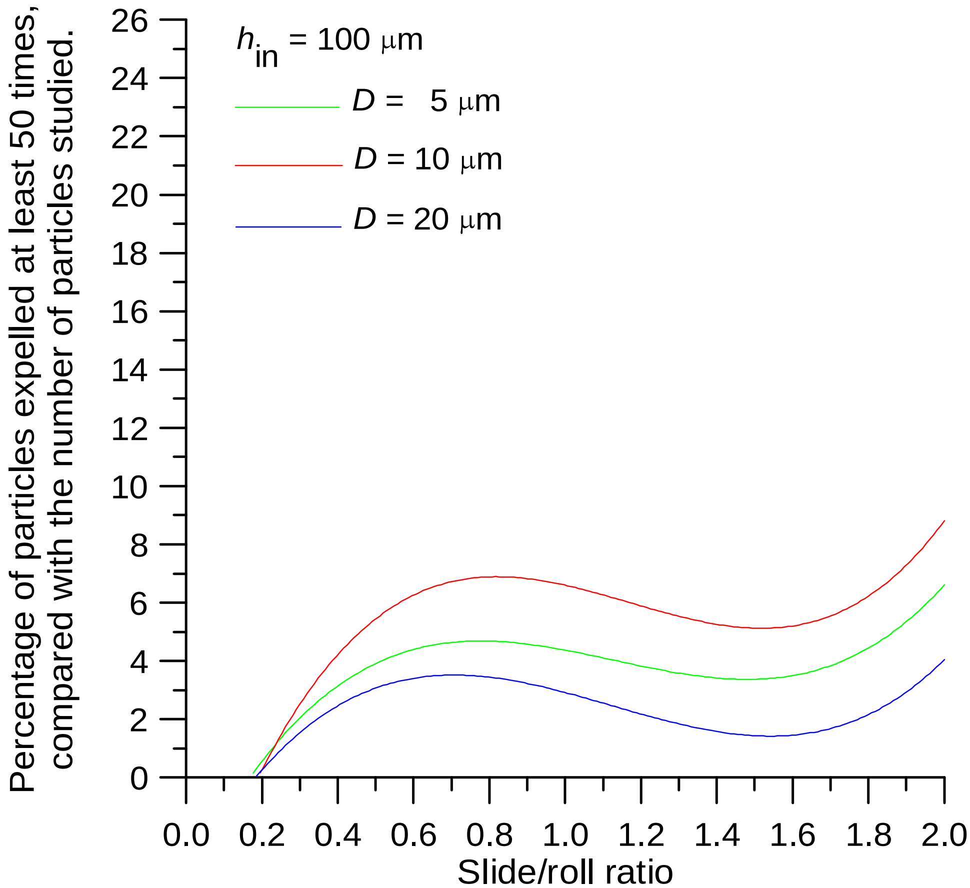

Figure 1.9

Figure 1.9 is similar to figure 1.8, but refers to medium-sized oil bath films (100 μm) instead of thinner films (50 μm). The findings are in qualitative agreement with those for figure 1.8. High-sliding conditions promote particle rejection and bigger particles are the most difficult to reject.

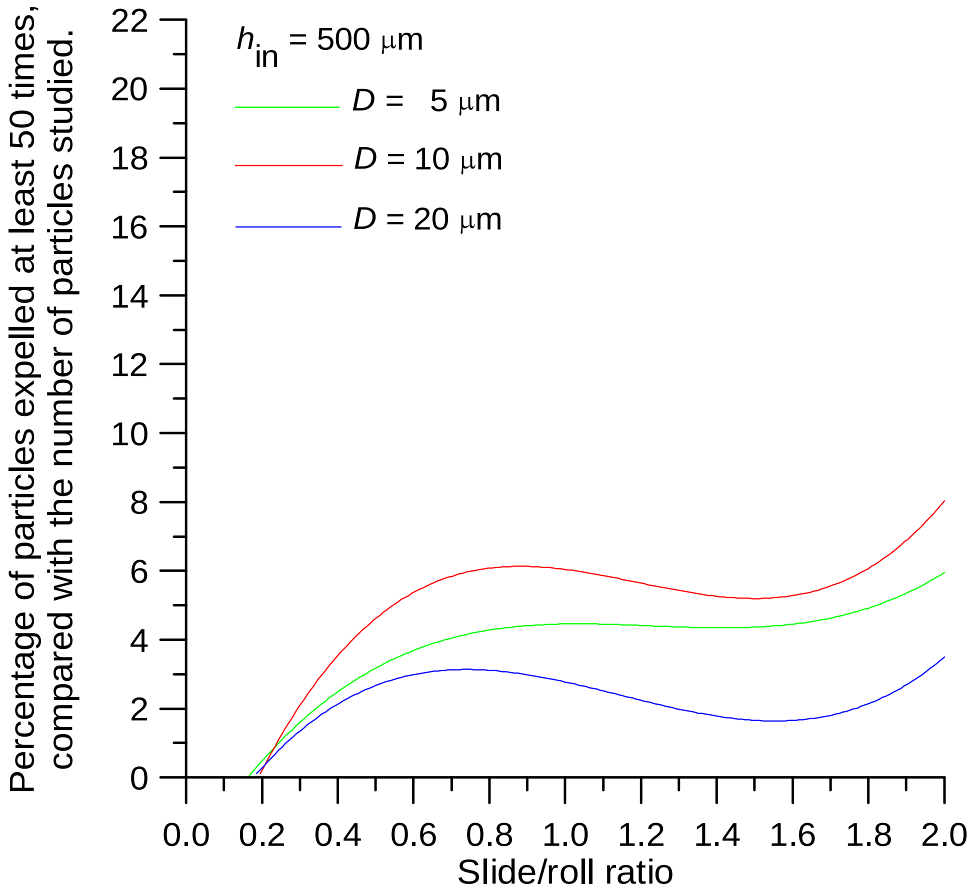

Figure 1.10

Figure 1.10, referring to relatively thicker oil bath films (500 μm) shows again that medium sized particles (10 μm) are more easily expelled from the contact, compared with smaller and larger particles. Low-sliding conditions promote particle entrapment whereas the opposite is true in the region of high sliding.

1.3.2 The likelihood of particle-ball collisions

The likelihood of particle-ball collisions is checked by finding the percentage of particles which are to collide with the ball, based on the number of particles studied. The *number of particles studied* is equivalent to the *number of initial positions of a particle in the reference volume.* If a particle is left free to travel in the flow from its initial position in the reference volume, its calculated trajectory shows if it will eventually collide with the ball or if it will bypass it without any contact (collision). Particles which bypass the ball by avoiding any contact with it could be considered as being virtually harmless, because they neither obstruct the lubricant flow nor cause any surface damage. Equivalently, the higher the number of particles which collide with the ball, the higher the risk of particle accumulation (which may result in lubricant starvation) and/or surface damage. Therefore, the knowledge of the likelihood of particle-ball collisions offers a good evaluation of the effectiveness of lubrication and the “healthy” operation of the contact.

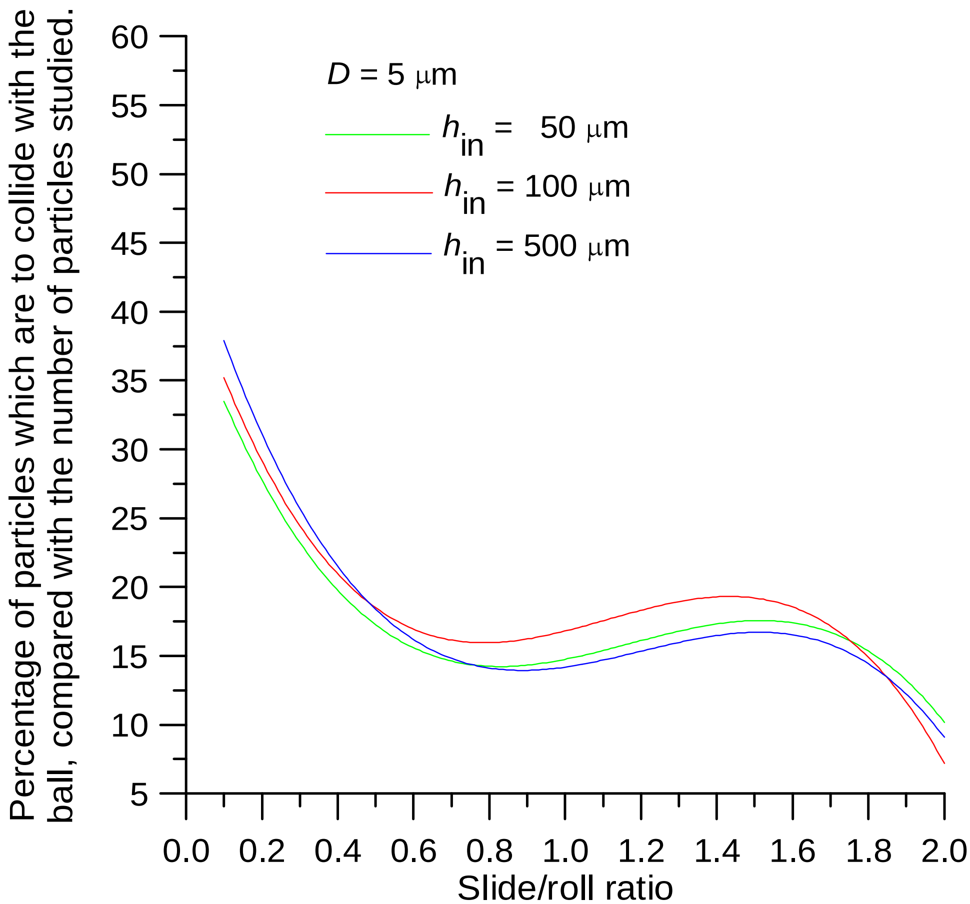

Figure 1.11

Figure 1.11 shows that the likelihood of first-time collisions of small particles with the ball is significantly increased for low slide/roll ratios ($S_r < 0.5$) and it gradually drops with increasing the sliding of the contact. The conclusion is that, in order to increase the number of small particles that bypass the ball, the operational area $S_r < 0.5$ must be avoided.

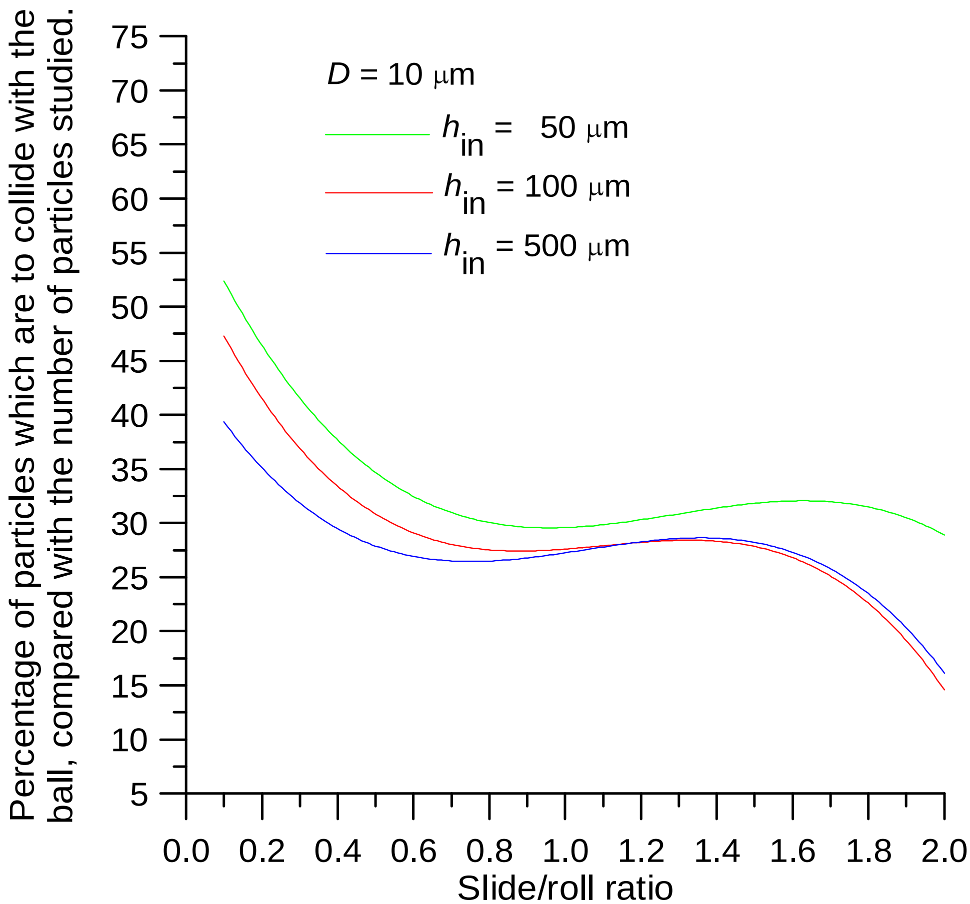

Figure 1.12

Figure 1.12 shows again that for $S_r < 0.5$, the likelihood of particle first-time collisions with the ball is significantly increased. In order to minimize the number of particles that are to collide with the ball, the slide/roll ratio must be kept to values around or above 1.0. Finally, figure 1.12 shows that thicker films (blue line) “help” the 10 μm particles bypass the ball.

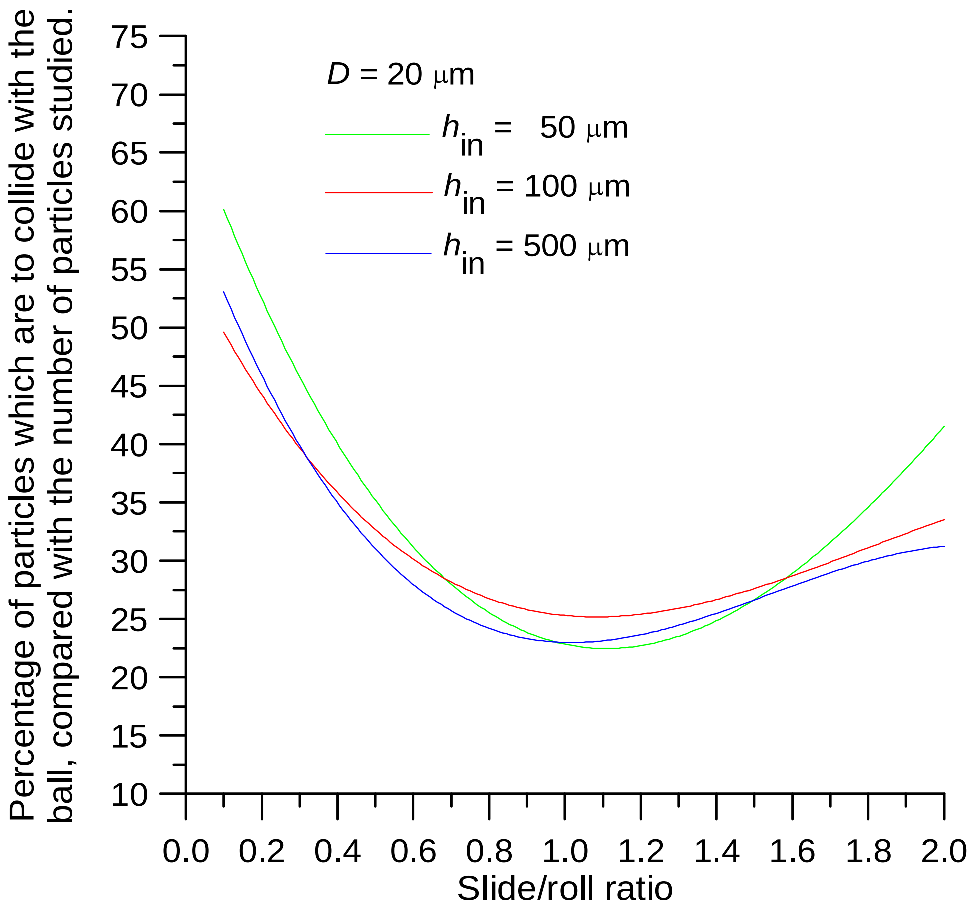

Figure 1.13

In agreement with figures 1.11 and 1.12, figure 1.13 shows that for $S_r < 1$, the likelihood of particle-first-time-collisions with the ball is significantly increased. On the other hand, high-sliding conditions seem to increase the possibility of particle-ball collisions when the oil bath thickness approaches the size of the particles (h_{in} = 50 µm versus D = 20 µm), which is to be expected due to the reduced back-flow of the oil against the size of the particles.

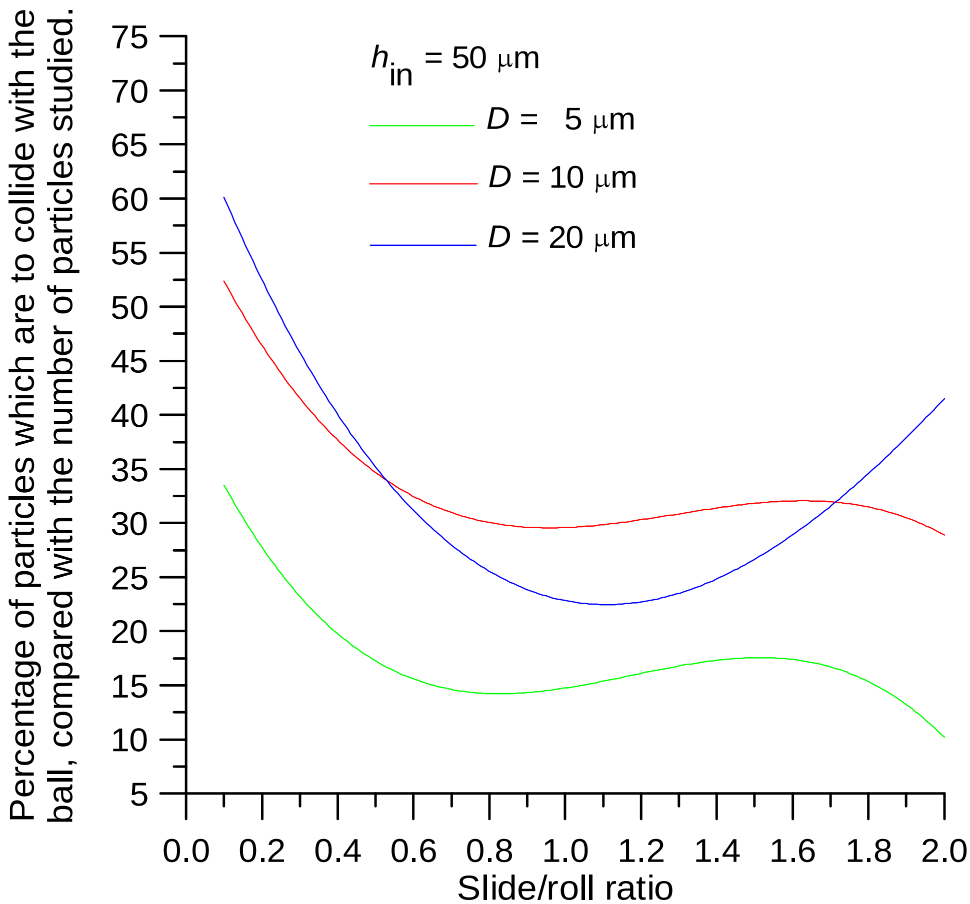

Figure 1.14

Figure 1.14 shows that for thin oil bath films (h_{in} = 50 µm), the smaller particles (D = 5 µm) are the most likely to bypass the ball. Low slide/roll ratios result in more particle-ball collisions for all sizes of particles.

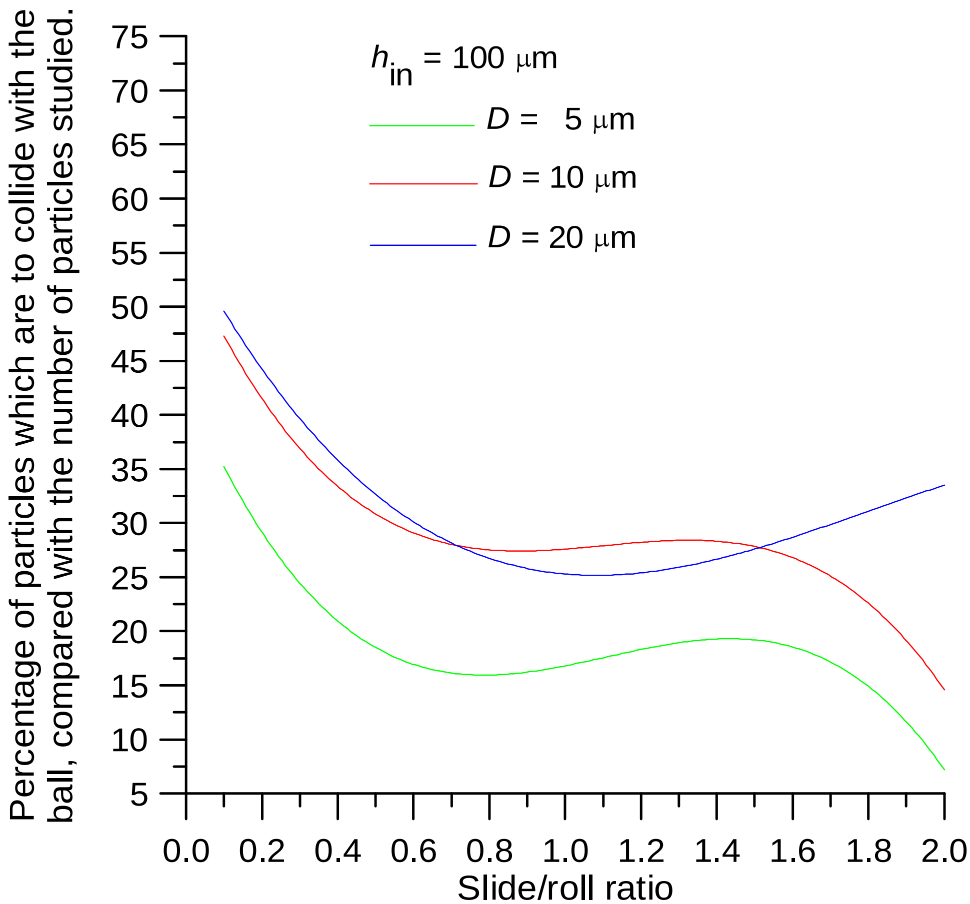

Figure 1.15

Like figure 1.14, figure 1.15 shows that the smaller particles are more easily by-passing the ball. The number of particle-ball collisions is profoundly maximized for low-sliding conditions of the contact (S_r < 0.5).

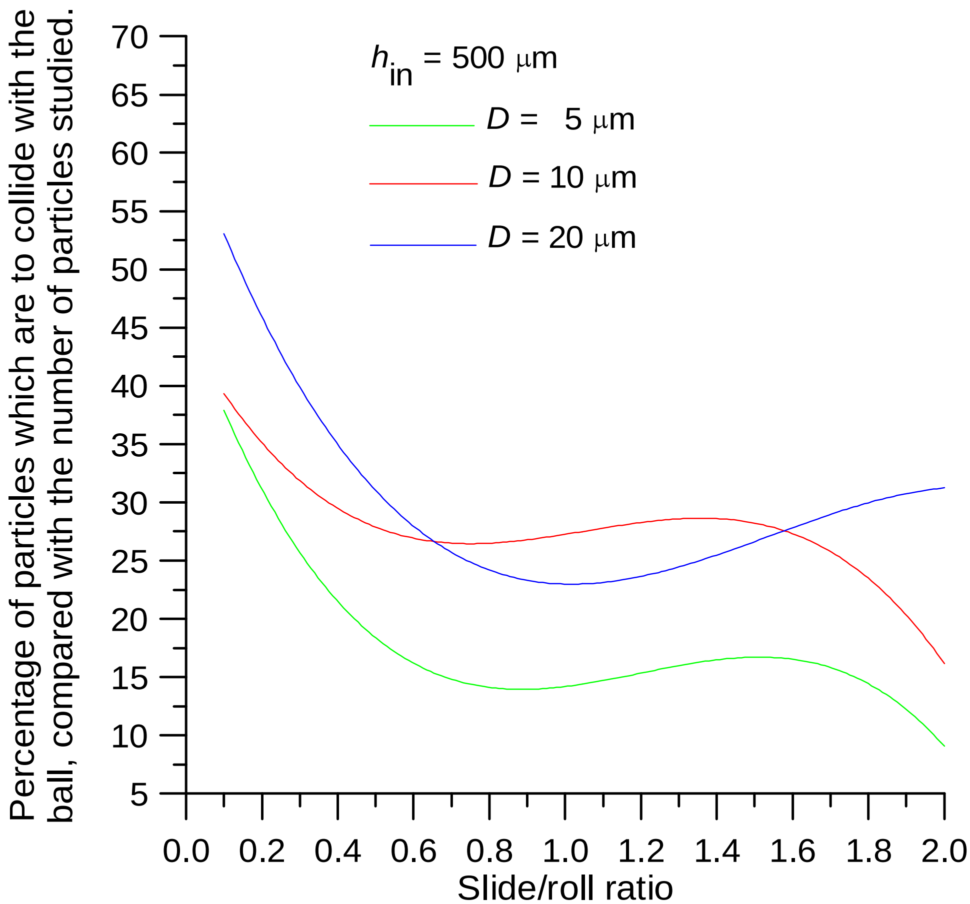

Figure 1.16

The study of figure 1.16, where h_{in} = 500 μm, leads to the same conclusions as in figures 1.14 and 1.15, where h_{in} is 50 μm and 100 μm, respectively. In other words, the smaller (5 μm) patrticles involve less risk to end-up colliding with the ball rather than bypassing it.

1.3.3 An early assessment of the likelihood of particle accumulation

In sub-section 1.3.1, the likelihood of particle accumulation in the inlet zone of the contact is evaluated by calculating the percentage of particles, which are expelled at least fifty times from the contact, based on the number of particles put in the reference volume. In the present sub-section, the calculation of the percentage of particles that are to be expelled at least once from the contact, based on the number of particles that are to collide with the ball, gives a pre-estimation of the likelihood of particle accumulation in the inlet zone of the contact. A first-time particle rejection is an indication of the beginning of particle accumulation. Obviously, the results of sub-section 1.3.1 are stronger than the results of the present sub-section as far as lubricant starvation is concerned, but the present sub-section serves as another approach of checking the same concept, namely the probability of lubricant starvation.

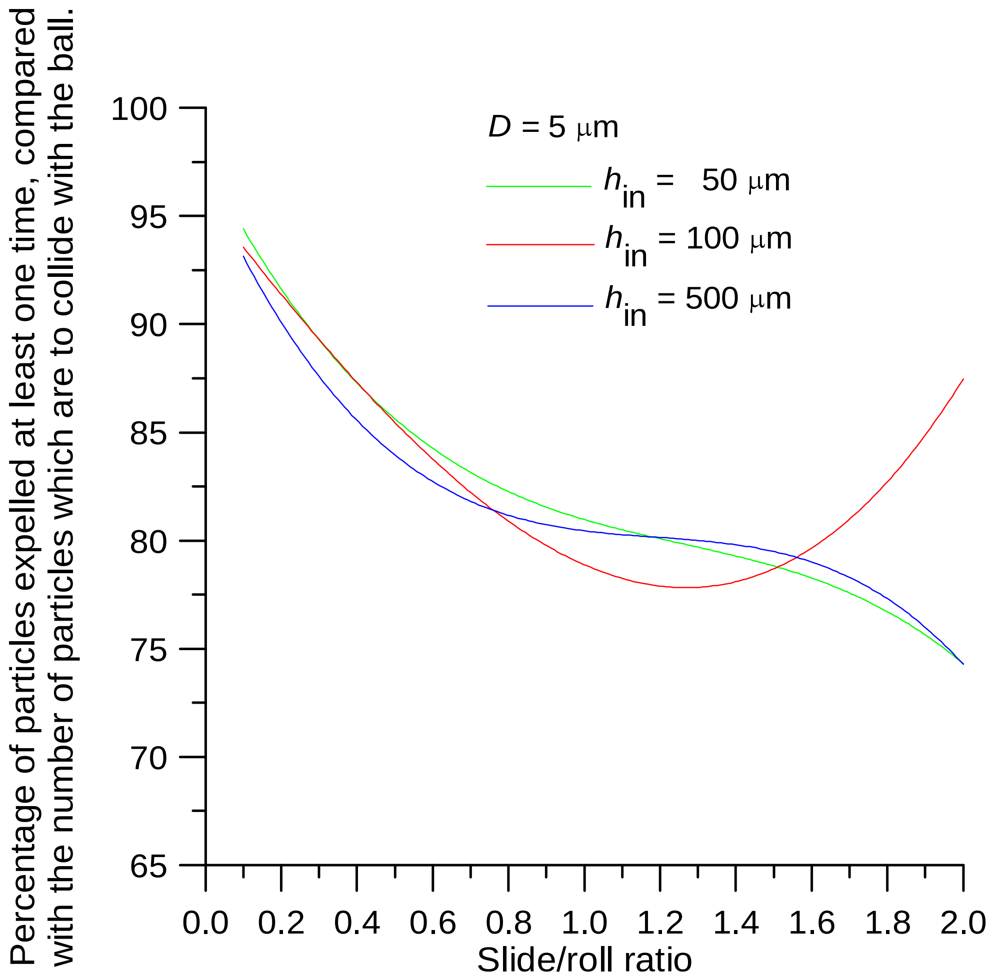

Figure 1.17

Figure 1.17 shows the likelihood of first-time rejection for a particle that will collide with the ball. The aforementioned likelihood is higher for low slide/roll ratios and is gradually reduced for increasing sliding. The marked difference for the red line is to be explained by the fitting method used (3rd degree polynomial). With linear regression, the red line would have a negative slope and follow closely the other two curves.

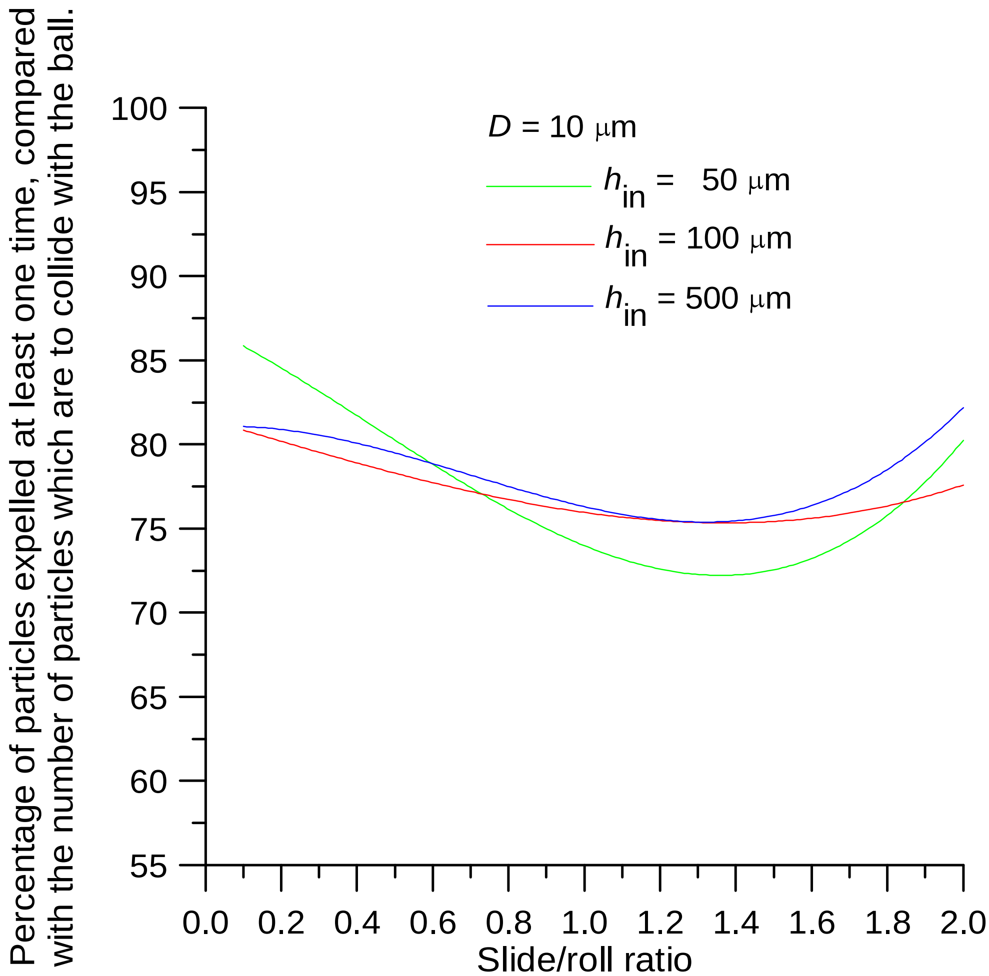

Figure 1.18

Figure 1.18 shows that the likelihood of first-time rejection of a medium-sized (10 μm) particle that is to collide with the ball is not greatly affected by either the oil-bath thickness or the slide/roll ratio. There is a tendency for rejection for high slide/roll ratios.

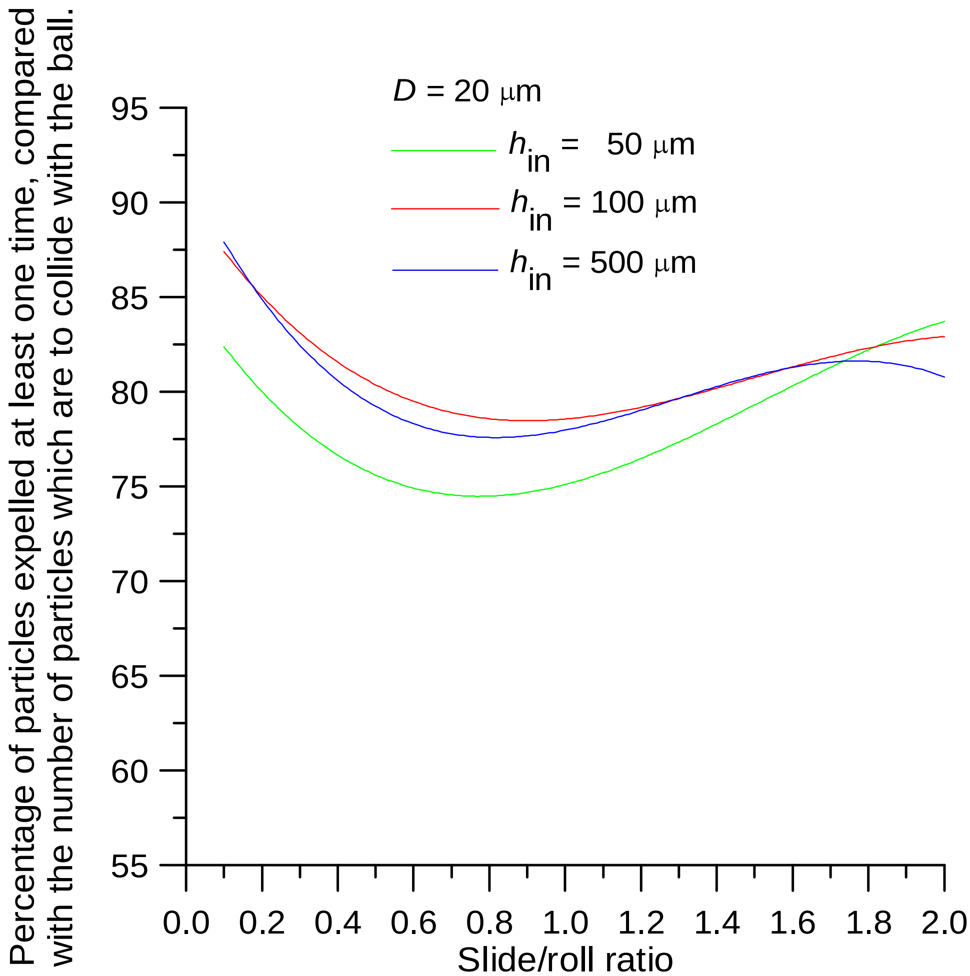

Figure 1.19

According to the above figure, larger (20 μm) particles are less easily expelled (or, equivalently, are more easily entrapped) for slide/roll ratios around 0.8-1.2.

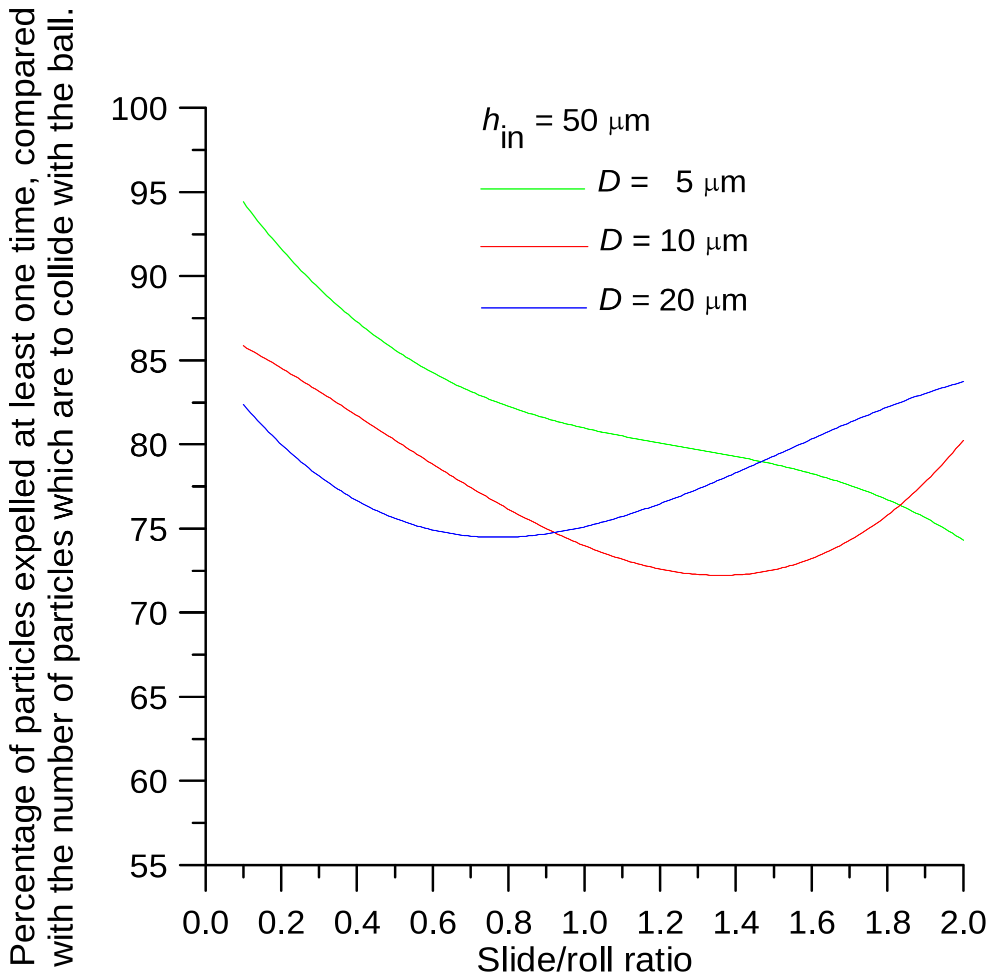

Figure 1.20

Figure 1.20 shows that, for thin oil-bath films, the smaller (5 μm) particles are more likely to be at least one time expelled, compared with the larger particles (10 μm and 20 μm ones). An explanation for this behaviour is the effect of lubricant backflow, which affects smaller particles more than the larger ones. The situation is reversed for higher slide/roll ratios, as shown in the figure, probably because surface curvature plays a more important role further outside the Hertzian zone of the contact against the lubricant backflow, which is weaker, as is expected for the larger particles (larger particles have obviously a greater contact distance r_a).

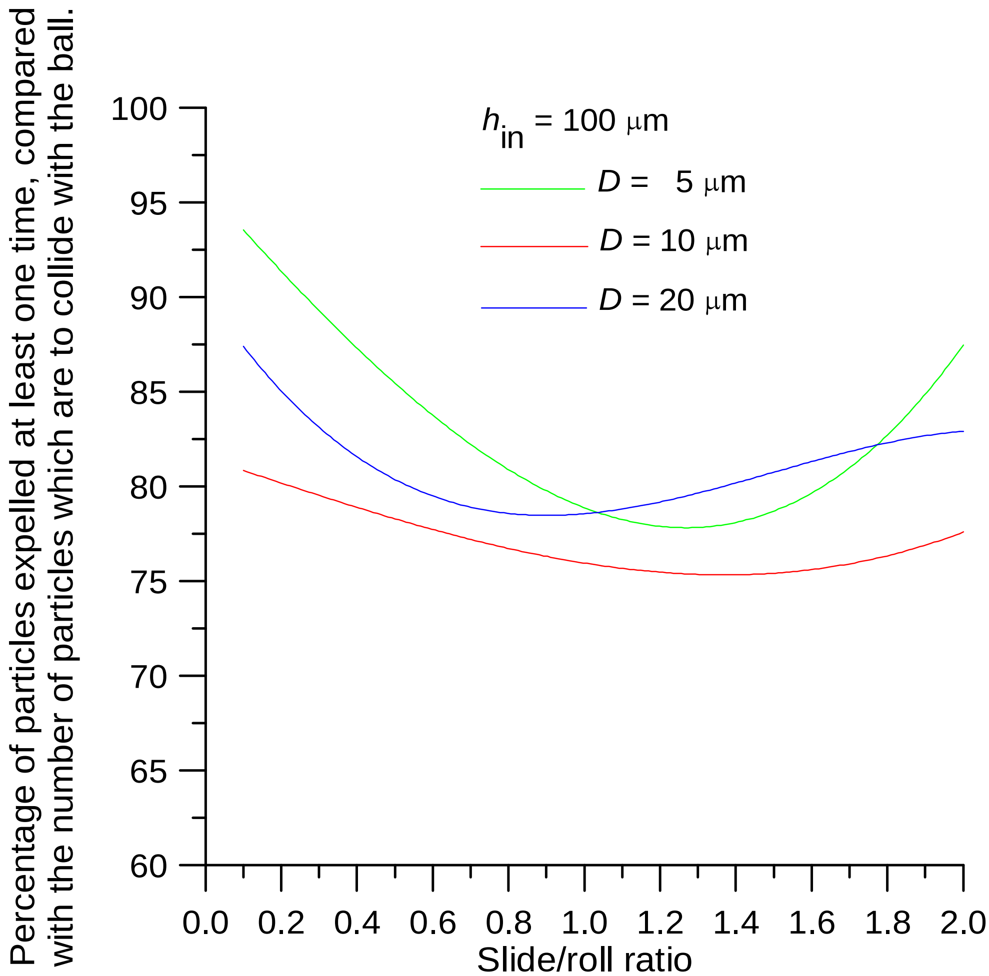

Figure 1.21

Figure 1.21 shows that, for medium (100 μm) oil-bath thickness, medium-sized (10 μm) particles are more likely to be immediately entrapped, after they collide with the ball, in comparison with smaller (5 μm) and larger (20 μm) particles.

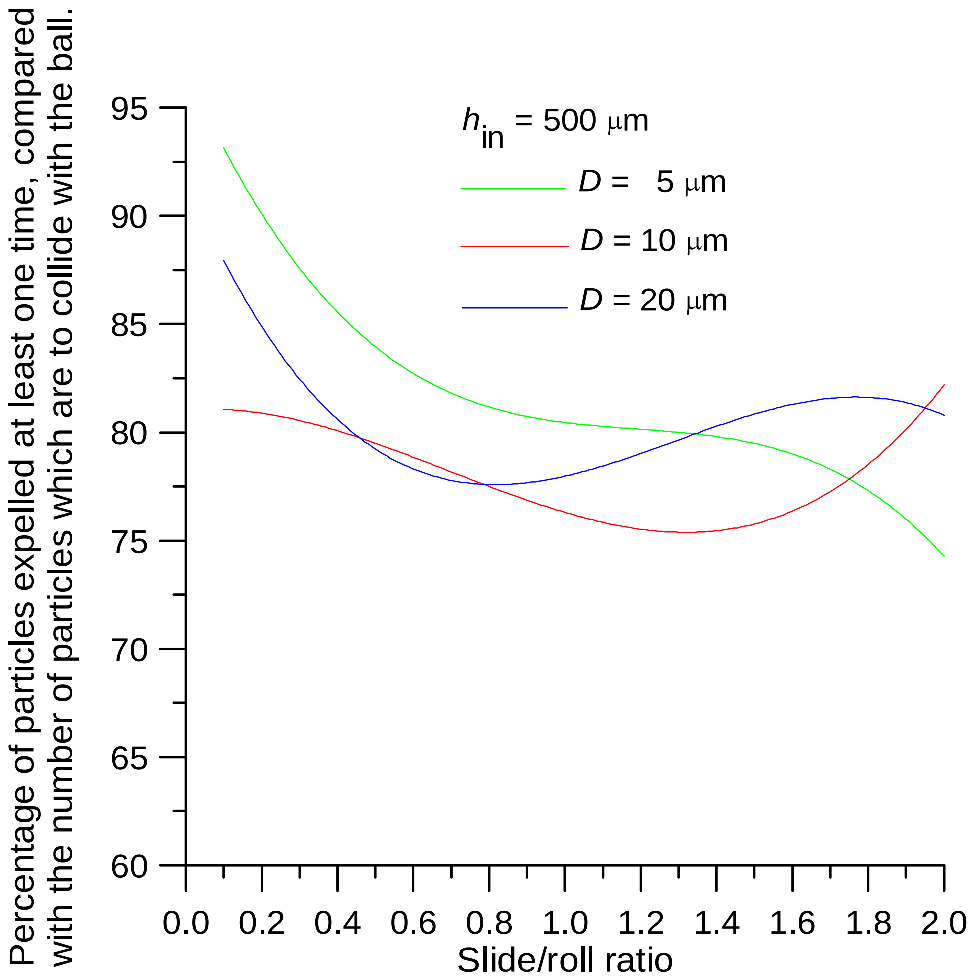

Figure 1.22

Figure 1.22 shows that, for relatively thick (500 μm) oil-bath films, smaller (5 μm) particles are more likely to be expelled (at least once), after a collision with the ball, compared with larger particles. This is obviously so for low slide/roll ratios, where lubricant backflow affects smaller particles more than larger ones.

1.3.4 The likelihood of particle accumulation

The likelihood of particle accumulation and lubricant starvation is assessed in sub-section 1.3.1, and is based on the number of particles studied (put in the reference volume). In the present sub-section, the likelihood of particle accumulation is approached in a slightly different way; namely, the study is based on the particles that are to collide with the ball, rather than the overall number of particles studied. In this way, the consequences of a particle colliding with the ball can more readily be realized and possible risks be evaluated.

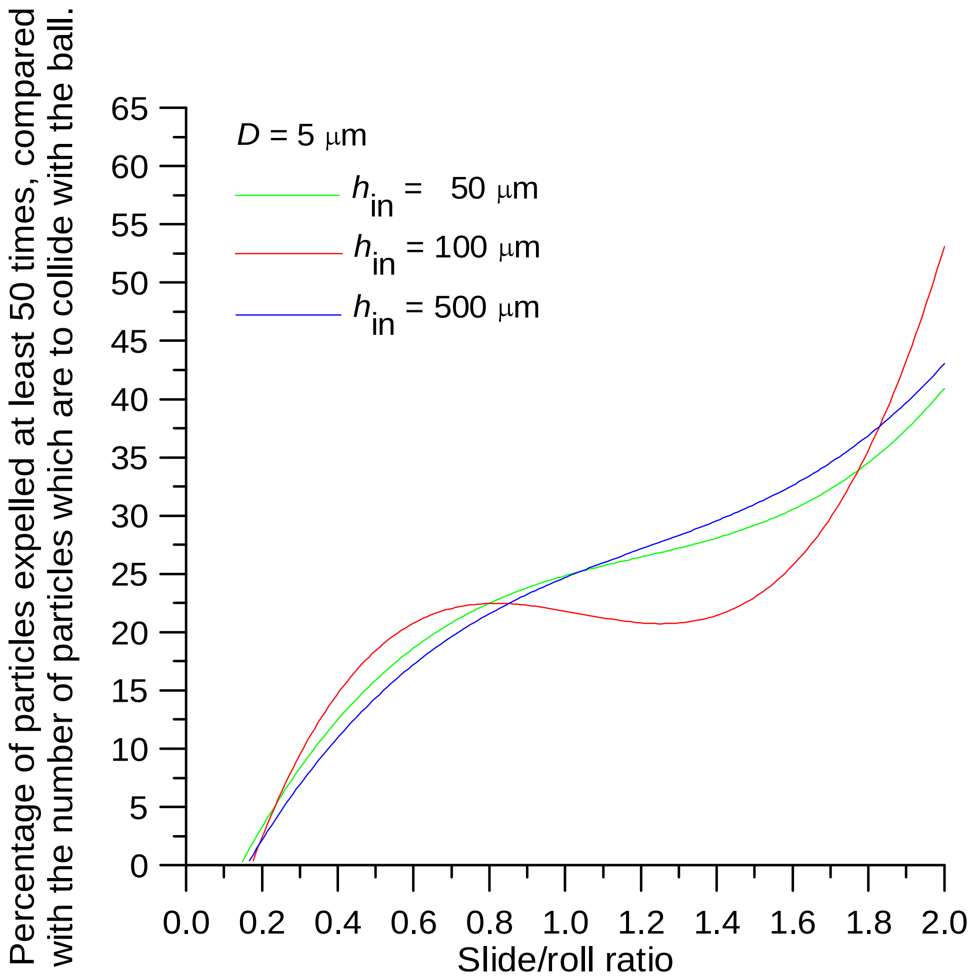

Figure 1.23

According to figure 1.23, the likelihood of repetitive small-particle rejection from the contact is generally increased by increasing the slide/roll ratio. The oil-bath thickness does not appear to play an important role. For reduced risk of particle accumulation and oil starvation, the preferred area of operation for the slide/roll ratio is the area $S_r < 1$. However, the latter may increase the number of particles being over-rolled and, thus, increase the risk of surface damage.

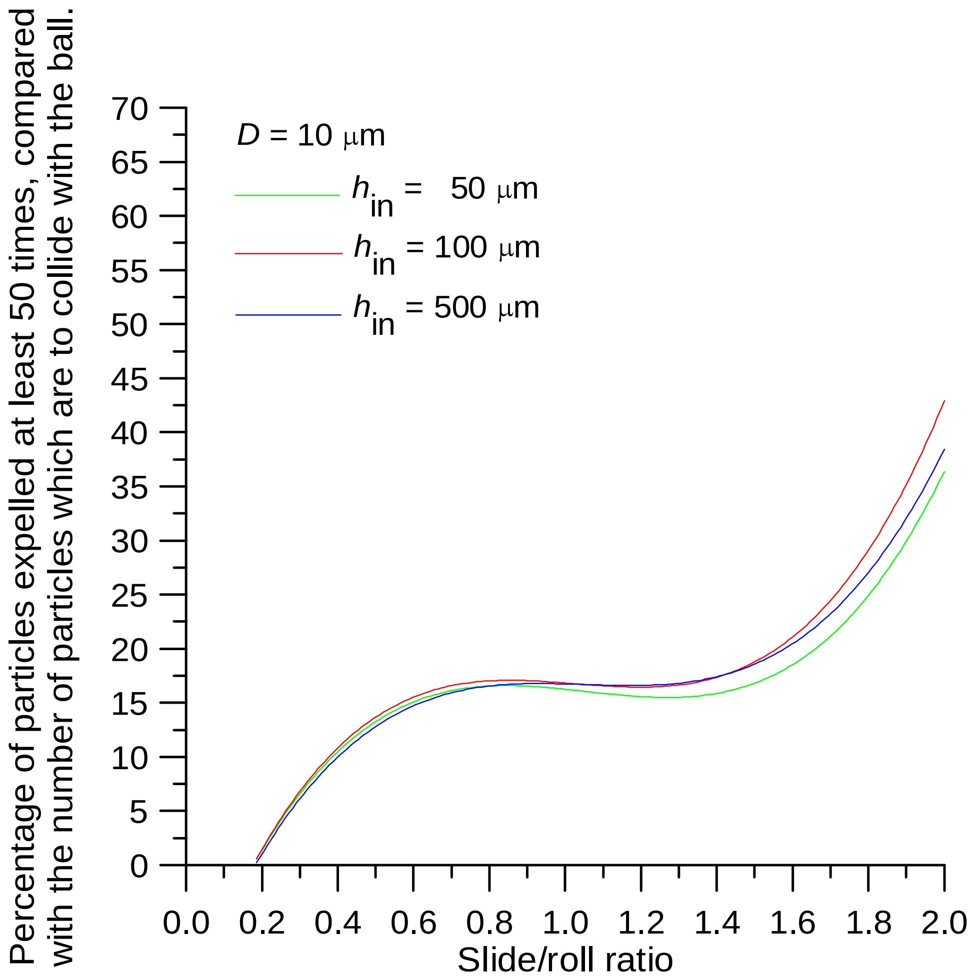

Figure 1.24

Figure 1.24 shows that medium-sized (10 μm) particles behave similarly to smaller (5 μm) ones, when considering the likelihood of repetitive particle rejection from the contact (see figure 1.23). The effect of the oil bath thickness is even less influential in this case and the preferred area of operation for the slide/roll ratio, in order to reduce the risk of particle accumulation and fluid starvation, is the area $S_r < 1$ (approximately).

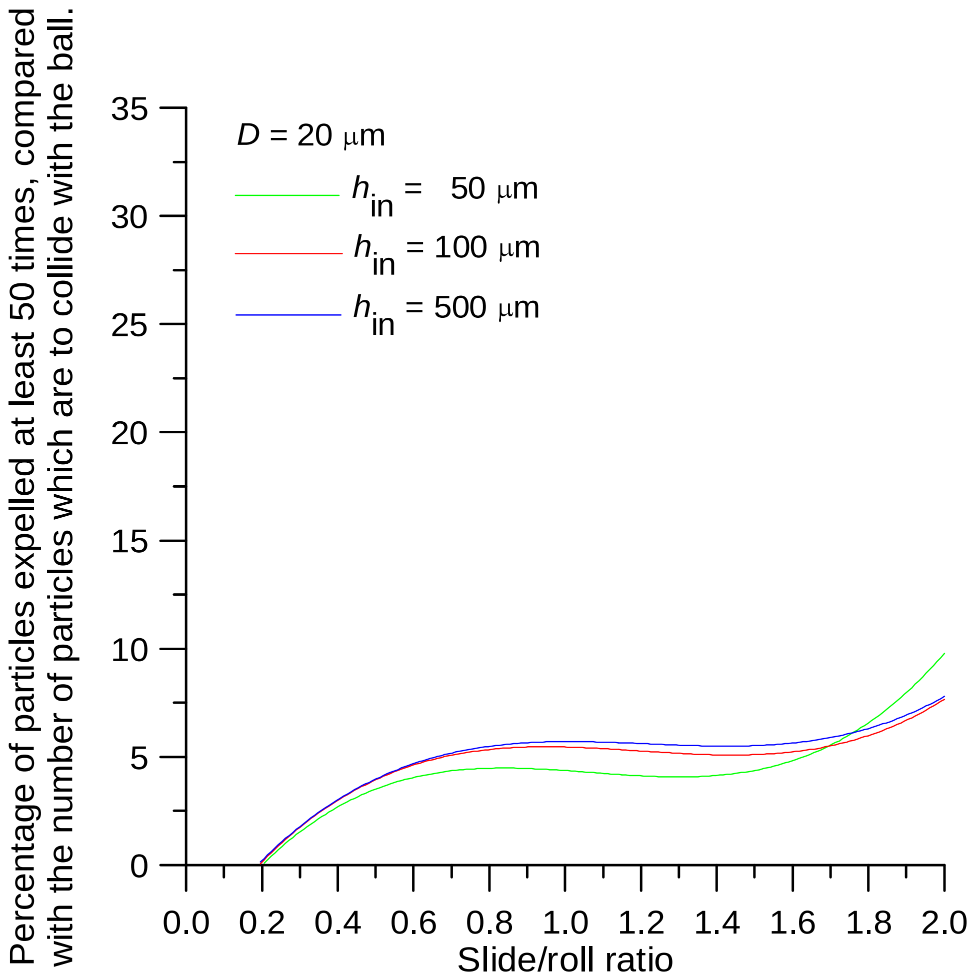

Figure 1.25

According to figure 1.25, repetitive particle rejection of the larger (20 μm) particles is less dependent on the slide/roll ratio. The most dangerous area for oil starvation is again close to the higher bound of the slide/roll ratio, whereas the risk is minimized for $S_r < 0.6$.

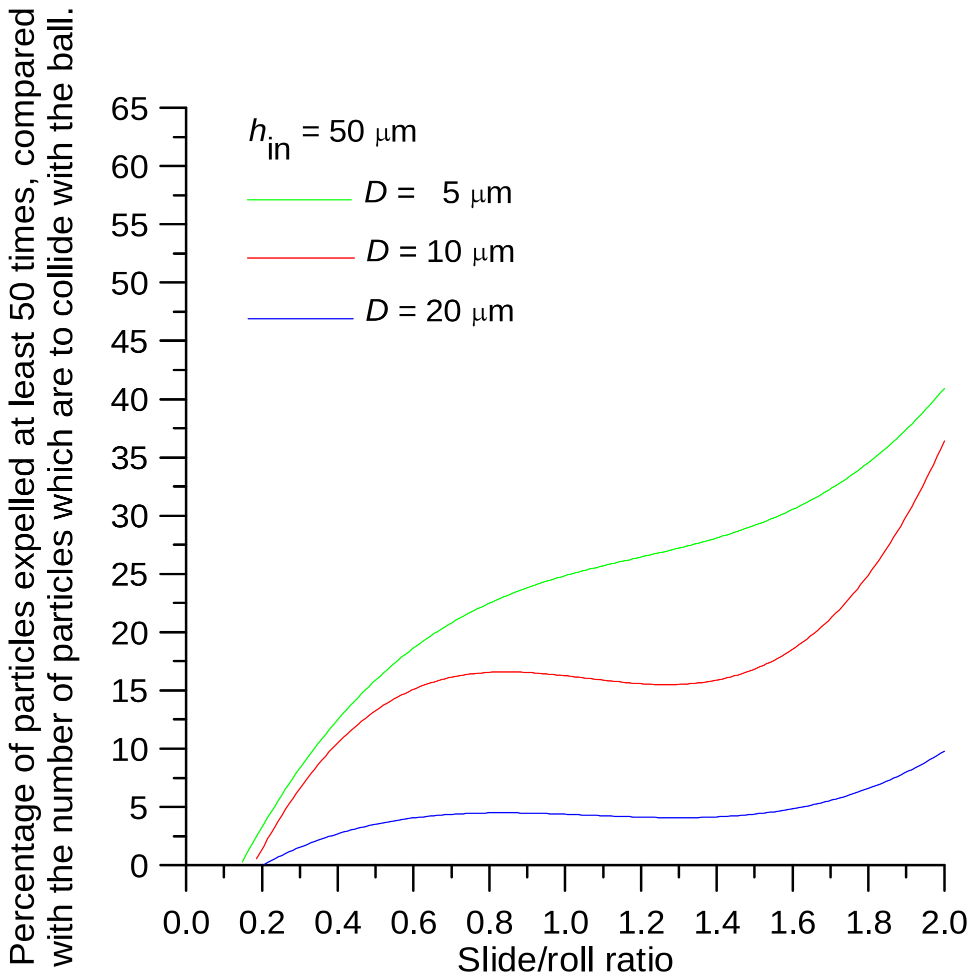

Figure 1.26

Figure 1.26 shows clearly that, for thin oil-bath films, the likelihood of repetitive particle rejection from the contact increases when the size of the particles is reduced. In general, the preferred area of operation in order to reduce the risk of oil starvation is the area $S_r < 1$ and, as has already been shown, high-sliding conditions increase the risk of particle accumulation.

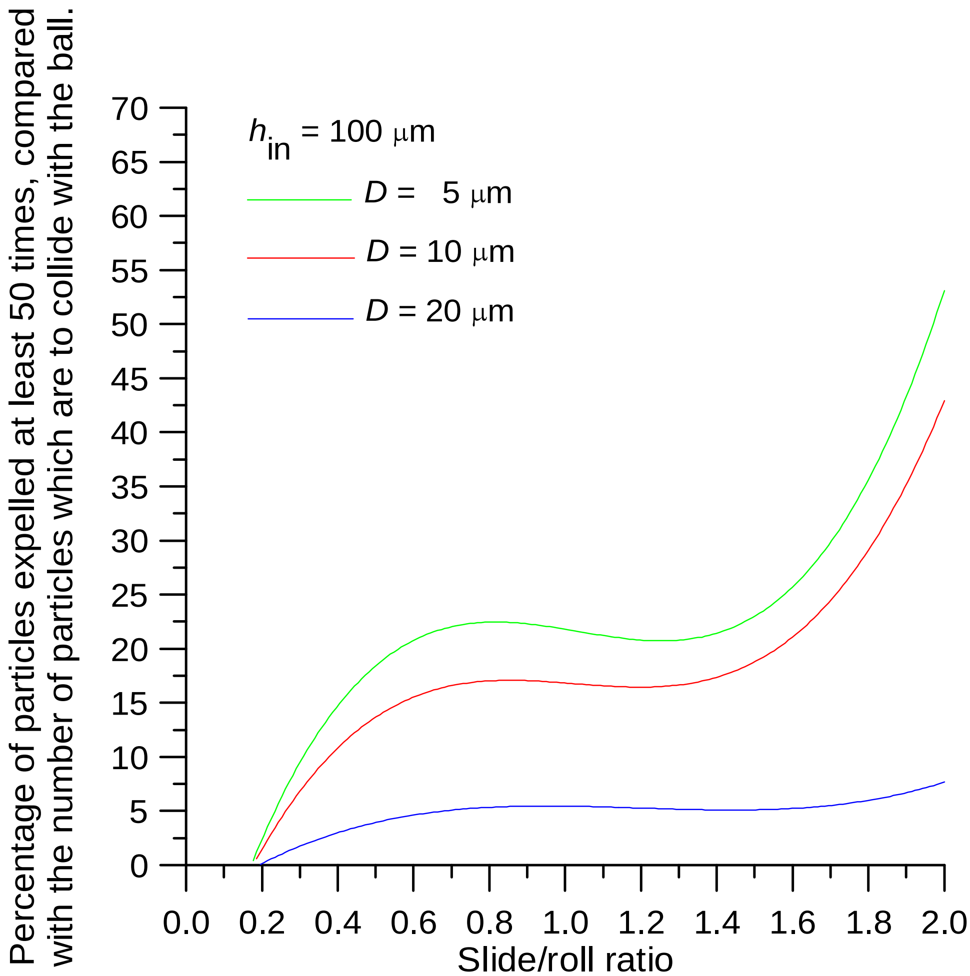

Figure 1.27

Figure 1.27 is qualitatively similar to figure 1.26 and refers to medium (100 μm) oil-bath thickness. The conclusions are the same as those for figure 1.26.

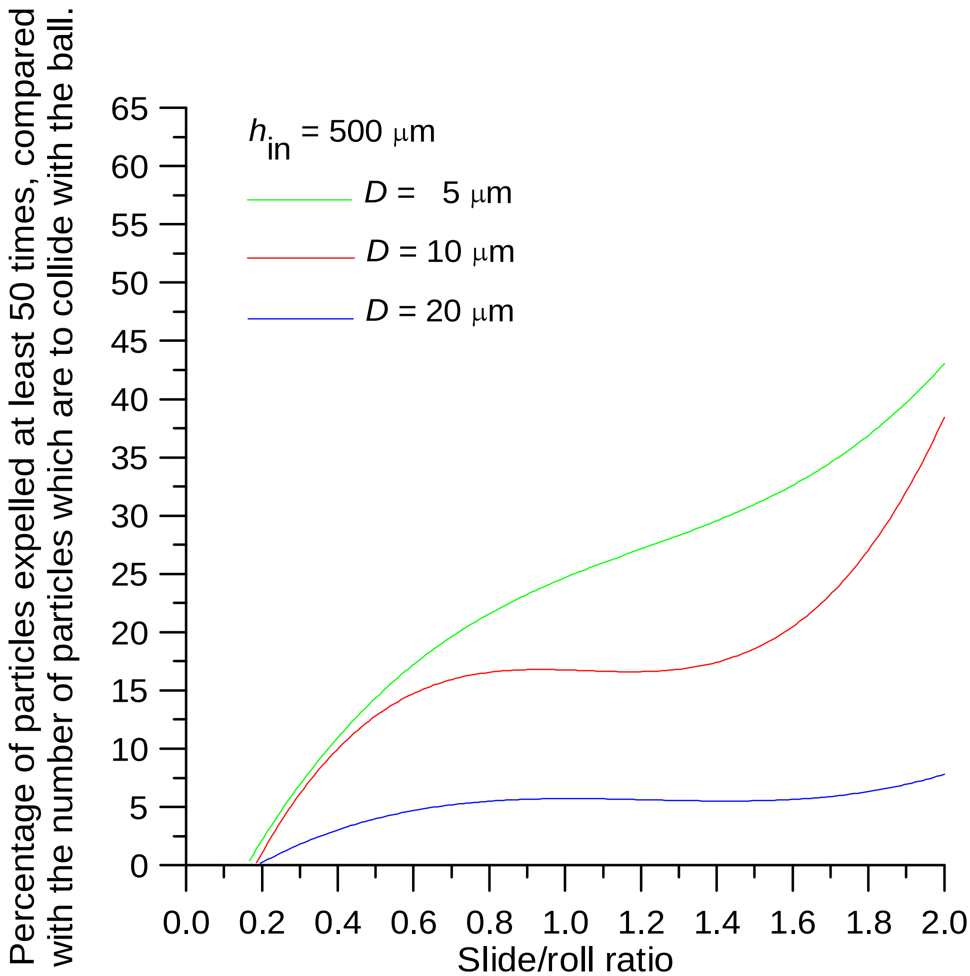

Figure 1.28

Figure 1.28, referring to relatively thick oil-bath films, confirms yet again the conclusions drawn from studying figures 1.26 and 1.27, which refer to small and medium oil-bath films. In other words, the risk of particle accumulation in the inlet zone of the contact is greater for smaller particles than for larger ones.

1.3.5 The likelihood of particle accumulation and entrapment – overall risk of damage

The likelihood of particle accumulation and entrapment is approached by calculating the percentage of particles trapped-although-initially-expelled, based on the number of particles initially expelled (expelled at least one time from the contact). An "initially" expelled particle is an early indication of possible particle accumulation, which may lead to lubricant starvation, as has already been explained. If the aforementioned "initially expelled particle" is finally trapped, the contact may further suffer from surface damage, because of the passage of the particle from the elasto-hydrodynamic gap. Therefore, the present sub-section provides information on the overall risk of damage, either due to lubricant starvation or due to surface damage owing to particle squashing in the elastohydrodynamic gap.

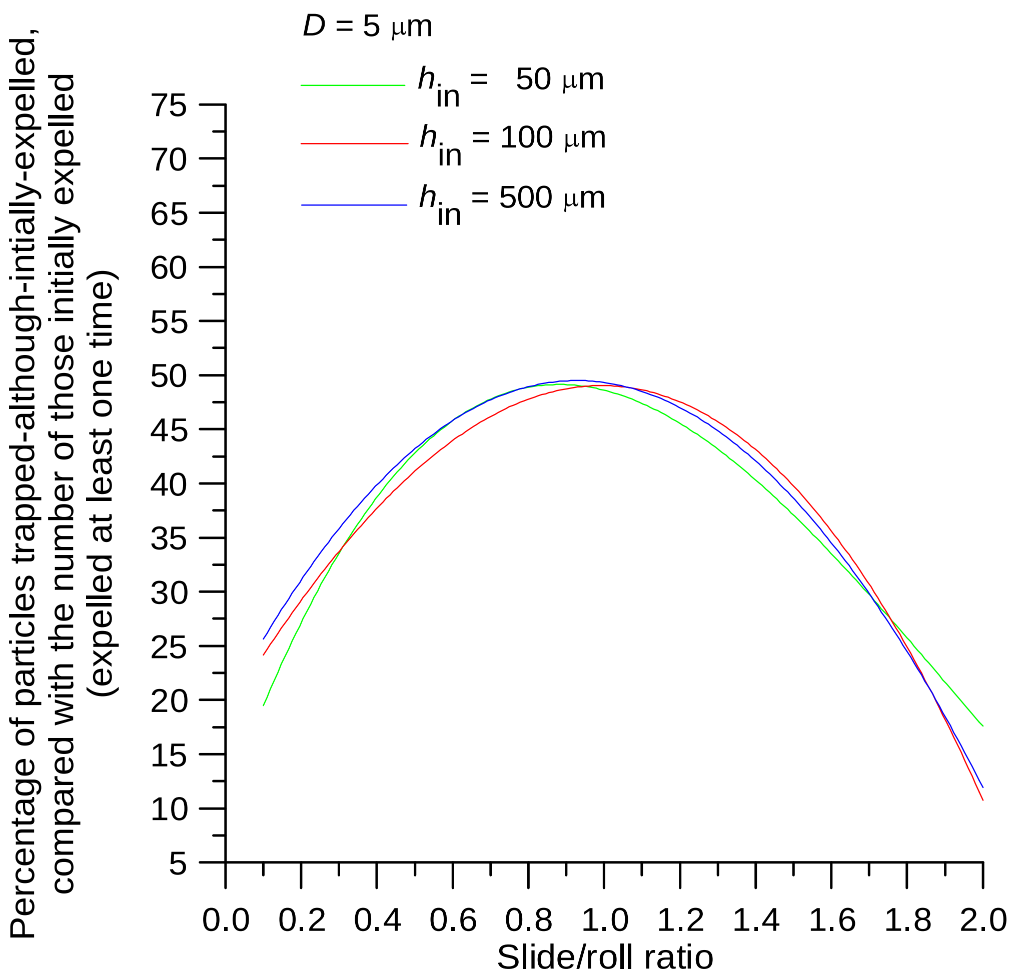

Figure 1.29

Figure 1.29 shows that the likelihood of an initially expelled, small (5 μm) particle to become entrapped is essentially independent of the oil-bath thickness and is maximized for slide/roll ratios around 1.

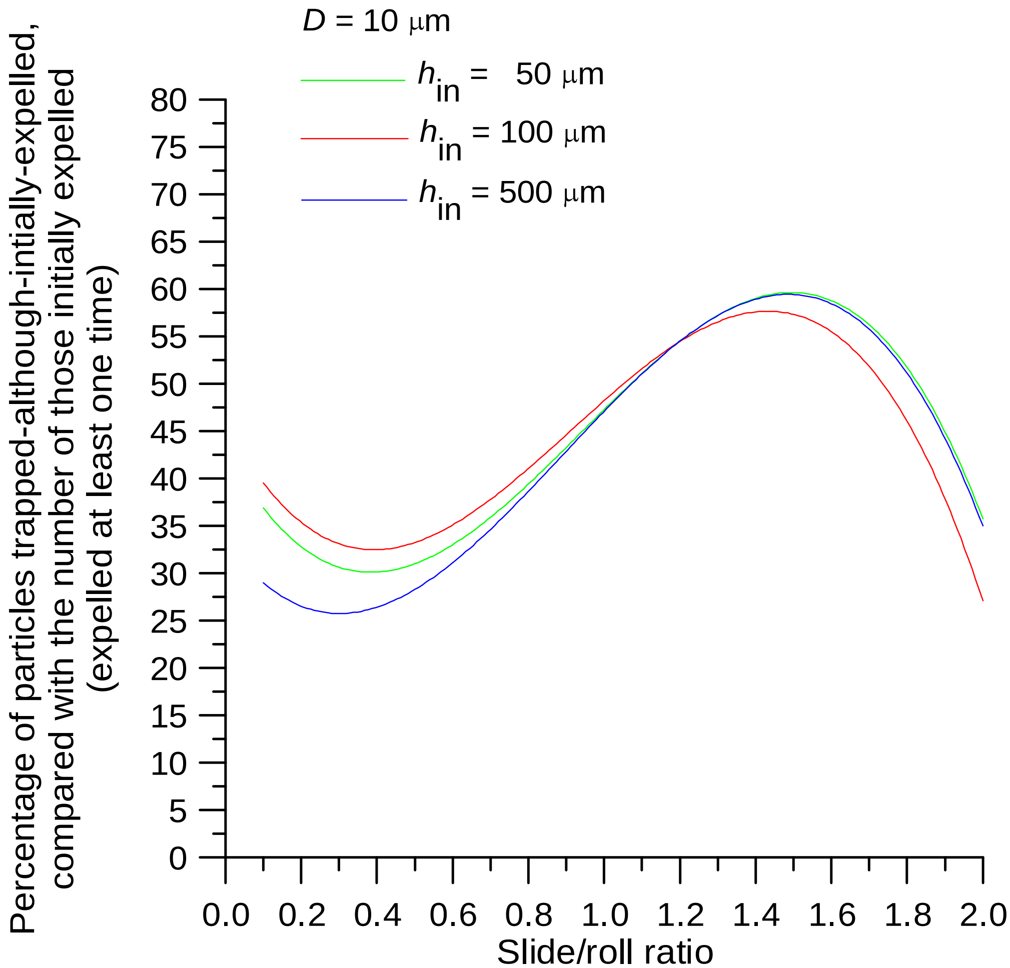

Figure 1.30

According to figure 1.30, medium-sized (10 μm) particles are more easily entrapped (after an initial rejection) for slide/roll ratio around 1.5. The oil-bath thickness does not appear to influence this behaviour.

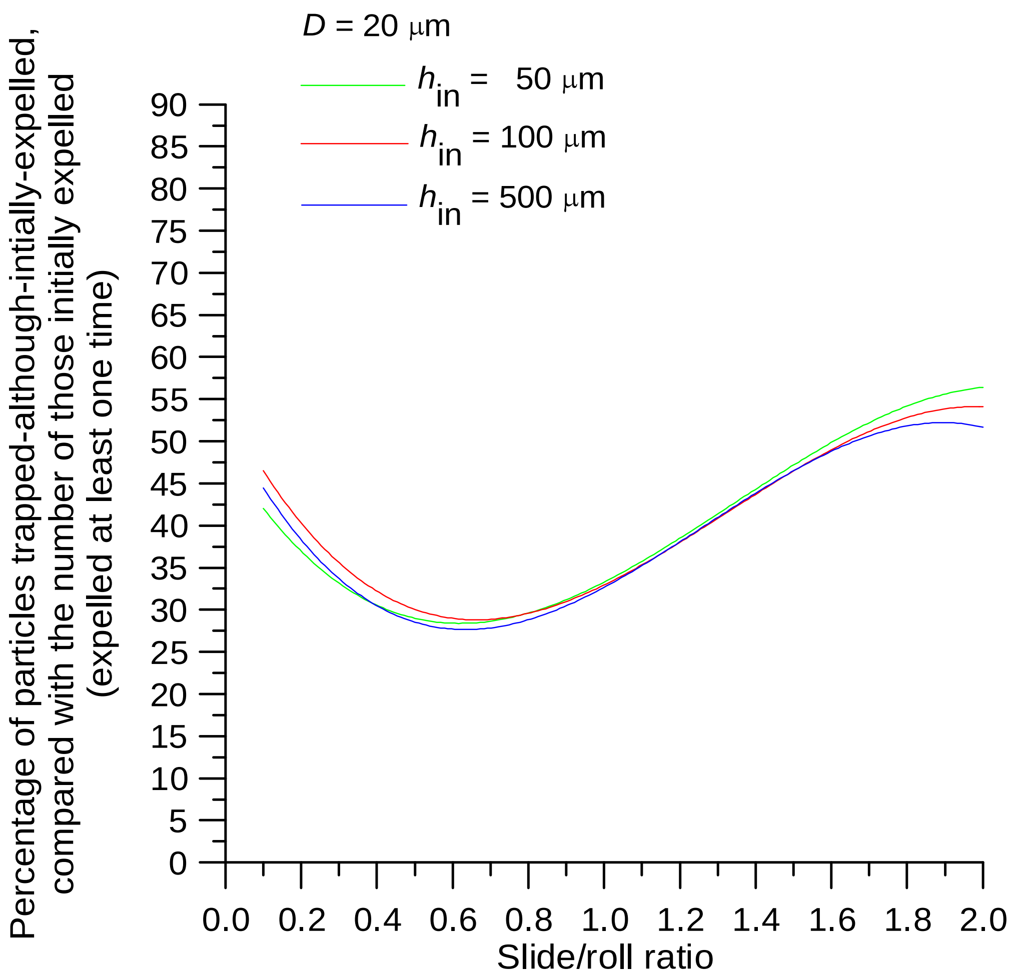

Figure 1.31

Figure 1.31 shows that for the larger (20 μm) particles, the likelihood of entrapment after an initial rejection from the contact tends to, generally, increase by increasing the slide/roll ratio, whereas it is essentially independent of the oil-bath thickness. The risk of entrapment is also relatively high for conditions of low sliding ($S_r < 0.5$) due to the reduced effect of the backflow of the lubricant on these big particles.

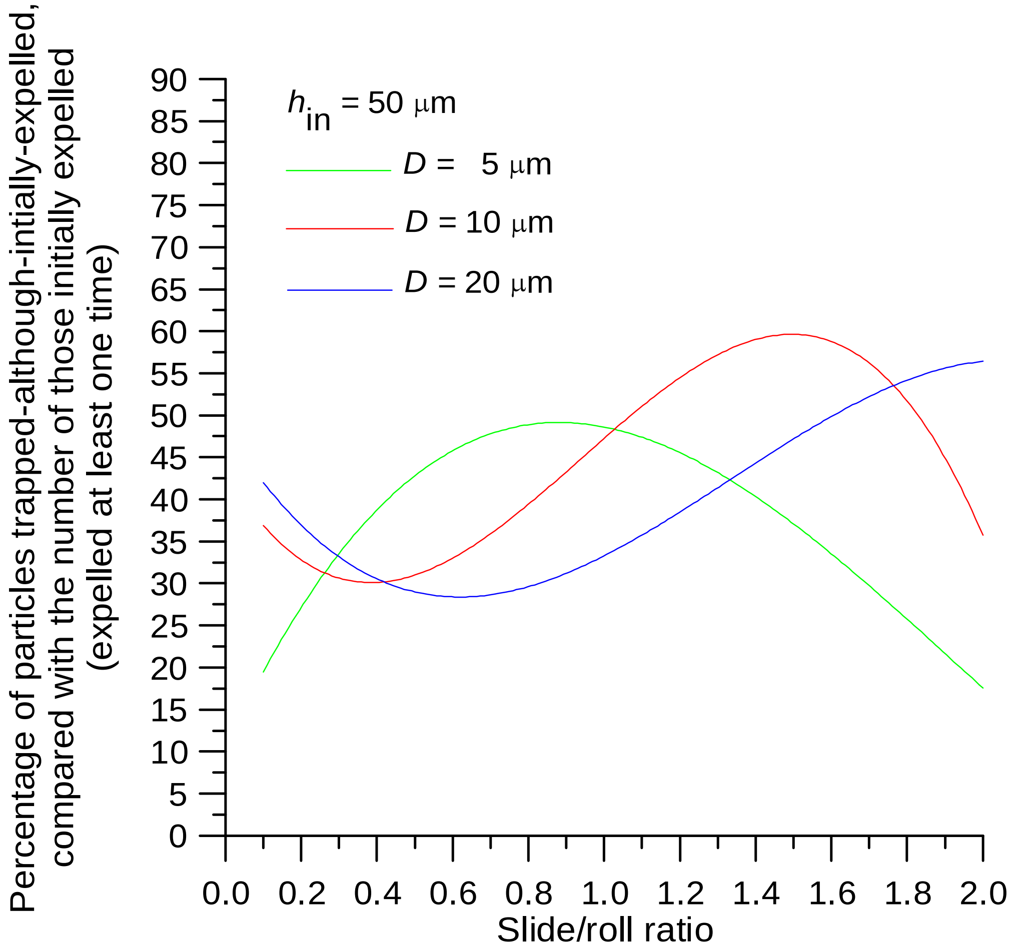

Figure 1.32

According to figure 1.32, which refers to thin oil-bath films (starved contacts), smaller particles behave rather differently in comparison with larger ones. This is due to the fact that smaller particles are affected by the changes of the oil flow more than the larger particles. For high sliding conditions, the combined risk of damage (particle accumulation + entrapment) is lower for the smaller particles.

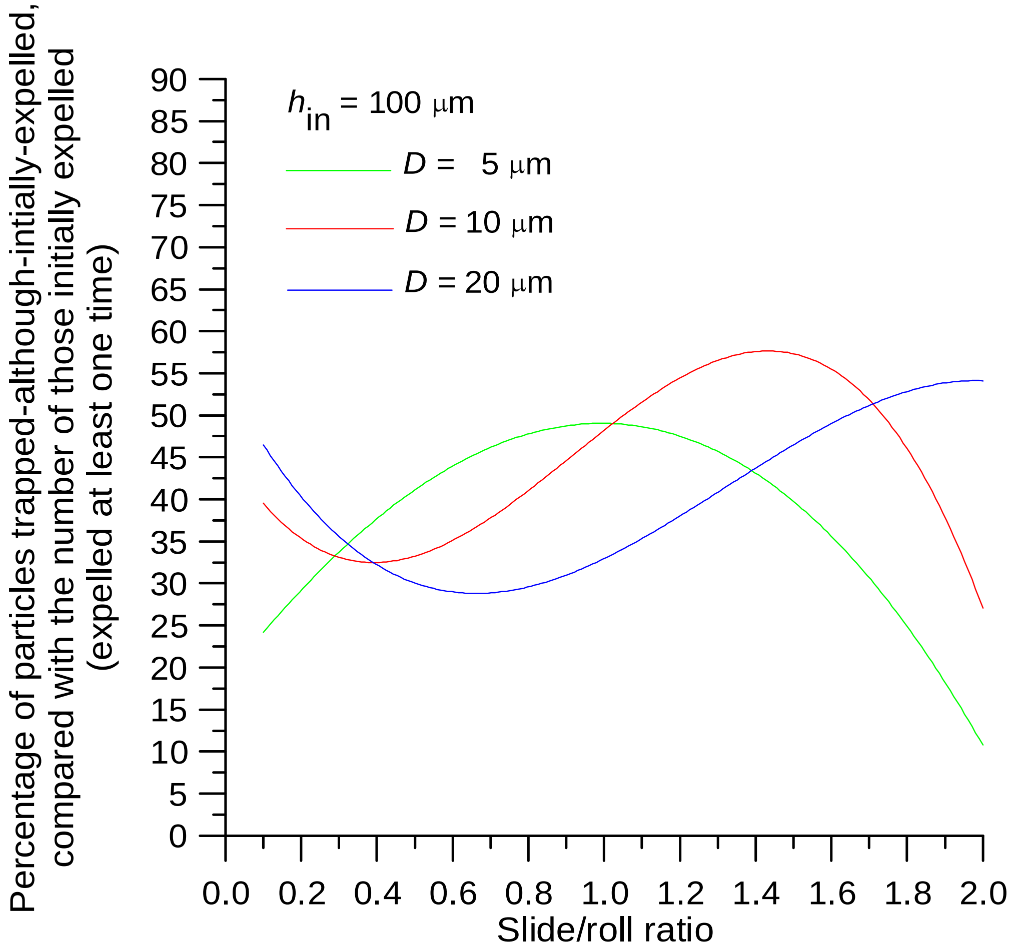

Figure 1.33

Figure 1.33, referring to medium oil-bath thickness, shows the same particle behaviour as in figure 1.32, namely larger particles are more easily entrapped (after an initial rejection) for high slide/roll ratios than smaller particles.

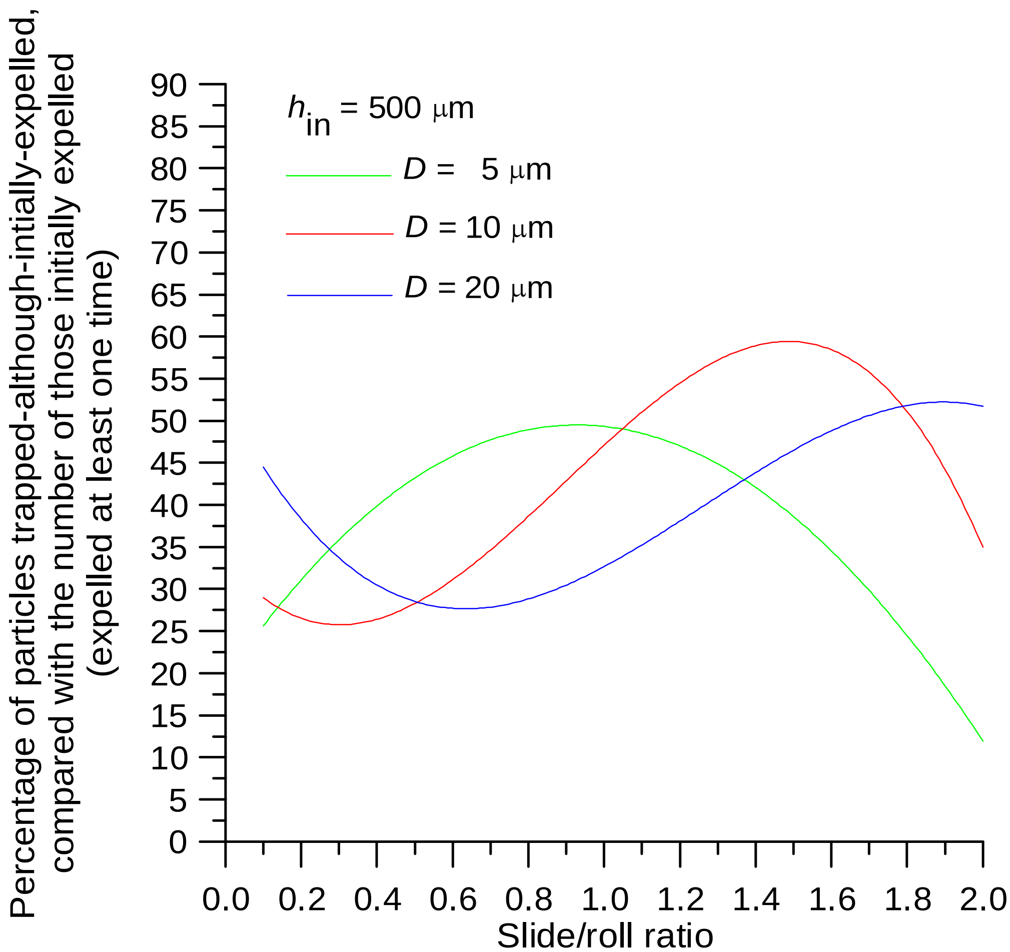

Figure 1.34

Figure 1.34 leads to the same conclusions as in figures 1.32 and 1.33, which refer to thinner oil bath films.

1.3.6 The likelihood of particle entrapment – risk of surface damage

The likelihood of particle entrapment is assessed by calculating the percentage of particles trapped in the elastohydrodynamic gap, based on the number of particles studied (put in the reference volume). In this way, it can readily be seen how risky it is for particle entrapment when a particle is “allowed” to be present in the lubricant. It must be noted that the risk of surface damage may not be proportional to the likelihood of particle entrapment, because the nature, extent and even possibility of surface damage depends on the hardness of the particles relatively to the hardness of the surfaces, the size of the particles relatively to the central film thickness of the contact, the material mechanical and thermal properties of both the particles and the counterfaces (ball and flat), etc. In other words, the likelihood of particle entrapment may be high and the risk of surface damage may be very low, because, for example, the particles are very small and/or very soft.

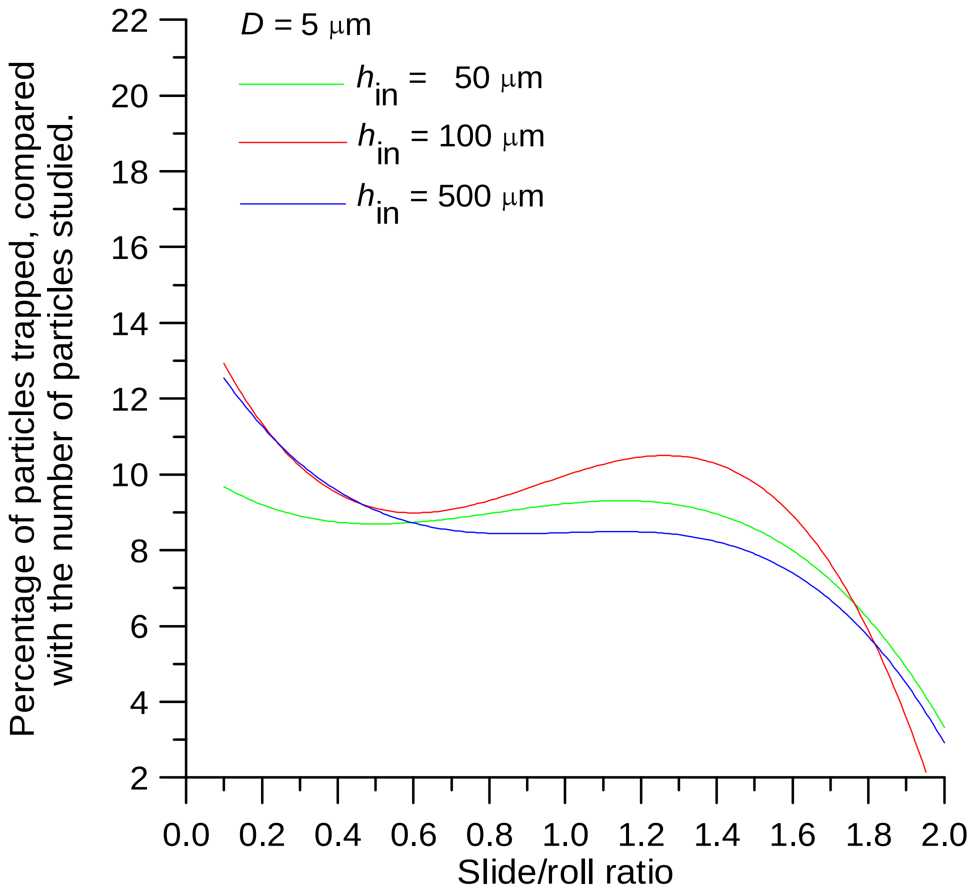

Figure 1.35

Figure 1.35 shows that the likelihood of particle entrapment is not greatly affected by the oil-bath thickness. An important observation is that the likelihood of entrapment (and thus the risk of surface denting or scratching) is significantly lower for high slide/roll ratios ($S_r > 1.5$). Moreover, low sliding conditions promote particle entrapment.

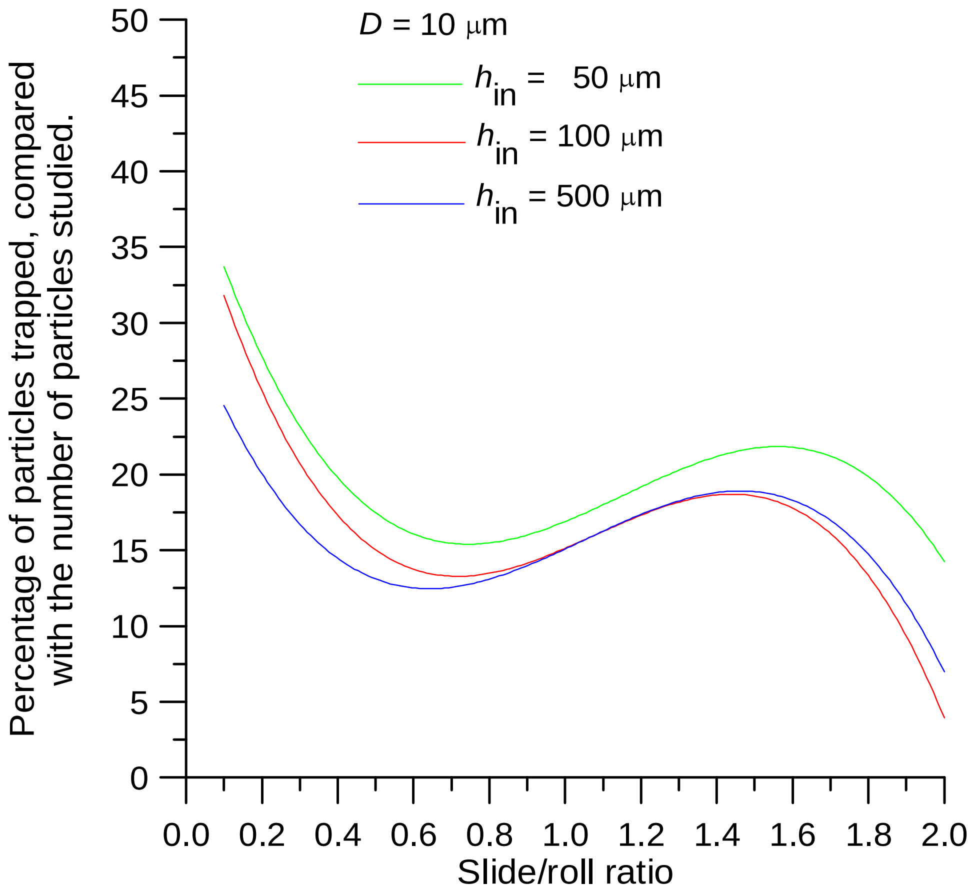

Figure 1.36

Figure 1.36 refers to medium-sized (10 μm) particles and shows again, as in figure 1.35, that the risk of particle entrapment is generally increased for low slide/roll ratios and decreased for high sliding conditions.

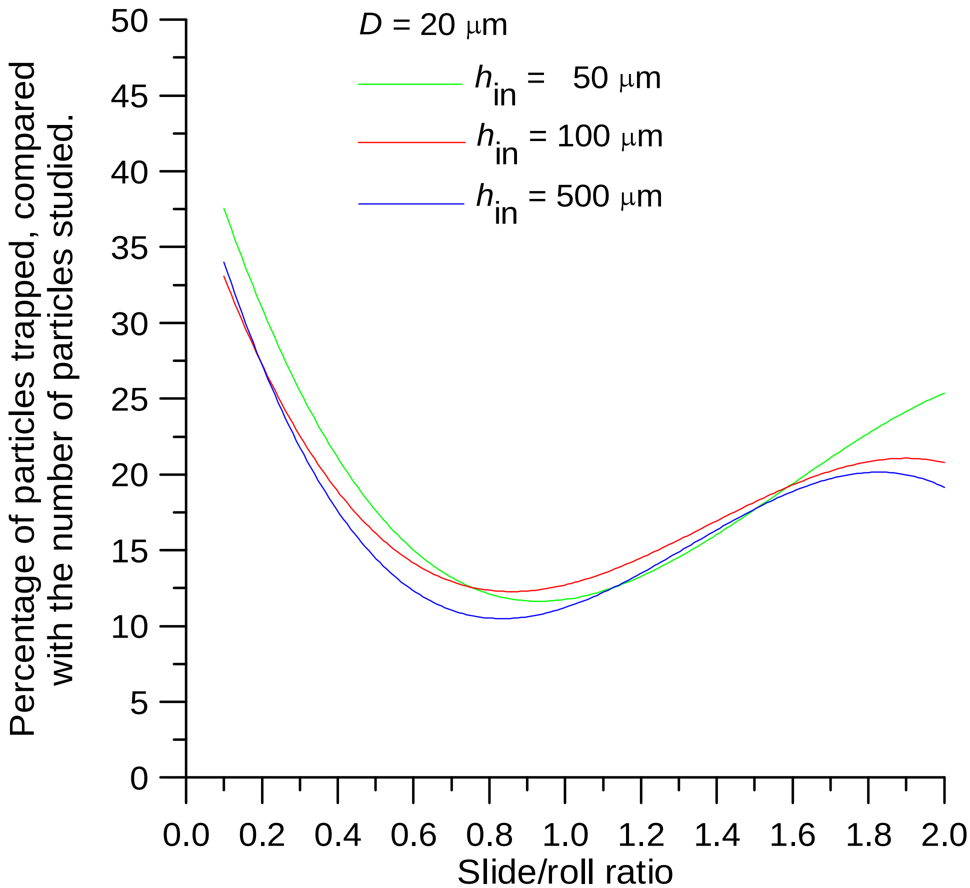

Figure 1.37

Figure 1.37 shows that large particles are more easily entraped for low slide/roll ratios ($S_r < 0.5$). There appears to be a preferred region of the slide/roll ratio around 1, where the risk of entrapment is minimized.

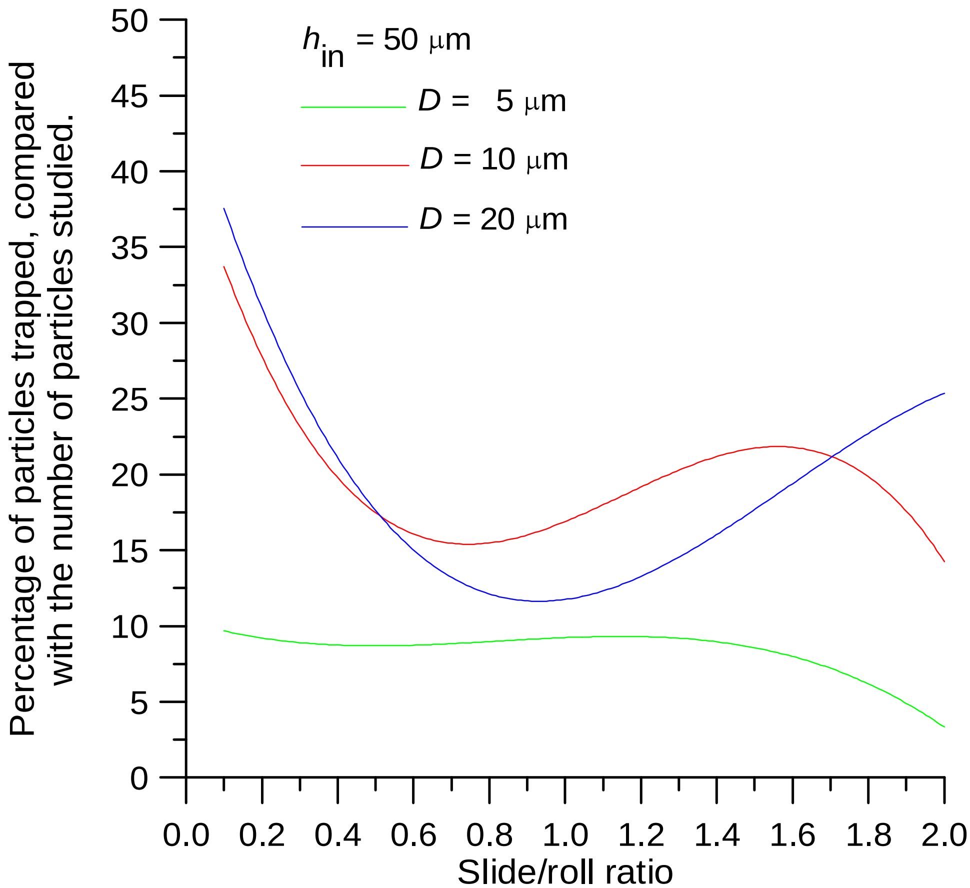

Figure 1.38

According to figure 1.38, the smaller (5 μm) particles are more difficult to get trapped in the elastohydrodynamic gap compared with the larger particles, for thin oil-bath films. The difference is less pronounced between the medium-sized and the larger particles.

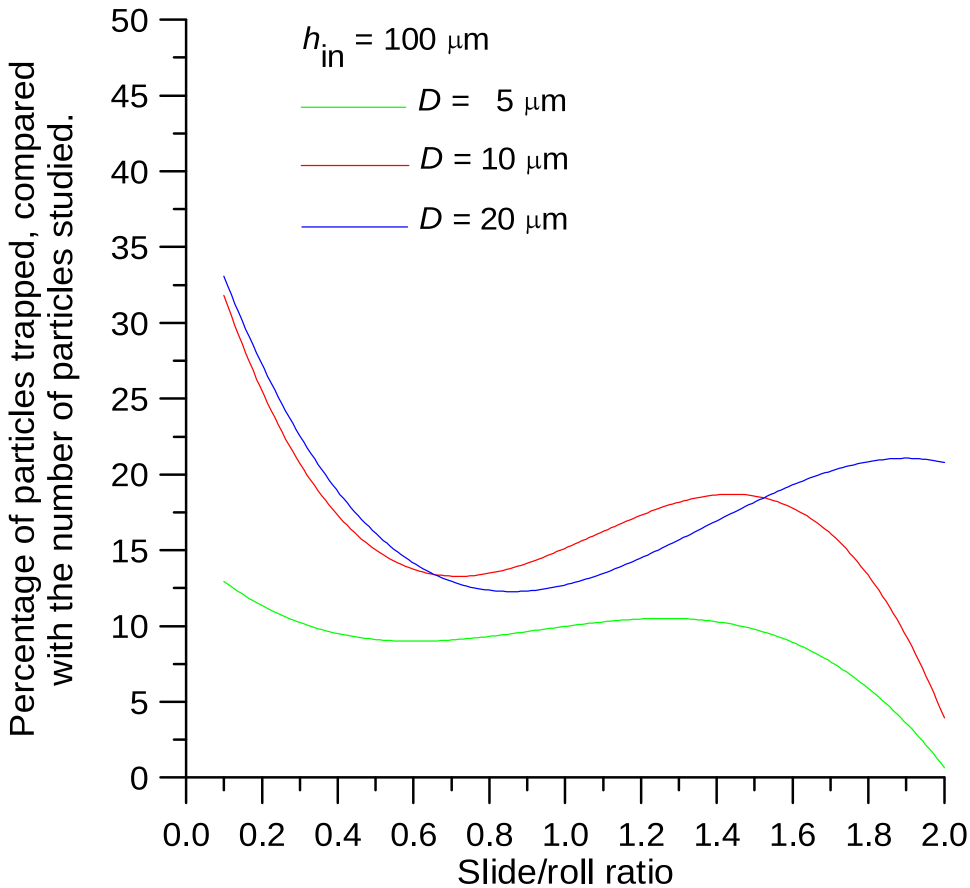

Figure 1.39

Qualitatively, figure 1.39, which refers to medium oil-bath films (h_{in} = 100 μm), shows the same behaviour as in figure 1.38. The risk of particle entrapment is maximized for low slide/roll ratios and decreases in the high slide/roll ratio region.

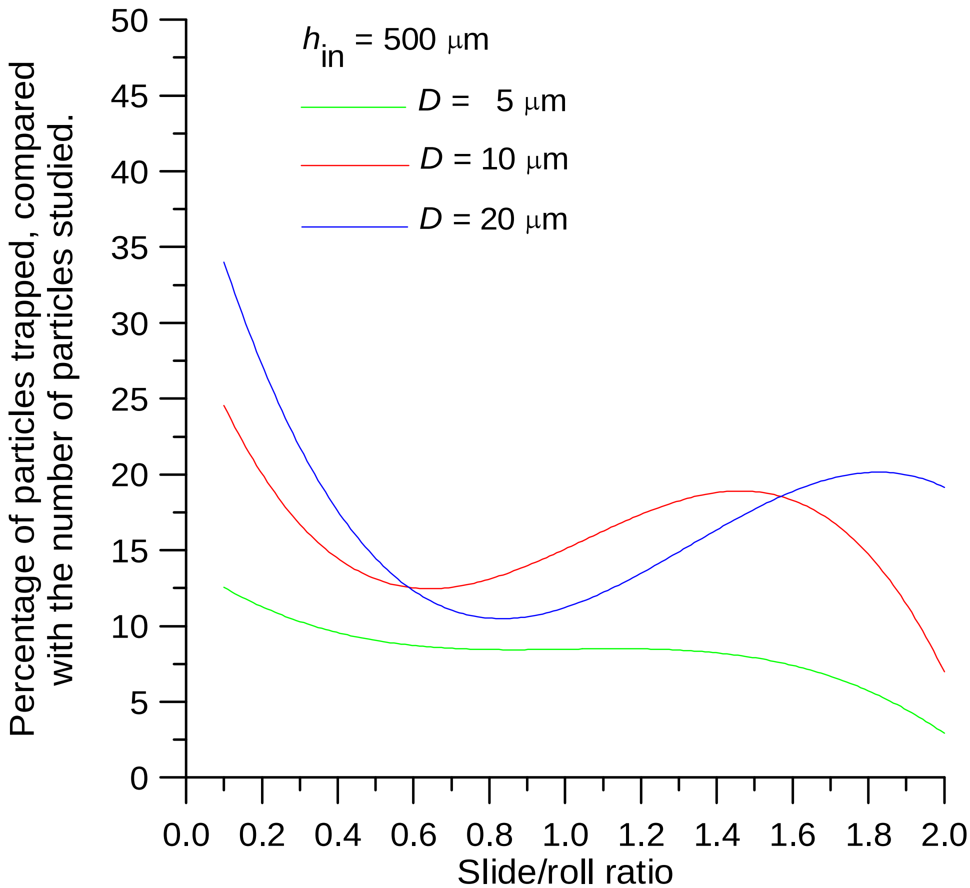

Figure 1.40

Finally, figure 1.40, which refers to relatively thick oil-bath films, confirms the results of figures 1.38 and 1.39, which refer to thinner oil-bath films; namely, the smaller particles are more difficult to become entrapped, with the risk being increased for low slide/roll ratios.

1.3.7 The likelihood of particle entrapment – another estimation

An alternative estimation of the likelihood of particle entrapment (as compared with sub-section 1.3.6) is achieved by calculating the percentage of particles trapped, based on the particles that are to collide with the ball. In this way, it can readily be seen how risky it is for particle entrapment when a particle is "allowed" to reach the ball and collide with it. In comparison with sub-section 1.3.6, the results of the study of the present sub-section take as granted the fact that the lubricant is contaminated by solid particles, whereas the results of sub-section 1.3.6 aim to show what might have been avoided if the lubricant were not contaminated.

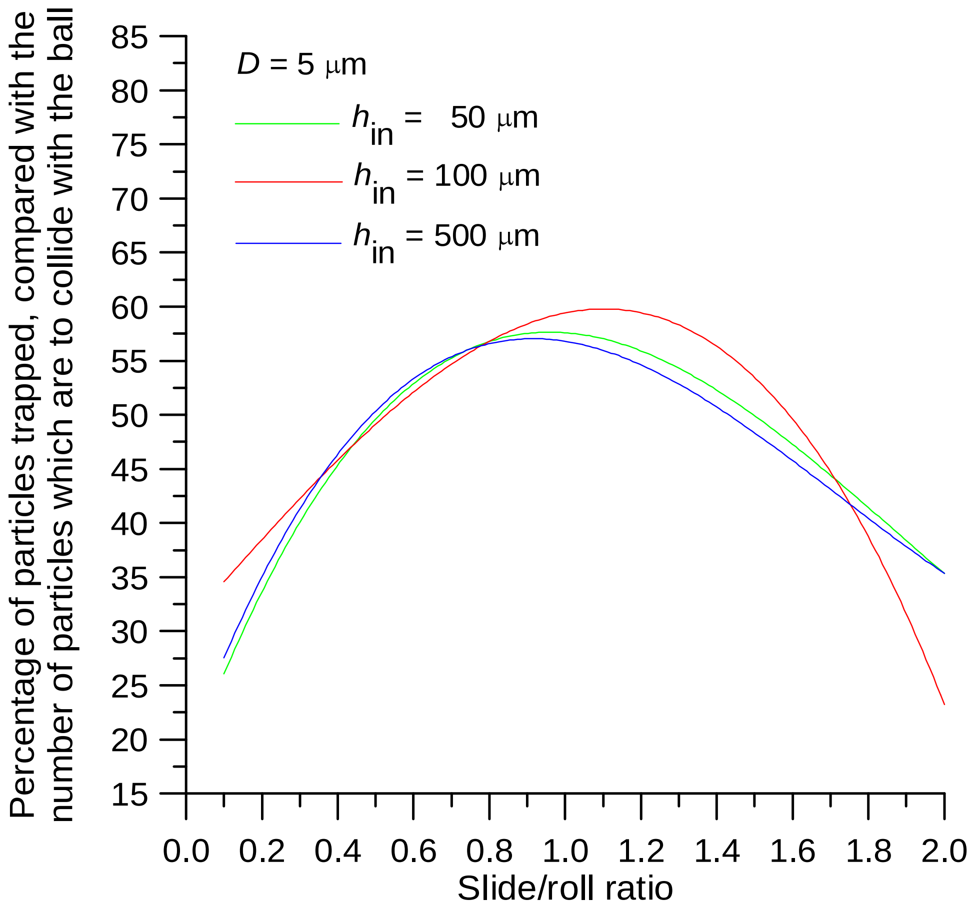

Figure 1.41

Figure 1.41 shows that smaller (5 μm) particles that collide with the ball are trapped more easily if the slide/roll ratio is around 1, regardless of the oil-bath thickness. The risk of entrapment is reduced for lower and higher slide/roll ratios.

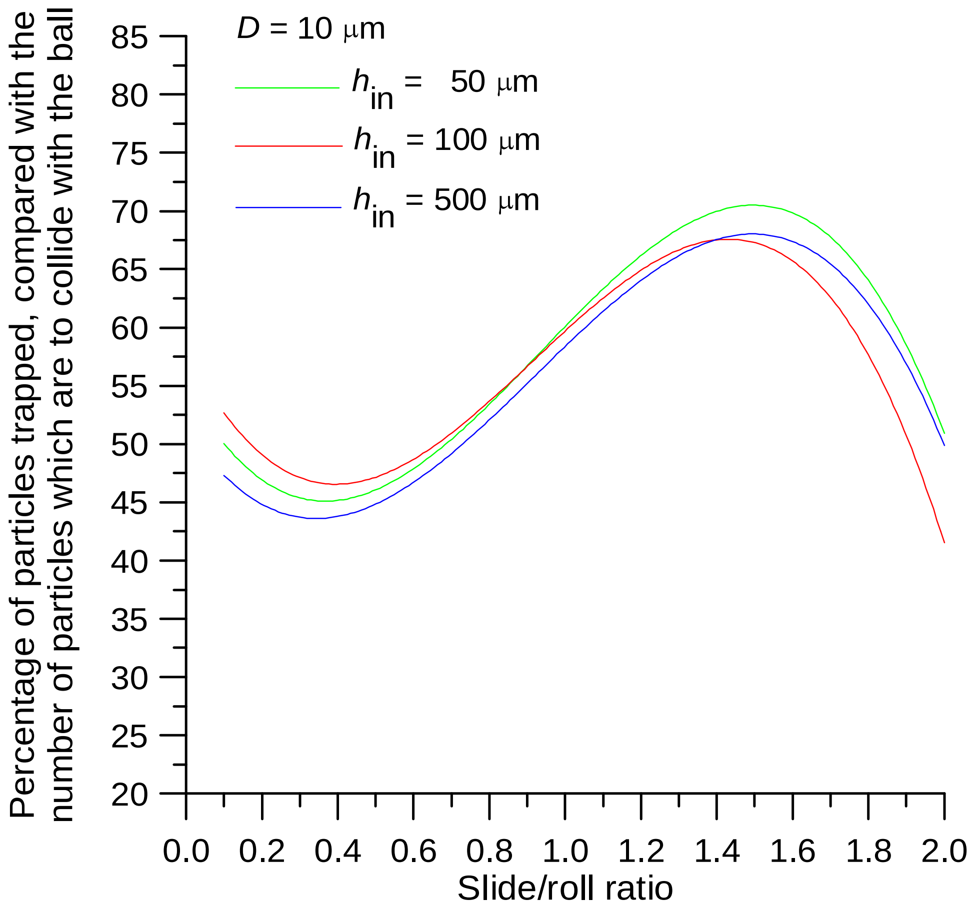

Figure 1.42

Figure 1.42 shows that medium-sized (10 μm) particles that collide with the ball are more easily trapped for slide/roll ratios around 1.5. Low and high sliding conditions are to be preferred in order to minimize the risk of particle entrapment and possible surface damage. The variation of oil-bath thickness has a weak effect on the results.

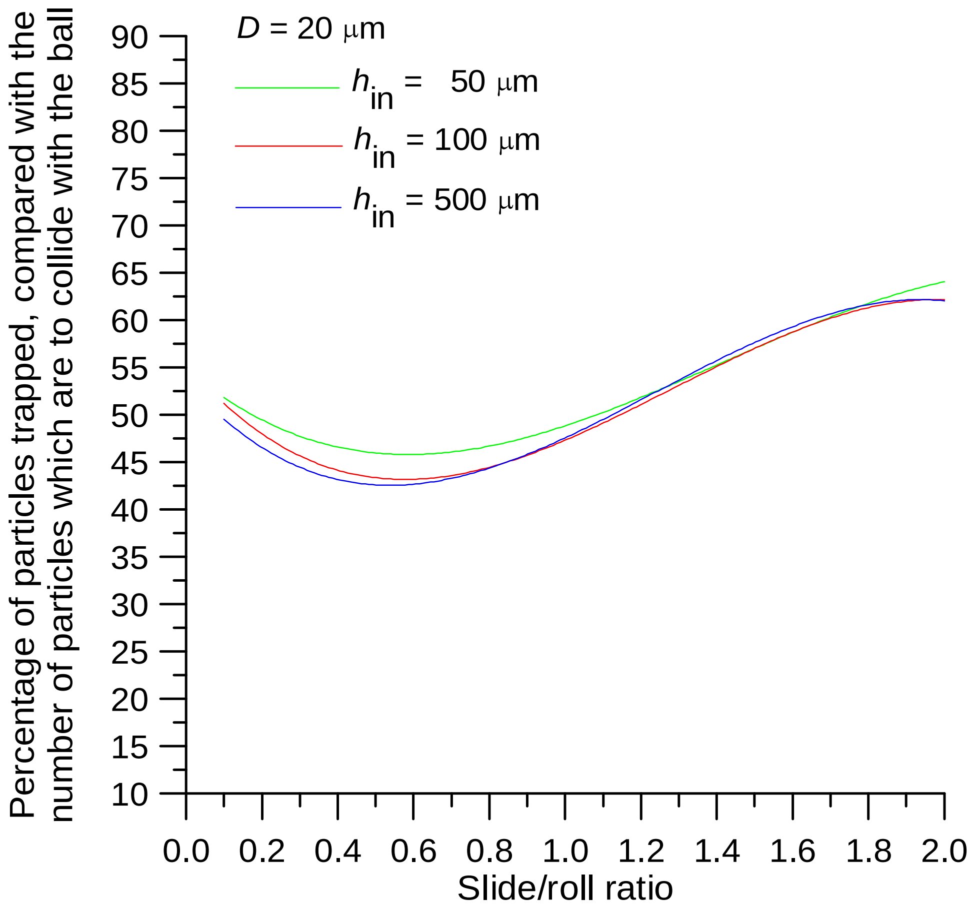

Figure 1.43

Larger (20 μm) particles behave similarly to medium-sized (10 μm) ones (figure 1.42). The maxima and minima of the likelihood of particle entrapment can easily be located on the above figure.

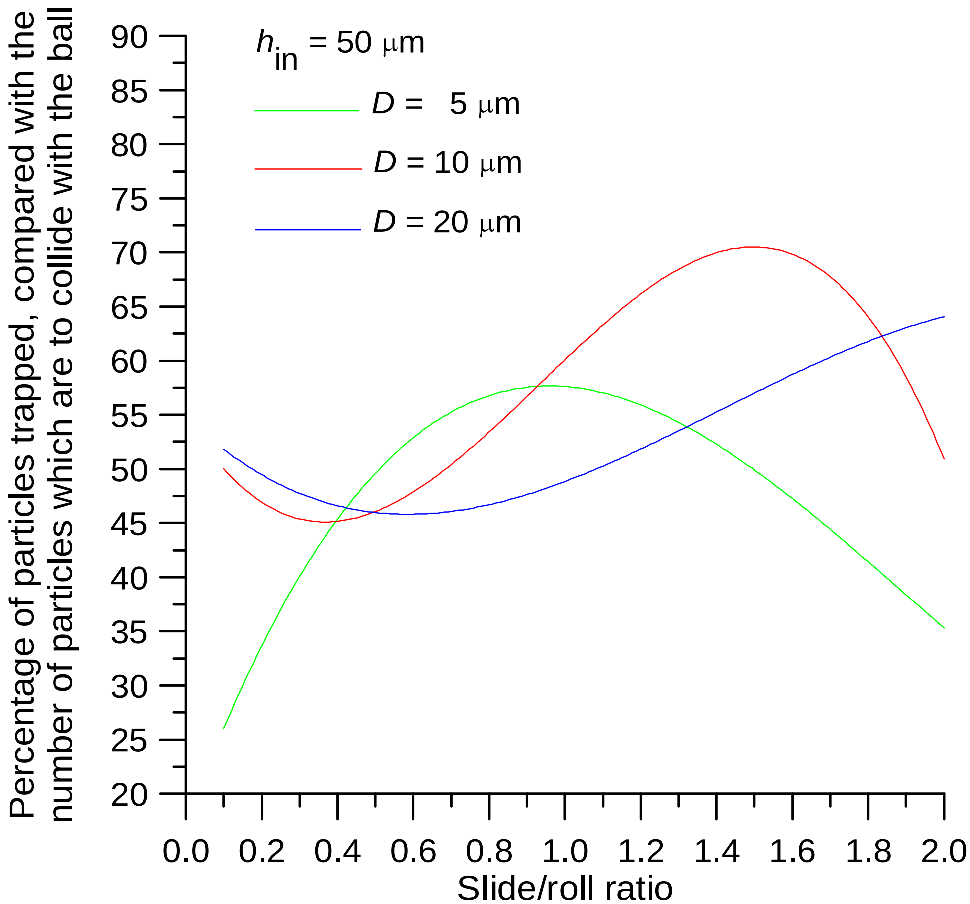

Figure 1.44

Figure 1.44 shows that, in the case of thin oil-bath films (starved contacts), 5 μm particles have a profoundly smaller likelihood of entrapment for low and high slide/roll ratios, compared with the larger particles. The differences appear to be largely dependent on the amount of sliding in the contact.

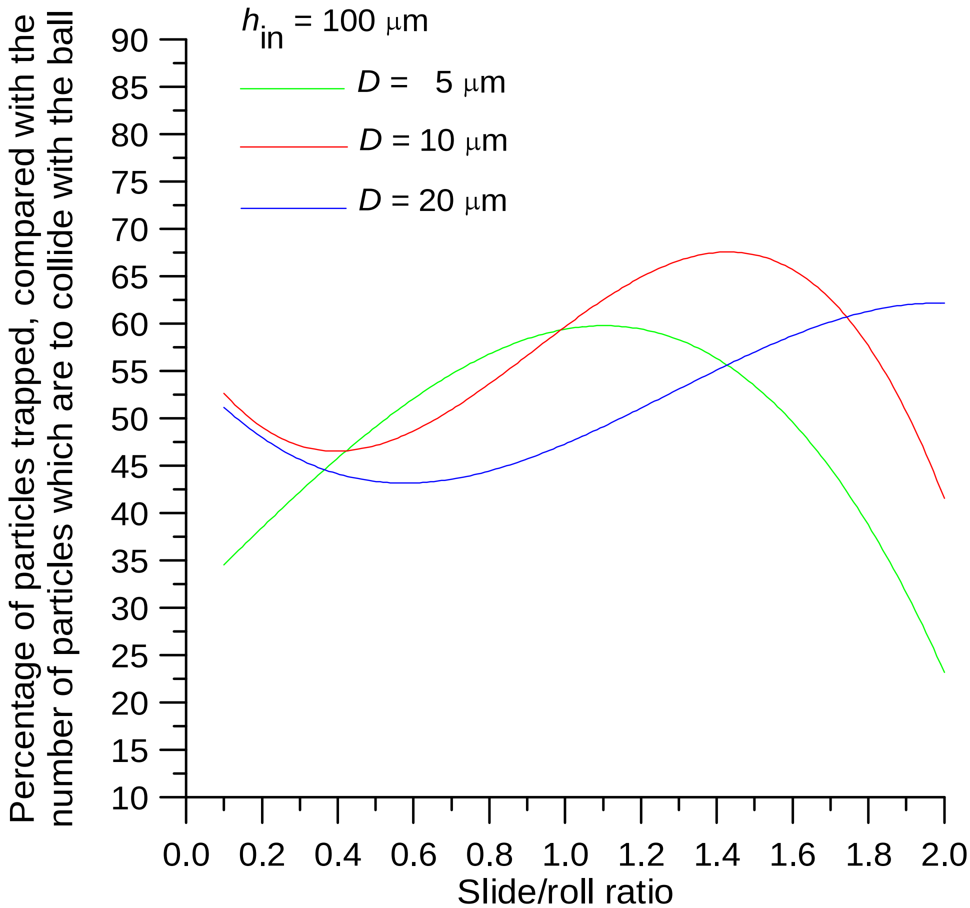

Figure 1.45

The results shown in figure 1.45 (which refers to medium oil-bath thickness) are in agreement with those of the previous figure 1.44 for thinner oil-bath films and the same conclusions apply here as well.

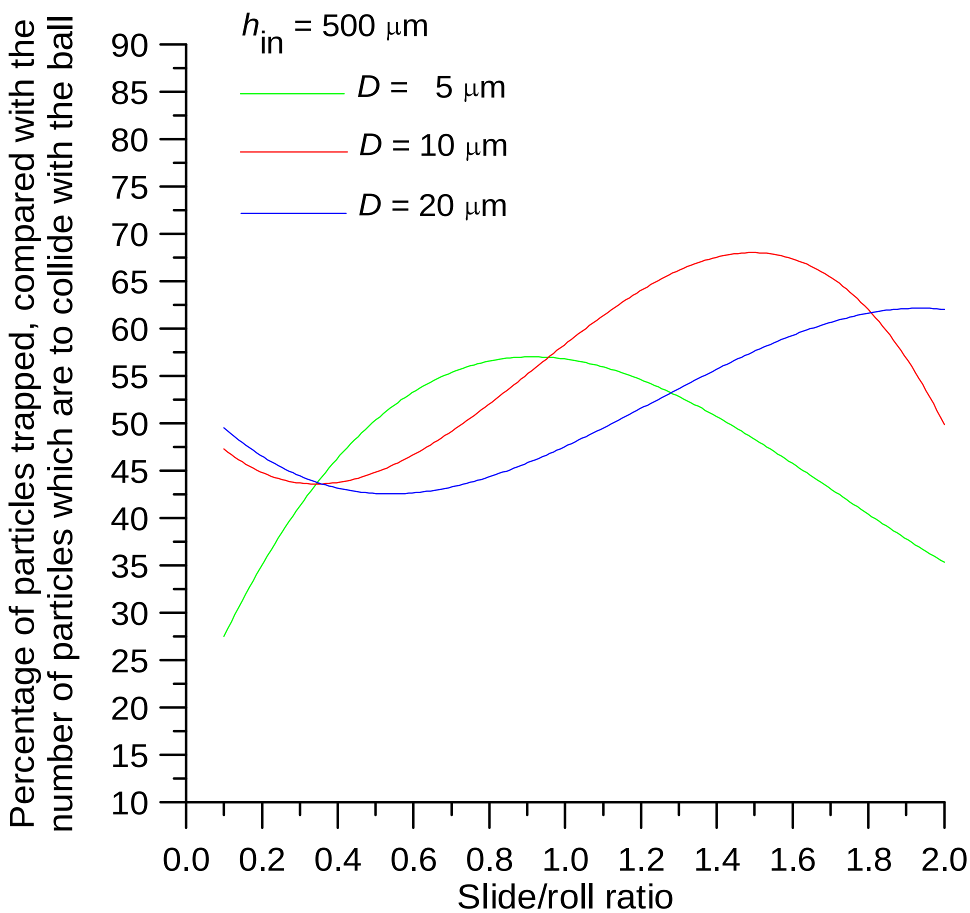

Figure 1.46

Figure 1.46, which refers to thicker oil-bath films, is qualitatively similar to figures 1.44 and 1.45, which refer to thinner films. The same conclusions apply here as well.

1.3.8 The likelihood of lubricant starvation – an indirect approach

An indirect approach of the likelihood of lubricant starvation, owing to particle presence in the inlet zone of the contact, is taken by calculating the average travelling time of those particles which are to be entrapped. Obviously, the more time a particle spends travelling in the lubricant (in the inlet zone, for specified sliding and rolling velocities of the contact) before being entrapped, the higher is the risk of lubricant-flow obstruction and, thus, the poorer the lubrication of the contact may be. The lubricant-flow upsetting, owing to the presence of particles in the flow, is of course directly dependent on the size of the particles. Therefore, the results of the present sub-section must be interpreted only as an indication of the likelihood of lubricant starvation.

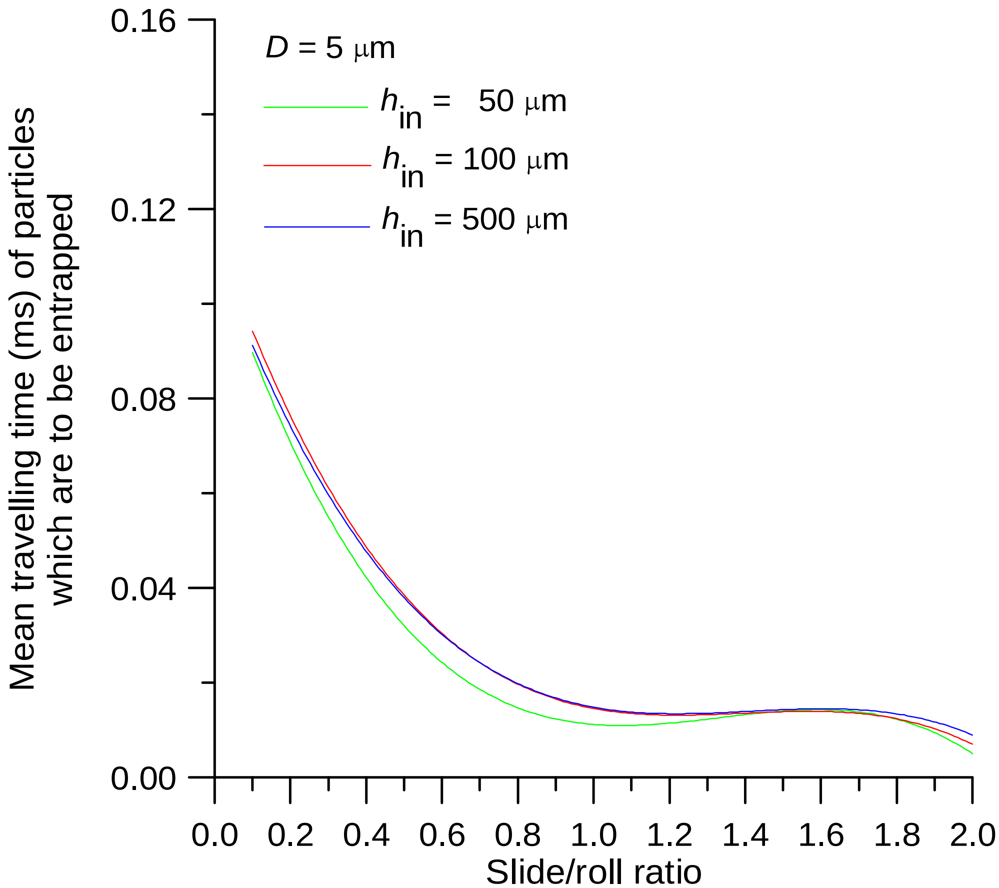

Figure 1.47

Figure 1.47 shows that the mean travelling time of small (5 μm) particles that are to become entrapped is significantly higher for the lowest bound of slide/roll ratios studied ($S_r < 1$). The influence of the oil-bath thickness on the results is insignificant.

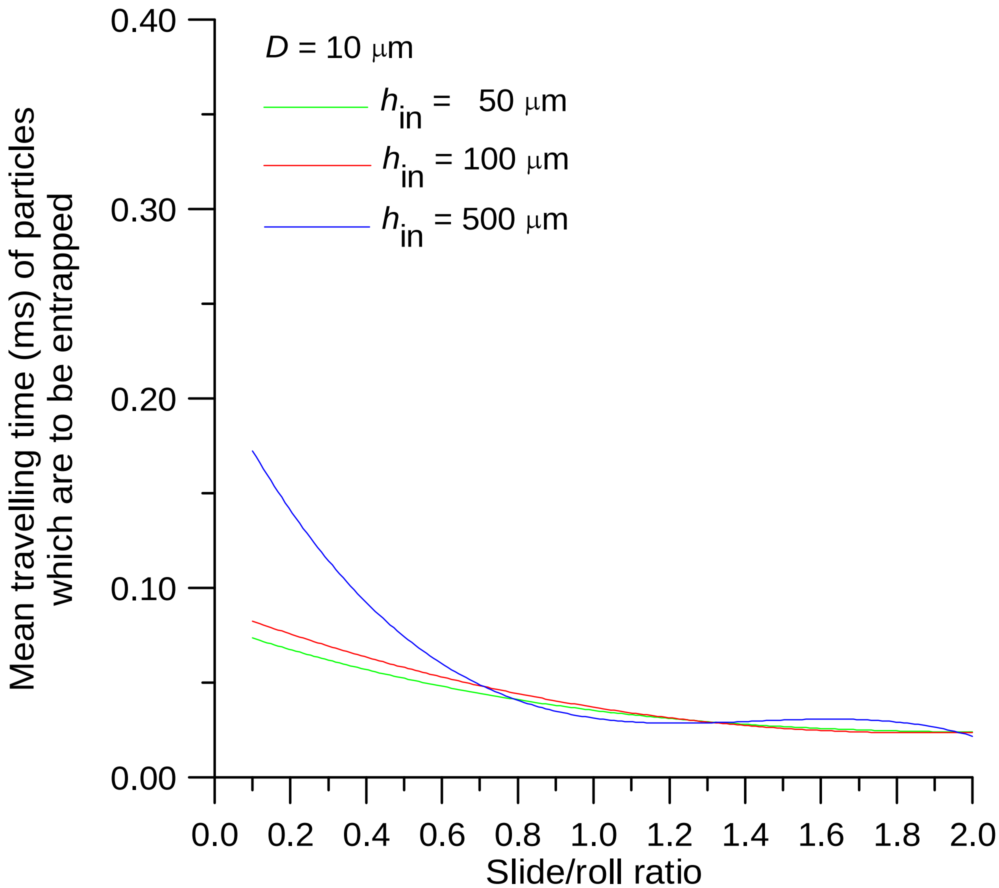

Figure 1.48

According to figure 1.48, medium-sized (10 μm) particles spend considerably more time travelling if the oil-bath is relatively thick (h_{in} = 500 μm) and the slide/roll ratio low.

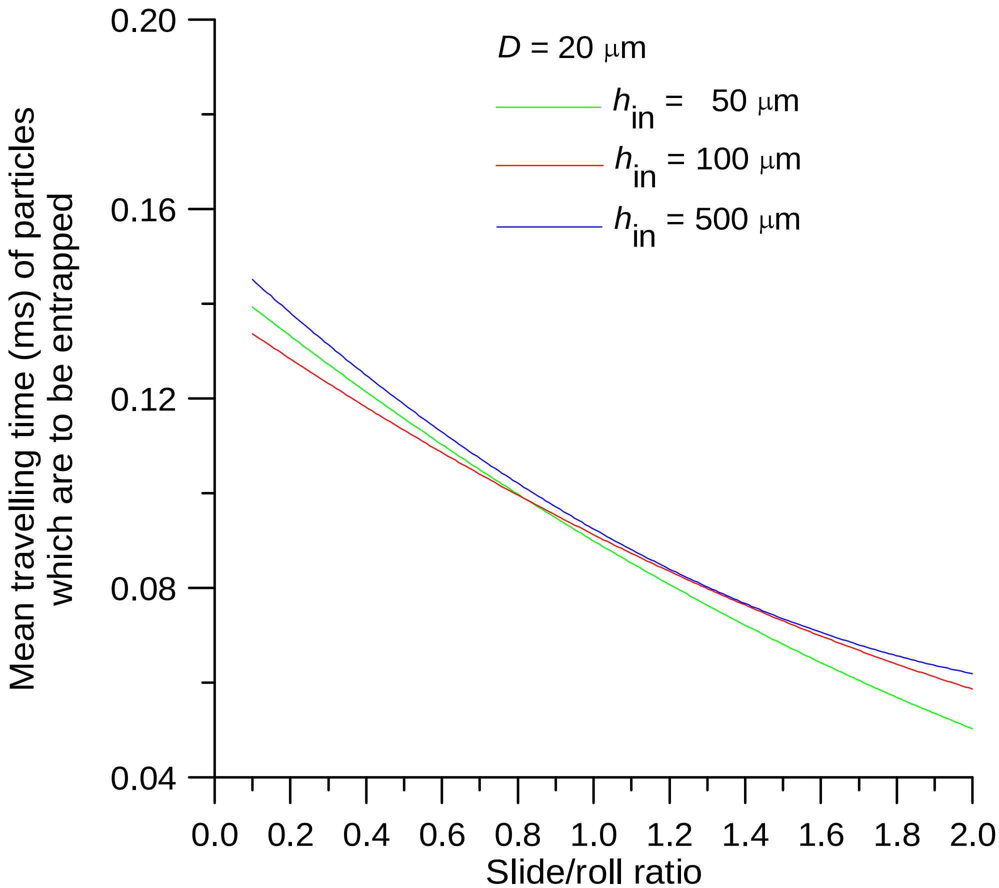

Figure 1.49

Figure 1.49 shows that, for larger (20 μm) particles, the mean travelling time before entrapment is gradually reduced as the sliding of the contact increases (obviously), and stays essentially insensitive to oil-bath thickness variations throughout the slide/roll ratio band studied. The behaviour (motion) of the larger particles is smoother, as can be realized by comparing figure 1.49 with figure 1.47, probably because the bigger particles are heavier and more difficult to follow flow changes.

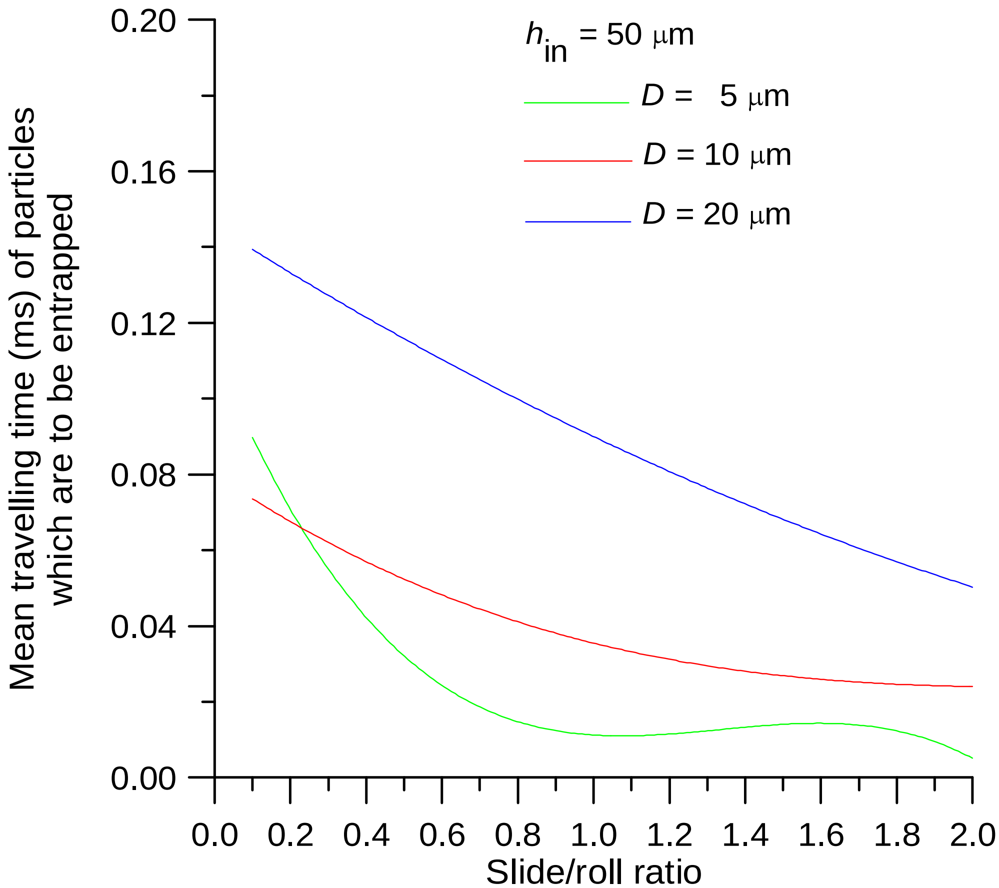

Figure 1.50

Figure 1.50 shows that, for thin oil-bath films (h_{in} = 50 μm), larger particles spend considerably more time travelling before entrapment, compared with smaller particles. This is what should be expected, considering the mass difference of the particles. It is easy to find that the 20 μm spherical particles are 64 times heavier than the 5 μm ones.

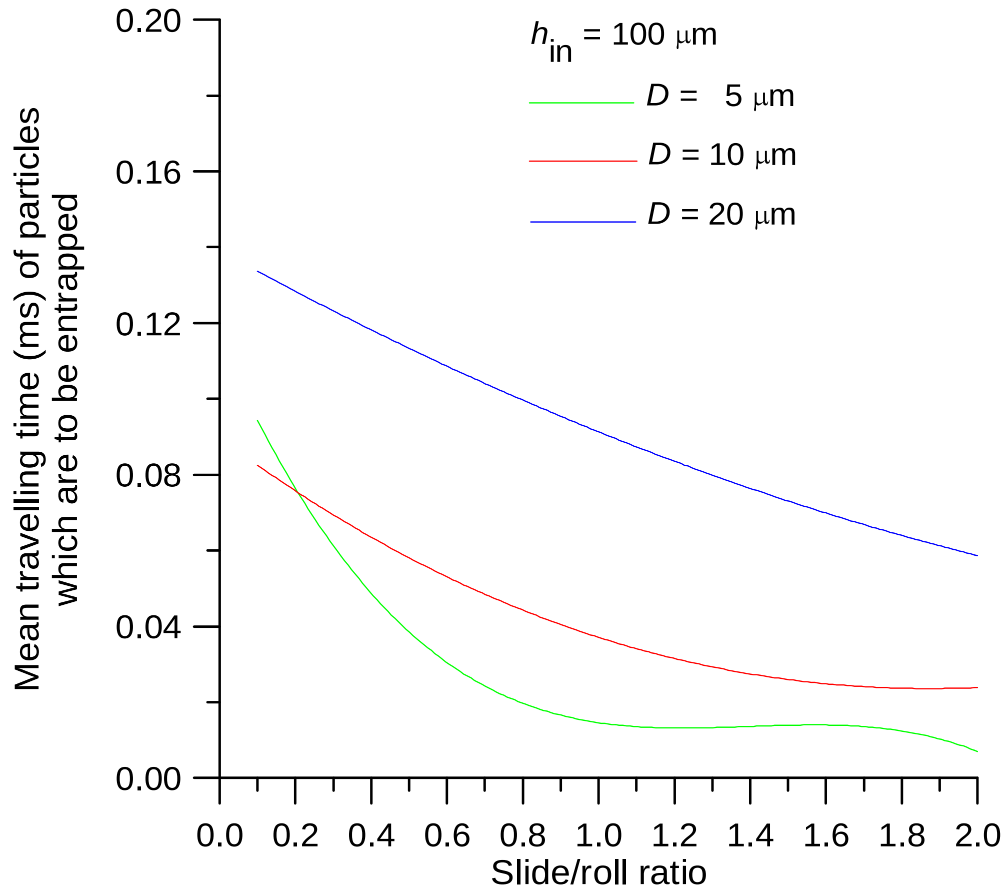

Figure 1.51

Figure 1.51 shows again (as in figure 1.50) that larger (20 μm) particles spend significantly more time travelling before entrapment, in comparison with smaller particles. The lower the slide/roll ratio, the greater is the travelling time.

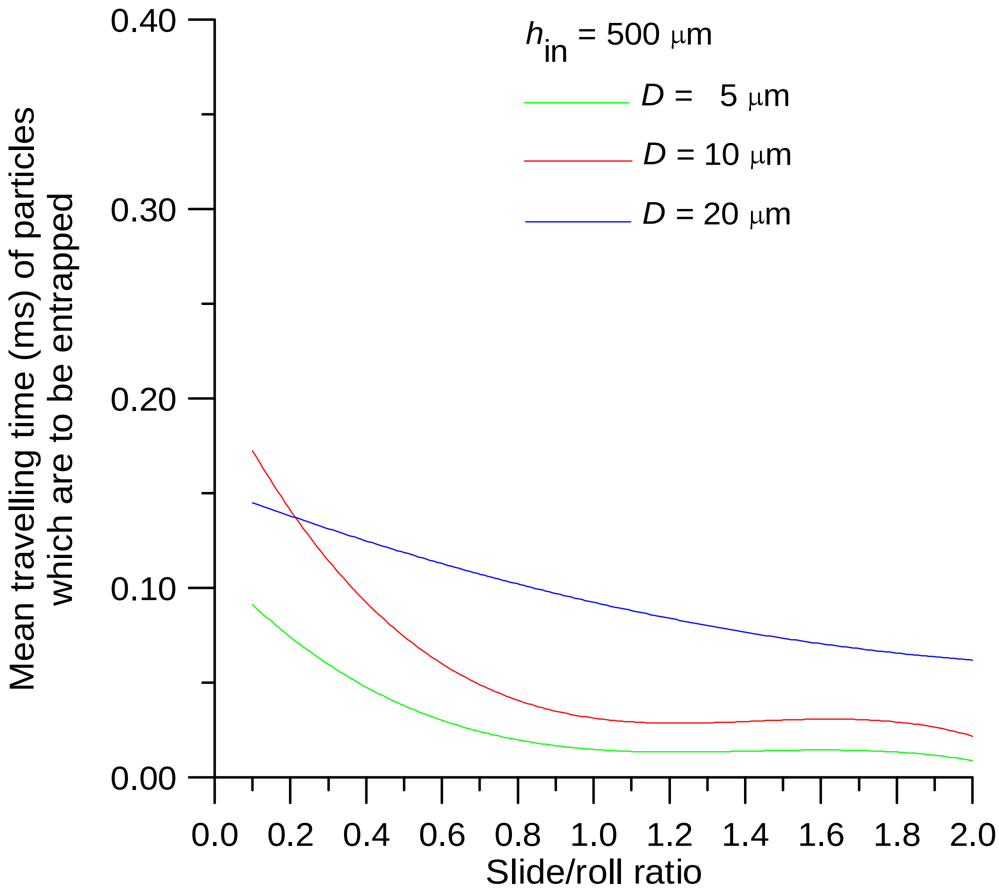

Figure 1.52

Finally, figure 1.52 shows again how larger (20 μm) particles need more travelling time before entrapment.

1.4 Conclusions

There are not many publications containing experimental results from assemblies set up to study the behaviour of particles in the inlet zone of lubricated contacts. Moreover, at the time of writing this thesis and to the best of the author's knowledge, theoretical models for the prediction of particle behaviour in the inlet oil flow of elastohydrodynamic contacts were virtually non-existent, at least as published material. There are two important publications containing experimental results, which fit the structure of the present theoretical model and provide readily comparable conclusions. The aforementioned publications are those of Wan and Spikes (1988), and Dwyer-Joyce and Heymer (1996). Useful results can also be found in an earlier paper of Wan and Spikes (1986).

Undoubtedly, a computer model has significant advantages when compared with experimental studies of this sort, mainly because of the following reasons.

(a) Minimal cost of running. Experiments are usually expensive to set up, whereas the computer comes as a very cheap alternative.

(b) Volume of simulation work and duration of experiments. It is obvious that a computer allows for an, essentially, unlimited number of simulations to be performed fast and always under completely controlled conditions. On the other hand, experiments suffer from dramatically longer running times and initial conditions are difficult to be controlled precisely. For example, the size of particles studied and the oil-bath thickness are not easily kept under strict control between successive experiments, whereas no such constraint exists for successive computer simulations. Moreover, a computer simulation can be completed in a few minutes, covering a large range of operational parameters like, for example, the slide/roll ratio, whereas an experimental study of the same informational content may require at least several days.

Detailed results and conclusions were presented in the examples of section 1.3. The study involved small (5 μm in diameter), medium (10 μm) and large (20 μm) particles, and thin (h_{in} = 50 μm), average (100 μm) and relatively thick (500 μm) oil-bath thicknesses in order to cover the cases of starved and flooded contacts. The slide/roll ratio was in the range [0.1,2.0], whereas the calculated central film thickness h_c (figure 1.1) was less than 1 μm. The geometry of the contact was that for a typical elastohydrodynamic application. The results obtained can be categorized as follows. It is useful at this point to comment on the unevenness of some of the curves presented in figures 1.5-1.52. A lack of smoothness in some curves is due to the following reasons:

(1) The curves shown are 3rd degree polynomial fits. A (smoother) 2nd or even 1st degree polynomial fitting was rejected because it would cover some important minima and maxima of the curves.

(2) The number of particle trajectories studied is finite (100). Some of the quantities shown on the vertical axis of the figures have very low values, such that a small change can have a big impact on the appearance of the curves. For example, if for h_{in} = 100 μm there is only one 5 μm particle trapped (out of eight particles that collide with the ball) and for h_{in} = 500 μm there are just two particles trapped, then the difference of the relevant curves at the specific slide/roll ratio would be $\frac{2-1}{8}\cdot 100 = 12.5\%$. If for a slightly different slide/roll ratio there is again one particle trapped, it starts to make sense why some curves would appear to be undulated.

(3) Small particles (like the 5 μm particles used in the study) are very light (64 times lighter than the 20 μm particles) and follow rather easily the changes of the oil flow for different slide/roll ratios. This has obvious effects on some curves, in the same way other curves, as those referring to the bigger particles may appear smoother. It is easy to understand this concept by visualizing the chaotic motion of smoke particles in the air. Another way of saying this is by considering that, as can be calculated, the limiting speed of the particles in the fluid under the action of gravity alone is 0.8 μm/s for the 5 μm particles, whereas it is 13.4 μm/s (sixteen times more) for the 20 μm particles.

(4) Smaller particles are able (due to their size) to approach the contact more than larger particles. Hence, smaller particles are able to approach an area where the back flow of the contact is stronger. The opposite is true for the larger particles, which essentially stay in an area where the streamlines of the flow are smoother.

After the previous explanations, it is now time to collect the results of section 1.3. These results are summarized below.

(a) **Thick oil bath (h_{in} = 500 μm) and small particles (D = 5 μm)**

This combination increases the risk of lubricant starvation due to increased accumulation of particles in front of the ball. As a further consequence, scuffing resulting from loss of lubricant support (film breakdown) is more likely to happen.

(b) **Thick oil bath (h_{in}= 500 μm) and large particles (D = 20 μm)**

Large particles are more easily trapped for two reasons:

1. As is known, in a closing elastohydrodynamic gap, there exists a small fluid jet directed outwards (upstream of the main flow) in front of the gap. Very small particles that come within the vicinity of this jet are actually pushed away from the gap or may be trapped in a micro-vortex (see for example Shieh and Hamrock, 1991). On the other hand, large particles are less susceptible to the lubricant back-flow since they collide with the ball relatively far away from the elastohydrodynamic gap. Therefore, they are more easily trapped, especially in combination with reason 2 below.
2. The solid frictional forces on the large particles (owing to their contact with the flat and the ball) are greater in comparison with those for smaller particles. This is due to the increased pressure between a large particle and the counterfaces.

Finally, particle accumulation is increased for higher slide/roll ratios. This means that inlet blockage by particles and oil starvation is more likely to happen for high sliding conditions. This has been shown experimentally by, for example, Wan and Spikes (see Wan and Spikes, 1988, page 20, conclusion 5), and Cusano and Sliney (1982).

(c) **Thin oil bath (h_{in} = 50 μm)**

A thin film results in a reduced lubricant back-flow as well as in a smaller elastohydrodynamic gap. Consequently, both small and large particles get more easily trapped and pass through the gap. This obviously increases the risk of surface damage as well as the risk of oil starvation.

(d) **Very large particles (*D* > 100 µm)**

Very large particles (in comparison with the central film thickness of the contact) find it more difficult to be entrapped owing to the surface curvature in the inlet zone of the contact, which means that, the further away from the gap, the higher is the x-component of the normal force of the ball on the particle ($N_{1,x}$), as can be realized from figure 1.1. For example, particles larger than 100 µm are more susceptible to being expelled than 10 µm particles in a 0.5 µm elastohydrodynamic gap. This way, and because of their size, very large particles tend to obstruct oil flow and to cause oil starvation. Experimental verification for this behaviour can found in Wan and Spikes (1988).

Figure 1.53 shows graphically a summary of the previously listed conclusions and serves as a rough general index.

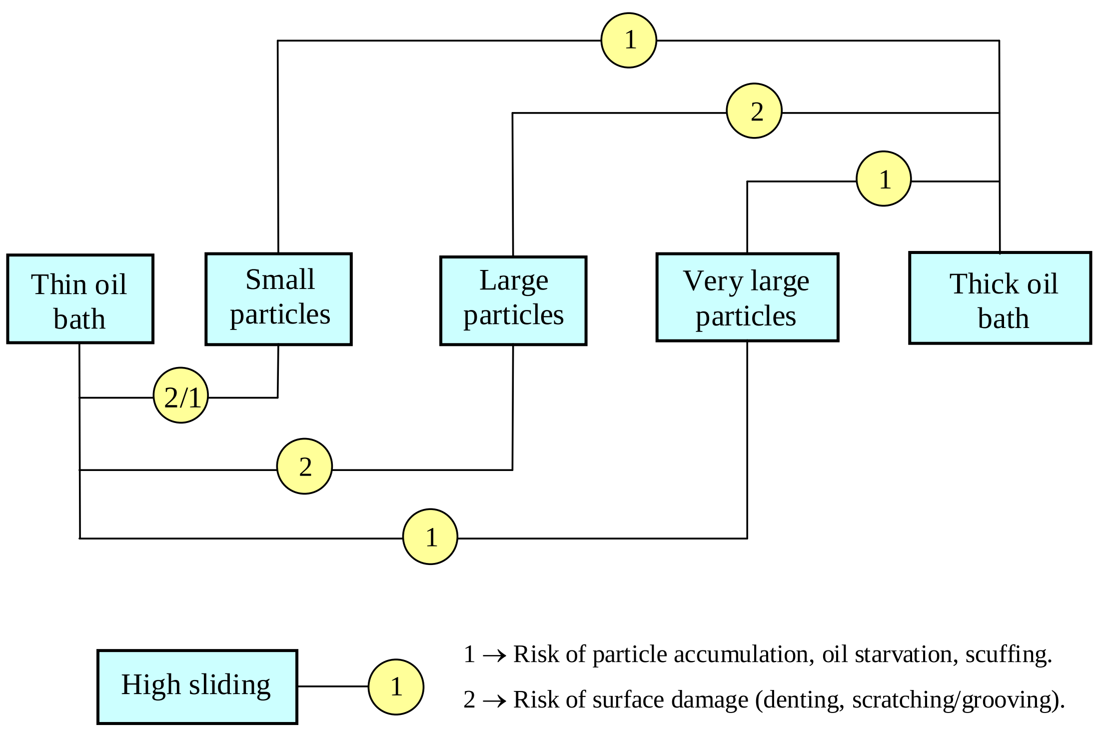

Figure 1.53 Summary of conclusions for chapter 1.

An example of the application of the model is presented in figure 1.54.

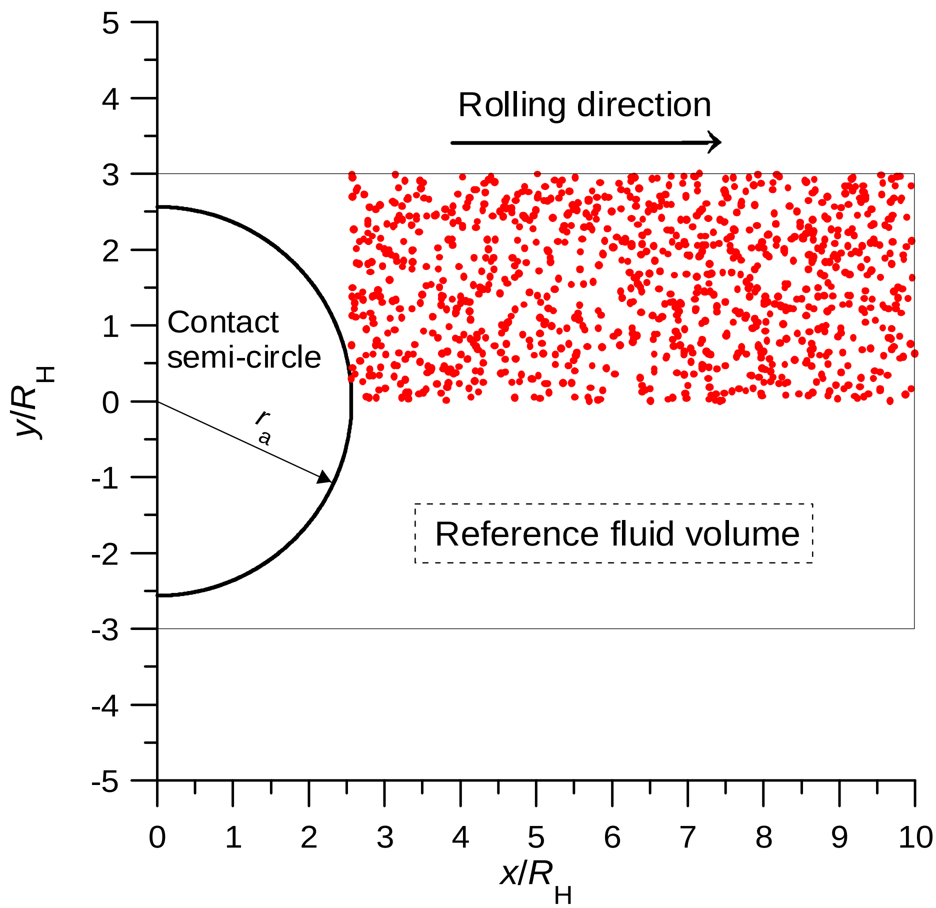

Figure 1.54 1000 randomly chosen initial positions of a particle in the upper half of the reference volume.

Figure 1.54 shows a typical example where the reference volume has length $L = 10{\cdot}R_H$ and semi-width $S = 3{\cdot}R_H$ (R_H is the radius of the Hertzian contact circle). In the figure, the randomly chosen initial positions of a test particle (1000 in total) are marked by red dots.

Following the same example, which refers to 20 μm particles in a 100 μm oil bath, figure 1.55 shows the locations in front of the ball that a particle, which is found to collide with the ball, will “choose”. The presented semi-circle marks the distance from the centre of the contact where a particle will come in contact with both the ball and the flat.

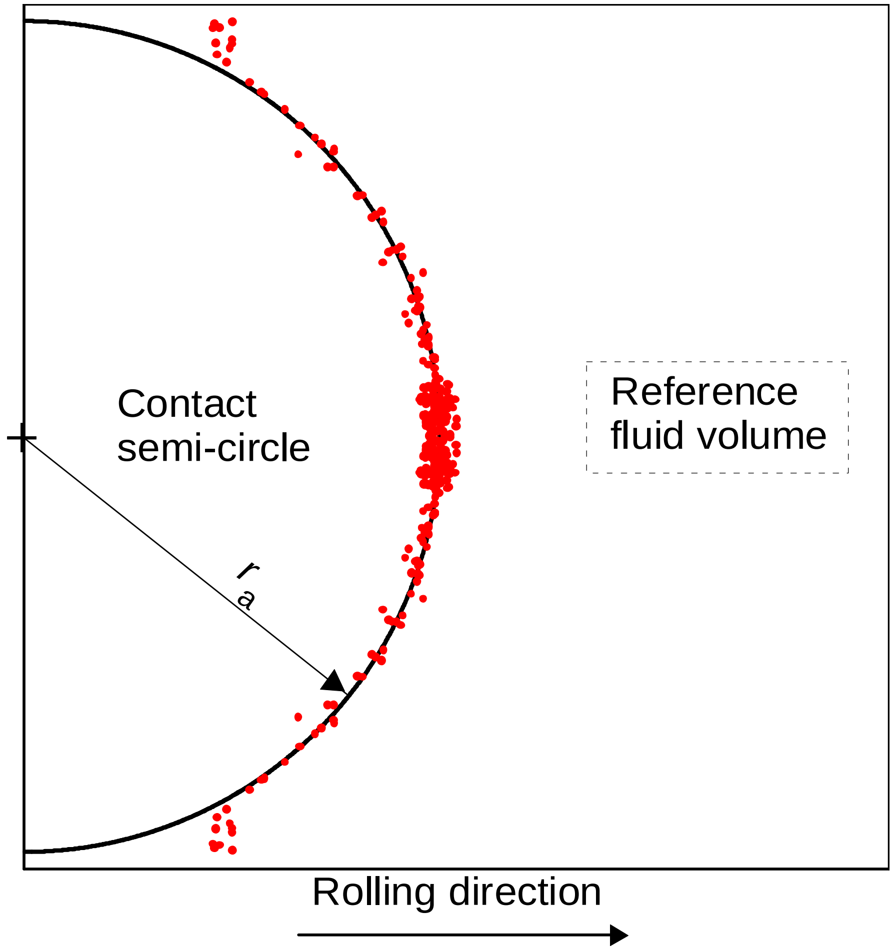

Figure 1.55 Example of particle distribution in front of a ball (data: D = 20 μm, h_{in} = 100 μm).

Finally, figure 1.56 shows the "preferred" trajectories of a particle in front of a ball (under the same conditions as in figure 1.55). The particle is initially put at a position on the upper half of the reference oil volume, which explains the lack of symmetry in the figure. It is immediately noticable how some particles bypass the ball, while others run onto it and are either entrapped or expelled. It must be noticed that a trajectory may start from anywhere in the reference volume and, therefore, some particles appear to have a shorter history in the figure compared with others.

For the example studied, it was found that, out of 100 particle trajectories calculated, 17 of them belong to particles that would, eventually, be entrapped and pass under the ball. Therefore, it may be said that, for this particular example, there is a 17 % chance of particle entrapment.

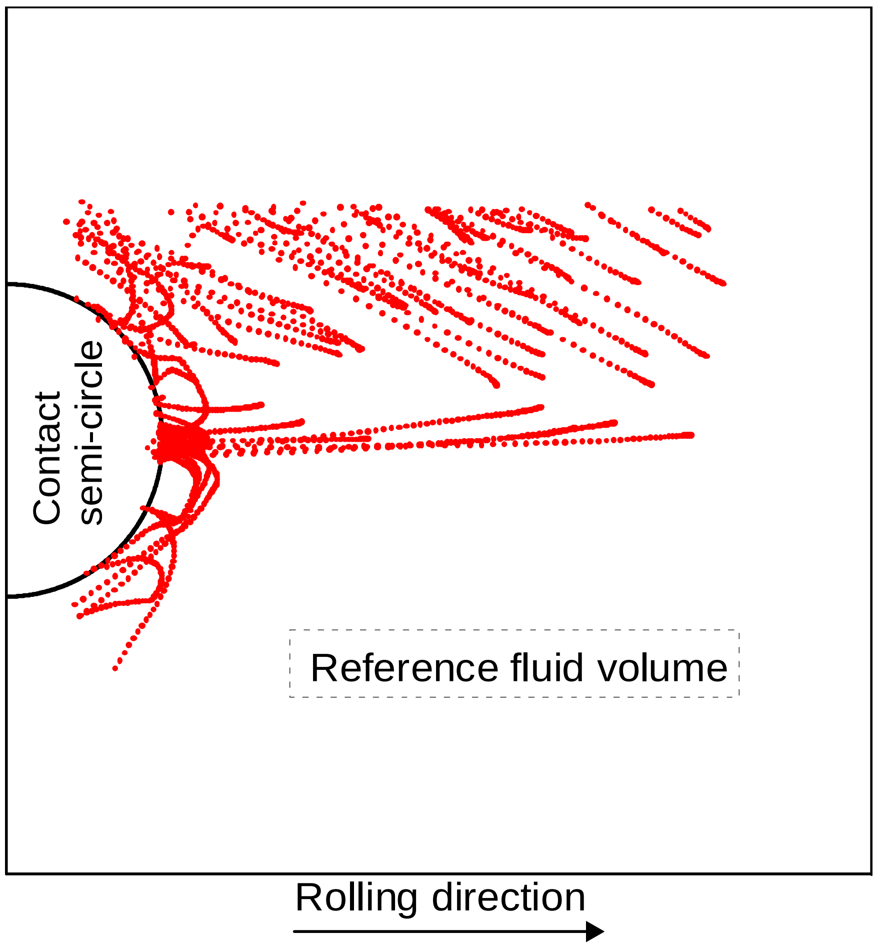

Figure 1.56 Example of possible trajectories of a single sized particle put in the upper half of the reference oil volume (data: D = 20 μm, h_{in} = 100 μm).

Figure 1.56 shows clearly that particles which are close to the centreline of the flow, will remain there until they meet the ball, whereas particles located away from the centreline of the flow are swept aside. This has been experimentally observed by Dwyer-Joyce and Heymer (1996, see figure 7 in their paper). The phenomenon is easily explained by the fact that the y-velocity component of the fluid is very weak near the centreline and, essentially, zero on the centreline (where $y = 0$), owing to the symmetry of the flow.

The accumulation of particles in some areas (figure 1.56) and especially in the centreline of the flow may have catastrophic effects in the lubrication of the contact, not only due to the obvious obstruction of the oil replenishment of the contact, but also due to the risk of large body formation. The latter happens when the accumulated particles form bonds which help them construct a bigger body. It is possible that this body may be entrapped and cause surface damage. There are then two possibilities:

(1) The large body enters the contact and remains one part as it is being squashed.
(2) The large body enters the contact and, at some point, agglomerates, resulting in numerous smaller particles, which, being deeper inside the elastohydrodynamic gap, are also entrained (see for example Oktay and Suh (1992)).

In either case, the risk of lubricant starvation and the (following) risk of surface damage are obvious.

1.5 Computer program and simulation

The results presented in this chapter were obtained by a computer program, compiled by the author for the purposes of this work. It is worth noting that the computer simulation serves as a very beneficial alternative to costly experimentation, having the advantages of speed, control over the initial conditions and versatility. The computer code is written in FORTRAN 90.

The simulation starts with the creation of a 3-dimensional grid of equidistant nodes in the three principal directions (figure 1.2), such that it covers a space of ten Hertzian contact circle radii in length (along the x-axis; $N_x = 10$), four Hertzian contact circle radii in width (along the y-axis; $N_y = 2$), and is bounded by the free surface of the lubricant, the wall of the ball and the flat. The number of grid nodes along a principal direction is chosen by the program user at the beginning of the program. The configuration is symmetrical about plane y = 0, and this is taken into account in the calculations. The space covered by the grid is the reference fluid volume. The fundamental fluid flow problem is solved in the reference volume according to the analysis of sub-section 1.2.1. The boundary conditions used in the solution are the prescribed velocities of the fluid at the boundaries of the reference volume.

The simulation begins by “putting” a particle at a randomly chosen position in the reference volume. The particle then starts a motion in the fluid, governed by the fluid forces and its inertia. If the particle meets the ball in its path, a local force equilibrium analysis reveals if it will be expelled or it will pass through the gap between the ball and the flat. The force analysis involves solid frictional forces between the particle and the surrounding solids (the ball and the flat), as well as the fluid forces and the inertial force of the particle. If the particle is expelled, it starts a new journey in the fluid at a somehow randomly chosen position, near the position of contact with the ball. A new trajectory is then calculated and the calculations are repeated until the particle either bypasses the ball or is trapped and passes under the ball. There is a pre-set maximum number of particle rejections in the program, chosen equal to fifty for the present study. A large number of rejections indicates that the particle tends to stay in the inlet zone of the contact for a relatively prolonged time. This behaviour may result in poor replenishment of the contact, because the particle obstructs the fluid flow. The situation can become much worse if other particles gather around the first one. In the latter case, severe fluid starvation can cause a film breakdown and result in scuffing wear. Therefore, the study of the particle rejection mechanism is of particular importance in assessing the effectiveness of the lubrication in contaminated environments.

Collecting the history of motions (trajectories) of several particles (usually more than 100), various useful conclusions can be drawn. Global conclusions can be drawn after a parametric study by studying the effects of parameters like the slide/roll ratio etc. It must be mentioned that all the parameters of the model can be conveniently altered by the user of the computer program. These parameters are:

- The number of nodes of the grid in all three principal directions.
- The radius of the ball.
- The moduli of elasticity and the Poisson ratios of the ball and the flat.

- The load on the ball.
- The dynamic viscosity, the density, and the pressure-viscosity coefficient of the fluid.
- The rolling speed of the ball.
- The slide/roll ratio.
- The oil bath thickness (figure 1.1)
- The diameter of the particle.
- The density of the material of the particle.
- The number of particles to study.
- The solid friction coefficients.

Other parameters depend on the above listed parameters and are automatically calculated in the program. It is noted here that the geometry of the contact is the actual deformed geometry, as this is found by accounting for the deformations of the ball and the flat due the elastohydrodynamic pressures in the contact.

Following the completion of the calculation of the trajectories of all particles, the whole process is repeated ten times, each time with different initial positions of the particles (always chosen randomly), to ensure the generality of the results. The results comprise the average figures from the ten loops of the program. The complexity of the calculations causes the program to run relatively slowly, especially if the number of particles is relatively large (like, for example, 500). In a personal computer with a 266 MHz INTEL Pentium-II processor, the program needs a CPU time that varies from a few minutes to one hour (roughly speaking), in order to complete all tasks. This is of course also dependent on the number of nodes used for the grid. For the examples of section 1.3, the grid in the reference volume has $400\times100\times10$ nodes (length×width×thickness). Consequently, spatial steps Δx and Δy are of the order of 2 μm, which is considered as adequate discretization. Finally, a flow chart of the model is shown in figure 1.4.

CHAPTER 2

MOTION AND DEFORMATION OF A SOFT PARTICLE IN AN ELASTOHYDRODYNAMIC LINE CONTACT

2.1 Introduction

In order to study the possibility of surface damage caused by a solid particle that is trapped in an elastohydrodynamic contact, a model of the behaviour of the particle inside the elastohydrodynamic gap has to be created. This model must give a good description of the motion of the particle as it is being squashed between the two co-operating surfaces (counterfaces). It must also provide a means to calculate the pressure and traction between the particle and the counterfaces if the particle is actually entrapped. However, prior to anything else, the model must “decide” whether a particle can be entrapped or not.

As of today, the literature lacks a detailed theoretical model of this kind, although there are several publications dealing with abrasive models for hard particles, like for example in Rabinowicz and Mutis (1965), Larsen-Badse (1968a, 1968b), Richardson (1968), and Williams and Hyncica (1992). The effects of contamination particles on cooperating surfaces had been observed as early as in the 15th century by Leonardo da Vinci. In recent years, meticulous work has been performed by Sayles and Ioannides to investigate the effects of contamination particles in the lubrication, performance and life of machine elements (Sayles and Ioannides, 1988). Dramatic effects have been demonstrated in many publications, as in Sayles (1995) and Chao *et al.* (1996). It has been repeatedly shown that debris particles can cause severe plastic deformation when over-rolled in concentrated contacts, the damage being in the form of either dents or scratches/grooves. However, the most impressive discovery was not the surface damage caused directly by the particles but the damage developed later, even after the particles have gone, due to the presence of the surface dents left by the particles. These dents are areas where plastic flow has occurred. Consequently, residual stresses are present and active (Xu *et al.* (1997), Ko and Ioannides (1989)). When these dents are over-rolled, sharp stress peaks appear at their edges, which are encountered in both dry contacts (Sayles, 1995) and elastohydrodynamic contacts (Venner and Lubrecht, 1994). These highly stressed areas are precursors of cracks and result in rolling fatigue, significantly reducing the life of machine elements (Sayles and Ioannides, 1988). Lubrecht *et al*. (1992) found that residual stresses around dents have only a small effect on the life of the dented surfaces in the case of line contacts. However, it is the effect of the high local surface pressure on the vicinity of the debris dent shoulders as well as the sub-surface concentration of shear stresses that cause the problem. Webster *et al.* (1986) showed analytically that such stress concentrations could be as much as three times greater than the sub-surface maximum that results from a corresponding ideal Hertzian loading. Webster *et al*. (1986) also showed analytically (using the Ioannides-Harris (1985) life model) that "*…the fatigue lives for bearings tested under 40 μm filtration are about 7 times less than those tested under 3 μm filtration*." Their tests involved roller bearings and the fatigue life reductions were associated with the surface indentations caused by the debris particles.

In the last few decades, the abrasion mechanisms have been classified in two categories, namely two-body abrasion and three-body abrasion. Three-body abrasion occurs when particles, known as third bodies, are trapped between two counterfaces that are in relative motion to each other (rolling, sliding or mixed rolling-sliding). In a three-body abrasion, the particles remain in suspension. Two-body abrasion occurs when the particles are embedded in one of the counterfaces and, hence, act as protuberances of the body they invade. In both two and three-body abrasion, the attacked surfaces exhibit wear marks which can vary from tumbling to ploughing, depending on the ratio of the film thickness over the average particle size, and on the relative hardness of the particles and the surfaces (see for example Dwyer-Joyce, 1993). However, abrasive wear is associated with relatively hard particles in sliding contacts. It has been observed that if the two counterfaces have different hardness, hard particles tend to embed the softer surface and scratch the harder (Williams and Hyncica (1992), Dwyer-Joyce (1993)). The wear scratches/grooves can easily be seen and the effects of hard particles can easily be realized. Therefore, research is mainly concentrated on hard contaminants.

However, soft and ductile particles, like for example copper, cast iron and low carbon steel particles, have also a role in surface wear, but because of the severity of the hard-particle abrasion wear, soft-particle wear remains a neglected part in the literature. It was only in recent years that it was made clear how soft and ductile particles could play an important role in surface wear of machine elements (Hamer *et al.* (1989b), Sayles *et al.* (1990), Dwyer-Joyce *et al.* (1992)). It is shown later in this Thesis that soft particles can cause surface wear and damage of equivalent severity as that caused by hard particles. The mode of surface damage associated with soft contaminants is of the adhesion type rather than of the abrasion type. The latter is more evident for softer particles than for harder. Hamer *et al.* (1989b) showed that, for purely rolling contacts, soft particles are extruded when compressed between the two counterfaces. The extrusion (or lateral expansion) of the particle is obstructed by the frictional forces between the particle and the counterfaces, as well as by the elastohydrodynamic pressure, especially in the central region of the contact, although the latter effect can vary significantly due to the variable fluid pressure along the periphery of the particles and for other reasons that are made clear later in this chapter. Consequently, high pressures can be developed between the particle and the counterfaces, which can even cause plastic deformations of the counterfaces.

It is also known (see for example Chao *et al.*, 1996) that soft and ductile particles can be reduced to sharp platelets when compressed. These platelets are harder than the matrix particles due to plastic work hardening, and if they are involved in further compression/sliding, could cause surface damage, because of their increased hardness. This is more obvious in sliding contacts, where the platelets can shear and remove material from the surfaces in a fashion similar to that of hard particles but it can also happen in rolling elliptical contacts. In the latter case, such work-hardened platelets may cause surface spalling due to spinning inside the contact, owing to the Heathcote differential slip effect (see Chao *et al.*, 1996).

In the present chapter, a preliminary model for the particle behaviour (motion and deformation) inside an elastohydrodynamic gap is developed for soft and ductile particles in line contacts. The fundamental equation of particle's motion is derived from the equilibrium of solid frictional and reaction forces between the particle and the counterfaces, as well as of fluid drag forces between the particle and the lubricating oil. Moreover, a criterion to test the possibility of particle entrapment or rejection from the contact is developed, based on the mechanical force equilibrium on the particle.

It is shown that, in sliding contacts, soft particles stick to one surface and slide on the other. For counterfaces of equal hardness, this adhesion-type particle behaviour is explained through the difference in the coefficients of friction of the two counterfaces (even for very small difference). For surfaces of different hardness, particles embed the softer surface and slide on the harder. The effects of this kind of behaviour are assessed in the remaining chapters of this Thesis. The experimental observations and theoretical predictions of other authors are all confirmed through the theoretical model developed in the present and the remaining chapters. Moreover, it is later shown that soft and ductile particles can also be responsible for local scuffing wear, due to high frictional heating produced during their squashing in concentrated, lubricated contacts.

2.2 Geometry of a typical elastohydrodynamic contact

The geometry of a typical line elastohydrodynamic contact, which is deformed due to elastohydrodynamic pressures, can be found by applying a Hertzian pressure between two cylinders, representing the two counterfaces at the vicinity of the contact (see for example Cameron, 1966). The former analysis was part of Grubin's model of 1949 (see Cameron, 1966) and predicts a flat film in the central (Hertzian) zone of the contact. The equations giving the film thickness in the contact are as follows:

$$\left.\begin{aligned} h &= h_{c} + \frac{4\cdot w}{\pi\cdot E}\cdot\left\{\frac{x}{b}\cdot\sqrt{\left(\frac{x}{b}\right)^{2}-1}-\ln\left[\frac{x}{b}+\sqrt{\left(\frac{x}{b}\right)^{2}-1}\right]\right\} \quad ,|x|>b \\ h &= h_{c} \quad ,|x|\le b \end{aligned}\right\} \tag{2.1}$$

where h_c is the central film thickness of the contact, w is the load per unit length of the contact, b is the Hertzian contact semi-width and E is the effective modulus of elasticity. The central film thickness h_c can be calculated from any available semi-empirical formula, as the one proposed by Pan and Hamrock (1989). The Hertzian contact semi-width is given by the following equation:

$$b = \sqrt{\frac{8\cdot w\cdot R_{eq}}{\pi\cdot E}} \tag{2.2}$$

where R_{eq} is the effective radius of curvature of the contact

$$R_{eq} = \frac{1}{\dfrac{1}{R_1}+\dfrac{1}{R_2}} \tag{2.3}$$

whereas R_1 and R_2 are the radii of curvature of surfaces 1 and 2 respectively. The effective modulus of elasticity E is defined as:

$$E \equiv \frac{2}{\dfrac{1-\nu_1^2}{E_1}+\dfrac{1-\nu_2^2}{E_2}} \tag{2.4}$$

where E_1, E_2 and ν_1, ν_2 are the moduli of elasticity and Poisson ratios of counterfaces 1 and 2 respectively.

The model of the deformed contact used in this study (figure 2.1) assumes that the counterfaces are parallel in the Hertzian zone of the contact. The sketch in figure 2.1 is not to scale and has been greatly exaggerated in the vertical direction (thickness).

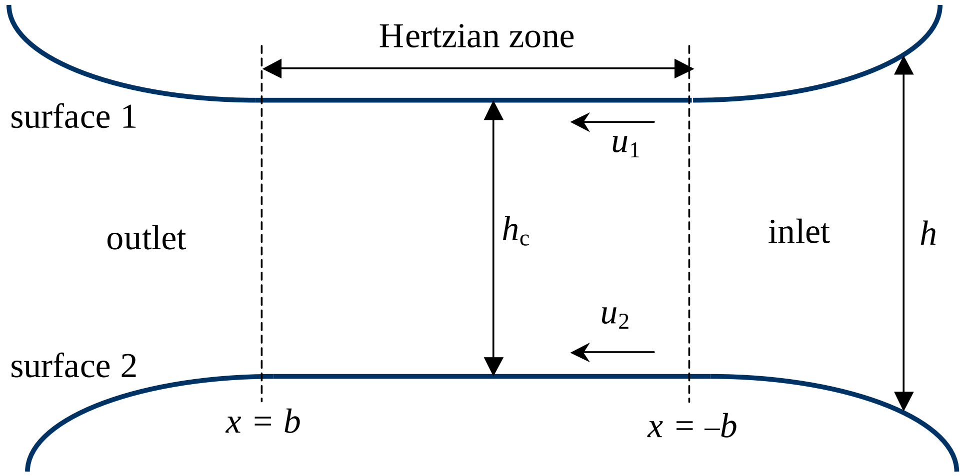

Figure 2.1 Geometry of line-elastohydrodynamic-contact model (not to scale).

According to the theory of Elastohydrodynamic Lubrication, there must be a film constriction at the exit of the Hertzian zone (entrance to the outlet zone) of the contact, which results in the well-known pressure spike. The explanation for this comes from the fact that the pressure gradient must be negative at the end of the Hertzian zone, which, when applied to the Reynolds' equation, demands that $h(x \rightarrow b^-) < h_c$ (see for example Johnson, 1985, p. 337). Therefore, the minimum film thickness is less than the central film thickness h_c. Numerical solutions have shown that the difference between the minimum film thickness and the central film thickness is very small indeed and the difference becomes smaller in heavily loaded conjunctions, where the magnitude of the pressure spike is diminished and the pressure distribution resembles closely the one given by Hertz for dry contacts (Hamrock, 1994).

On the other hand, there might exist a slight surface curvature inside the Hertzian zone of the contact (the two counterfaces still being parallel), resulting from the fact that bodies 1 and 2 might have slightly different material mechanical properties. This curvature, if existing, is anyway small enough to be ignored and is considered of secondary importance in the present study, as it is not expected to affect the motion of the particle.

Following the previous observations, it is now clear why the model assumes a constant film thickness throughout the Hertzian zone of the contact, as is shown in figure 2.1. Moreover, in the presence of a solid particle in the elastohydrodynamic gap, surface deformations in the vicinity of the particle are governed by the particle itself and not by the lubricant, provided of course that the particle is thicker than the central film thickness. This means that as the particle approaches the exit of the Hertzian zone, where the film constriction exists, surface deformations in the vicinity of the particle are almost solely a result of the pressure developed between the particle and the counterfaces. This further means that the particle’s presence cancels the film constriction due to the elastohydrodynamic lubrication mechanism and imposes its own constraints, as this can be found by solving the Contact Mechanics problem of the compression and shearing of a solid object between two parallel surfaces.

Having established a satisfactory model of the contact, the various forces affecting the particle’s motion can now be determined. However, before that, a criterion of the likelihood of particle entrapment must be developed, in order to decide if a particular particle can indeed become entrapped and pass through the elastohydrodynamic gap.

2.3 Criterion to evaluate the likelihood of particle’s entrapment

Large particles are more difficult to become entrapped and pass through the elastohydrodynamic gap because of the reaction forces between a particle and the counterfaces in the inlet zone of the contact (figure 2.1). Assuming the particle is spherical, there is an upper limit in its diameter, beyond which the particle cannot enter the contact without first being plastically deformed. This “critical” diameter can be found from the force equilibrium on the particle. At this stage, only mechanical forces, owing to the particle’s interaction with the counterfaces, are taken into account, whereas fluid forces on the particle are omitted. It will actually be shown later in this chapter that fluid forces on the particle are negligible when compared with solid frictional forces, which arise from the compression and shearing of the particle between the counterfaces. Therefore, the omission of fluid forces at this stage is justified.

Calculation of the "critical diameter" is done in two ways:

(a) by an approximate but fast method, resulting in minimal CPU (Central Processing Unit) times when programmed for a computer, and

(b) by an accurate but more time-consuming (in terms of CPU time) method.

It must be mentioned that both methods cover the cases of pure rolling and rolling-sliding contacts simultaneously.

2.3.1 Criterion for particle's entrapment - approximate method

A simplified analysis can be set up if it is assumed that the counterfaces have a constant radius of curvature, equal to their radius of curvature at the nominal point of "contact" ($x = 0$) when being undeformed. Figure 2.2 shows a particle that has just touched both counterfaces.

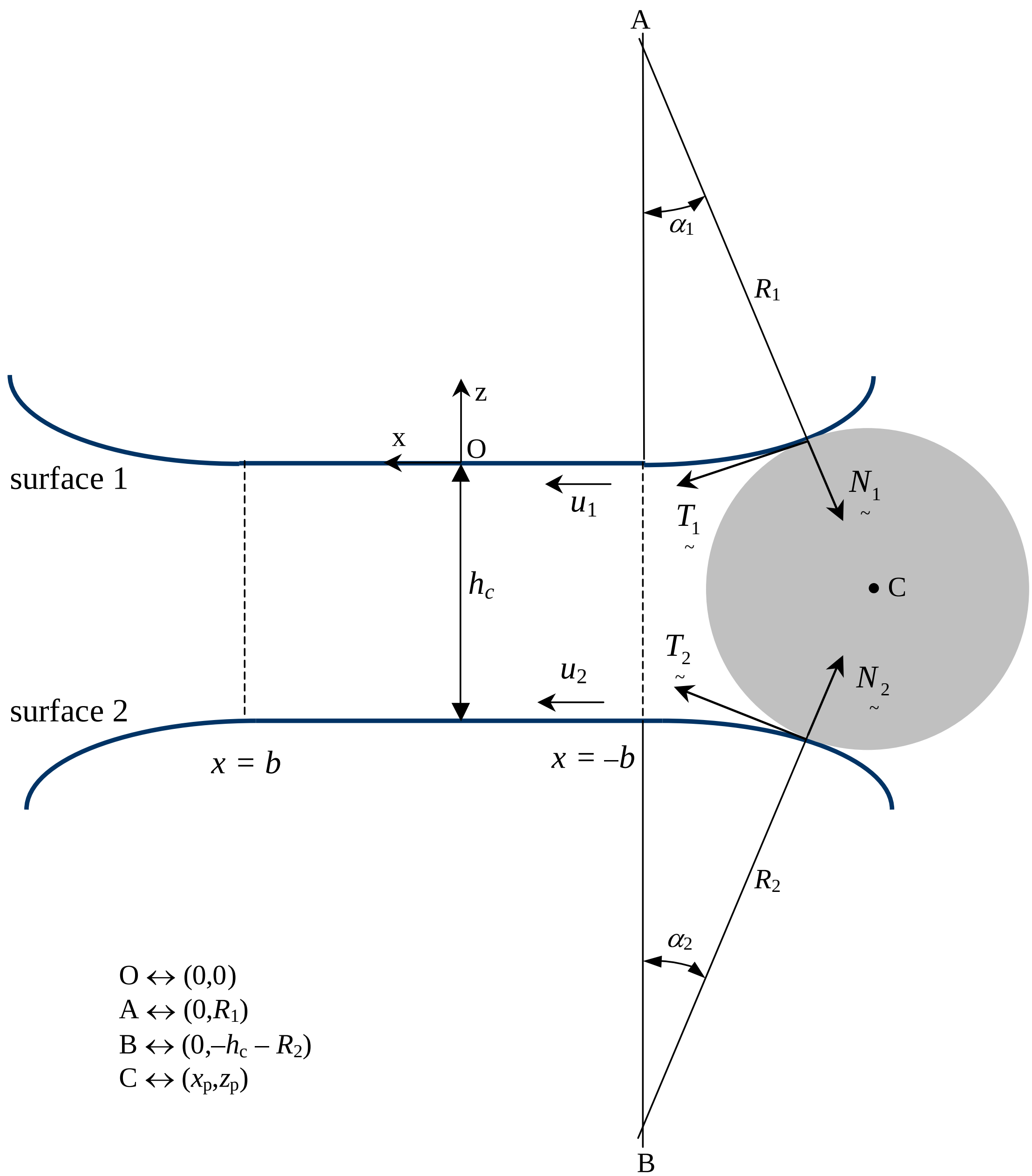

Figure 2.2 A particle at the equilibrium stage.

The interaction between the particle and the counterfaces is expressed by the normal (reaction) forces $\underset{\sim}{N_1}, \underset{\sim}{N_2}$, and the frictional forces $\underset{\sim}{T_1}, \underset{\sim}{T_2}$. It is assumed, without loss of generality, that the tangential speeds of surfaces 1 and 2 satisfy the following constraints: $u_1 \geq u_2 \neq 0$.

From the force equilibrium on the particle in directions x and z, the following algebraic equations are derived:

$$T_1 \cdot \cos(\alpha_1) \pm T_2 \cdot \cos(\alpha_2) - N_1 \cdot \sin(\alpha_1) - N_2 \cdot \sin(\alpha_2) = 0 \tag{2.5}$$

$$-T_1 \cdot \sin(\alpha_1) \pm T_2 \cdot \sin(\alpha_2) - N_1 \cdot \cos(\alpha_1) + N_2 \cdot \cos(\alpha_2) = 0 \tag{2.6}$$

The plus signs in front of the T_2 terms in equations (2.5) and (2.6) hold for the case presented in figure 2.2, whereas the minus signs hold in the case where the vector $\underset{\sim}{T_2}$ has the opposite direction, which occurs immediately after the particle is pinched. The implications of the latter are discussed later in this study.

In both the cases of rolling-sliding and of pure rolling (zero sliding) of the counterfaces, the friction forces are given by the following equations:

$$T_1 = \mu_1 \cdot N_1 \quad , \quad T_2 = \mu_2 \cdot N_2 \tag{2.7}$$

where μ_1 and μ_2 are the coefficients of kinetic (sliding) friction between the particle and surfaces 1 and 2 respectively. Using equations (2.7), equations (2.5) and (2.6) yield:

$$\left.\begin{array}{l} [\mu_1 \cdot \cos(\alpha_1) - \sin(\alpha_1)] \cdot N_1 + [\pm \mu_2 \cdot \cos(\alpha_2) - \sin(\alpha_2)] \cdot N_2 = 0 \\ [-\mu_1 \cdot \sin(\alpha_1) - \cos(\alpha_1)] \cdot N_1 + [\pm \mu_2 \cdot \sin(\alpha_2) + \cos(\alpha_2)] \cdot N_2 = 0 \end{array}\right\} \tag{2.8}$$

For the system of equations (2.8) to have non-trivial solutions, its determinant has to be equal to zero. Thus:

$$\begin{vmatrix} \mu_1 \cdot \cos(\alpha_1) - \sin(\alpha_1) & \pm \mu_2 \cdot \cos(\alpha_2) - \sin(\alpha_2) \\ -\mu_1 \cdot \sin(\alpha_1) - \cos(\alpha_1) & \pm \mu_2 \cdot \sin(\alpha_2) + \cos(\alpha_2) \end{vmatrix} = 0 \tag{2.9}$$

Equation (2.9) finally gives:

$$\tan(\alpha_1 + \alpha_2) = \frac{\mu_1 \pm \mu_2}{1 \mp \mu_1 \cdot \mu_2} \tag{2.10}$$

where the upper sign holds during the particle equilibrium stage and the lower sign holds immediately after the particle starts entering the gap, provided that there is sliding in the contact ($u_1 \neq u_2$). The case that is related with the use of the upper signs in equation (2.10) is important when one counterface is stationary to a fixed coordinate system while the other is moving. In the latter case, immediately after the particle passes the equilibrium point, the frictional force on the stationary surface reduces the particle's chance of getting deeper in the gap, because it changes direction and points towards the inlet zone of the contact. Depending on the particular case, the particle could then be temporarily expelled from the contact. However, owing to its compression at the equilibrium point, the particle may be slightly plastically deformed and hence may become thinner. In the latter case, the next time the particle is pinched, it will be deeper inside the gap. This behaviour may be repeated until the particle, owing to this "micro-forging" process, becomes thin enough to enter deep inside the gap and become utterly trapped. On the other hand, if both counterfaces are moving in reference to a space-fixed coordinate system ($u_1 \neq 0$ and $u_2 \neq 0$), the overcoming of the equilibrium point by the particle results in the particle starting to move towards the centre of the contact, with a minimum speed equal to the minimum of the two tangential speeds u_1 and u_2. The latter is a result of both counterfaces moving towards the centre of the contact (figure 2.2) and the fact that the particle is trapped between them, although this is not a general conclusion because fluid forces on the particle must also be taken into account, as is done later in this chapter.

Using figure (2.2), angles α_1 and α_2 must satisfy the following equations:

$$\tan(\alpha_1) = \frac{-x_p}{R_1 - z_p} \quad , \quad \tan(\alpha_2) = \frac{-x_p}{R_2 + h_c + z_p} \tag{2.11}$$

Finally, using equation (2.10):

$$\tan(\alpha_1 + \alpha_2) = \frac{\tan(\alpha_1) + \tan(\alpha_2)}{1 - \tan(\alpha_1) \cdot \tan(\alpha_2)} \Rightarrow \frac{\tan(\alpha_1) + \tan(\alpha_2)}{1 - \tan(\alpha_1) \cdot \tan(\alpha_2)} = \frac{\mu_1 \pm \mu_2}{1 \mp \mu_1 \cdot \mu_2} \tag{2.12}$$

For the spherical particle to be in touch (undeformed) with surfaces 1 and 2, the following equations must hold:

$$\left.\begin{aligned} d(A,C) &= R_1 + \frac{D}{2} = \sqrt{x_p^2 + (R_1 - z_p)^2} \\ d(B,C) &= R_2 + \frac{D}{2} = \sqrt{x_p^2 + (R_2 + z_p + h_c)^2} \end{aligned}\right\} \tag{2.13}$$

where D is the diameter of the undeformed particle. The previous equations are easily derived from the configuration of figure 2.2. Equations (2.13) form a non-linear system. Initially, the diameter D is considered significantly smaller than the radius R_2 and, thus, the term involving D in the lower of equations (2.13) is omitted in order to obtain an approximate value for z_p. In the following step, the system is solved by applying the method of bisection. An optimized under-relaxation technique accelerates significantly the convergence to the final solution. Using a modern personal computer, the algorithm claims an infinitesimal CPU time.

In both cases of pure rolling and rolling-sliding of the contact, the direction of force $\underset{\sim}{T_2}$ is as shown in figure 2.2, because it is assumed that, at the equilibrium stage, the particle stays fixed in space and simply rotates around its geometrical centre. Immediately after the particle is first pinched and starts entering the gap, the direction of vector $\underset{\sim}{T_2}$ is reversed (becomes opposite than in figure 2.2). This may cause temporary rejection of the particle from the contact. In the latter case, there are two options.

(a) The particle is hard enough to retain its shape under the action of the normal and frictional forces. This means that after being expelled, the particle will start a new journey in the lubricant flow, in the inlet zone of the contact, at a starting distance $x < x_p$ (note that $x_p < 0$). In such a case, the particle may be expelled many times in succession, and the risk of poor lubrication of the contact starts becoming visible, considering that the particle stands as an obstruction in the replenishment of the contact with fresh oil. In extreme cases this behaviour may lead to oil starvation and scuffing, especially when other particles start accumulating around the rejected particle.

(b) The particle is soft enough to be plastically deformed under the action of all forces. Normal forces $\underset{\sim}{N_1}$ and $\underset{\sim}{N_2}$ will reduce particle's thickness (dimension along the z-direction in figure 2.2), thus giving it the opportunity to enter deeper inside the gap and to become finally entrapped. Depending on the local conditions around the particle, this "micro-forging" process may take enough time as to cause oil starvation, by giving other particles, which are being obstructed by the aforementioned particle, time to accumulate in the inlet zone.

2.3.2 Criterion for particle's entrapment – accurate method

The assumption of constant radii of curvature of the counterfaces, used in sub-section 2.3.1, is removed here and the exact geometry of the deformed contact is used instead, as it is described by equations (2.1). The analysis of sub-section 2.3.1 up to equation (2.10) is also used here. Figure 2.3 shows the geometry of the deformed gap. Equations (2.11) and (2.13) are replaced here by equations (2.14) and (2.15).

$$\left(x_\mathrm{a} - x_\mathrm{p}\right)^2 + \left(w_1 - z_\mathrm{p}\right)^2 = \frac{D^2}{4} \tag{2.14}$$

$$\left(x_b - x_\mathrm{p}\right)^2 + \left(w_2 + h_\mathrm{c} + z_\mathrm{p}\right)^2 = \frac{D^2}{4} \tag{2.15}$$

If α_1 is the angle between line AC and axis z, then:

$$\tan(\alpha_1) = \frac{4 \cdot w \cdot (1 - \nu_1^2)}{\pi \cdot E_1 \cdot b} \cdot \sqrt{\left(\frac{x_\mathrm{a}}{b} + 1\right)^2 - 1} = \frac{x_\mathrm{p} - x_\mathrm{a}}{w_1 - z_\mathrm{p}} \tag{2.16}$$

Similarly, if α_2 is the angle between line BC and axis z, then:

$$\tan(\alpha_2) = \frac{4 \cdot w \cdot (1 - \nu_2^2)}{\pi \cdot E_2 \cdot b} \cdot \sqrt{\left(\frac{x_\mathrm{b}}{b} + 1\right)^2 - 1} = \frac{x_\mathrm{p} - x_b}{z_\mathrm{p} + h_\mathrm{c} + w_2} \tag{2.17}$$

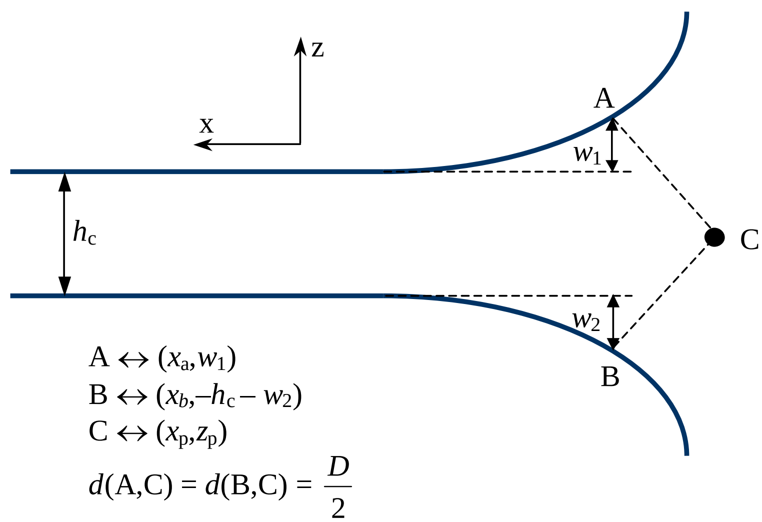

Figure 2.3 Geometry of an elastohydrodynamic gap.

Equations (2.10) and (2.14)-(2.17) constitute a non-linear system. This system is solved iteratively by a trial-and-error method, using an initial guess D = 0. This method has the disadvantage of being slow in comparison with the approximate method of sub-section 2.3.1, but this can be compensated by using a faster computer (the CPU time needed is generally less than 1 min, using a modern PC).

2.3.3 Comparison of the two methods

Despite the assumption of rigid counterfaces, the approximate method gives results which are less than 5 % away of those obtained by using the accurate method, for the range of typical values studied. Figure 2.4a shows the critical particle diameter for entrapment in rolling/sliding contact, using both methods, for a typical range of operational parameters.

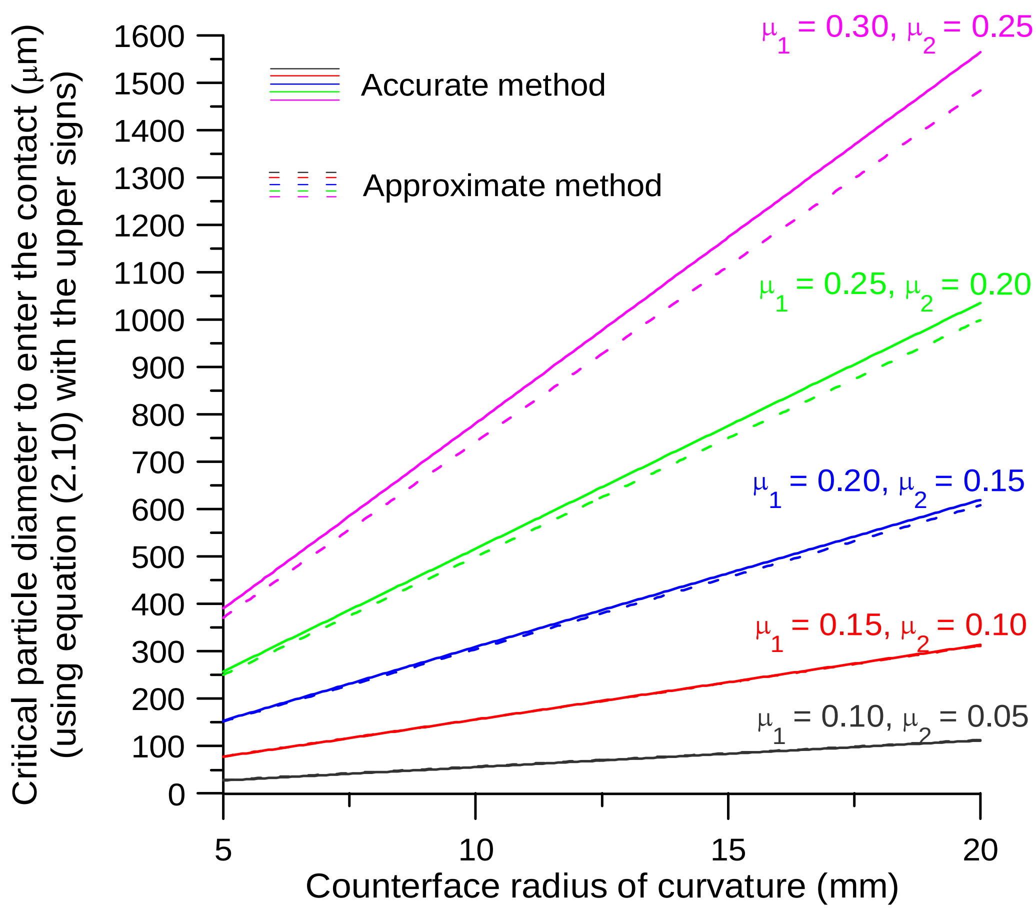

Figure 2.4a Critical particle diameter for a rolling/sliding contact, <u>applicable only when *both counterfaces are moving in the same direction*</u>. (The counterfaces have equal radii of curvature. Central film thickness: from 0.38 μm for the 5 mm radius of curvature up to 0.68 μm for the 20 mm one.)

It is noted that the values given in figure 2.4a have been calculated by applying equation (2.10) with the upper signs (see equation (2.10) and the explanations that follow it). Therefore, the use of figure 2.4a is useful either for purely rolling contacts or for contacts where both counterfaces are moving towards the centre of the contact. If the lower signs in equation (2.10) are used or, in other words, if the sliding of the contact is taken into account, the values of the critical diameter in figure 2.4a become significantly lower. This is shown in figure 2.4b.

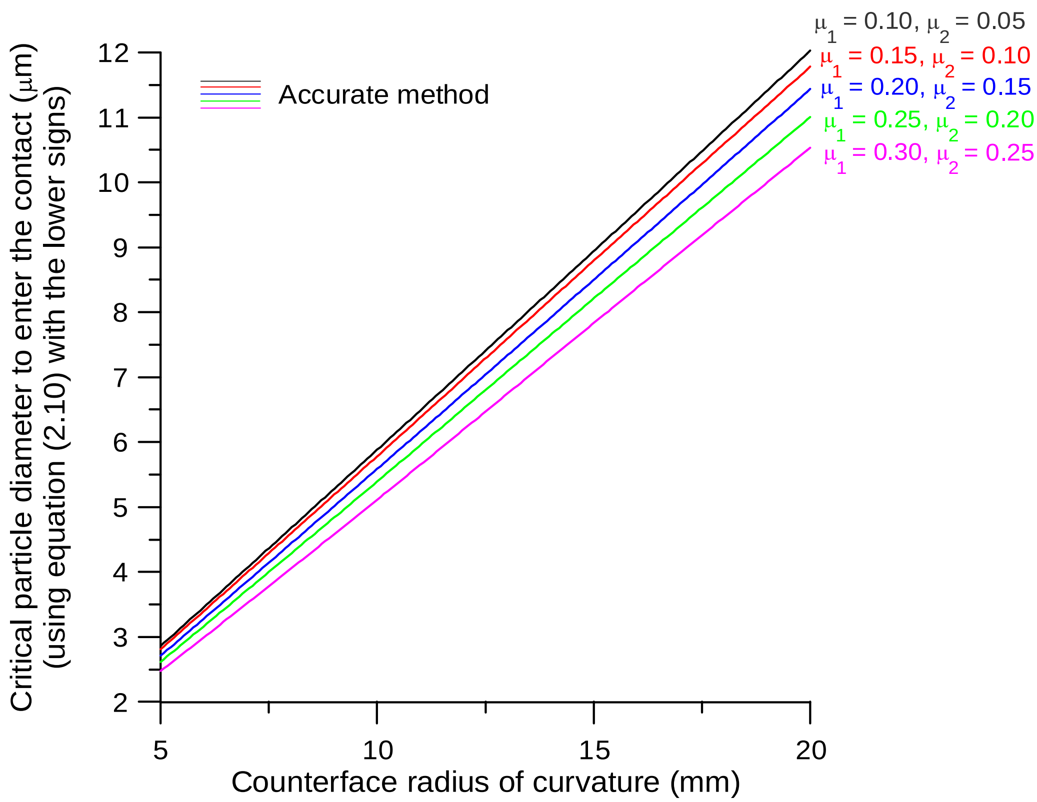

Figure 2.4b Critical particle diameter for a rolling/sliding contact, applicable only when *one counterface is stationary* or when *the counterfaces are moving in opposite directions*. (The counterfaces have equal radii of curvature. Central film thickness: from 0.38 μm for the 5 mm radius of curvature up to 0.68 μm for the 20 mm one.)

However, figure 2.4b is applicable only when one counterface is stationary (see the explanations below equation (2.10)). It may seem surprising that figure 2.4b gives very low values for the critical particle diameter, although this effect was particularly noted in the experimental work of Cusano and Sliney (1982), and Wan and Spikes (1986 and 1988). It has also been extensively demonstrated in the first chapter of this Thesis (see figure 1.53 referring to "High Sliding"). Nevertheless, it must be made clear that the calculations involved perfectly spherical and rigid particles. In reality, neither of the previous two assumptions is true. Particle plasticity allows particles to be compressed plastically and enter deeper inside an elastohydrodynamic gap. Of course, if the particles are brittle, they may well break down to smaller fragments, which then may readily enter the contact zone. On the other hand, a sphere has no edge. It is therefore much more difficult to be dragged or grabbed as compared to an irregularly shaped object. Moreover, the analysis at this stage omits any fluid-force effects on the particle. It is shown later in this chapter that fluid forces may have an effect on particle's motion at the stage of particle's pinching between the counterfaces. For all the previous reasons, figure 2.4b must be used only as an indicative and not as a strictly accurate guide. Assuming that the counterfaces have equal friction coefficients, and that one of the counterfaces is stationary (is not moving towards the centre of the contact), then the analysis of sub-section 2.3.2 gives unsurprisingly that the critical particle diameter is equal to the central film thickness of the contact (the minimum gap). Finally, the results are very much dependent on the difference of the friction coefficients ($\mu_1 - \mu_2$).

2.4 Shape of a deformed soft and ductile particle

The model of the present chapter refers to spherical ductile particles, which are much softer than the counterfaces. As is shown later in this Thesis, stress calculations are normally done for particles with hardness lower than 50 % of the minimum hardness of the two counterfaces. Moreover, the counterfaces can be considered as nearly parallel, as is explained in section 2.2. Therefore, a particle that has started deforming and being squashed inside the elastohydrodynamic gap can be simulated by a short cylinder (disk) pressed between two parallel, flat surfaces, which generally have a relative sliding and normal-approaching velocity to each other. Experimental support for this behaviour can be found in Dwyer-Joyce (1993) and Wan and Spikes (1988), in the form of photographs showing deformed copper particles. High sliding conditions are expected to produce particle shapes which are elliptical rather than circular, but this is not going to significantly affect the results of this Thesis, namely the magnitude of stresses and flash temperatures, as is shown later.

Summarizing the model, the particle is initially considered spherical. This is done for two reasons.

(a) Simplicity of reference; only one number is needed to describe particle's dimensions, namely its diameter.

(b) Although a particle can have an infinite variety of shapes, smooth shapes are more common for soft and ductile particles, owing to the way they are created. On the other hand, there must be a starting point in the analysis, and the assumption of an initially spherical particle is not unrealistic. It is interesting to report that Leng and Davies (1988) performed a ferrographic examination of unused lubricants for Diesel engines and found that the majority of metallic debris were iron-based and of <u>spherical</u> shape, with diameters ranging from a few microns to about 20 μm. Kjer (1981), searching for particles in new motor oils, was surprised to find a great number of spherical particles with diameters ranging from a few microns to about 30 μm, but the majority of those were non-metallic. It is noted that spherical particles are often found to be associated with fatigue. They are thought to be the result of debris being rolled around within a spalling crack. Their generation is believed to be typical of spalling fatigue (see Tallian, 1992, page 176, plate No: 10:31 for a good description with photographs).

After its entrapment, the particle starts forming a disk-shaped object, named here the "equivalent cylindrical particle", and its thickness is progressively reduced as it enters deeper inside the gap. This model can be viewed simplified in figure 2.5.

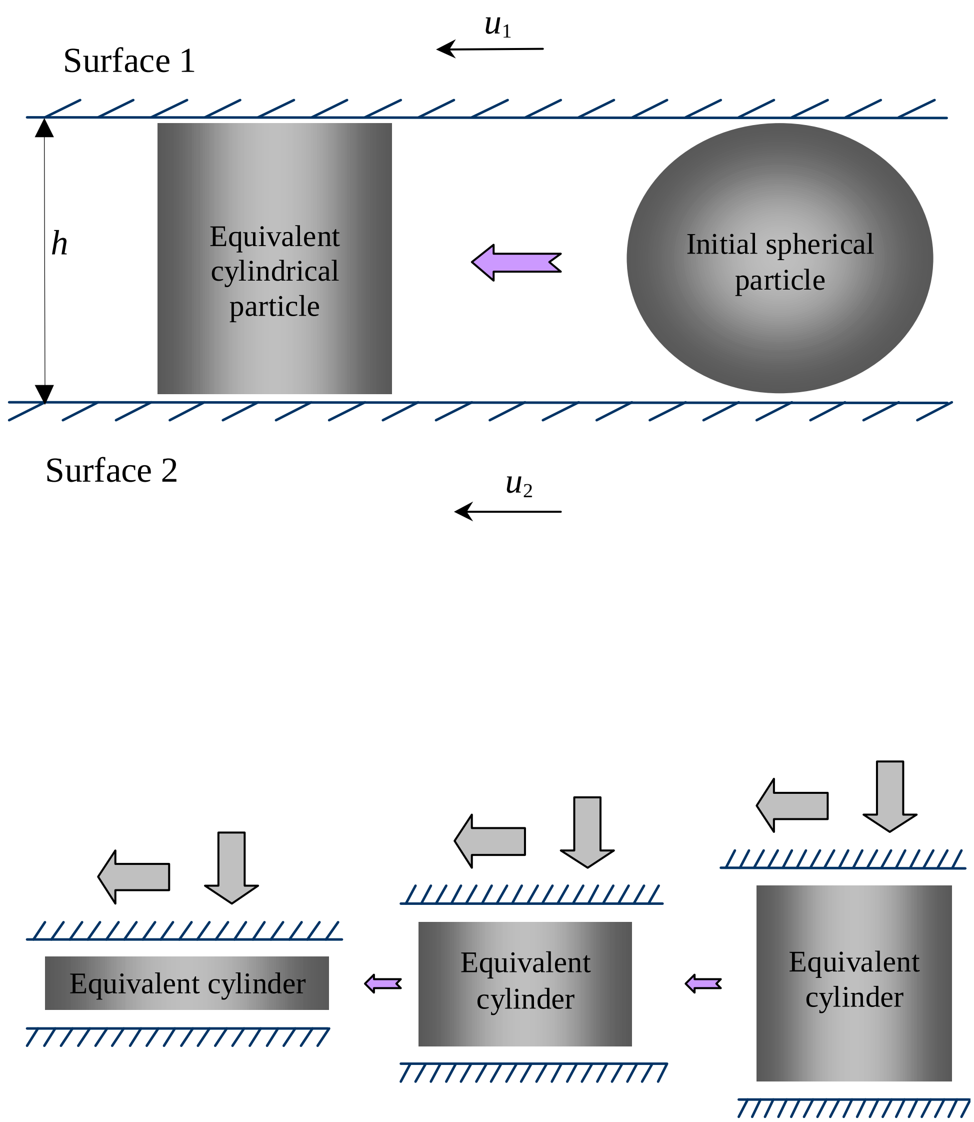

Figure 2.5 Simplified model of a deforming soft ductile particle.

2.5 Fluid force on the particle

A trapped particle that is "flowing" towards the elastohydrodynamic gap is under the influence of the lubricant that surrounds it. This influence is expressed in two ways.

(a) Owing to the variable elastohydrodynamic pressure in the contact, different points on the circumference of the particle are subjected to different static pressure. Integration around particle's circumference can reveal the magnitude and direction of the resultant static-pressure force on the particle.

(b) The particle occupies its own space in the lubricant flow, thus disturbing the flow by its presence. The lubricant then reacts by applying a "dynamic-pressure" force on the particle (drag force).

The previous two fluid forces are modelled in the following two sub-sections.

2.5.1 Static-pressure fluid force on the particle

After being trapped, the particle starts moving along the x-direction (figure 2.2), being flattened as it enters the gap. An intermediate stage of its deformation is presented in figure 2.6. The radius *R* of the deformed (disk shaped) particle is calculated using the principle of conservation of volume:

$$\pi \cdot R^2 \cdot h = V_\sigma \tag{2.18}$$

where V_σ is the volume of the initially spherical particle, hence:

$$V_\sigma = \frac{\pi}{6} \cdot D^3 \tag{2.19}$$

Using equation (2.18), radius *R* is:

$$R = \sqrt{\frac{V_\sigma}{\pi \cdot h}} \tag{2.20}$$

where the thickness h refers to the position of the particle's geometrical centre and is calculated from equation (2.1).

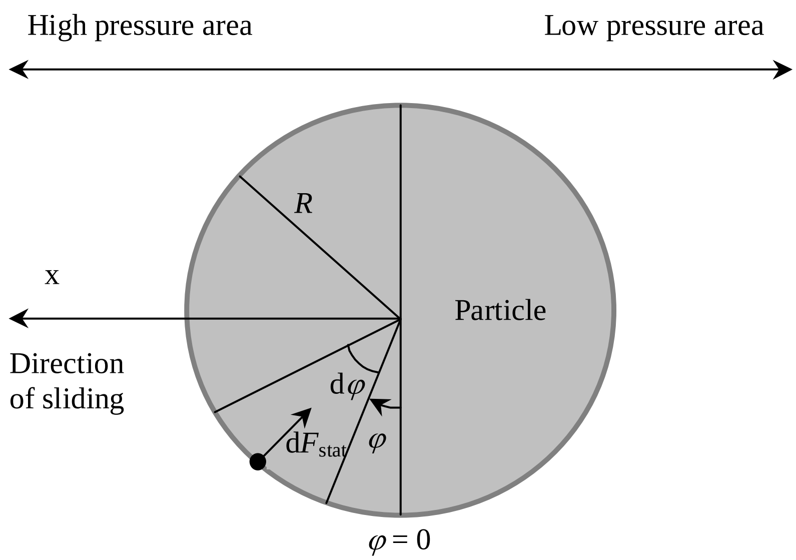

Figure 2.6 Calculation of the "static-pressure" fluid force on the particle.

Dividing the particle into elemental sectors as shown in figure 2.6, the elemental "static pressure" fluid force on a sector, owing to the fluid static pressure p, is

$$\mathrm{d}F_{\mathrm{stat}} = p \cdot h \cdot R \cdot \mathrm{d}\varphi \tag{2.21}$$

and the component in the x-direction is

$$\mathrm{d}F_{\mathrm{stat,x}} = p \cdot \sin(\varphi) \cdot h \cdot R \cdot \mathrm{d}\varphi \tag{2.22}$$

Angle φ is measured clockwise, as is shown in figure 2.6. Integration along the periphery of the particle yields the overall fluid force due to the static-fluid-pressure gradient:

$$F_{\text{stat}} = 2 \cdot R(x) \cdot \int_0^{\frac{\pi}{2}} \sin(\varphi) \cdot \begin{bmatrix} p(x - R(x) \cdot \sin(\varphi)) \cdot h(-x - R(x) \cdot \sin(\varphi)) - \\ \\ \varepsilon(\varphi) \cdot p(x + R(x) \cdot \sin(\varphi)) \cdot h(-x + R(x) \cdot \sin(\varphi)) \end{bmatrix} \cdot \mathrm{d}\varphi \quad (2.23)$$

where ε is a “flow perturbation” parameter, used here to simulate the disturbance of the fluid flow caused by the presence of the particle. It is obvious that near the particle, lubricant streamlines are not the same as in the case of the unperturbed flow. Generally ε depends on location – more precisely on the angle φ, but in any case it can be chosen in the region

$$0 < \varepsilon(\varphi) < 1 \quad (2.24)$$

Theoretically, ε could be slightly outside the previous region, but this is very difficult to be precisely calculated because of the uncertainty of the fluid conditions around the particle, especially at such small scale. In the proposed model, $\varepsilon = 0$ represents the hypothetical case where the right-hand side of the particle according to figure 2.6 (the particle moves from right to left in the figure) is under zero lubricant static pressure. Similarly, $\varepsilon = 1$ represents the case where the lubricant’s pressure along the periphery of the right-hand side of the particle (figure 2.6) is the one predicted by the Elastohydrodynamic Theory, as if there were no obstacle (particle) present.

With a particle present inside the elastohydrodynamic gap, some of the contact’s load will be carried by the particle. Therefore, the elastohydrodynamic pressure around the particle is expected to be reduced, which implies a partial local film collapse. The proposed model addresses the worst case scenario, where the elastohydrodynamic pressure has its maximum value, as predicted by the classical theory. If the particle could overcome (as is shown later) the full elastohydrodynamic pressure “obstacle” and could move into the gap, then the same would happen in the more realistic case where the elastohydrodynamic pressure is lower than its maximum theoretical strength, due to the presence of the particle.

2.5.2 Dynamic-pressure fluid force on the particle

The particle occupies some space in the lubricant and thus disturbs the flow by its presence. Because of the differing local velocity of the lubricant relatively to the particle, a fluid drag force is exerted on the particle, which, in Fluid Mechanics terminology, is known as a force due to "dynamic pressure". This force can be calculated from the following equation:

$$F_{\mathrm{dyn}} = C_D \cdot \frac{\rho}{2} \cdot A \cdot U^2 \tag{2.25}$$

where C_D is the drag coefficient, ρ is the density of the lubricant, U is the (macro) speed of the lubricant relatively to the particle and A is the facial surface of the deformed particle (disk)

$$A = \pi \cdot R^2 \tag{2.26}$$

The lubricant in the high-pressure area of the contact (Hertzian zone) is assumed to remain in the liquid state, so that equation (2.25) is directly applicable. It is however speculated that, in heavily loaded contacts, the lubricant may behave like a soft solid, although lubricant's behaviour at very high pressure is not yet well understood and modelled. If there is partial solidification of the lubricant, a more simple equation can be used in place of equation (2.25), as for example: $F_{\mathrm{dyn}} = C_D \cdot \rho \cdot U \cdot A$. Because of the ambiguity of the actual state of the lubricant in the high pressure area of the contact, it is difficult to estimate the exact value of the drag coefficient C_D, which depends on the position of the shear plane in the lubricant and on the density of its solidified part. Nevertheless, in view of the extremely small thickness of the particle in the high pressure region (Hertzian zone), it is not expected that a partly solidified film will be a serious obstruction in the sliding of the particle, especially when the high sliding frictional forces between the particle and the counterfaces are taken into account, as is shown in the example at the end of this chapter.

The Reynolds number of the local fluid flow around the particle (or particle Reynolds number) is defined as

$$\mathrm{Re}_{\mathrm{p}} \equiv \frac{2 \cdot R \cdot \rho \cdot U}{\eta} \tag{2.27}$$

where η is the (variable) dynamic viscosity of the lubricant, known also as absolute viscosity. It is found that the particle Reynolds number is low, usually less than 1. Therefore, the local flow is creeping. For a thin circular disk, which is aligned in parallel to the streamlines of a creeping flow, the drag coefficient C_D is evaluated by the following equation (Munson *et al.* (1990), Table 9.4, page 611):

$$C_D = \frac{13.6}{\mathrm{Re}_{\mathrm{p}}} \tag{2.28}$$

Equation (2.28) is not fully applicable in this case because the upper and lower faces of the particle are in contact with surfaces 1 and 2 respectively. Nevertheless, it is used here to obtain an estimation of the magnitude of the dynamic-pressure fluid force on the particle. As is shown later in the example quoted in this chapter, the dynamic-pressure fluid force on the particle is very weak compared to the sliding frictional forces, having practically no effect on the motion of the particle.

Using equations (2.26)-(2.28), equation (2.25) gives

$$F_{\mathrm{dyn}} = 3.4 \cdot \pi \cdot \eta \cdot R \cdot U \tag{2.29}$$

The most widely used formula in the literature, which gives the dynamic viscosity as a function of pressure and temperature, is the one proposed by Roelands (1963, 1966), which in SI units reads as:

$$\eta = \eta_0 \cdot \exp\left\{ \left[\ln(\eta_0) + 9.67\right] \cdot \left[\left(1 + 5.1 \cdot 10^{-9} \cdot p\right)^{Z_1} \cdot \left(\frac{\theta - 138}{\theta_0 - 138} \right)^{-S_0} - 1 \right] \right\} \tag{2.30}$$

where η_0 is the dynamic viscosity at environmental conditions, Z_1 and S_0 are the viscosity-pressure and viscosity-temperature coefficients respectively, θ_0 is the environmental temperature, and θ is the temperature of the lubricant (both temperatures in degrees Kelvin).

Finally, the density of the lubricant is also a function of pressure and temperature. For mineral oils, a widely used formula, which originated from Dowson and Higginson (1966) for the density-pressure relationship and later extended (see for example Yang and Wen, 1993) to include the temperature factor, is the following (valid for SI units only):

$$\rho = \rho_0 \cdot \left[1 + \frac{6 \cdot 10^{-10} \cdot p}{1 + 17 \cdot 10^{-10} \cdot p} - 65 \cdot 10^{-5} \cdot (\theta - \theta_0) \right] \qquad (2.31)$$

where ρ_0 is the density of the lubricant at environmental conditions. For a given change of pressure and temperature, the corresponding change of the density is much lower than that of the dynamic viscosity. Moreover, thermal effects influence the viscosity much more than the density. For example, for p = 1 GPa, θ = 150 °C and θ_0 = 20 °C, the contribution of the pressure to the density increase is +22 %, whereas the contribution of the temperature is –8 %, according to equation (2.31). As far as the dynamic viscosity is concerned, if the temperature factor were omitted, the calculated viscosity would be 30,000 times higher (using η_0 = 0.08 Pa·s, Z_1 = 0.6 and S_0 = 1.1, which are typical values for lubricating oils) than if both pressure and temperature effects were accounted for!

Alternatives to the relation (2.31) have been proposed by other researchers, who attempted to overcome the increasing inaccuracy of equation (2.31) for higher pressures (usually for pressures higher than 0.5 GPa). Hamrock (1994) suggested a complicated model, which takes into account the possibility of film solidification. More recently, Wong *et al.* (1996) proposed a model, which originated from the well-known van der Waals equation for perfect gases, and showed that their model agrees well with experimental values over a wide range of pressures (their tests were restricted to 1.2 GPa). However, equation (2.31) will be used in the present analysis, were the pressures (in the examples used) are not very high.

Thermal elastohydrodynamic solutions (see for example Yang and Wen, 1993) for line contacts have shown that the temperature variation across the film (direction of film thickness) is rapid. Accordingly, viscosity variations across the film are rapid, too. Therefore, the effective viscosity used in the calculation of the Reynolds number (equation (2.27)) must be an intermediate value of the highest viscosity (environmental temperature) and lowest viscosity (maximum flash temperature for position x) in the contact. By omitting the thermal factor in the calculation of the dynamic viscosity, we allow for the maximum possible viscosity, under the specific pressure in the contact. This means that, since the dynamic-pressure fluid force F_{dyn} is proportional to the dynamic viscosity (equation (2.29)) and varies relatively insignificantly due to the other factors (R and U) as can easily be proved, the omission of the thermal effects on the dynamic viscosity results in the maximum-possible calculated F_{dyn}. It is actually shown in the example presented later in this chapter that even this maximum force F_{dyn} is still significantly lower than the solid frictional forces between the particle and the counterfaces, and that the solid frictional forces rule the motion of the particle along most of the particle's trajectory. Moreover, and because of the latter reason, the non-Newtonian behaviour of some lubricants at high shear rates (where their viscosity is also affected by the shear rate) is considered of secondary importance and of limited value in the present study.

Finally, a note must be made on the magnitude of speed U (equation (2.25)). This refers to a macro-speed of the lubricant relatively to the particle, in the area around the particle and depends on the local conditions of the lubricant, which, for high pressures - temperatures and shear rates, are not accurately known. Therefore, a rather ambiguous choice has to be made. For example, it is rather obvious to assume that $0 < U < u_1 - u_2$. The x-speed profile of the lubricant around the particle depends on the position of lubricant's shearing plane. If it is assumed that this speed profile is linear, then a suitable choice for speed U is the sliding semi-speed of the contact: $U = (u_1 - u_2)/2$. However, this choice is not crucial because, as is shown later in this chapter, the dynamic-pressure fluid force on the particle, which is proportional to speed U, is significantly lower than the solid frictional forces and, hence, is not affecting essentially the motion of the particle.

2.6 Solid pressure on the particle – preliminary model

The particle is plastically deformed as it enters the elastohydrodynamic gap. According to the model of section 2.4, it is expected to become a thin flat disk with a more-or-less cylindrical shape, especially if the sliding speed of the contact is low. The pressure between the particle and the counterfaces can be found by considering the particle as a small mass in a completely plastic state. A rather simple but effective model has been presented by Hamer *et al.* (1989), which takes into account surface deformations due to the pressure between the particle and the counterfaces. That model will be adopted here as a first approximation. Due to the softness of the particles considered in this Thesis, surface deformations are omitted at this stage and the counterfaces are considered as rigid. A more thorough and extensive model, including surface deformations and lubricant pressure on the particle, is developed in the last chapter of this Thesis.

Following the analysis of Hamer *et al.* (1989), the solid pressure on the particle is calculated from the following equations:

$$\left.\begin{aligned} p_{\mathrm{s}} &= Y_{\mathrm{p}} \cdot \mathrm{e}^{\frac{2\cdot\mu_f\cdot(R-r)}{h}} && ,\text{if } \mu_f \cdot p < k_{\mathrm{p}} \\ p_{\mathrm{s}} &= \frac{k_{\mathrm{p}}}{\mu_f} + \frac{2\cdot k_{\mathrm{p}}}{h}\cdot\left(R_s - r\right) && ,\text{if } \mu_f \cdot p \geq k_{\mathrm{p}} \end{aligned}\right\} \tag{2.32}$$

where Y_{p} is the yield stress in uniaxial tension of the material of the particle, k_{p} is the yield stress in simple shear of the particle's material (taken here as $k_{\mathrm{p}} = Y_{\mathrm{p}}/\sqrt{3}$ according to the von Mises yield criterion, which is more suitable for ductile materials, as in the present case), R_s is the radius of the stick region between the particle and a counterface, if any, and μ_f is the friction coefficient between a particle and a counterface. The friction coefficient μ_f may be slightly different for each counterface. The latter means that the upper and the lower base of the particle will have slightly different radii. These radii (which are almost equal to each other) are accurately calculated in the model, although only one radius R is reported, which is the average of the two aforementioned radii.

Equations (2.32) constitute a version of the “friction hill” theory, which is basic textbook material in the Theory of Plasticity. In any case, equations (2.32) are a good starting point for the following two reasons.

(a) The model is for ductile particles, which are much softer than the counterfaces, usually 50 % to 90 % softer. Hence, the counterfaces can be considered as rigid for a first approximation.

(b) The relative sliding of the counterfaces does actually little to upset the circularity of the deforming particle, especially in the all important Hertzian zone of the contact, due to the extremely small thickness of the elastohydrodynamic gap and the nearly parallel, flat counterfaces. The circularity of plastically deformed particles has been experimentally shown in Wan and Spikes (1988), in the case of copper particles. For high sliding speed of the contact, this circularity may be distorted and the particle may adopt a more-or-less elliptical shape, being elongated along the direction of sliding of the contact.

The particle’s thickness is assumed to remain constant throughout the area of the particle, owing to the nearly parallel counterfaces. For a typical surface dent caused by a soft particle, with a depth of around 1 μm and a radius of around 100 μm, the average dent slope is easily calculated to be less than 1°. This slope is sufficiently small to be ignored.

If the counterfaces are harder than the particle, the pressure on the particle cannot exceed the maximum hardness of the counterfaces. Forging experiments with disks pressed between flat platens have shown that the assumption of rigid platens is not unreasonable if the hardness of the disks is much less than 90 % of the hardness of the platens, whereas above this threshold, the assumption of platens’ rigidity is no longer valid. Therefore, and in view of the previous observation, particles used throughout this study are assumed at least 10 % softer than the counterfaces.

2.7 Motion of the particle

In this section, the equation of particle's motion is developed, based on all forces acting on the particle, namely solid frictional forces between the particle and the counterfaces, fluid forces and particle's inertia. The instantaneous motion of the particle is described in a local Cartesian coordinate system OX′Z, as is shown in figure 2.7. The origin O of system OX′Z is the centre of contact of the particle with body 2. In general, the particle has a velocity $\underset{\sim}{V}_{p1}$ relatively to surface 1 and a velocity $\underset{\sim}{V}_{p2}$ relatively to surface 2. Equivalently, surfaces 1 and 2 have velocities $\underset{\sim}{V}_{1p}$ and $\underset{\sim}{V}_{2p}$ respectively, relatively to the particle (figure 2.7).

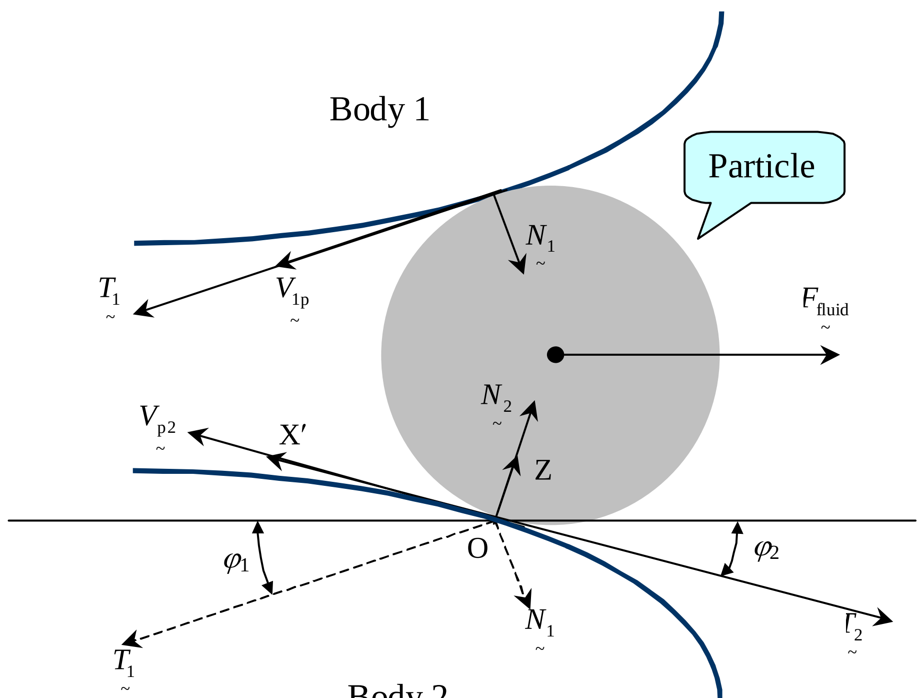

Figure 2.7 Forces acting on the particle and other notation.

Using figure 2.7, the force equilibrium on the particle is written as follows:

$$T_1 \cdot \cos(\varphi_1 + \varphi_2) - T_2 \cdot \mathrm{sgn}(X') - N_1 \cdot \sin(\varphi_1 + \varphi_2) - F_{\mathrm{fluid}} \cdot \cos(\varphi_2) = m \cdot \ddot{X}' \tag{2.33}$$

where m is the mass of the particle and X' is the instantaneous displacement of particle's geometrical centre (centre of the particle disk) relatively to surface 2.

The sign function sgn(X′) is defined as follows:

$$\mathrm{sgn}(X') = \begin{cases} +1 & \text{if } X' > 0 \\ -1 & \text{if } X' < 0 \end{cases} \tag{2.34}$$

This term is introduced in equation (2.33) because the direction of vector $\underset{\sim}{T_2}$ depends on the direction of the motion of the particle relatively to surface 2 (this direction is not known beforehand).

The distance between the counterfaces during the motion of the particle is equal to the lubricant film thickness $h(x)$ (figure 2.5), where x is the distance of the centre of particle's disk from the centre of the contact ($x = 0$, in other words the centre of the Hertzian zone or the "nominal point of contact"). The idealized cylindrical particle collapses progressively (figure 2.5, from right hand to left hand) as it moves towards the centre of the contact. It must be noted that the curvature of the counterfaces in the inlet zone of the contact is actually taken into account in deriving the force equilibrium on the particle (see equation (2.33)).

Angles φ_1 and φ_2 are easily calculated using figure 2.7 and equation (2.1):

$$\varphi_i = \arctan\left[\frac{4 \cdot w \cdot \left(1 - \nu_i^2\right)}{\pi \cdot E_i \cdot b} \cdot \sqrt{\left(\frac{x}{b}\right)^2 - 1}\right] \quad , i = 1, 2 \tag{2.35}$$

Normal forces N_1 and N_2 (figure 2.7) are calculated from the solid-pressure distribution on the particle ($N_1 = N_2$ according to the model of figure 2.5):

$$N_1 = N_2 = 2 \cdot \pi \cdot \int_0^R p_{\mathrm{s}} \cdot r \cdot \mathrm{d}r \tag{2.36}$$

Frictional forces T_1 and T_2 are related to the normal forces N_1 and N_2 respectively through the following equations:

$$T_i = \mu_i \cdot N_i \quad , i = 1, 2 \tag{2.37}$$

Each one of equations (2.37) holds as long as the particle is in motion relatively to the corresponding counterface. If the particle is stationary to one counterface and slides on the other, the traction force between the particle and the counterface it sticks to is calculated from equation (2.33), with the right-hand side of that equation being equal to zero. For example, if the particle sticks to surface 1 and slides on surface 2, then:

$$\left.\begin{aligned} T_1 &= N_1 \cdot \tan(\varphi_1 + \varphi_2) + \frac{\operatorname{sgn}(X') \cdot T_2 + F_{\mathrm{fluid}} \cdot \cos(\varphi_2)}{\cos(\varphi_1 + \varphi_2)} \\ T_2 &= \mu_2 \cdot N_2 \end{aligned}\right\} \tag{2.38}$$

Similarly, if the particle sticks to surface 2 and slides on surface 1, then $T_1 = \mu_1 \cdot N_1$ and force T_2 is calculated from an equation similar to equation (2.33), written for a coordinate system associated with surface 1, as OX′Z is put on surface 2.

The overall fluid force on the particle consists of the static and the dynamic-pressure fluid force components, according to the analysis of sub-sections 2.5.1 and 2.5.2, respectively. Combining these components, the overall fluid force on the particle, directed along the x-axis (figure 2.7) is:

$$F_{\mathrm{fluid}} = F_{\mathrm{stat}} \pm F_{\mathrm{dyn}} \tag{2.39}$$

Since the characteristic speed U of the lubricant around the particle may change direction during the motion of the particle, both the plus and minus signs were used in writing equation (2.39).

All terms of the equation of particle's motion (2.33) are at this point clearly defined. Before attempting to obtain a solution, a relation between distances x and X' must be found. Using figures 2.1 and 2.7, the following equation is derived:

$$x = \left(X' + u_2 \cdot t\right) \cdot \cos\left(\varphi_2\right) + x_{t=0} \tag{2.40}$$

where t represents time elapsed since the particle was first pinched. However, according to equation (2.35), the term cos(φ_2) in equation (2.40) is a non-linear function of the variable x. In order to avoid this complexity, the term cos(φ_2) is linearized by expanding into a Taylor series and keeping only first-order terms:

$$\cos\left(\varphi_2\right) \cong 1 + c_0 \cdot b \cdot \left(b - x\right) \tag{2.41}$$

where c_0 is a constant, defined as

$$c_0 \equiv \left[\frac{4 \cdot w \cdot \left(1 - \nu_2^2\right)}{\pi \cdot E_2 \cdot b^2}\right]^2 \tag{2.42}$$

Using equation (2.41), equation (2.40) gives:

$$x \cong \frac{\left(X' + u_2 \cdot t\right) \cdot \left(1 + c_0 \cdot b^2\right) + x_{t=0}}{1 + \left(X' + u_2 \cdot t\right) \cdot c_0 \cdot b} \tag{2.43}$$

When $\varphi_2 = 0$ (in the Hertzian zone), equation (2.40) can be used directly in the place of the approximation (2.43).

The equation of motion (2.33) is now discretized with a classical, second-order accuracy, finite difference scheme:

$$X'_{k+1} \cong \frac{(\Delta t)^2}{m} \cdot \left\{ \begin{bmatrix} \left[\mu_1 \cdot \cos\left(\varphi_{1_k} + \varphi_{2_k}\right) - \sin\left(\varphi_{1_k} + \varphi_{2_k}\right)\right] \cdot N_1(x_k) - \mu_2 \cdot N_2(x_k) \cdot \mathrm{sgn}(X'_k) - \cos\left(\varphi_{2_k}\right) \cdot \\ \left[2 \cdot R(x_k) \cdot \int_0^{\frac{\pi}{2}} \sin(\varphi) \cdot \begin{bmatrix} p(x_k - R(x_k) \cdot \sin(\varphi)) \cdot h(-x_k - R(x_k) \cdot \sin(\varphi)) - \\ \varepsilon(\varphi) \cdot p(x_k + R(x_k) \cdot \sin(\varphi)) \cdot h(-x_k + R(x_k) \cdot \sin(\varphi)) \end{bmatrix} \cdot \mathrm{d}\varphi \right. \\ \left. -3.4 \cdot \pi \cdot \mu(x_k) \cdot R(x_k) \cdot U \right] \end{bmatrix} \right\}$$

$$+ 2 \cdot X'_k - X'_{k+1} \tag{2.44}$$

where Δt is the time step. Equation (2.44) is applicable only if the particle is in motion relatively to both counterfaces; otherwise, the particle sticks to one counterface and slides on the other. In the latter case, particle's motion and velocity are obviously known.

The initial conditions that accompany equation (2.44) are as follows:

(a) At $t = 0$ (k=1): $X_1' = 0$.

(b) At $t = 0$: $V_{p2} = c \Rightarrow (X_2' - X_1')/\Delta t \cong c \Rightarrow X_2' \cong c \cdot \Delta t$ (using condition (a)). Assuming that, before its entrapment, the particle was carried by surface 1, then $c = V_{12}/\cos(\varphi_1 + \varphi_2)_{t=0}$, where $V_{12} = u_1 - u_2$ is the sliding speed of the contact. If it is assumed that the particle was carried by surface 2 prior to its entrapment, then $c = 0$. An intermediate value for c can also be used, thinking that the particle was carried by the lubricant.

(c) At $t = 0$: $h(x_p) \cong D$. This means that the separation of the counterfaces at the point where the particle is first pinched is approximately equal to the particle's diameter (the particle is considered spherical prior to its plastic deformation). This assumption has been checked through the proposed model and found fully justified (up to an accuracy of several decimal digits).

It is now straightforward to calculate the instantaneous speeds V_{p2} and V_{1p}. They are as follows:

$$V_{\mathrm{p}2} = \dot{X}' = \frac{X'_{k+1} - X'_{k-1}}{2 \cdot \Delta t} \tag{2.45}$$

$$V_{1\mathrm{p}} = V_{p2} \cdot \cos(\varphi_1 + \varphi_2) - V_{12} \tag{2.46}$$

The limiting shear stress between the particle and a counterface is the particle's yield stress in simple shear (k_{p}). If this limit is exceeded, the particle sticks to the relevant counterface. Therefore, the following constraints must hold:

$$\left.\begin{array}{l} \text{If } \ \mu_1 \cdot p > k_{\mathrm{p}} \ \text{ then } \ V_{1\mathrm{p}} = 0 \\ \\ \text{If } \ \mu_2 \cdot p > k_{\mathrm{p}} \ \text{ then } \ V_{\mathrm{p}2} = 0 \end{array}\right\} \tag{2.47}$$

If the particle sticks to both counterfaces, it will be internally sheared to the point its thickness will be reduced, until the traction between the particle and the counterface with the lower friction coefficient falls below the critical limit, so that the particle starts sliding again. The latter case is not covered in the present work and does not alter the essence of the results and conclusions obtained later.

At this point of the analysis, there is only one step to go before achieving the complete description of particle's kinematics, based on the model outlined in figure 2.5. The remaining step is the calculation of particle's "extrusion" speed, which is the speed of the lateral expansion of the particle during its plastic compression. The extrusion speed is simply expressed as follows:

$$V_{\mathrm{extr}} = \dot{R} \tag{2.48}$$

where the dot above R denotes time differentiation. Using equation (2.20), the time derivative of radius R is given as:

$$\dot{R} = -\frac{\dot{h}}{2 \cdot h} \cdot \sqrt{\frac{V_\sigma}{\pi \cdot h}} \tag{2.49}$$

From equation (2.1), the thickness h is a function of the following time-dependent variables: x, b, h_c and w. Time variations of the load w are out of interest in this study ($\dot{w} = 0$). Using the rest of the variables, the time derivative of thickness h is given as follows:

$$\dot{h} = \frac{\partial h}{\partial x} \cdot \dot{x} + \frac{\partial h}{\partial b} \cdot \dot{b} + \frac{\partial h}{\partial h_c} \cdot \dot{h}_c \qquad (2.50)$$

The Hertzian semi-width b and the central film thickness h_c can be considered constant for the purposes of this study, because transient elastohydrodynamic effects in the contact are of secondary importance and are not affecting significantly the damage that the particle is likely to cause. Besides, as is shown later, the passage of the particle from the elastohydrodynamic gap is rapid and lasts usually less than one millisecond, depending on the rolling and sliding speeds of the contact. Hence, the time derivative of thickness h is finally given by the following equations:

$$\dot{h} \cong \frac{\partial h}{\partial x} \cdot \dot{x} = \frac{\sqrt{x^2 - b^2}}{R_{eq}} \cdot \dot{x} \qquad (2.51)$$

Finally, using equations (2.49) and (2.51), equation (2.48) gives:

$$V_{extr} \cong -\frac{\sqrt{x^2 - b^2}}{2 \cdot h \cdot R_{eq}} \cdot \sqrt{\frac{V_\sigma}{\pi \cdot h}} \cdot \dot{x} \qquad (2.52)$$

2.8 Example

The analysis presented in this chapter is applied here in a detailed example. It is noted that this is a typical example, representative of the kind of results the proposed model yields. The data used in the example are shown in tables 2.1-2.3.

Table 2.1

Particle data	
Diameter (spherical particle – undeformed)	30 μm
Hardness	100 HV (981 MPa)
Material density	7850 kg/m^3

Table 2.2

Counterface data	
Radius of curvature	R_1 = 20 mm, R_2 = 28 mm
Hardness	800 HV (7848 MPa)
Modulus of elasticity	$E_1 = E_2$ = 207 GPa
Poisson ratio	$\nu_1 = \nu_2 = 0.3$
Friction coefficient	$\mu_1 = 0.20$, $\mu_2 = 0.15$

Table 2.3

Contact and other data	
Sliding speed	V_{12} = 1 m/s
Slide/roll ratio	$S_r = 2 \cdot V_{12}/(u_1 + u_2) = 1$
Load per unit length of the contact	w = 100 N/mm
Viscosity-pressure coefficient	$Z_1 = 0.5$
Dynamic viscosity at environmental conditions	η_0 = 0.1 Pa·s
Flow perturbation parameter	$\varepsilon = 0.5$
Environmental temperature	θ_0 = 60 °C
Speed U	$U = V_{12}/2$ = 0.5 m/s
Initially the particle is carried by surface	2 (c = 0)

Using the present model, the following results are easily obtained, as are presented in table 2.4.

Table 2.4

Some interesting results	
Central film thickness	$h_c \cong 0.7$ μm
Hertzian contact semi-width	$b \cong 114$ μm
Tangential speeds of the counterfaces	$u_1 = 1.5$ m/s, $u_2 = 0.5$ m/s
Point where the particle is first pinched	$x_{t=0} \cong -852$ μm
Maximum particle (cylinder – deformed) radius	$R \cong 80$ μm
Mass of the particle	$m \cong 0.1$ μgr
Time when the geometrical centre of the particle enters the Hertzian zone of the contact	0.50 ms
Particle pass time (from $x = x_{t=0}$ to $x = b$)	0.70 ms
Particle Reynolds number (equation (2.27)): - ignoring thermal effects due to internal shearing in the fluid - including thermal effects	 $\mathrm{Re}_p = O(10^{-3})$ $\mathrm{Re}_p = O(1)$
Maximum particle diameter to enter the contact: - Approximate method (see sub-section 2.3.1) - Accurate method (see sub-section 2.3.2)	 710 μm 723 μm

The accuracy of the classical finite difference scheme used in equation (2.44) is adequate. Around 340 points are used along the trajectory of the particle, from the point it is first pinched ($x = -852$ μm) to the point its centre enters the outlet zone of the contact ($x = 114$ μm). This means that the spatial step along the x-axis is $(852 + 114)/340 \cong 3$ μm.

According to the model developed in section 2.4 (figure 2.5), the particle collapses progressively as it enters deeper in the elastohydrodynamic gap, adopting the shape of a thin circular disk. The radius R of this disk is calculated from equation

(2.20) and varies during the squashing of the particle. Figure 2.8 shows the calculated radius *R* during the motion of the particle in the gap. The horizontal axis in the figure refers to the distance of the centre of the particle disk from the centre of the contact, namely from point $x = 0$. As can be seen, the radius changes smoothly from the point where the particle starts deforming plastically to the point where the centre of the particle enters the Hertzian zone of the contact. Inside the Hertzian zone, where the elastohydrodynamic gap has a constant thickness equal to h_c, the radius *R* has a constant value. It must be noted that the radius which corresponds to $x = x_{t=0}$ is less than 15 μm (the radius of the undeformed spherical particle – table 2.1) because, as already mentioned, radius *R* refers to the *equivalent cylinder* of volume equal to the volume of the initially spherical particle (in other words, it is not the radius of the sphere).

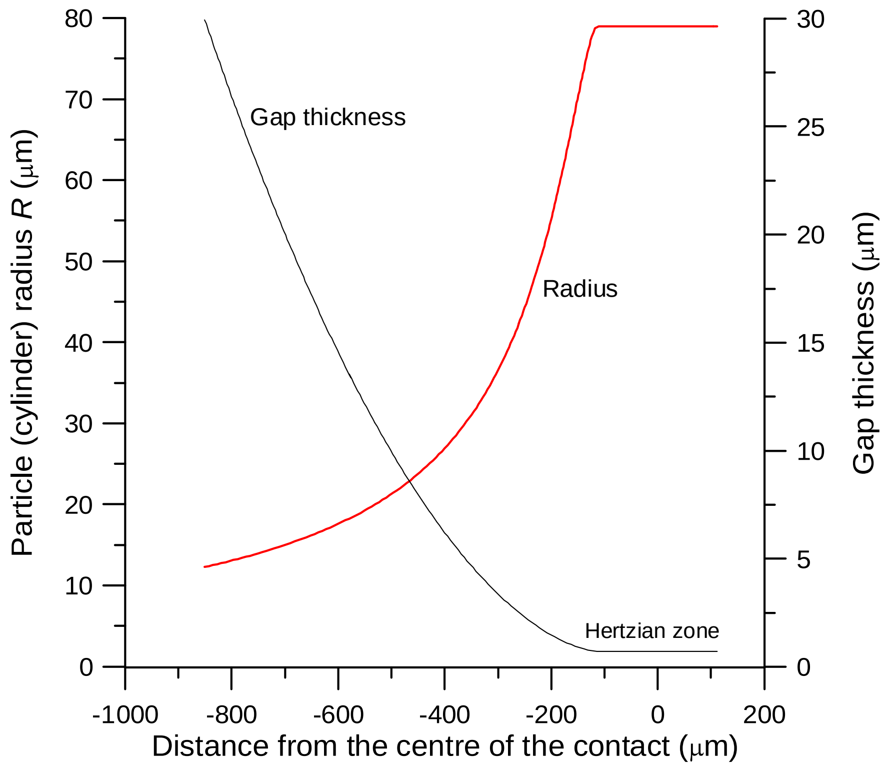

Figure 2.8 Calculated particle (cylinder) radius *R* during deformation of the particle in the elastohydrodynamic gap.

The normal and the solid frictional forces on the particle are shown in figure 2.9, where $N = N_1 = N_2$. The forces have been normalized by the maximum normal force N_{max}, which is applied on the particle when the particle is inside the Hertzian zone. The figure shows that the frictional forces T_1 and T_2 have almost the same magnitude along the trajectory of the particle. This is because the fluid force on the particle is significantly lower than the frictional forces, especially in the Hertzian zone of the contact, as is shown later.

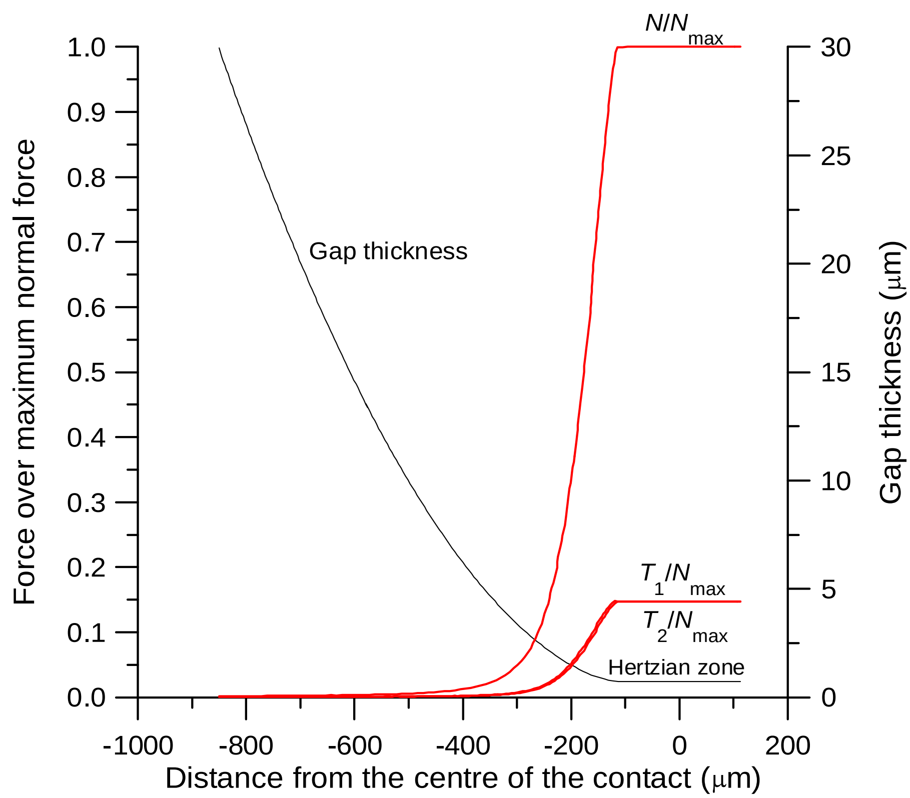

Figure 2.9 Normalized normal force (N/N_{max}) and solid frictional forces (T_1/N_{max} and T_2/N_{max}) on the particle, during passage through the contact.

Figure 2.10 shows how the two fluid force components (static and dynamic-pressure fluid forces) compare with the solid frictional forces. All forces are presented normalized by the maximum normal force N_{max}. The dynamic-pressure fluid force is negligible. Despite the high viscosity of the lubricant in the high-pressure area of the contact (Hertzian zone), the smallness of the particle results in a very low force. This can be realized from equation (2.29), where it is shown that the dynamic-pressure fluid force is proportional to particle's (cylinder – deformed) radius R, which, according to figure 2.8, has a maximum value of around 80 μm. It must also be noted that thermal effects in the lubricant film due to internal shearing are ignored at this stage (see the explanations below equation (2.31)). This results in higher calculated values of the dynamic viscosity and, according to equation (2.29), higher calculated values of the dynamic-pressure fluid force F_{dyn}. However, as explained above, F_{dyn} is still too small in comparison to the solid frictional forces.

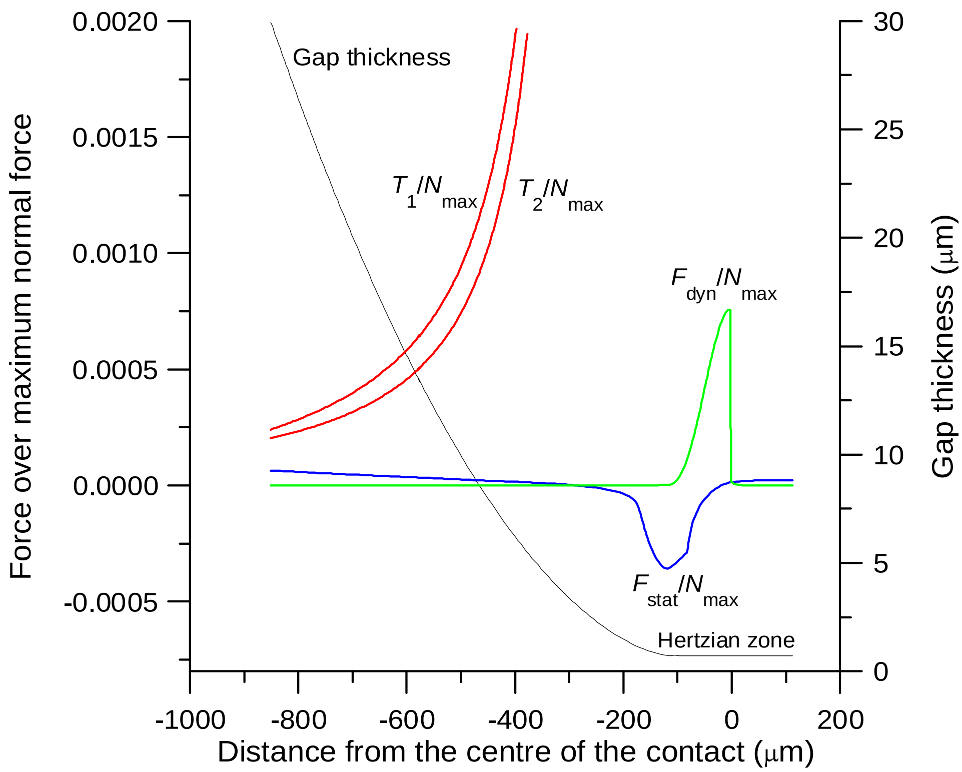

Figure 2.10 Normalized solid frictional forces (T_1/N_{max} and T_2/N_{max}) and fluid forces (F_{stat}/N_{max} and F_{dyn}/N_{max}) on the particle, during its passage through the contact.

On the other hand, the static-pressure fluid force is also very low, despite the fact that the flow perturbation parameter ε used in the example is relatively lower than what should be expected. It is the feeling of the author that a value of 0.8 or greater for ε would be more reasonable (instead of the $\varepsilon = 0.5$ used in the example), because of the low particle Reynolds number ($Re_p < 1$) of the flow around the particle (see table 2.4), which results in a laminar local flow. The latter means that the streamlines of the flow follow closely the circumference of the particle and micro-vortices are absent. The lower the value of parameter ε, the higher is the calculated static-pressure fluid force F_{stat} in the inlet zone of the contact, as can be realized from equation (2.23). However, the choice $\varepsilon = 0.5$ is deliberate to show that, even if F_{stat} is artificially allowed to be higher than normal, it is still significantly lower than both solid frictional forces, which, essentially, govern the motion of the particle inside the elastohydrodynamic gap. There is actually only one area where the fluid forces may have some strength over the solid frictional forces, and that is at the point where the particle is first pinched ($x = x_{t=0}$), as is shown in figure 2.10. If the particle overcomes this critical point and starts moving towards the centre of the contact, the fluid forces have no chance of preventing it from being totally trapped and squashed, or, in other words, the likelihood of rejection from the contact is ruled out. As a matter of fact, the static-pressure fluid force may even "assist" in the dragging of the particle deeper inside the contact as it becomes negative (directed towards the centre of the contact) somewhere near the entrance to the Hertzian zone, as can be seen in figure 2.10.

Table 2.5 presents a parametric study, aimed to show the strength of the fluid forces in comparison to the solid frictional forces, for a wide range of working conditions in the contact. Some of the cases in the table are specifically chosen to show under which conditions the fluid forces may have a better chance of standing a comparison to the frictional forces (last two rows of the table). However, it must be clearly understood that the fluid drag forces calculated in these examples are artificially exaggerated to show the worst possible scenario, as has already been explained. In reality, the fluid forces should be lower than those used in the comparisons of table 2.5. The aforementioned exaggeration comes from the fact that thermal effects due to lubricant shearing are ignored (which results in higher lubricant viscosity and hence higher dynamic-pressure fluid force), and also due to the lower-than-expected flow perturbation parameter used in the examples (which results in higher static-pressure fluid forces).

Table 2.5

Parametric study – Comparison of fluid and solid frictional forces								
D [mm]	H_p [HV]	V_{12} [m/s]	μ_1	μ_2	ε	h_c [μm]	$\max\left\{\frac{F_{stat}}{\max\{T_1, T_2\}}\right\}$ [%]	$\max\left\{\frac{F_{dyn}}{\max\{T_1, T_2\}}\right\}$ [%]
30	100	5.0	0.20	0.15	0.5	2.2	17.8	12.4
30	100	1.0	0.25	0.20	0.5	0.7	14.8	0.4
30	200	1.0	0.20	0.15	0.5	0.7	9.8	0.5
30	100	1.0	0.20	0.15	0.5	0.7	17.8	0.5
30	80	1.0	0.20	0.15	0.5	0.7	21.3	0.5
30	100	0.5	0.20	0.15	0.5	0.4	17.8	0.2
30	100	1.0	0.15	0.10	0.5	0.7	22.0	0.8
20	100	1.0	0.20	0.15	0.5	0.7	17.6	1.2
10	100	1.0	0.20	0.15	0.5	0.7	17.4	7.3
10	80	5.0	0.15	0.10	0.5	2.2	–86.8	113.5
10	80	5.0	0.15	0.10	0.5	2.2	–132.2	109.9
Other data used in the study: $S_r = 1$, $R_1 = 20$ mm, $R_2 = 28$ mm								

The particle has negligible mass. For the example studied, the mass of the particle is $m = \rho_p \cdot V_\sigma = \rho_p \cdot \frac{4}{3} \cdot \pi \cdot \left(\frac{D}{2}\right)^3 = 7850 \cdot \frac{4}{3} \cdot \pi \cdot \left(\frac{30 \cdot 10^{-6}}{2}\right)^3 \cong 0.1\,\mu\text{gr}$ (one tenth of a microgram). Therefore, particle's inertia is infinitesimal and the only forces left to govern particle's motion are the solid frictional forces. This is shown indirectly in figure 2.11.

Figure 2.11 shows the calculated speeds V_{p1} and V_{p2}, which are the speeds of the particle relatively to surface 1 and 2 respectively (see equations (2.45) and (2.46), noting that $\underset{\sim}{V}_{p1} = -\underset{\sim}{V}_{1p}$). The extrusion speed, which is the speed of particle's lateral expansion due to its compression (equations (2.48) and (2.52)), is also shown in the figure for comparison with the other two speeds. As is obvious in this figure, the particle sticks to surface 1 ($V_{p1} = 0$) immediately after being pinched and slides on the other surface with a constant speed, which is equal to the sliding speed of the contact ($V_{p2} = V_{12}$). This is a direct effect of the application of the high solid frictional forces, in combination with the fact that all other forces are much weaker. As a result, the particle experiences a very high acceleration at the moment it is first pinched and, essentially, sticks to the surface with the higher friction coefficient (surface 1) almost instantaneously.

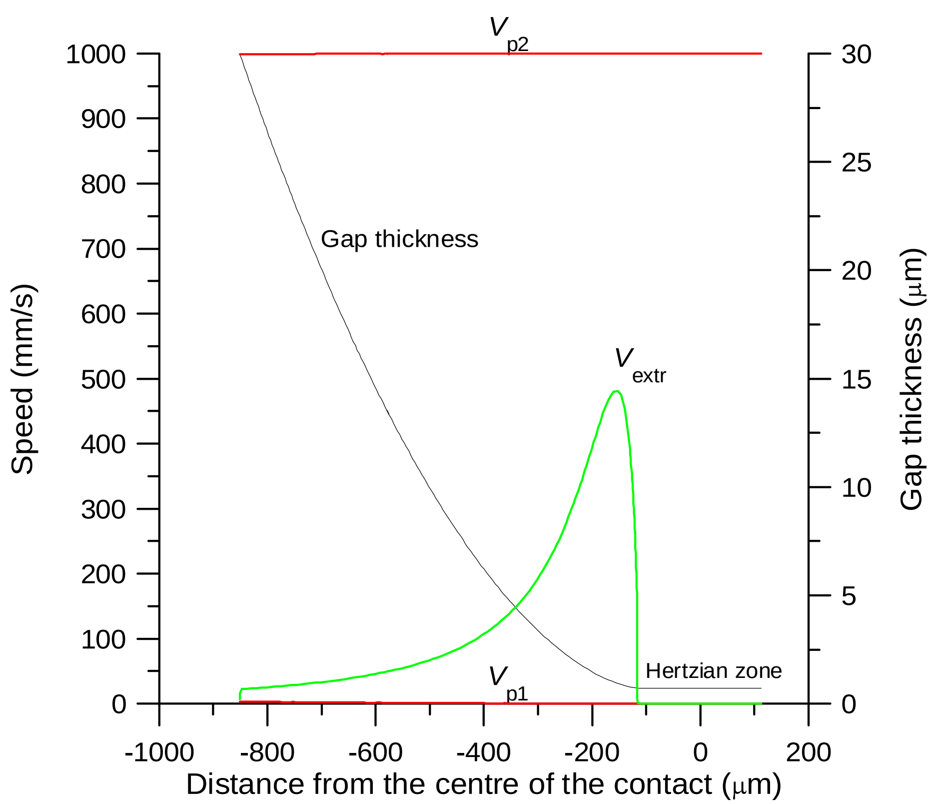

Figure 2.11 Relative sliding and extrusion speeds of the particle during its motion inside the elastohydrodynamic gap.

As a matter of fact, the sticking of the particle to one counterface and ploughing on the other has been experimentally observed by, for example, Williams and Hyncica (1992), Dwyer-Joyce *et al.* (1994), Nicolson (1996, p. 127 in his Thesis), Hamilton *et al.* (1998), and many others. If the counterfaces are assumed rigid, then the particle will obviously stick to the counterface with the higher friction coefficient. This is exactly the result derived when applying the present model. On the other hand, if the counterfaces are considered deforming, the sticking of the particle to one counterface or to the other, or even to both, depends additionally on the relative hardness of the counterfaces and the particle, and all possibilities are open. However, for counterfaces with equal hardness and particles that are moderately soft, particle sticking to the counterface with the higher friction coefficient is the result obtained from the advanced model of the last chapter of this Thesis, where surface deformations and many other factors are taken into account.

Experience suggests however that in many situations, particles appear to stick to the faster moving surface, even if the faster moving surface may have a lower friction coefficient than the slower moving surface. For example, this principle is applied in callendering processes such as grease conditioning for low noise bearings and food processing. This behaviour may be attributed to the fact that, oil and (especially) grease or other semi-solid/liquid substances tend to stick to the faster moving surface. An interesting discussion can be found in Dawson and Coyle (1969), where the authors were unable to reassuringly explain why a small piece of plasticine, when introduced into the inlet of the contact between two discs, rotating at different speeds, was always sticking to the faster disk, even when the speeds of the two discs were reversed (the faster became the slower). Nevertheless, the authors speculated that "*…since a greater length of the surface of the faster disc passed through the contact in any interval of time, the Plasticine stuck to the faster disc because there was potentially a greater area for adhesion*.". Although this hypothesis sounds promising, the experimental evidence collected by Dawson and Coyle did not provide sound proof for its validity and left some unanswered questions.

It is beyond the scope of this Thesis to explain the latter phenomenon. The typical soft particle of this study (100 HV) is significantly harder than a "*small piece of Plasticine*" and it becomes harder during its severe plastic compression in the contact due to strain hardening. It is interesting to note that Dawson and Coyle reported that the direction of transfer of “their” Plasticine depended on the materials used, when the two discs were made of different materials (for example: aluminium for one disc and copper for the other). In other words, the semi-solid substance (Plasticine) could very well adhere to the slower surface when the two discs were of different material.

In the particular case of this Thesis, by entering the outlet zone of the contact, the particle has to decide which surface to follow and it is rather clear that it will prefer the surface that carries most of the sticky substance, because the particle itself is usually attracted to the substance. For the particle to eventually adhere to the faster moving surface is by no means proof that the particle followed the faster moving surface all along the inlet and the Hertzian zone of the contact. The model presented in this chapter simulates the motion of the particle only in the inlet and Hertzian zone of the contact and is obviously not involved with what happens in the outlet zone. However, another explanation that could be applied in some cases is presented in the example of chapter 5 and is basically associated with the possible melting of debris due to the high frictional heat caused by their shearing in an elastohydrodynamic gap, as is shown in chapters 3 and 5. Nevertheless, possible melting of the particle would mark the end of the current analysis, because, at that point, the particle has already caused the greatest harm it could possibly do to the counterfaces.

2.9 Conclusions

The example of section 2.8 is representative of the kind of results derived from the model developed in this chapter. The theoretical simulation of the entrapment and motion of a ductile and soft debris particle in an elastohydrodynamic contact, has led to a plethora of important conclusions, most of which have been experimentally verified. A summary of these conclusions follows below.

(a) The likelihood of entrapment of a particle in an elastohydrodynamic contact depends mainly on the friction coefficients of the counterfaces, the geometry of the deformed contact (central film thickness and radii of curvature in the inlet zone), and the size of the particle. If there is sliding in the contact and one of the counterfaces is stationary (not moving towards the centre of the contact), then even if a particle is initially “accepted” in the contact, the reversal of the direction of one of the solid frictional forces on it may change the situation, resulting in a temporary particle rejection. The same mechanism is proposed in Wan and Spikes (1988). In the latter case, it is speculated that the particle will undergo a “micro-forging” process and, if it is sufficiently soft, it will be plastically deformed to the point its thickness is reduced, allowing it to enter deeper inside the elastohydrodynamic gap, until it becomes irreversibly trapped. This kind of behaviour may result in lubricant starvation because the particle (and possibly other particles that gather around it) stands as an obstacle in the oil replenishment of the contact. All this is analyzed in section 2.3.

(b) There is a fluid drag force on the particle, which comprises two components. The first component is due to the elastohydrodynamic static-pressure gradient in the contact (see sub-section 2.5.1). The second component is due to the dynamic pressure of the lubricant on the particle, because the particle distorts the streamlines of the flow (see sub-section 2.5.2). Both of these components are usually very small and do not contribute to the motion of the particle inside the elastohydrodynamic gap (see figure 2.10 and table 2.5). However, their role may become significant in some circumstances, and contribute to the temporary or final rejection of a particle from a contact. Such circumstances involve generally the following two cases.
    - Sliding contacts where one counterface is stationary and has a friction coefficient higher than the friction coefficient of the other (moving) counterface.
    - Sliding contacts and small particles, in cases where the central film thickness is relatively large and the elastohydrodynamic pressure is high.

(c) The solid frictional forces between the particle and the counterfaces are usually significantly higher than the fluid drag forces (figure 2.10). Due to the low magnitude of the fluid drag forces as well as the small inertia of the particle, owing to its infinitesimal mass, the two solid frictional forces are almost equal to each other (figure 2.9) and are the prevailing forces which govern the motion of the particle inside the elastohydrodynamic gap.

(d) If the particle is entrapped, it sticks to the counterface with the higher friction coefficient (which is usually the softer), immediately after being pinched (see figure 2.11). This is true even if the difference between the friction coefficients of the two counterfaces is relatively small, as for example, of the order of 0.01. Experimental verification for the sticking of the particle to one counterface can be found, for example, in Williams and Hyncica (1992), Dwyer-Joyce *et al.* (1994), Nicolson (1996), and Hamilton *et al.* (1998). However, the reader is advised to read the comments in the last paragraph of section 2.8.

(e) Soft and ductile particles are flattened and become thin, roughly circular disks as they are plastically deformed (see section 2.4). Experimental verification for this behaviour can be found in, for example, Wan and Spikes (1988), Dwyer-Joyce *et al.* (1992), Nelias *et al.* (1992), Dwyer-Joyce (1993), and in others. The circularity of the deformed particles depends on the amount of sliding in the contact. For high sliding conditions, deformed particles are expected to acquire a rather elliptical shape.

CHAPTER 3

THERMAL MODELLING OF THE FRICTIONAL HEATING BETWEEN A SOFT PARTICLE AND THE COUNTERFACES IN AN ELASTOHYDRO-DYNAMIC LINE CONTACT

3.1 Introduction

In chapter 2, it is shown that a particle entering an elastohydrodynamic contact encounters some degree of sliding with the counterfaces. This is obviously expected when there is sliding in the contact, which happens when the counterfaces have different tangential speeds. However, even in the case when the contact is a purely rolling one, there is still relative sliding between the particle and the counterfaces, owing to the plastic compression of the particle, which results in its lateral expansion. The latter is expressed by the extrusion speed of the particle, as is analyzed in section 2.7 (see equation (2.52) and figure 2.11). Because of this relative sliding, there is friction between the particle and the counterfaces, which produces heat. This heat is absorbed from the particle, the counterfaces and the lubricant in variable proportions, defined by the thermal properties of the elements involved in the process. Moreover, heat is produced inside the particle, owing to its plastic deformation. There is also a rather small amount of heat produced due to the rapid elastic/plastic displacement of the counterfaces in the area where the particle resides. The latter is better known with the term "*volumetric effects*" in the case where there are plastic deformations involved. Volumetric effects include two sources of plastic deformation (Kennedy, 1984).

(a) Ploughing of hard surface asperities through the surface of a softer material (Bowden and Tabor, 1986).

(b) Near surface plastic deformation owing to adhesive surface tractions (Rigney and Hirth, 1979).

Protasov and Kragelskii (1982) developed a molecular-mechanical model of friction interactions and estimated that for copper sliding against steel (this example is of particular importance in the present study where the particles are much softer than the counterfaces), 85 % of the frictional energy is dissipated by volumetric processes, especially by plastic deformation. However, this estimate may be low because the example is concentrated on dry rather than lubricated contacts.

If most of the frictional energy is dissipated at the upper surface layers as plastic deformation, then the obvious question is *what happens* to that energy. Numerous studies (see for example Uetz and Föhl (1978), and McLean (1962)) have indicated that around 95 % of the plastic deformation energy is transformed into thermal energy - in other words, it is dissipated as heat. This takes place at the top surface layers, within a few microns beneath the surface.

Frictional heating is often responsible for significant temperature increase of sliding bodies. The temperature increase, which is known as *flash* temperature (temperature increment above the bulk temperature), plays an important role in the reliability of the sliding components, especially in terms of scuffing and fatigue. High skin temperatures affect the way in which wear is developed and can also be responsible for increased oxidation, corrosion and other structural changes, either microscopically or macroscopically (see for example Earles and Powell, 1967). Sliding surface temperatures can be detected experimentally and predicted analytically.

Experimental methods involve the following techniques (Kennedy, 1984).

(a) Embedded subsurface thermocouples. This method is best suited for the measurement of bulk temperatures rather than the actual contact temperatures.

(b) Dynamic thermocouples.

(c) Contact thermocouples.

(d) IR (infrared) techniques. These involve the detection of IR radiation by focusing an IR detector (pyrometer) either at the outlet region of a contact or directly on the contact zone. Alternatively, an IR sensitive film can be used to obtain photographs or movies of the contact zone. These methods are considered to be among the most accurate.

(e) Metallographic techniques. These concentrate on the examination of the microstructure of the top surface layers of worn specimens, for example, through micro-hardness measurements.

For more information and references on the previous techniques, the reader is directed to the excellent paper of Kennedy (1984).

Experimental techniques sometimes fail to give reassuringly accurate measurements of the real contact-temperatures, mainly due to the fact that the contact is a rather inaccessible area, comprising a number of small contact spots within the "macroscopic" contact area, which vary in number and location, the variation being rapid and very difficult to simulate (as in a random process). Those contact spots encounter temperatures that are much higher than the temperatures in closely situated regions, as has been shown in analytical simulations and verified in experiments. For example, Griffioen *et al.* (1986) showed experimentally (using an infrared scanning camera) that the dry contact temperature of asperities of a silicon nitride pin sliding against a sapphire disk can be as high as 2700 °C, concentrated in areas of about 100 μm in diameter. Wolf (1991) showed experimentally (using an IR technique) as well as analytically that the local temperature between sliding asperities (in longitudinal roughness) in a lubricated contact could be as high as 1500 °C. Quinn and Winer (1985) reported flash temperatures of the order of 1200 °C in contact spots of about 50 μm in diameter on the surface of a steel pin sliding on a sapphire disk and photographed those elusive hot spots (see figure 3 of their paper). The interesting observation in the latter study was that the duration of the radiating hot spots was in the order of 1 ms.

Due to the difficulties and inaccuracies in experimental studies of flash temperatures, the problem is often better approached analytically. Important analytical work has been initiated by Blok (1937a) and Jaeger (1942). They both simplified the problem by studying the equations associated with a single point or band source of heat, later extending their horizon to include a wider variety, like a circular and a square or rectangular heat source of either constant or variable strength. Those initial studies have undergone extensive testing during the past 50 years with improved methodologies and have proved to be surprisingly accurate, despite the assumptions used to produce them, as is explained in detail later.

It is now clear that extreme heat conditions can often be expected in sliding contacts, when the pressures and/or sliding speeds are relatively high. Consequently, thermal failure of a contact is a possibility that must be studied as part of the design of Machine Elements, like gears, cams and followers etc. Even if the frictional heating is not solely responsible for a failure, the thermal stresses due to this heating must, in many cases, be superposed to the mechanical stresses (for example, due to particle's plastic compression in the contact) in order to assess the true risk of any damage. It is generally accepted that roughness asperities can cause high temperature increments; then it also follows that debris particles, which are usually bigger than roughness asperities, could produce similar, or even more severe, thermomechanical effects, albeit affecting larger areas than in the case of two engaging asperities.

This possibility has been given minimal attention in the literature. Almost all published studies are confined to isothermal contacts, which are modelled as a slow compression process (see for example Hamer *et al.* (1989b), and Ko and Ioannides (1989)). At the time of writing this Thesis, the author is aware of only one publication dealing with the theoretical modelling of flash temperatures produced by the sliding of debris particles in concentrated contacts (Khonsari and Wang, 1990). In the latter publication, the authors attempt to relate abrasive particles and scuffing failure, by postulating that if the flash temperatures owing to particle frictional heating exceed a specific value, then scuffing takes place.

As is well-known, scuffing (known as "scoring" or "galling" in America), is a form of catastrophic wear, which, in lubricated contacts, is associated with sudden lubricant film breakdown and metal-to-metal contact. Scuffed surfaces appear to be thermally distorted, with clear evidence of material melting. Although there is a lot of controversy regarding the probable mechanisms responsible for the onset of scuffing, experimental findings support the idea that scuffing is a debris-sensitive phenomenon (see Chandrasekaran *et al.* (1985), who found that systems, which operate safely with clean oil, can fail when the oil becomes contaminated, and the mode of such failure resembles scuffing). The idea behind a particle-related onset of scuffing has been proposed by Enthoven and Spikes (1995), who found that for a purely sliding contact of a steel ball and a sapphire disk, "*…the onset of scuffing is* *always preceded by the build-up of fine particles of wear debris in the contact inlet which result in starvation and consequently scuffing.*”.

In the first chapter of this Thesis, it is shown how the accumulation of particles in the inlet zone of a contaminated elastohydrodynamic contact can occur and be a likely cause of lubricant starvation. Poor lubrication and bad contact replenishment are reported to result in sudden film breakdown, which is then followed by increased wear and, depending on the load and sliding speed, in scuffing.

In addition, as explained above, sliding roughness asperities may encounter high flash temperatures, which could be high enough as to cause material melting or at least tempering reactions and metallurgical changes in the materials involved. Consequently, it may be assumed that debris particles, which resemble sliding roughness asperities in two-body contacts, may be responsible, under specific conditions, for high frictional heating and scuffing-like wear mechanisms. This has been suggested by Chandrasekaran *et al.* (1985), based on experimental results regarding scuffing tests in 4-ball machines.

The present chapter sets the foundation to test the hypothesis of the possible association between lubricant contamination particles and scuffing in elastohydrodynamically lubricated contacts. This is done on a purely theoretical level, and the proposed model is developed mainly for soft and ductile particles, which, in the modern literature, are considered much safer than hard particles, for obvious reasons. Nevertheless, it is later shown that even soft particles can be responsible for high flash temperatures in lubricated contacts, and that there exists a rather hidden mode of <u>local</u> scuffing, which may explain some of the wear observed in failed contaminated contacts.

3.2 Frictional heating caused by a soft particle in a lubricated contact

In this section, a model of the frictional heating process, due to the squashing of a debris particle in an elastohydrodynamic contact, is developed for soft and ductile particles. The model is made as general as possible, involving the following.

- 3-dimensional flash temperature and thermoelastic stress calculations for both counterfaces.
- Internal heating of the particle due to its rapid plastic compression.
- Counterface cooling due to convection to the lubricant.
- Particle cooling due to convection to the lubricant.
- Temperature-dependent mechanical and thermal material properties of all bodies.
- Thermal anisotropy of both counterfaces.

As is explained in section 2.4, a soft and ductile particle is modelled as a cylinder, immediately after its entrapment (figure 2.5). That cylinder collapses progressively due to the plastic compression inside the elastohydrodynamic gap, and adopts a rather circular disk shape at the final stage of its deformation, inside the Hertzian zone of the contact. Because of particle's friction with the counterfaces, the particle resembles a heat source of variable strength. It is worth noting here that soft particles defer from hard particles when squashed, in that the area covered by a soft particle when fully compressed in order to pass through an elastohydrodynamic gap is quite larger than the corresponding area covered by a hard particle. For the example analyzed in section 2.8, a 30 μm soft (100 HV) particle becomes a 160 μm disk (see table 2.4 and figure 2.8) when forced to pass through an elastohydro-dynamic contact with a central film thickness equal to 0.7 μm. Treating the particle as a single heat source may not be particularly valid and the variable pressure and, hence, variable heat source strength on the facial surfaces of the particle, *must* be properly accounted for.

To simulate this variable strength, the particle is divided in a number of point sources of heat. This is achieved by dividing each of the two faces of the particle, namely the top and bottom base of the equivalent cylinder (figure 2.5), into a series of concentric rings (tracks), which are further divided into a series of elemental segments, called sectors, as is shown in figure 3.1. Each of these sectors is represented by a point source of heat. The velocity of each sector, relative to a space-fixed coordinate system (earth) has two components.

(a) A sliding component V_{slid} due to the sliding motion of the particle as a rigid body, relatively to surface 1 or 2 (either $V_{\text{slid}} = V_{\text{p1}}$ or $V_{\text{slid}} = V_{\text{p2}}$, see the nomenclature for chapter 2).

(b) An extrusion component, owing to the local extrusion speed of the particle (equation (2.52)).

Axis x in figure 3.1 coincides with the direction of rolling/sliding in the contact. Using axes x and y as shown in figure 3.1, the resultant velocity of a sector is analyzed in two components V_{x} and V_{y} as follows:

$$\left.\begin{aligned} V_{\text{x}} &= V_{\text{slid}} - V_{\text{extr}} \cdot \cos(\vartheta) \\ V_{\text{y}} &= V_{\text{extr}} \cdot \sin(\vartheta) \end{aligned}\right\} ,0 \le \vartheta \le 2 \cdot \pi \tag{3.1}$$

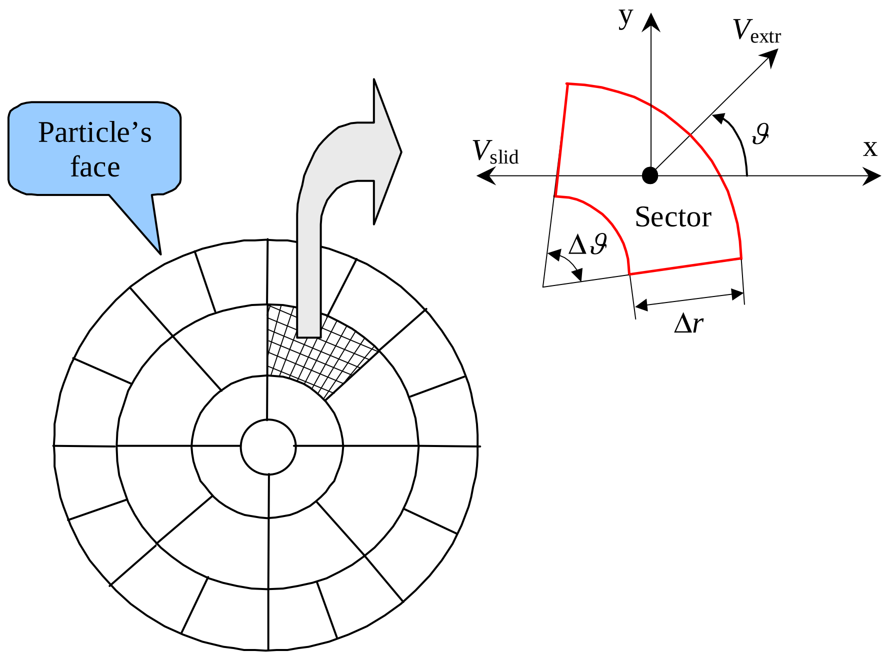

Figure 3.1 Particle segmentation for the thermal model.

Angle ϑ is measured starting from the positive part of axis x. The resultant speed of a sector is:

$$V = \sqrt{V_x^2 + V_y^2} \tag{3.2}$$

The heat generated due to friction between a sector and a counterface is:

$$q = \alpha \cdot \mu \cdot V \cdot p \cdot r \cdot \Delta\vartheta \cdot \Delta r \tag{3.3}$$

where α is the heat partition coefficient, μ is the friction coefficient between the particle and a counterface, p is the solid pressure on the particular sector, and r is the distance of the sector from the centre of the particle.

The differential equation of heat conduction

$$\frac{\partial^2\theta}{\partial x^2} + \frac{\partial^2\theta}{\partial y^2} + \frac{\partial^2\theta}{\partial z^2} = \frac{1}{\lambda} \cdot \frac{\partial\theta}{\partial t} \tag{3.4}$$

where θ is temperature, t is time and λ is thermal diffusivity, is satisfied by

$$\theta = \frac{Q}{8 \cdot (\pi \cdot \lambda \cdot t)^{3/2}} \cdot \exp\left[-\frac{(x - x')^2 + (y - y')^2 + (z - z')^2}{4 \cdot \lambda \cdot t} \right] \tag{3.5}$$

where Q is the "strength" of the heat source (Carslaw and Jaeger, 1959). Solution (3.5) can be interpreted as the temperature at position (x,y,z) in an infinite solid due to a quantity of heat $Q \cdot \rho \cdot c$ (ρ being the material density and c being the specific heat), instantaneously generated at time $t = 0$ at a point (x',y',z'). Equation (3.5) gives the temperature due to an instantaneous point source of heat.

Allowing the thermal properties to vary with direction (not temperature-related variations), materials which are thermally anisotropic can be studied. Although this is not expected to alter significantly the temperature fields in the counterfaces, it will certainly distort them (even slightly). Changing the temperature distributions results in changes in the thermal and overall stress distributions. The latter is of particular importance during the study of fatigue and the risk of plastic deformations as is shown in chapter 5. In any case, the concept of thermal anisotropy is incorporated in this analysis mainly for reasons of completeness, and it is fully applied in the example of chapter 5.

Introducing complete thermal anisotropy in the heat conduction equation, results in a complicated, non-linear, partial differential equation, involving cross derivatives of the spatial variables x, y and z. This can be simplified considerably by assuming that the materials are thermally orthotropic. The latter means that these materials have three planes, perpendicular to each other, which are planes of material symmetry. The thermal properties of a thermally orthotropic material are the same in directions symmetrical about the principal planes of thermal orthotropy. (An example of a *mechanically* orthotropic material is a cold-rolled metallic sheet.)

Thankfully, the assumption of orthotropy is a good approximation of the behaviour of carbon steels (the material used for the counterfaces throughout this Thesis), which belong to the cubic atomic system. Alloys of steel, especially after heat treatment, may not have a cubic-system atomic structure. However, the assumption of orthotropy is still a good compromise.

The heat conduction equation for an orthotropic medium is written as follows:

$$K_\mathrm{x} \cdot \frac{\partial^2 \theta}{\partial x^2} + K_\mathrm{y} \cdot \frac{\partial^2 \theta}{\partial y^2} + K_\mathrm{z} \cdot \frac{\partial^2 \theta}{\partial z^2} = \rho \cdot c \cdot \frac{\partial \theta}{\partial t} \tag{3.6}$$

where K_x, K_y and K_z are the principal thermal conductivities in the directions of axes x, y and z respectively. Using the transformation

$$X = x \cdot \sqrt{\frac{K_\mathrm{x}}{K}} \quad , \quad Y = y \cdot \sqrt{\frac{K_\mathrm{y}}{K}} \quad , \quad Z = z \cdot \sqrt{\frac{K_\mathrm{z}}{K}} \tag{3.7}$$

(see for example Özisik, 1993), where

$$K \equiv \left(K_\mathrm{x} \cdot K_\mathrm{y} \cdot K_\mathrm{z}\right)^{1/3} \tag{3.8}$$

equation (3.6) gives

$$\frac{\partial^2\theta}{\partial X^2}+\frac{\partial^2\theta}{\partial Y^2}+\frac{\partial^2\theta}{\partial Z^2}=\frac{1}{\lambda}\cdot\frac{\partial\theta}{\partial t} \tag{3.9}$$

whereas

$$\lambda \equiv \left(\lambda_\mathrm{x}\cdot\lambda_\mathrm{y}\cdot\lambda_\mathrm{z}\right)^{1/3} \tag{3.10}$$

and λ_x, λ_y and λ_z are the principal thermal diffusivities in the directions of axes x, y and z respectively, defined as

$$\lambda_i=\frac{K_i}{\rho\cdot c} \quad ,i\leftrightarrow x,y,z \tag{3.11}$$

The transformed equation (3.9) is of the same form as equation (3.4) and, hence, it has a solution of the form (3.5). Using equation (3.5) and transforming back to the original coordinates *x*, *y* and *z*, the solution of the "anisotropic" equation (3.6) is finally written as follows:

$$\theta=\frac{Q}{8\cdot(\pi\cdot\lambda\cdot t)^{3/2}}\cdot\exp\left\{-\frac{1}{4\cdot t}\cdot\left[\frac{(x-x')^2}{\lambda_\mathrm{x}}+\frac{(y-y')^2}{\lambda_\mathrm{y}}+\frac{(z-z')^2}{\lambda_\mathrm{z}}\right]\right\} \tag{3.12}$$

The flash temperature at time *t*, at point (*x*,*y*,*z*), due to the heat $q\cdot\mathrm{d}t'$ emitted at time t' at surface point $(\bar{x},\bar{y},0)$ of a semi-infinite medium, can now be calculated by the following expression:

$$\frac{q\cdot\mathrm{d}t'}{4\cdot\rho\cdot c\cdot[\pi\cdot\lambda\cdot(t-t')]^{3/2}}\cdot\exp\left\{-\frac{1}{4\cdot(t-t')}\cdot\left[\frac{(x-x_V-\bar{x})^2}{\lambda_\mathrm{x}}+\frac{(y-y_V-\bar{y})^2}{\lambda_\mathrm{y}}+\frac{z^2}{\lambda_\mathrm{z}}\right]\right\} \tag{3.13}$$

The point of the medium, which at time *t* is at position (*x*,*y*,*z*), at a past time t' was at position $(x-x_V, y-y_V, z)$, where

$$x_V = \int_{t'}^{t} V_{\mathrm{x}} \cdot \mathrm{d}t' \quad \text{and} \quad y_V = \int_{t'}^{t} V_{\mathrm{y}} \cdot \mathrm{d}t' \tag{3.14}$$

Moreover,

$$\bar{x} = r \cdot \cos(\vartheta) \quad \text{and} \quad \bar{y} = r \cdot \sin(\vartheta) \tag{3.15}$$

It must be noted that equations (3.5) and (3.12) refer to an infinite medium whereas expression (3.13) refers to a semi-infinite medium. Therefore, the temperature in the semi-infinite-medium case is double the temperature of the infinite-medium case, as can be realized from the dividers used; 4 for the former and 8 for the latter.

Before integration in time and space, integration steps Δr and $\Delta\vartheta$ must be defined. Using a constant number of tracks N_{t} (for example $N_{\mathrm{t}} = 50$), it is defined that

$$\Delta r \mathrel{\hat{=}} \frac{R}{N_{\mathrm{t}}} \tag{3.16}$$

where R is the radius of the deformed particle (see equation (2.20)). Since radius R varies during the deformation of the particle, the spatial step Δr varies, too. The angular step $\Delta\vartheta$ is defined as

$$\Delta\vartheta \mathrel{\hat{=}} \frac{\Delta r}{r} \tag{3.17}$$

The previous definition means that there are more sectors on an outer track than on an inner one. The number of sectors N_{s} on a track can then easily be found:

$$N_{\mathrm{s}} = \left[\frac{2 \cdot \pi \cdot r}{\Delta r} \right] \tag{3.18}$$

where the brackets in the previous equation denote the integer part of the enclosed expression.

The temperature θ at time t, at point (x,y,z) of the medium, is finally given by the following equation:

$$\theta = \theta_0 + \frac{\mu}{4 \cdot \rho \cdot \pi^{3/2}} \cdot \int_0^t (\Delta r)^2 \cdot \sum_{i=1}^{N_t} p_i \cdot \sum_{j=1}^{N_s} \frac{\alpha \cdot V \cdot [\lambda \cdot (t - t')]^{-3/2} \cdot \mathrm{d}t'}{c \cdot \exp\left\{ \frac{1}{4 \cdot (t - t')} \cdot \left[\frac{(x - x_V - \bar{x})^2}{\lambda_x} + \frac{(y - y_V - \bar{y})^2}{\lambda_y} + \frac{z^2}{\lambda_z} \right] \right\}} \tag{3.19}$$

where θ_0 is the initial temperature, which is considered the same throughout the bodies and equal to the bulk temperatures.

Heat partitioning, surface cooling and other related subjects are studied and modelled in the following sections. It is noted that the analysis of this section does not account directly for temperature-dependent thermal properties of the materials taking part in the heating process. This is imposed through corrections of the results by means of a correction loop in the computer code, as is explained later (section 3.7 and chapter 5).

3.3 Heat generation inside the particle

The model is developed for soft and ductile particles, as is explained in chapter 2. Therefore, the particle can be considered behaving as a rigid-perfectly-plastic solid. At the time when the particle starts to deform, it shears internally. To simplify the analysis, the shearing is assumed to take place on one plane, which can suitably be chosen as the mid-plane of the equivalent cylinder, as is shown in figure 3.2. Although a different shearing profile (shearing surface inside the particle) could be chosen, taking into account that the particle sticks to one counterface and shears on the other, this choice is not of particular importance because, as is shown in the example of chapter 5, the heat generated inside the particle accounts for only about 1 % of the maximum flash temperature of both counterfaces. Therefore, the temperature changes induced by choosing different shearing surfaces inside the particle would be negligible.

The friction coefficient between the two relatively sliding material-layers at that plane and the solid pressure on the particle are then related through the following equation:

$$\mu_{\text{int}} \cdot p = k_{\text{p}} \tag{3.20}$$

where k_p is the yield stress of the material of the particle in simple shear.

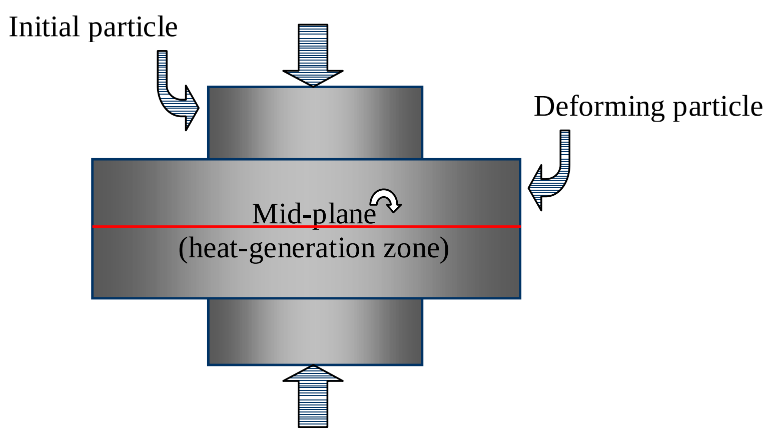

Figure 3.2 Heat generation inside the particle.

The internal frictional heat for any sector is

$$q_{\text{p}} = \mu_{\text{int}} \cdot p \cdot V_{\text{extr}} \cdot r \cdot \Delta\vartheta \cdot \Delta r = k_{\text{p}} \cdot V_{\text{extr}} \cdot \frac{R^2}{N_{\text{t}}^2} \tag{3.21}$$

(using equations (3.16), (3.17) and (3.20)). From equations (3.21) it is seen that there are two variables that define the level of internal particle heating (heat per unit area of a sector, q_p/R^2): the extrusion speed and the particle's yield stress in simple shear (k_p). The extrusion speed varies as the particle moves in the inlet zone of the contact and is practically zero inside the flat Hertzian zone (see figure 2.11). Literally speaking, the extrusion speed is slightly greater than zero inside the Hertzian zone of the contact due to the thermal expansion of the counterfaces as the passing particle heats them up, but this movement is infinitesimal to make any noticeable difference in the results (although this is taken into account in the calculations). On the other hand, k_p is temperature dependent, but its contribution in altering q_p is much smaller than the contribution of the extrusion speed in the inlet zone of the contact. Nevertheless, temperature-dependent properties are a fact, and this is taken fully into account in all calculations, as is explained in section 3.7.

Conclusively, q_p depends largely on the extrusion speed. Finally, integration throughout the base area of the particle (taking into account the variable solid pressure on the particle) gives the total amount of heat, which is generated internally.

3.4 Heat partition

The heat produced due to friction between the particle and the counterfaces is partitioned between the particle and the counterfaces in proportions, which are defined by the thermal properties of the materials involved in the process. The subject of partitioning of the frictional heat produced between two relatively sliding surfaces has been studied for several decades and there are, basically, two methods to estimate a heat partition coefficient. The first method, due to Blok (1937a, 1937b) is to equate the *maximum* temperatures in the contact zone of two cooperating surfaces, assuming equal bulk temperatures. The second method, due to Jaeger (1942), is, similarly, to equate the two *average* temperatures in the contact zone (again for equal bulk temperatures). Archard (1958) used a rather hybrid method by assuming successively that all of the produced heat goes to each of the rubbing surfaces and calculated an average contact temperature by interpolating the two results using the parallel (electric analogue) model.

A more accurate approach is to match the temperatures of all integration points inside the contact. This leads to a significantly complicated and time-consuming analysis, involving the solution of integral equations (see for example Cameron *et al*., 1964, and Bos and Moes, 1994). However, as Barber (1970) points out, the solutions of Blok and Jaeger are remarkably accurate when compared with corresponding integral solutions, and hence, can be used when accuracy is not of the utmost importance.

The heat partition depends on the sliding speed between the two rubbing surfaces, as well as on the thermal properties of the surfaces and the shape and dimensions of the heat source. Firstly, the following parameter is defined:

$$\beta_{\mathrm{p}} \triangleq \frac{V \cdot \Delta r}{4 \cdot \lambda_{\mathrm{p}}} \tag{3.22}$$

where λ_{p} is the thermal diffusivity of the material of the particle. Assuming perfect thermal contact between the contacting bodies (particle and counterfaces) and a square heat source, the heat partition coefficient can be calculated by the following equations:

$$\alpha_i = \frac{K_i}{K_i + K_{\mathrm{p}}} \quad \text{, if } \beta_{\mathrm{p}} \leq 0.1 \quad , (i = 1, 2) \tag{3.23}$$

$$\alpha_i = \frac{K_i}{K_i + 0.8644 \cdot K_{\mathrm{p}} \cdot \sqrt{1 + \beta_{\mathrm{p}}}} \quad \text{, if } 0.1 < \beta_{\mathrm{p}} < 5 \quad , (i = 1, 2) \tag{3.24}$$

$$\alpha_i = \frac{K_i}{K_i + 1.2918 \cdot K_{\mathrm{p}} \cdot \sqrt{\beta_{\mathrm{p}}}} \quad \text{, if } \beta_{\mathrm{p}} \geq 5 \quad , (i = 1, 2) \tag{3.25}$$

where index i refers to the surface to which a proportion α_i of the total heat is transferred and K_{p} is the thermal conductivity of the material of the particle. The completeness of thermal contact is guaranteed by the high pressures developed between the particle and the counterfaces, which are of the order of a few hundred MPa for soft particles and up to a few GPa for hard particles. Such high pressures lead to boundary films between the particle and the counterfaces, which are of the order of nanometers. For interfacial temperatures higher than about 150 °C, the aforementioned lubricant films are known to collapse due to adsorption or melting, which results in higher friction coefficients and even more intimate contact, similar to the case of a dry contact (see for example Russell *et al.* (1965), and Lai and Cheng (1985)).

The quoted heat-partition equations (3.23)-(3.25) refer to a square heat source, as already mentioned. These equations are applied to each sector of the particle. A sector has polar dimensions Δr and $r \cdot \Delta\vartheta$ (figure 3.1). The choice of the angular step $\Delta\vartheta$ (see equation (3.17)) was intentional in order to produce a more-or-less square sector: $(r \cdot \Delta\vartheta) \cdot \Delta r = (r \cdot \Delta r / r) \cdot \Delta r = \Delta r \cdot \Delta r$.

Equations similar to (3.23) and (3.25) are used extensively in modern literature and originated from the preliminary analyses of Blok and Jaeger. Equation (3.24) is an interpolation result based on the initial graphs of Jaeger (1942), the interpolation done by Greenwood (1991).

A question comes on surface when considering that the bodies participating in the study (the counterfaces and – especially – the particle) are not semi-infinite. The assumption of infinity was fundamental in deriving the heat partition equations quoted earlier. The problem of infinity is related to the bulk temperature rise due to insufficient cooling and the limited heat capacity of the finite bodies. However, considering the minute dimensions of a debris particle in comparison with the dimensions of the two counterfaces and, especially, the very short duration of the frictional heating incident (of the order of 1 ms, as is shown in the examples to follow), the assumption of infinity is not expected to affect the results significantly. For example, in a typical case of two engaging gear teeth and a 20 μm particle, each tooth could typically have at least 60 million times the volume of the particle, excluding the tooth's foundation (gear body). Moreover, the engaging elements that squash the particle usually encounter heat losses at their boundaries, either by convection or by radiation. It is, therefore, safe to regard the counterfaces as large heat sinks. Similar considerations are reported by Tian and Kennedy (1993), who support the use of Blok's formulation for sufficiently accurate analyses. On the other hand, the particle is relatively small and becomes very thin as it enters the Hertzian zone of the contact. In the latter area, the thickness of the particle is of the order of the unperturbed average film thickness of the lubricated surfaces (usually less than 1 μm - see for experimental proof in Wan and Spikes (1988)). Therefore, the particle can be seen as a thin layer, incapable of storing any substantial amount of heat due to its limited heat capacity. Consequently, the particle behaves solely like an idealistic heat source. A case with great similarity to this description (albeit not particle related) was analyzed by Ryhming (1979). Further comments on this follow later. Conclusively, the analyses of Blok and Jaeger are adequate for the purposes of this study. It is interesting to mention at this point the work of Quinn and Winer (1985) on the thermal aspects of oxidational wear. In the previous paper, the importance of an always-present oxide film on the rubbing surfaces was made clear, as that film acts as that ever-elusive “interface” mentioned in many publications regarding the heat partitioning between sliding surfaces (see for example Johnson, 1985, section 12.4). The oxide films act as intermediaries in the division of the frictional heat between the sliding surfaces and their role has great similarity with the typical soft particle of this Thesis.

After the previous clarifications, the formulation can proceed by examining what happens to the heat that goes to the particle. As already explained, the particle has a very limited heat capacity due to its very small size. Hence, it cannot store significant amounts of heat. Moreover, as the particle approaches the centre of the contact, its thickness is obviously reduced, the pressure on it is obviously increased (figure 2.9) and, as a consequence (see equation (3.3)), the frictional heat is increased. Because of its very small thickness, the primary heat transfer mechanism inside the particle is one-dimensional conduction along the z-axis. Heat convection from the periphery of the particle to the counterfaces (which is modelled later) will be shown to be infinitesimal. Therefore, because of its

(a) very small thickness (looking like a thin layer)

(b) very small heat capacity, and

(c) complete thermal contact with the counterfaces (due to the high solid pressures),

the particle is visualized to behave like a heat source, transferring the heat, which is temporarily stored to it, back to the counterfaces (and to the lubricant). In the mathematical model of this chapter, the aforementioned temporary storage and back transfer is simulated as is shown in the following two steps.

Step 1:

From time $(t - \Delta t)$ to time t, a particle sector receives an amount of heat

$$q_{\mathrm{p,total}} = (1-\alpha_1)\cdot q_{\mathrm{p},1} + (1-\alpha_2)\cdot q_{\mathrm{p},2} + q_{\mathrm{p}} \tag{3.26}$$

where $q_{p,1}$ and $q_{p,2}$ are the amounts of frictional heat per sector, which are generated at the interfaces of the particle and counterfaces 1 and 2 respectively (calculated by equation (3.3)), a_1 and a_2 are the heat partition coefficients giving the proportion of frictional heat which goes to counterfaces 1 and 2 respectively, and q_p is the amount of heat (for the particular sector) generated inside the particle (see equation (3.21)).

Step 2:

During a time step Δt, in other words from time t to time $(t + \Delta t)$, the particle sector emits an amount of heat q_e, which is

$$q_e = q_{p,\text{total}} - \delta \cdot \left[q_{p,\text{conv}}\right]_{t^-} \tag{3.27}$$

where $q_{p,\text{conv}}$ is the heat lost from a peripheral sector of the particle by convection to the lubricant and δ is a parameter, defined as

$$\delta \mathrel{\hat{=}} \begin{cases} 0 \text{ , for an internal sector} \\ 1 \text{ , for a periheral sector} \end{cases} \tag{3.28}$$

As can be realized from equation (3.28), heat convection is assumed to affect only the peripheral sectors, whereas the inner sectors act as one-dimensional heat conductors along the z-axis, as was explained earlier.

The amount of heat q_e is shared between two opposing counterface sectors (sectors belonging to the two counterfaces) in proportions defined by a heat partition coefficient, derived from equations (3.23)-(3.25). If a_{22} is the fraction of the heat q_e that goes to a sector of counterface 2 (assuming the particle sticks to counterface 1), then, similarly to equations (3.22)-(3.25), the following equations are used:

$$\alpha_{22} = \frac{K_2}{K_2 + K_1} \qquad \text{, if } \beta_{12} \le 0.1 \tag{3.29}$$

$$\alpha_{22} = \frac{K_2}{K_2 + 0.8644 \cdot K_1 \cdot \sqrt{1+\beta_{12}}} \qquad \text{, if } 0.1 < \beta_{12} < 5 \tag{3.30}$$

$$\alpha_{22} = \frac{K_2}{K_2 + 1.2918 \cdot K_1 \cdot \sqrt{\beta_{12}}} \qquad \text{, if } \beta_{12} \geq 5 \tag{3.31}$$

where

$$\beta_{12} \equiv \frac{V_{12} \cdot \Delta r}{4 \cdot \lambda_{z,1}} \tag{3.32}$$

whereas $\lambda_{z,1}$ is the principal thermal diffusivity of counterface 1 in the z-axis. Therefore, counterface 2 receives an amount of heat equal to $a_{22} \cdot q_e$, whereas counterface 1 receives the remaining amount $(1 - a_{22}) \cdot q_e$. As has already been shown (see figure 2.11), the particle always sticks to one counterface and slides on the other. Hence, it acts like a protuberance, but with different mechanical and thermal properties compared with the surface to which it sticks.

In conclusion, here follow the amounts of heat (per sector) q_1 and q_2, which are transferred to counterfaces 1 and 2 from time t to time $(t + \Delta t)$:

$$q_1 = \alpha_1 \cdot q_{p,1} + (1 - \alpha_{22}) \cdot q_e \tag{3.33}$$

$$q_2 = \alpha_2 \cdot q_{p,2} + \alpha_{22} \cdot q_e \tag{3.34}$$

3.5 Heat losses due to convection from the particle to the lubricant

The frictional heat transferred to the counterfaces and the particle is further partly transferred to the lubricant through convection. The particle loses heat from its periphery, since both of its faces are in intimate contact with the counterfaces. In the present section, a rough estimation of the heat losses to the lubricant is attempted by assuming that the temperature of the lubricant is constant throughout the solution domain, and equal to the bulk temperature of the solids, although this can be varied in the simulation. In reality, the lubricant is heated due to its internal shearing and by the heat emitted by the counterfaces and the particle. However, it is shown later that these heat losses are infinitesimal and produce unnoticeable changes in the overall temperature results. The latter is shown so due to the extremely small value of the heat convection coefficient. Therefore, the choice of lubricant's reference temperature is, essentially, of no particular importance.

Firstly, the heat loss from the particle is modelled. Applying Newton's law of heat convection, a peripheral sector of the particle loses an amount of heat $q_{\mathrm{p,conv}}$ during the time step Δt, where

$$q_{\mathrm{p,conv}} = h_L \cdot A \cdot \left(\theta_{\mathrm{p}} - \theta_{\mathrm{fluid}}\right) \tag{3.35}$$

where h_L is the surface-length convection coefficient, A is the wet area of a peripheral sector, θ_{p} is the temperature of the sector and θ_{fluid} is the reference fluid temperature at the vicinity of the sector.

The wet area A of a sector is

$$A = r \cdot \Delta\theta \cdot h = \Delta r \cdot h \tag{3.36}$$

where h is the lubricant film thickness at the position of the sector.

The temperature θ_{p} of the sector is considered to be equal to the average temperature of the two counterfaces (θ_1 and θ_2) at the position of the sector:

$$\theta_{\mathrm{p}} = \frac{\theta_1 + \theta_2}{2} \tag{3.37}$$

The convection coefficient is given by the following equation:

$$h_L = \mathrm{Nu}_L \cdot \frac{K_p}{L} \tag{3.38}$$

where K_{p} is the thermal conductivity of the particle, L is an integration reference length, chosen here as

$$L \mathrel{\hat{=}} \frac{r \cdot \Delta\vartheta + h}{2} = \frac{\Delta r + h}{2} \tag{3.39}$$

and Nu_L is the surface-length Nusselt number. The calculation of the Nusselt number depends on the mechanism of the heat convection: forced, free or mixed convection. The convection mechanism can be established through the following criterion:

$$\left.\begin{array}{l} \text{If } \dfrac{\mathrm{Gr}}{\mathrm{Re}^2} << 1 \rightarrow \text{pure forced convection} \\[2ex] \text{If } \dfrac{\mathrm{Gr}}{\mathrm{Re}^2} >> 1 \rightarrow \text{pure free convection} \\[2ex] \text{If } \dfrac{\mathrm{Gr}}{\mathrm{Re}^2} \approx 1 \rightarrow \text{mixed convection} \end{array}\right\} \tag{3.40}$$

where "Gr" is the Grashof number and "Re" is the Reynolds number. According to Chapman (1987), the surface-length Nusselt number can be estimated as follows:

$$\mathrm{Nu}_L \cong \left\{\begin{array}{ll} 0.664 \cdot \sqrt{\mathrm{Re}_L} \cdot \mathrm{Pr}^{1/3} & \text{, for pure free convection} \\[2ex] 0.637 \cdot \left(\dfrac{\mathrm{Ra}_L}{1 + \dfrac{0.861}{\mathrm{Pr}}}\right)^{1/4} & \text{, for pure forced convection} \end{array}\right\} \tag{3.41}$$

where "Pr" is the Prandtl number and Ra_L is the surface-length Rayleigh number. The mixed convection regime will be shown (in chapter 5) to be of no particular importance in this study and, hence, it is not studied any further. The surface-length Reynolds number is

$$\mathrm{Re}_L = \frac{U \cdot L \cdot \rho_{\text{fluid}}}{\eta} \tag{3.42}$$

where η is the lubricant's dynamic viscosity (see equation (2.30)), ρ_{fluid} is the density of the lubricant at the vicinity of the sector for the local elastohydrodynamic pressure of the lubricant (see equation (2.31)), and U is the speed of the lubricant relatively to the sector

$$U = V_{12} \cdot \left| \sin(\vartheta) \right| \tag{3.43}$$

whereas angle ϑ is the angle of the sector (figure 3.1).

The Prandtl number is defined as

$$\text{Pr} \equiv \frac{\eta \cdot c_{\text{fluid}}}{K_{\text{fluid}}} \tag{3.44}$$

where c_{fluid} and K_{fluid} are the specific heat and the thermal conductivity of the lubricant, respectively.

The surface-length Grashof number is defined as

$$\text{Gr}_L \equiv \frac{\text{g} \cdot L^3 \cdot \beta \cdot \left(\theta_p - \theta_{\text{fluid}}\right)}{\left(\dfrac{\eta}{\rho}\right)^2} \tag{3.45}$$

where g is the gravitational acceleration (g $\cong$ 9.81 m/s^2) and β is the following parameter:

$$\beta = -\frac{1}{\rho_{\text{fluid}}} \cdot \frac{\partial \rho_{\text{fluid}}}{\partial \theta_{\text{fluid}}} \tag{3.46}$$

Using equation (2.31), equation (3.46) gives

$$\beta = c_3 \frac{\rho_0}{\rho} \tag{3.47}$$

Finally, the surface-length Rayleigh number is calculated as

$$\mathrm{Ra}_L = \mathrm{Gr}_L \cdot \mathrm{Pr} \tag{3.48}$$

All variables are now defined, so that the calculation of the convection coefficient h_L is feasible. The total heat lost along the particle's periphery, during a time step Δt, is

$$q_{\mathrm{p,conv,total}} = \sum_{\substack{\text{All}\\ \text{peripheral}\\ \text{sectors}}} q_{\mathrm{p,conv}} \tag{3.49}$$

3.6 Heat losses due to convection from the counterfaces to the lubricant

The counterfaces are cooled by the lubricant, losing heat through convection at the area where they are not in contact with the particle. The heat losses can be calculated in exactly the same way it is done for the particle (see section 3.5). Partitioning both counterfaces into elemental rectangles of area S, the heat lost by such a surface element during a time step Δt is

$$q_{\mathrm{cool}} = h_L \cdot S \cdot (\theta - \theta_{\mathrm{fluid}}) \tag{3.50}$$

where θ is the local skin temperature of a counterface. The surface-length convection coefficient h_L is calculated from equation (3.38), applying the analysis of section 3.5.

A rectangular surface element that loses heat due to convection can be seen as a heat sink (the opposite of a heat source). This way, the analysis of section 3.2 can readily be applied to this case. The flash temperature at time t, at point (x,y,z), due to the heat absorbed from a surface point $(x_s, y_s, 0)$ of a semi-infinite medium, is (similarly to equation (3.13))

$$\frac{-q_{\mathrm{cool}} \cdot \mathrm{d}t'}{4 \cdot \rho \cdot c \cdot [\pi \cdot \lambda \cdot (t - t')]^{3/2}} \cdot \exp\left\{ -\frac{1}{4 \cdot (t - t')} \cdot \left[\frac{(x - x_s)^2}{\lambda_x} + \frac{(y - y_s)^2}{\lambda_y} + \frac{z^2}{\lambda_z} \right] \right\} \tag{3.51}$$

Finally, the temperature θ_s at time t, at point (x,y,z) of a counterface, combining frictional heating and surface cooling, is

$$\theta_s = \underbrace{\theta}_{\text{Equation (3.19)}} - \frac{1}{2\cdot\rho\cdot\pi^{3/2}}\cdot\int_0^t\iint_{\bar{S}} \frac{h_L\cdot\left(\theta_s-\theta_{\text{fluid}}\right)\cdot \mathrm{d}x_s\cdot\mathrm{d}y_s\cdot\mathrm{d}t'}{c\cdot\exp\left\{\dfrac{1}{4\cdot\left(t-t'\right)}\cdot\left[\dfrac{\left(x-x_s\right)^2}{\lambda_x}+\dfrac{\left(y-y_s\right)^2}{\lambda_y}+\dfrac{z^2}{\lambda_z}\right]\right\}} \tag{3.52}$$

where θ is calculated from equation (3.19) and the surface $\bar{S}$, where the internal double integral is calculated, is located as follows:

$$\bar{S} = \left\{\left(x_s - x_{\mathrm{p}}\right)^2 + y_s^2 > R^2,\quad x_{\text{init}} < x_s < x_{\text{fin}} \quad\text{and}\quad 0 < y_s < y_{\text{fin}}\right\} \tag{3.53}$$

whereas x_{p} is the distance of the centre of the particle from the centre of the contact (given by x in equation (2.40)), R is the radius of the (deformed) particle disk (given by equation (2.20)), and x_{init}, x_{fin} and y_{fin} are limits of the calculation grid (suitably chosen as is shown in chapter 5). In the way it is defined, surface $\bar{S}$ excludes the area occupied by the particle at a specific time t, because there is, obviously, no heat loss at the aforementioned area.

As can be realized from equation (3.52), the temperature $[\theta_s]_t$ appears in both sides of the equation, whereas it is part of the integrand in the right side for the last step of the time integration. This is resolved by a correction loop in the computer code, as is explained in chapter 5. As an initial guess, it is obvious to assume that $[\theta_s]_t \cong [\theta_s]_{t-\Delta t}$. In the computer code, the temperature θ_s is calculated at each time step before proceeding to the next time step. Therefore, the whole past of θ_s is known when it is attempted to calculate θ_s for the next time "point".

3.7 Temperature-dependent properties

In reality, all material properties are more-or-less temperature dependent. Therefore, for the sake of completeness, all properties of all bodies involved in the process (counterfaces and particle) are taken as temperature-dependent. Table 3.1 shows a list of these variable properties.

Table 3.1

List of temperature-dependent material properties	
Thermal properties	Thermal conductivity
	Specific heat
	Thermal diffusivity (as function of the thermal conductivity and the specific heat)
Mechanical properties	Modulus of elasticity
	Shear modulus (function of the elasticity modulus)
	Hardness
	Yield stress in simple shear
	Yield stress in simple tension/compression

Parameters of anisotropy, like for example the principal thermal conductivities, are, accordingly, temperature dependent. Moreover, any other variable that is function of any of the temperature-dependent properties of table 3.1 is obviously also affected (an example is the Lamé constants).

It must be noted that the solid friction coefficients are expected to vary with temperature, but the form of these variations is very ambiguous and difficult to predict as they strongly depend on the materials used and the specific conditions at the sliding contact interface (see for example Peterson *et al.*, 1960). The temperature dependence of the (dry) friction coefficient is related to the formation of oxide films at higher temperatures. Those oxide films act as lubricants, reducing the friction between two rubbing surfaces, but are sensitive to temperature, load and time. Their presence is not persistent and may break down, leaving the surfaces unprotected with an increase in friction and wear. In the important case of austenitic stainless steels, Peterson *et al*. (1960) reported that increasing the temperature did not cause a noticeable change in friction and in surface damage. The present author speculates that this may be attributed to the resistance of stainless steels to oxidation. After an extensive literature research, the present author concluded that there exists no universal model for the friction coefficient-temperature relation in either dry or wet friction, as this changes for every particular application and the performed experiments do not give satisfactorily consistent results. However, it has already been mentioned that, when the surface temperature exceeds a limit of around 150 ºC (or slightly higher if special lubricant additives are used), there is lubricant adsorption and a rapid increase of the friction coefficient, which can even be doubled. It is shown later that the calculated surface temperatures are high enough to cause serious problems (damage), even if the friction coefficient used in the analysis is the one for the low temperature regime, in other words for temperatures lower than 150 ºC.

The inclusion of temperature effects on the properties is achieved via a correction loop in the computer code, as is explained in chapter 5. This adds significantly to the complexity of the algorithm, because pressures, tractions, sub-surface stresses and surface deformations are all directly affected, and corrections are needed until convergence is achieved. All these effects are presented in the detailed example of chapter 5. At this point, it can already be revealed that the effect of variable *thermal* properties is generally small for typical engineering materials, especially those that have been heat-treated. Effects of greater importance are expected when temperatures reach the level of metallurgical phase change. For example, Earles and Powell (1967) report cases where the temperatures encountered in unlubricated sliding steel surfaces are so high that surface white layers appear (covered by oxide films), which, after removing the oxide films and using X-ray diffraction techniques, are shown to contain austenite. They, therefore, inferred that the surfaces must have attained a temperature in excess of 730 °C, in other words the martensite-to-austenite transformation temperature.

In general, when tempering reactions are absent, the dependency of the thermal properties to temperature is shown to be of limited importance. This can be seen in the work of Storm (1951), Chu and Abramson (1960), and Ling and Rice (1966). Due to the increased complexity and non-linearity of the relevant equations, the inclusion of temperature-dependent thermal properties is rarely encountered in the literature. However, it is fully taken into account in this Thesis, coupled by thermal anisotropy in a non-linear model.

3.8 Example

The data used in the example of this section are the same as those used for the example of section 2.8. Those data are listed in tables 2.1-2.3. Interesting results are quoted in table 2.4. In the present example, all mechanical and thermal properties of the materials involved are considered independent of temperature and the materials isotropic. This is done in order to concentrate on *basic* results first. Table 3.2 shows the data used and the assumptions made for the present example.

In section 2.8, it is shown that the particle sticks to the surface with the higher friction coefficient, which is counterface 1. Therefore, the particle slides on counterface 2 with the sliding speed of the contact (V_{12}). In this example, the focus is on counterface 2, assuming that counterface 2 receives only its share of the amount of heat that is produced at the interface with the particle. This means that $\alpha_{22} = 0$. Moreover, particle's internal heating is omitted at this stage. It is shown later that even in this case, the flash temperatures encountered are so high that they cannot be disregarded. In chapter 5, where none of the previous arbitrary assumptions is made, it is shown that the flash temperatures are actually much higher!

Table 3.2

Data for the example and assumptions	
<u>Assumptions (all assumptions are removed in chapter 5)</u> (1) All mechanical and thermal properties are considered independent of temperature. (2) The materials are considered isotropic. (3) The heat generation inside the particle is neglected. (4) $\alpha_{22} = 0$ (it is assumed that surface 2 receives only its share of the amount of heat produced at its contact with the particle – see explanations below). (5) Particle and surface cooling due to convection is omitted. (It is shown in chapter 5 that it is negligible anyway.) (6) The solid pressure on the particle is calculated using the rigid-counterface model of section 2.6. That model does not account for the effect of the elastohydro-dynamic pressure on the particle (in chapter 5, a completely new pressure model that removes all previous restrictions is developed and applied).	
Thermal conductivity of the particle at temperature θ_0	57.7 W/(m·°C)
Thermal conductivity of the counterfaces at temperature θ_0	25.3 W/(m·°C)
Thermal diffusivity of the particle at temperature θ_0	$1.5 \cdot 10^{-5}$ m^2/s
Thermal diffusivity of the counterfaces at temperature θ_0	$6.6 \cdot 10^{-6}$ m^2/s
Particle material	Ferrite
Counterface material	Martensite
Number or tracks on the particle	$N_t = 50$
All other data as in tables 2.1-2.3	

Proceeding with the example, figure 3.3 shows the temperature history of four points, which lie on and below surface 2.

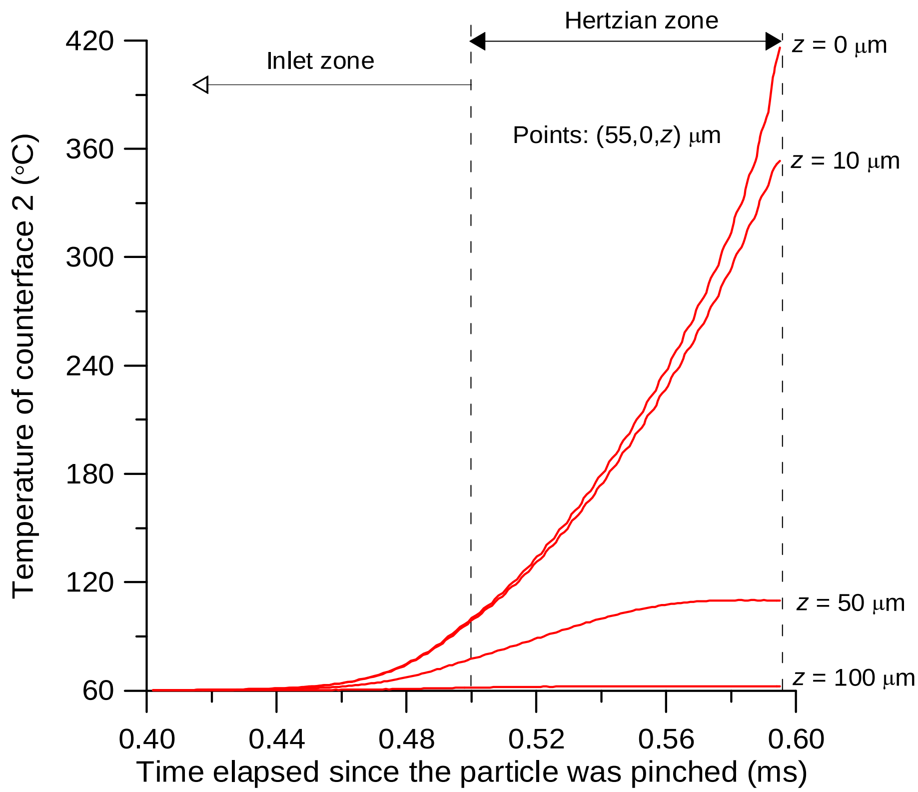

Figure 3.3 Temperature at selected points of counterface 2 versus time.

The coordinates of the points (55,0,z) whose temperatures are shown in figure 3.3, are relative to the centre of the contact (x = 0, see figure 2.1) at time t = 0.6 ms, and the corresponding (maximum) temperatures are given in table 3.3.

Table 3.3

Temperature at selected points of counterface 2 at time t = 0.6 ms (bulk temperature θ_0 = 60 °C)	
Point coordinates (x,y,z) [μm]	Maximum temperature [°C]
(55,0,0)	416
(55,0,10)	353
(55,0,50)	110
(55,0,100)	62

The temperatures shown in the previous table are encountered at the time when the particle starts entering the outlet zone of the contact (figure 2.1). At a depth of 100 μm below surface 2, the temperature is practically equal to the bulk temperature θ_0, the latter being equal to 60 °C. This is in agreement with the Saint-Venant's principle, known from the theory of Elasticity. It has been shown (see for example Boley and Weiner, 1960, section 6.8) that the equivalent of the Saint-Venant's principle is also applicable in the area of Thermoelasticity. This practically means that the flash temperature field is stronger close to the heat source and becomes weaker away from the source, the weakening being fast (often noted as being "exponential"). It is obvious that this weakening is faster in transient heat conduction problems, like the one studied here, than in the corresponding steady-state ones, because of the time duration of the application of the heat source (infinite in the steady-state case, which allows the heat wave to "penetrate" the solids as far as possible).

According to figure 3.3, the frictional heating in the inlet zone of the contact is relatively weak. Severe heating starts essentially close to the entrance to the Hertzian zone, where the temperature increase is accelerated, especially for the near-surface points at the exit of the Hertzian zone. This is due to the rapid decrease of the film thickness as the particle approaches the Hertzian zone, which results in a considerable increase of the level of pressure and traction forces on the particle, together with an increase of the area occupied by the particle (see figures 2.8 and 2.9). Consequently, the amount of frictional heat produced is largely dependent on the width of the Hertzian zone. As a result, the frictional heating effects observed here are expected to be weaker in purely rolling contacts.

Figure 3.3 shows also the decrease of temperature with depth. High temperatures are encountered close to the surface, which means that the corresponding thermal stresses, added to the mechanical stresses from the compression of the particle and the lubricant pressure in the contact, will bring the high-risk area for yield closer to the surface, as is indeed shown in chapter 5.

The flash temperature effects are more clearly demonstrated in figure 3.4.

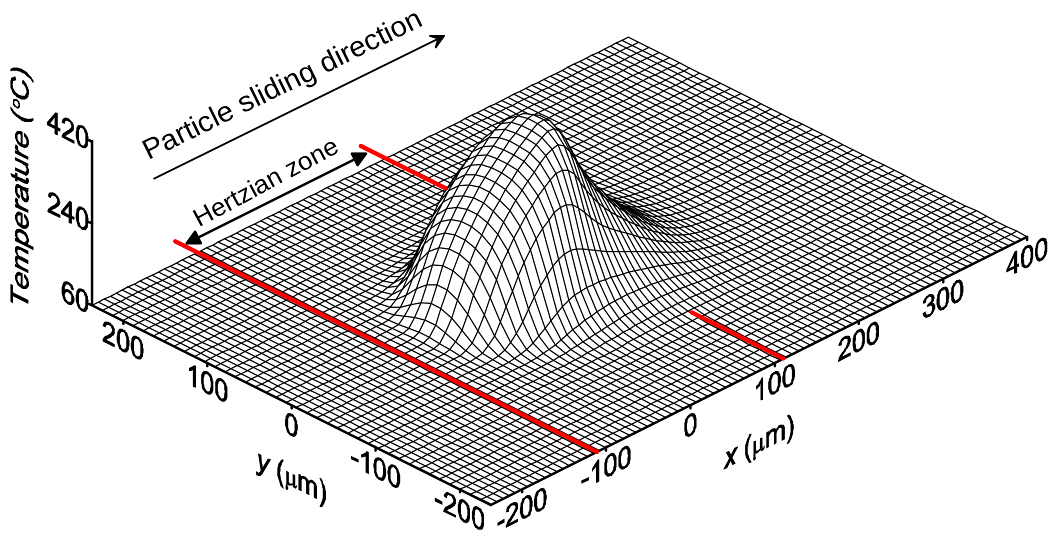

Figure 3.4 Temperature distribution on counterface 2 as the particle starts exiting the Hertzian zone of the contact.

The particle slides along the x-axis, from the negative to the positive part. The plane defined by the axes x and y is located on counterface 2. In order to reduce the temperature-calculation times (which are in the order of hours), 90 % of the inlet zone was left out. It was actually found that this gives fairly accurate results (using the model developed in chapters 2 and 3) in the vast majority of cases studied. However, it is mentioned here in order to explain the relatively late "appearance" of the temperature rise, which should have taken place further outside the entrance of the Hertzian zone. Using the full model as shown in chapter 5, the omission of the inlet zone from the temperature calculations is no longer acceptable. This argument is made clear in the relative figures of the main example of chapter 5.

The maximum flash temperature (temperature above the bulk temperature) on counterface 2 is 356 °C. It is shown in chapter 5 that this is a significant underestimation, mainly owing to the assumptions (3) and (4) in table 3.2. It must be noted that in other cases tested by the author, the maximum flash temperature is higher, depending on the size of the particle in relation to the central film thickness, as well as on the hardness of the particle relatively to the hardness of the counterfaces. It should be remembered that the present example refers to a particle that is 8 times softer than the counterfaces. For larger and harder particles, the temperatures may even exceed the melting point of the material of the counterfaces. A parametric study, which reveals the level of flash temperatures for various combinations of particle and contact data, is presented in table 3.4. Time t, shown in table 3.4, is the time elapsed from when the particle was first pinched to when it starts exiting the Hertzian zone of the contact. As can be realized from this table, significantly high flash temperatures can be encountered in very short times as a particle passes through the contact.

Table 3.4

Parametric study – Maximum flash temperatures								
D [μm]	H_p [HV]	V_{12} [m/s]	μ_1	μ_2	ε	h_c [μm]	t [ms]	Maximum flash temperature on counterface 2 [°C]
30	100	5.0	0.20	0.15	0.5	2.2	0.13	549
30	100	1.0	0.25	0.20	0.5	0.7	0.59	465
30	200	1.0	0.20	0.15	0.5	0.7	0.59	371
30	100	1.0	0.20	0.15	0.5	0.7	0.59	350
30	80	1.0	0.20	0.15	0.5	0.7	0.59	344
30	100	0.5	0.20	0.15	0.5	0.4	1.16	262
30	100	1.0	0.15	0.10	0.5	0.7	0.59	229
20	100	1.0	0.20	0.15	0.5	0.7	0.52	207
10	100	1.0	0.20	0.15	0.5	0.7	0.40	38
10	80	5.0	0.15	0.10	0.5	2.2	0.08	8
10	80	5.0	0.15	0.10	0.5	2.2	0.08	8
Other data used in the study: $S_r = 1$, $R_1 = 20$ mm, $R_2 = 28$ mm								

Coming back to the main example studied in this section, it is interesting to have a 2-dimensional view of the temperature distribution of figure 3.4. Figure 3.5 shows a contour map of isothermal lines, based on the 3-dimensional temperature field. From figure 3.5, the core of the heated zone can readily be seen and compared with the location of the particle, which, in the figure, is denoted by a white circle. The outer isothermal line corresponds to a temperature close to the bulk temperature (60 °C). It is immediately noticeable that there is a fast development of a high-temperature spot on counterface 2, with dimensions 200 μm × 200 μm, where the temperature is risen from 60 °C (the bulk temperature) to a maximum of 416 °C in just 0.6 ms.

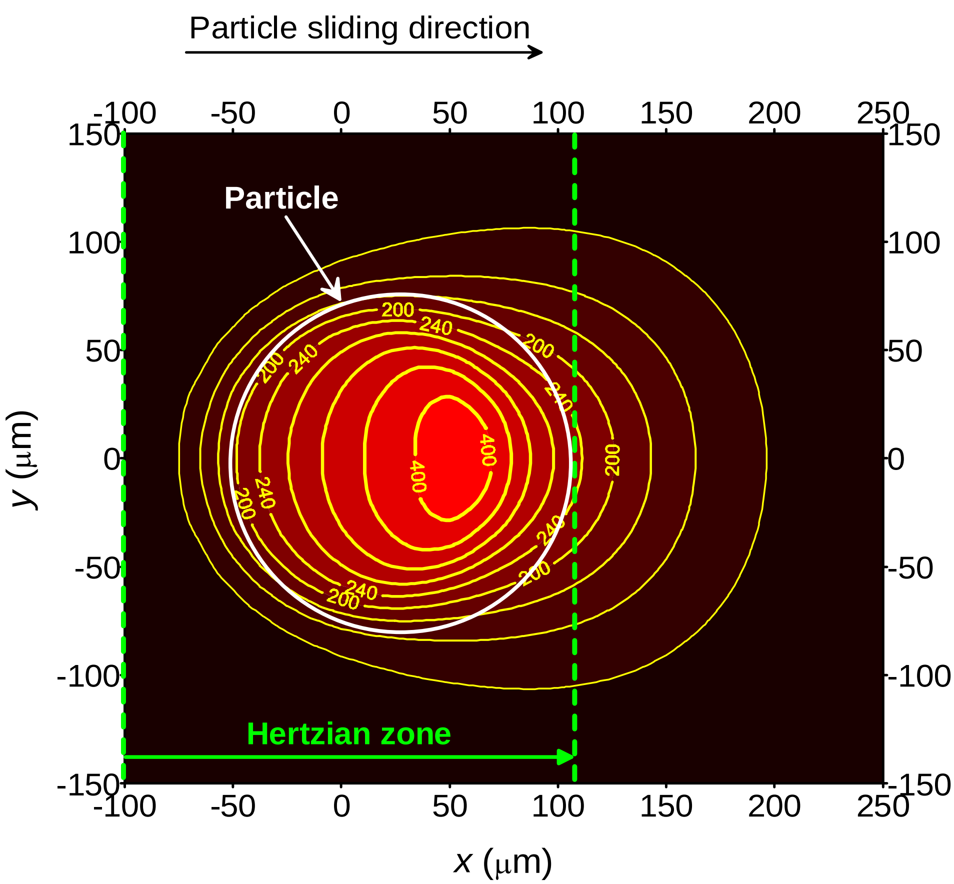

Figure 3.5 Contour map of the temperature distribution on surface 2 as the particle starts exiting the Hertzian zone of the contact (particle denoted by the white circle). Temperatures shown are in degrees C.

An important observation is that the severely heated area extends outside the particle, especially behind the particle but also laterally and in front of the leading edge of it. This obviously affects the lubrication conditions around the particle. It is shown (see the main example of chapter 5) that the surface temperatures are high enough to affect the local temperature of the lubricant. However, it is also shown that the heat convection coefficient is very small and, hence, the heat convection from the surfaces to the lubricant is not significant. Nevertheless, this phenomenon may become significant when more than one particle is trapped in the contact, in which case the individual heat waves are combined and amplified. The latter mechanism was proposed by Chandrasekaran *et al.* (1985) to explain the scuffing failures encountered during standard 4-ball machine tests with contaminated oils. However, at that time, there was no available theoretical model to test their proposition. More on this follows in chapter 5.

These results suggest that the effect of frictional heating of the sliding counterfaces, caused by the squashing of a debris particle, is very important in understanding the thermal aspects of scuffing observed in failed machine elements such as gears, cams and followers, bearings, etc. It is known that scuffed surfaces exhibit global melting marks. On the other hand, lightly scuffed surfaces often exhibit spots of white color (although covered by oxide films), known as "white-layers", where the white color shows that the material underneath has undergone a metallurgical phase change (see for example Earles and Powell, 1967). Based on the findings of the present Thesis, it is likely that some of those spots are the remains of the catastrophic presence of rather soft debris particles. The argument is that hard particles tend to retain their initial shape, causing abrasion (long scratches, grooving) rather than a more-or-less localized spot. On the other side, soft-ductile particles are flattened during compression in the inlet zone of the contact, become thin disks, and as such enter the main contact zone (Hertzian zone), producing a stress field, which has its maximum strength near the exit of the Hertzian zone, where the core of the heated area is located (figure 3.5). Therefore, the damage to the counterfaces is more likely to be localized in a relatively narrow area than to be extended in an elongated zone. Taking into account the motion of the particle combined with its lateral expansion, these spots must have the appearance of a falling water drop or a pencil (with its head created by the initial lateral expansion of the particle in the inlet zone of the EHD contact), having a different color than their neighborhood due to the high local frictional heating. The author was pleasantly surprised to discover (after the analytical work of this Thesis had been completed) a similar description in the excellent book of Tallian (1992, see section 12.4 – case 3). Such effects can also be seen in the work of Zantopoulos (1998), who experimentally studied scuffing in tapered roller bearings. Zantopoulos' paper contains photographs showing white-layers, which are the result of high flash temperatures (in excess of 700-800 °C), followed by quick cooling to room temperature. The high flash-temperature incidents were part of scuffing failure, where material had been adhered to the Cone Rib and/or the Roller End of the tapered roller bearings. Although Zantopoulos has not directly related these incidents with debris particles, he speaks of teardrop dent formations observed on the scuffed surfaces, which have a smooth shiny appearance. Based on the findings of the present Thesis, this is a clear indication of squashing of soft ductile debris between two sliding surfaces. Whether these debris are soft/ductile before compression or they become soft during shearing/squashing (due to high frictional heating) is not of importance. What *is* important is the effect of the over-rolling of such debris in sliding contacts, and this is in agreement with the analytical findings of this Thesis. More information on this follows in the example of chapter 5.

Moreover, surface 1 (the surface to which the particle sticks) is expected to receive a significant amount of heat owing to particle's extrusion speed and the heat transferred from the particle to it. The latter is a part of the heat produced at the interface of particle and surface 2, as well as part of the particle's internally generated heat. If both counterfaces have thermal properties with correspondingly equal magnitudes, then it is shown in chapter 5 that the difference of the maximum flash temperatures of the two counterfaces is of the order of 20 % - 40 %, with counterface 1 receiving most of the heat. Therefore, the counterface to which the particle sticks is the hotter one. For different thermal properties, the latter result could be slightly altered.

The effect of particle's internal heating is not negligible either. If it *is* taken into account in the calculations, the resultant maximum flash temperature in the quoted example is 8 % higher for surface 1 and 5 % higher for surface 2. More on this and on the effect of surface and particle cooling due to convection follows in chapter 5.

As already mentioned, the effect of temperature-dependent thermal properties on the flash temperature results is relatively weak. This is shown in chapter 5, but a first indication is presented in figure 3.6. The two flash temperature curves in that figure are for point (55,0,0) μm of counterface 2 and refer to different bulk temperatures: 60 °C and 500 °C. The difference in the calculated maximum flash temperatures for the two cases is only 2 °C, which is quite low in comparison with the maximum flash temperatures, which are of the order of 356 °C. This means that even if the maximum flash temperature in our example were 500 °C (and not 356 °C), omitting the change of thermal properties with temperature would lead to insignificant errors. Similar results have been reported by other researchers. See for example Storm (1951), and Ling and Rice (1966), both presenting detailed analyses.

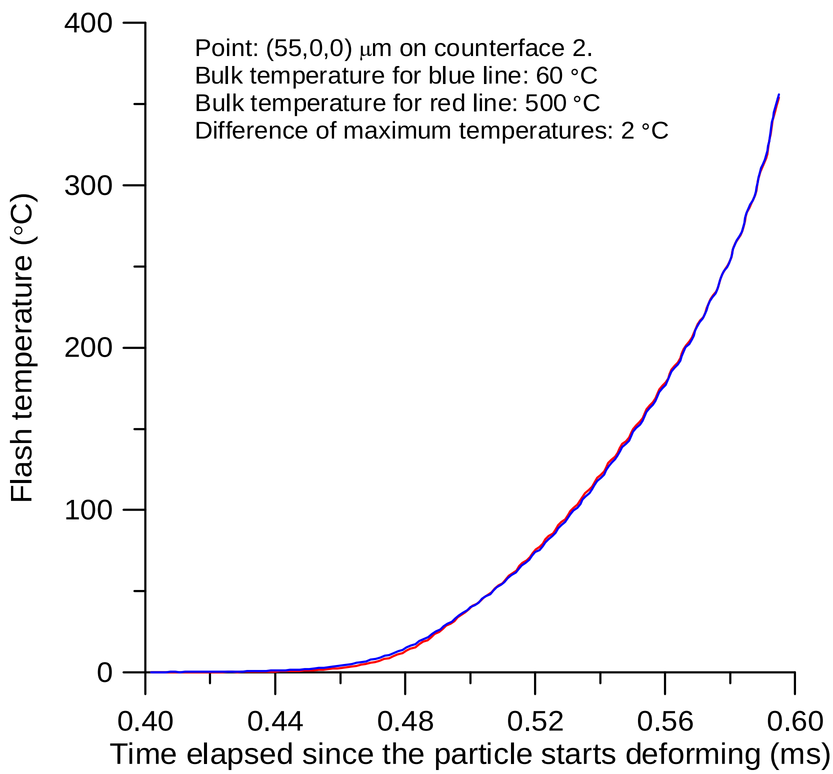

Figure 3.6 Flash temperature at a point of counterface 2 versus time elapsed since the particle was pinched, for two different bulk temperatures.

3.9 Conclusions

In the present chapter, a model has been developed to simulate the frictional heating process when a soft-ductile debris particle is squashed between two counterfaces in an elastohydrodynamic rolling-sliding contact. The model covers the following issues:

- Heat generation due to friction between the particle and the counterfaces.
- Internal heat generation of the particle due to its plastic compression.
- Heat partition between the counterfaces and the particle.
- 3-dimensional heat conduction in the counterfaces.
- Heat convection from the counterfaces and the particle to the lubricant.
- Transient variations of all mechanical and thermal properties of the materials involved in the process (counterfaces and particle) due to the temperature changes.
- Thermal anisotropic effects, considering thermally orthotropic materials.

It is shown theoretically that apart from the obvious mechanical contribution of debris particles to the damage of lubricated contacts, there exists a thermal contribution, which can be very important in the case where there is relative sliding between the two cooperating counterfaces in the contact, and could – sometimes all alone – explain the catastrophic effects of soft particles in machine elements like gears, bearings, cams and followers, etc. The flash temperatures encountered in contaminated elastohydrodynamic contacts (see table 3.4) could be high enough as to cause local melting of the materials involved, resulting in a failure mechanism that resembles scuffing, even if the particles are small and much softer than the counterfaces, as in the example of section 3.8. The variation of the thermal properties of both counterfaces and particle has been accounted for and the first indication is that it is insignificant (for the temperature levels of this study, meaning for temperatures at the order of 500 °C), as has already been shown by other researchers in the past. In chapter 5, it is shown that the same conclusion holds for more severe conditions where the temperatures may exceed 1500 °C). It is noted again here that all material properties used in the example are typical of engineering steels, so that the results and conclusions have a general applicability.

Here follows a summary of the main conclusions drawn after a large number of examples studied.

(1) The friction between the particle and the counterfaces results in the rapid generation of heat, which is usually high, even when the particle is small and much softer than the counterfaces. Consequently, high flash temperatures are encountered in the contact (figure 3.4), which may cause metallurgical changes and even local melting of the materials of the counterfaces and/or the particle.

(2) If the particle survives the heat and reaches the outlet zone of the contact, it will have produced a hot spot in the Hertzian zone (figure 3.5), with dimensions comparable to the average diameter of the squashed particle disk.

(3) The magnitude of the peak flash temperature is directly dependent on the central film thickness and the width of the Hertzian zone. The central film thickness obviously affects the level of pressure on the particle and through this, the traction forces and the amount of frictional heat produced (equation (3.3)). The width of the Hertzian zone affects the time the particle will spend sliding under high pressure/traction conditions (see figure 3.3). The latter does not affect purely rolling contacts (contacts without sliding motion).

(4) There is a temperature difference between the counterfaces after frictional heating has ceased. First calculations show that the counterface where the particle sticks is generally 20 % – 40 % hotter than the other counterface (not applicable in purely rolling contacts).

(5) The variation of thermal properties with temperature has essentially insignificant effect on the level of the flash temperatures. A preliminary indication is shown in figure 3.6; more information follows in chapter 5.

(6) Particle’s internal heating accounts for additional heating of the counterfaces. For the typical example studied in section 3.8, the maximum flash temperatures are raised by 8 % for surface 1 and 5 % for surface 2.

(7) As a final conclusion, flash temperatures owing to frictional heating of rolling-sliding elastohydrodynamic contacts during the passage of soft debris particles can be high (in the order of hundreds of degrees C). Hence, debris particles can often be responsible for a ***high-heat failure mechanism***, which, for temperatures of the order of the melting point of the materials, can be attributed as ***local scuffing***.

Finally, it is important to report that, using the present model, is was found that very soft particles (10 times softer than the counterfaces) could produce significant amounts of frictional heat if they have a diameter of at least 5 to 10 μm, assuming a solid-friction coefficient in the order of 0.2 and a film thickness around 0.5 μm. Consequently, very soft particles, smaller than around 5 μm, cannot be held responsible – under typical operating conditions – for significant frictional heating (see the bottom two examples in table 3.4).

CHAPTER 4

THERMOELASTIC ANALYSIS OF THE SQUASHING OF A SOFT PARTICLE IN AN ELASTOHYDRODYNAMIC LINE CONTACT

4.1 Introduction

According to chapter 3, the passage of a debris particle through a concentrated contact is associated with the encounter of heat, arising from the friction between the particle and the counterfaces. It was shown that the heat could be high enough as to result in high flash temperatures in the contact, which are often so high that local damage in the form of metallurgical changes or even material melting could occur. Although one could indirectly conclude that damage is expected when the surface temperature exceeds a known value, this conclusion lacks a detailed description of the way that damage is going to appear and progress.

In order to assess the risk of damage in a strictly mathematical manner, the mechanical and thermal stresses arising from the specified loading must be calculated, followed by a yield check. The mechanical part of the loading is known, because the solid pressure between the particle and the counterfaces as well as the elastohydrodynamic pressure separating the two counterfaces are both approximately known. Moreover, the temperature field associated with each counterface is also known (see chapter 3), which means that thermal stresses can be calculated through an appropriate analysis. However, the situation is complicated by the fact that the produced frictional heat causes thermal expansion of the counterfaces, which alters the solid pressure between the particle and the counterfaces and vice versa. Other complexities arise from the fact that the thermal and mechanical properties of the particle and the counterfaces are temperature dependent. All these account for a complicated thermomechanical system, which needs to be modelled partially, before trying to understand it globally. More specifically, the relations of the various parts of the whole model must be postulated mathematically. These relations are shown schematically in figure 4.1.

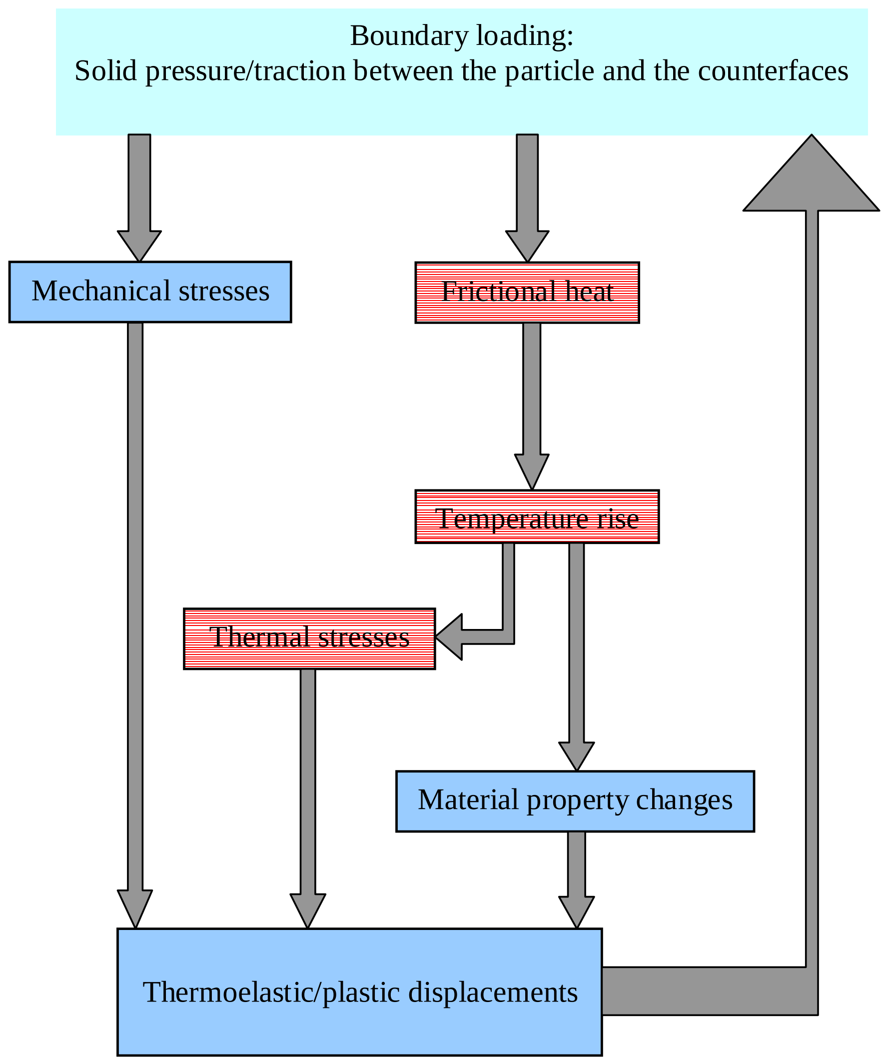

Figure 4.1 Flow chart of the interrelation of the thermomechanical effects.

It is the purpose of this chapter to provide a complete mathematical analysis for the calculation of the thermoelastic stress-strain-displacement fields in the most general way possible. This has been done in various ways by other researchers in the past. General results and methods are employed in the papers of Barber (1972, 1980a), and Barber and Martin-Moran (1982). Interesting theoretical contributions have been made by Korovchinski (1965), Mercier *et al*. (1978), Tseng and Burton (1982), Ju and Huang (1982), and Kulkarni *et al*. (1991, FEM thermo-elastoplastic analysis). However, most of the previous studies contain geometrical and/or loading simplifications that restrict the applicability of the results obtained. Such simplifications include the assumption of constant sliding velocity of the rubbing surfaces, plane stress or plain strain, ideal geometrical shapes (like spheres, or rectangles) for the sliding bodies, and simplified (arbitrary) heat partitioning, such as the assumption that all of the frictional heat goes to one body while the other behaves as an insulator. Moreover, many studies are overcomplicated by the use of tensor algebra or integral equations and transformations, which, although being neat mathematical tools, could be avoided in favor of a more simple and straightforward approach from an engineer's rather than a mathematician's point of view. Such a "simple" approach is feasible, as is shown later in this chapter, where the only mathematical techniques used are the differentiation and numerical integration of multivariable functions.

Starting with the formulation of the mechanical stress analysis, there are many publications dealing with the Theory of Elasticity where the mathematical problem is attacked in various analytical ways, as with Tensorial, Differential or Complex analysis. However, the complete equations of the Contact Mechanics aspects of Elasticity were very early given in differential notation by (independently) Boussinesq and Cerruti. A presentation of those equations in differential form can be found in the excellent book of Love (1944). Johnson (1985) presents a more useful form of the same equations. However, all these presentations are in a coupled differential form, which prevents a researcher/reader from straightforward analytical calculations. At the time of writing this Thesis, the author was not aware of a publication listing the complete Boussinesq-Cerruti equations in the most developed form possible. Therefore, the author undertook the awkward task of expanding the complex differential equations into a more usable analytic form, as is shown in section 4.2.

Thermal stress analysis on the other hand is equivalently laborious. There is, again, a great number of publications addressing various problems of thermal stressing, most of which are mathematically challenging. A good source of general information, albeit not for the mathematically incompetent, are the books of Boley and Weiner (1960), and Nowacki (1986). The general problem of Thermoelasticity is one of considerable complexity, resembling the solution of the general Navier-Stokes equations in Fluid Mechanics. The problems arise when attempting to solve for the *coupled* thermal and elastic stress fields. The coupling of the thermal and elastic stress fields becomes unavoidable when the rate of change of the thermal loading and, thus, the rate of movement of the flash temperature field, is close to or exceeds the speed of sound in the solids under consideration. Thankfully, the majority of industrial applications do not involve such high-speed processes. This means that, in the latter case, the simplified quasi-static theory can be used with good approximation.

Finally, on the question of the necessity of a thermal stress analysis, the answer comes very easily: the magnitude of the flash temperatures caused by the friction between a particle and the counterfaces in an elastohydrodynamic contact suggests that the thermal stresses should be relatively high. This is indeed shown in several publications. Marscher (1982b), in a general study of thermal versus mechanical effects in high-speed sliding, showed that thermal stresses were higher than the corresponding mechanical stresses in the majority of the rub events studied. More pronounced were the differences found by Ju and Huang (1982), again in favor of the thermal stresses. All this suggests that thermal stresses caused by the squashing of debris particles have a very important role in the failure of machine elements. In the next chapter, it is actually shown that thermal stresses increase dramatically the risk of surface damage and often have the principal role when it comes to the combined action of thermal and mechanical stress fields.

4.2 Mechanical elastic stress analysis

According to the model of section 2.4 (figure 2.5), a soft and ductile particle is being squashed between two parallel counterfaces, which have a vertical (approaching) and a horizontal (sliding) velocity, relatively to each other. Because of the smallness of the particle, as compared to the counterfaces, and the level of stresses developed in the contact, the counterfaces can be seen as elastic half-spaces.

Assuming surface A is one of these two half-spaces, Figure 4.2 shows surface A together with the coordinate system notation as well as the surface pressure and tractions, which are used as part of the boundary conditions. The coordinate system Oxyz is fixed on surface A and travels in space with the tangential velocity of surface A. The origin O is suitably located as the point where the particle first comes in contact with both counterfaces and can be found following the analysis of sub-section 2.3.2.

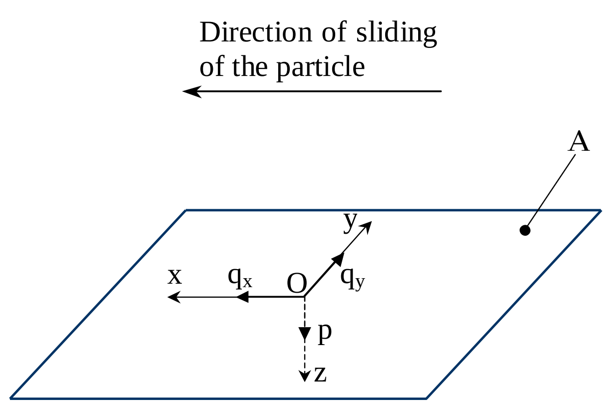

Figure 4.2 System of coordinates and notation.

In order to calculate the subsurface stress field, owing to a general surface loading as in figure 4.2, the Boussinesq-Cerruti equations are applied. These equations can be found in differential form in Johnson (1985). In order to be used in the calculations, the equations are further developed into more useful analytical relations. This task proved very cumbersome because of the amount of the symbolic calculations involved. However, the author repeated the algebraic manipulations three times in order to ensure the correctness of the results.

Following Johnson (1985), the subsurface stresses are given by the following equations:

$$\sigma_x = \frac{2 \cdot \nu \cdot G}{1 - 2 \cdot \nu} \cdot \left(\frac{\partial u_x}{\partial x} + \frac{\partial u_y}{\partial y} + \frac{\partial u_z}{\partial z} \right) + 2 \cdot G \cdot \frac{\partial u_x}{\partial x} \tag{4.1}$$

$$\sigma_y = \frac{2 \cdot \nu \cdot G}{1 - 2 \cdot \nu} \cdot \left(\frac{\partial u_x}{\partial x} + \frac{\partial u_y}{\partial y} + \frac{\partial u_z}{\partial z} \right) + 2 \cdot G \cdot \frac{\partial u_y}{\partial y} \tag{4.2}$$

$$\sigma_z = \frac{2 \cdot \nu \cdot G}{1 - 2 \cdot \nu} \cdot \left(\frac{\partial u_x}{\partial x} + \frac{\partial u_y}{\partial y} + \frac{\partial u_z}{\partial z} \right) + 2 \cdot G \cdot \frac{\partial u_z}{\partial z} \tag{4.3}$$

$$\tau_{xy} = G \cdot \left(\frac{\partial u_x}{\partial y} + \frac{\partial u_y}{\partial x} \right) \tag{4.4}$$

$$\tau_{yz} = G \cdot \left(\frac{\partial u_y}{\partial z} + \frac{\partial u_z}{\partial y} \right) \tag{4.5}$$

$$\tau_{zx} = G \cdot \left(\frac{\partial u_z}{\partial x} + \frac{\partial u_x}{\partial z} \right) \tag{4.6}$$

where G is the shear modulus. The displacements are given by the following equations:

$$u_x = \frac{1}{4 \cdot \pi \cdot G} \cdot \left[\begin{array}{l} 2 \cdot \dfrac{\partial^2 F_1}{\partial z^2} - \dfrac{\partial^2 H_1}{\partial x \partial z} + 2 \cdot \nu \cdot \left(\dfrac{\partial^2 F_1}{\partial x^2} + \dfrac{\partial^2 G_1}{\partial x \partial y} + \dfrac{\partial^2 H_1}{\partial x \partial z} \right) - \\ z \cdot \left(\dfrac{\partial^3 F_1}{\partial x^2 \partial z} + \dfrac{\partial^3 G_1}{\partial x \partial y \partial z} + \dfrac{\partial^3 H_1}{\partial x \partial z^2} \right) \end{array} \right] \tag{4.7}$$

$$u_y = \frac{1}{4 \cdot \pi \cdot G} \cdot \begin{bmatrix} 2 \cdot \frac{\partial^2 G_1}{\partial z^2} - \frac{\partial^2 H_1}{\partial y \partial z} + 2 \cdot \nu \cdot \left(\frac{\partial^2 F_1}{\partial x \partial y} + \frac{\partial^2 G_1}{\partial y^2} + \frac{\partial^2 H_1}{\partial y \partial z} \right) - \\ z \cdot \left(\frac{\partial^3 F_1}{\partial x \partial y \partial z} + \frac{\partial^3 G_1}{\partial y^2 \partial z} + \frac{\partial^3 H_1}{\partial y \partial z^2} \right) \end{bmatrix} \tag{4.8}$$

$$u_z = \frac{1}{4 \cdot \pi \cdot G} \cdot \begin{bmatrix} \frac{\partial^2 H_1}{\partial z^2} + (1 - 2 \cdot \nu) \cdot \left(\frac{\partial^2 F_1}{\partial x \partial z} + \frac{\partial^2 G_1}{\partial y \partial z} + \frac{\partial^2 H_1}{\partial z^2} \right) - \\ z \cdot \left(\frac{\partial^3 F_1}{\partial x \partial z^2} + \frac{\partial^3 G_1}{\partial y \partial z^2} + \frac{\partial^3 H_1}{\partial z^3} \right) \end{bmatrix} \tag{4.9}$$

where

$$F_1 \equiv \iint_A q_x(\xi, \eta) \cdot \Omega \cdot \mathrm{d}\xi \cdot \mathrm{d}\eta \tag{4.10}$$

$$G_1 \equiv \iint_A q_y(\xi, \eta) \cdot \Omega \cdot \mathrm{d}\xi \cdot \mathrm{d}\eta \tag{4.11}$$

$$H_1 \equiv \iint_A p(\xi, \eta) \cdot \Omega \cdot \mathrm{d}\xi \cdot \mathrm{d}\eta \tag{4.12}$$

where

$$\Omega \equiv \mathrm{z} \cdot \ln(\rho + \mathrm{z}) - \rho \tag{4.13}$$

and

$$\rho \equiv \sqrt{(\xi - x)^2 + (y - \eta)^2 + z^2} \tag{4.14}$$

In order to calculate the stresses, it is necessary to find the spatial derivatives of the displacements. Using equations (4.7)-(4.9), the results are as follows:

$$\frac{\partial u_x}{\partial x} = \frac{1}{4\cdot\pi\cdot G}\cdot\left[\begin{array}{l} 2\cdot\dfrac{\partial^3 F_1}{\partial x\partial z^2} - \dfrac{\partial^3 H_1}{\partial x^2\partial z} + 2\cdot\nu\cdot\left(\dfrac{\partial^3 F_1}{\partial x^3} + \dfrac{\partial^3 G_1}{\partial x^2\partial y} + \dfrac{\partial^3 H_1}{\partial x^2\partial z}\right) - \\ z\cdot\left(\dfrac{\partial^4 F_1}{\partial x^3\partial z} + \dfrac{\partial^4 G_1}{\partial x^2\partial y\partial z} + \dfrac{\partial^4 H_1}{\partial x^2\partial z^2}\right) \end{array}\right] \tag{4.15}$$

$$\frac{\partial u_y}{\partial y} = \frac{1}{4\cdot\pi\cdot G}\cdot\left[\begin{array}{l} 2\cdot\dfrac{\partial^3 G_1}{\partial y\partial z^2} - \dfrac{\partial^3 H_1}{\partial y^2\partial z} + 2\cdot\nu\cdot\left(\dfrac{\partial^3 F_1}{\partial x\partial y^2} + \dfrac{\partial^3 G_1}{\partial y^3} + \dfrac{\partial^3 H_1}{\partial y^2\partial z}\right) - \\ z\cdot\left(\dfrac{\partial^4 F_1}{\partial x\partial y^2\partial z} + \dfrac{\partial^4 G_1}{\partial y^3\partial z} + \dfrac{\partial^4 H_1}{\partial y^2\partial z^2}\right) \end{array}\right] \tag{4.16}$$

$$\frac{\partial u_z}{\partial z} = \frac{1}{4\cdot\pi\cdot G}\cdot\left[\begin{array}{l} \dfrac{\partial^3 H_1}{\partial z^3} - 2\cdot\nu\cdot\left(\dfrac{\partial^3 F_1}{\partial x\partial z^2} + \dfrac{\partial^3 G_1}{\partial y\partial z^2} + \dfrac{\partial^3 H_1}{\partial z^3}\right) - \\ z\cdot\left(\dfrac{\partial^4 F_1}{\partial x\partial z^3} + \dfrac{\partial^4 G_1}{\partial y\partial z^3} + \dfrac{\partial^4 H_1}{\partial z^4}\right) \end{array}\right] \tag{4.17}$$

$$\frac{\partial u_x}{\partial y} = \frac{1}{4\cdot\pi\cdot G}\cdot\left[\begin{array}{l} 2\cdot\dfrac{\partial^3 F_1}{\partial y\partial z^2} - \dfrac{\partial^3 H_1}{\partial x\partial y\partial z} + 2\cdot\nu\cdot\left(\dfrac{\partial^3 F_1}{\partial x^2\partial y} + \dfrac{\partial^3 G_1}{\partial x\partial y^2} + \dfrac{\partial^3 H_1}{\partial x\partial y\partial z}\right) - \\ z\cdot\left(\dfrac{\partial^4 F_1}{\partial x^2\partial y\partial z} + \dfrac{\partial^4 G_1}{\partial x\partial y^2\partial z} + \dfrac{\partial^4 H_1}{\partial x\partial y\partial z^2}\right) \end{array}\right] \tag{4.18}$$

$$\frac{\partial u_x}{\partial z}=\frac{1}{4\cdot\pi\cdot G}\cdot\left[\begin{array}{l}2\cdot\frac{\partial^3 F_1}{\partial z^3}-\frac{\partial^3 H_1}{\partial x\partial z^2}+(2\cdot\nu-1)\cdot\left(\frac{\partial^3 F_1}{\partial x^2\partial z}+\frac{\partial^3 G_1}{\partial x\partial y\partial z}+\frac{\partial^3 H_1}{\partial x\partial z^2}\right)-\\ \\ z\cdot\left(\frac{\partial^4 F_1}{\partial x^2\partial z^2}+\frac{\partial^4 G_1}{\partial x\partial y\partial z^2}+\frac{\partial^4 H_1}{\partial x\partial z^3}\right)\end{array}\right] \tag{4.19}$$

$$\frac{\partial u_y}{\partial x}=\frac{1}{4\cdot\pi\cdot G}\cdot\left[\begin{array}{l}2\cdot\frac{\partial^3 G_1}{\partial x\partial z^2}-\frac{\partial^3 H_1}{\partial x\partial y\partial z}+2\cdot\nu\cdot\left(\frac{\partial^3 F_1}{\partial x^2\partial y}+\frac{\partial^3 G_1}{\partial x\partial y^2}+\frac{\partial^3 H_1}{\partial x\partial y\partial z}\right)-\\ \\ z\cdot\left(\frac{\partial^4 F_1}{\partial x^2\partial y\partial z}+\frac{\partial^4 G_1}{\partial x\partial y^2\partial z}+\frac{\partial^4 H_1}{\partial x\partial y\partial z^2}\right)\end{array}\right] \tag{4.20}$$

$$\frac{\partial u_y}{\partial z}=\frac{1}{4\cdot\pi\cdot G}\cdot\left[\begin{array}{l}2\cdot\frac{\partial^3 G_1}{\partial z^3}-\frac{\partial^3 H_1}{\partial y\partial z^2}+(2\cdot\nu-1)\cdot\left(\frac{\partial^3 F_1}{\partial x\partial y\partial z}+\frac{\partial^3 G_1}{\partial y^2\partial z}+\frac{\partial^3 H_1}{\partial y\partial z^2}\right)-\\ \\ z\cdot\left(\frac{\partial^4 F_1}{\partial x\partial y\partial z^2}+\frac{\partial^4 G_1}{\partial y^2\partial z^2}+\frac{\partial^4 H_1}{\partial y\partial z^3}\right)\end{array}\right] \tag{4.21}$$

$$\frac{\partial u_z}{\partial x}=\frac{1}{4\cdot\pi\cdot G}\cdot\left[\begin{array}{l}\frac{\partial^3 H_1}{\partial x\partial z^2}+(1-2\cdot\nu)\cdot\left(\frac{\partial^3 F_1}{\partial x^2\partial z}+\frac{\partial^3 G_1}{\partial x\partial y\partial z}+\frac{\partial^3 H_1}{\partial x\partial z^2}\right)-\\ \\ z\cdot\left(\frac{\partial^4 F_1}{\partial x^2\partial z^2}+\frac{\partial^4 G_1}{\partial x\partial y\partial z^2}+\frac{\partial^4 H_1}{\partial x\partial z^3}\right)\end{array}\right] \tag{4.22}$$

$$\frac{\partial u_z}{\partial y}=\frac{1}{4\cdot\pi\cdot G}\cdot\left[\begin{array}{l}\frac{\partial^3 H_1}{\partial y\partial z^2}+(1-2\cdot\nu)\cdot\left(\frac{\partial^3 F_1}{\partial x\partial y\partial z}+\frac{\partial^3 G_1}{\partial y^2\partial z}+\frac{\partial^3 H_1}{\partial y\partial z^2}\right)-\\ \\ z\cdot\left(\frac{\partial^4 F_1}{\partial x\partial y\partial z^2}+\frac{\partial^4 G_1}{\partial y^2\partial z^2}+\frac{\partial^4 H_1}{\partial y\partial z^3}\right)\end{array}\right] \tag{4.23}$$

In order to calculate the derivatives of F_1, G_1 and H_1, the corresponding derivatives of Ω (equation (4.13)) have to be evaluated first. The lengthy results are listed below.

$$\frac{\partial\Omega}{\partial x} = \frac{\xi - x}{\rho + z} \quad , \quad \frac{\partial\Omega}{\partial y} = \frac{\eta - y}{\rho + z} \quad , \quad \frac{\partial\Omega}{\partial z} = \ln(\rho + z) \tag{4.24}$$

$$\frac{\partial^2\Omega}{\partial x^2} = \frac{-\rho\cdot(\rho + z) + (x - \xi)^2}{\rho\cdot(\rho + z)^2} \tag{4.25}$$

$$\frac{\partial^2\Omega}{\partial y^2} = \frac{-\rho\cdot(\rho + z) + (y - \eta)^2}{\rho\cdot(\rho + z)^2} \tag{4.26}$$

$$\frac{\partial^2\Omega}{\partial z^2} = \frac{1}{\rho} \tag{4.27}$$

$$\frac{\partial^2\Omega}{\partial x\partial y} = \frac{(x - \xi)\cdot(y - \eta)}{\rho\cdot(\rho + z)^2} \tag{4.28}$$

$$\frac{\partial^2\Omega}{\partial x\partial z} = \frac{x - \xi}{\rho\cdot(\rho + z)} \tag{4.29}$$

$$\frac{\partial^2\Omega}{\partial y\partial z} = \frac{y - \eta}{\rho\cdot(\rho + z)} \tag{4.30}$$

$$\frac{\partial^3\Omega}{\partial x^3} = (x - \xi)\cdot\frac{\left[\rho - \frac{(x - \xi)^2}{\rho}\right]\cdot(\rho + z) + 2\cdot\left[\rho\cdot(\rho + z) - (x - \xi)^2\right]}{\rho^2\cdot(\rho + z)^3} \tag{4.31}$$

$$\frac{\partial^3\Omega}{\partial y^3} = (y - \eta)\cdot\frac{\left[\rho - \frac{(y - \eta)^2}{\rho}\right]\cdot(\rho + z) + 2\cdot\left[\rho\cdot(\rho + z) - (y - \eta)^2\right]}{\rho^2\cdot(\rho + z)^3} \tag{4.32}$$

$$\frac{\partial^3\Omega}{\partial z^3} = -\frac{z}{\rho^3} \tag{4.33}$$

$$\frac{\partial^3\Omega}{\partial x^2 \partial z} = \frac{\rho^2 \cdot (\rho + z) - (x-\xi)^2 \cdot (z + 2\cdot\rho)}{\rho^3 \cdot (\rho + z)^2} \tag{4.34}$$

$$\frac{\partial^3\Omega}{\partial x \partial z^2} = \frac{\xi - x}{\rho^3} \tag{4.35}$$

$$\frac{\partial^3\Omega}{\partial y^2 \partial z} = \frac{\rho^2 \cdot (\rho + z) - (y-\eta)^2 \cdot (z + 2\cdot\rho)}{\rho^3 \cdot (\rho + z)^2} \tag{4.36}$$

$$\frac{\partial^3\Omega}{\partial y \partial z^2} = \frac{\eta - y}{\rho^3} \tag{4.37}$$

$$\frac{\partial^3\Omega}{\partial x \partial y \partial z} = \frac{(x-\xi)\cdot(\eta - y)\cdot(2\cdot\rho + z)}{\rho^3 \cdot (\rho + z)^2} \tag{4.38}$$

$$\frac{\partial^3\Omega}{\partial x \partial y^2} = \frac{\rho^2 \cdot (\rho + z) - (y-\eta)^2 \cdot (3\cdot\rho + z)}{[\rho \cdot (\rho + z)]^3} \cdot (x - \xi) \tag{4.39}$$

$$\frac{\partial^3\Omega}{\partial x^2 \partial y} = \frac{\rho^2 \cdot (\rho + z) - (x-\xi)^2 \cdot (3\cdot\rho + z)}{[\rho \cdot (\rho + z)]^3} \cdot (y - \eta) \tag{4.40}$$

$$\frac{\partial^4\Omega}{\partial x^3 \partial z} = \frac{\xi - x}{\rho^5 \cdot (\rho + z)^3} \cdot \left\{ \begin{array}{l} \rho\cdot(\rho + z)\cdot\left[\rho^2 + 2\cdot(x-\xi)^2\right] + \\ (5\cdot\rho + 3\cdot z)\cdot\left[\rho^2\cdot(\rho + z) - (x-\xi)^2\cdot(z + 2\cdot\rho)\right] \end{array} \right\} \tag{4.41}$$

$$\frac{\partial^4\Omega}{\partial x^2\partial y\partial z}=\frac{y-\eta}{\rho^5\cdot(\rho+z)^3}\cdot\begin{Bmatrix}\left[\rho\cdot(3\cdot\rho+2\cdot z)-2\cdot(x-\xi)^2\right]\cdot\rho\cdot(\rho+z)- \\ \left[\rho^2\cdot(\rho+z)-(x-\xi)^2\cdot(z+2\cdot\rho)\right]\cdot(5\cdot\rho+3\cdot z)\end{Bmatrix} \tag{4.42}$$

$$\frac{\partial^4\Omega}{\partial x^2\partial z^2}=\frac{3\cdot(x-\xi)^2-\rho^2}{\rho^5} \tag{4.43}$$

$$\frac{\partial^4\Omega}{\partial x\partial y^2\partial z}=\frac{\xi-x}{\rho^5\cdot(\rho+z)^3}\cdot\begin{Bmatrix}\left[\rho\cdot(2\cdot\rho+z)+2\cdot(y-\eta)^2\right]\cdot\rho\cdot(\rho+z)- \\ (y-\eta)^2\cdot(z+2\cdot\rho)\cdot(5\cdot\rho+3\cdot z)\end{Bmatrix} \tag{4.44}$$

$$\frac{\partial^4\Omega}{\partial y^3\partial z}=\frac{\eta-y}{\rho^5\cdot(\rho+z)^3}\cdot\begin{Bmatrix}\rho\cdot(\rho+z)\cdot\left[\rho^2+2\cdot(y-\eta)^2\right]+ \\ (5\cdot\rho+3\cdot z)\cdot\left[\rho^2\cdot(\rho+z)-(y-\eta)^2\cdot(z+2\cdot\rho)\right]\end{Bmatrix} \tag{4.45}$$

$$\frac{\partial^4\Omega}{\partial y^2\partial z^2}=\frac{3\cdot(y-\eta)^2-\rho^2}{\rho^5} \tag{4.46}$$

$$\frac{\partial^4\Omega}{\partial x\partial z^3}=\frac{3\cdot z\cdot(x-\xi)}{\rho^5} \tag{4.47}$$

$$\frac{\partial^4\Omega}{\partial y\partial z^3}=\frac{3\cdot z\cdot(y-\eta)}{\rho^5} \tag{4.48}$$

$$\frac{\partial^4\Omega}{\partial z^4}=\frac{3\cdot z^2-\rho^2}{\rho^5} \tag{4.49}$$

$$\frac{\partial^4\Omega}{\partial x\partial y\partial z^2}=\frac{3\cdot(x-\xi)\cdot(y-\eta)}{\rho^5} \tag{4.50}$$

$$\frac{\partial^4 \Omega}{\partial x^2 \partial y \partial z} = \frac{\eta - y}{\rho^5 \cdot (\rho + z)^3} \cdot \begin{Bmatrix} \left[\rho \cdot (2 \cdot \rho + z) + 2 \cdot (x - \xi)^2\right] \cdot \rho \cdot (\rho + z) - \\ \\ (x - \xi)^2 \cdot (z + 2 \cdot \rho) \cdot (5 \cdot \rho + 3 \cdot z) \end{Bmatrix} \tag{4.51}$$

All the previous lengthy expressions must be fitted to the equations giving the stresses. Numerical integration is then applied using the prescribed surface loading. More about this integration and the construction of a suitable grid follow in section 4.4, after the presentation of the thermal stress analysis in the next section.

4.3 Thermoelastic stress analysis

As is explained in the introductory section 4.1, the general problem of Thermoelasticity is one of considerable mathematical difficulty because stress/strain and temperature changes are interrelated. Moreover, sudden (or shock) heat waves cause inertia effects that must be taken into account before attaining a complete solution.

If variable stresses are applied in an elastic body, the resulting displacements, however small, are associated with internal friction of the body and, thus, a temporary increase of the entropy of the system. The internal friction produces heat, which is dissipated in the body. This heat produces thermal stresses, which finally cause the body to thermally expand. Therefore, a boundary stress loading results in a temperature increase that causes further internal stresses translated as thermal expansion. This example shows the coupling effect, which is inherent in the energy equation of Thermoelasticity.

On the other hand, a heat wave is associated with a thermal-stress wave, whose rate of change is, generally, proportional to the rate of change of the heat wave. Furthermore, the thermal-stress wave produces a thermal-displacement wave. Thermal-displacement waves are forms of inertial waves and, therefore, result in inertial stresses (Newton's law). The inertia effects are obviously more intense as the rate of change of the heat wave increases (due to either temperature increase or movement of the temperature field).

Boley and Weiner (1960, chapter 2 of their book), give a rigorous analysis of the relative weight of both the coupling and inertia effects. They showed that for common industrial applications, the coupling effect is of minimal importance. Similarly, when the rate of temperature change is sufficiently small, inertia effects can be disregarded. Practically, this means that inertia effects are very small as long as the rate of temperature increase is much lower than the speed of dilatational waves in a solid. This can be tested mathematically through the following criterion:

$$\boxed{\text{If} \quad \upsilon_\theta << \upsilon_e = \sqrt{\frac{(1-\nu^2)\cdot E}{(1-2\cdot\nu)\cdot\rho_{\mathrm{m}}}} \quad \text{then the inertia effects are negligible.}}$$

where υ_θ is the speed of the temperature increase, υ_e is the speed of dilatational waves, ν is the Poisson ratio, E is the modulus of elasticity, and ρ_{m} is the material density. In our particular application, using the typical example of section 2.8 ($\nu = 0.3$, $E = 207 \cdot 10^9$ Pa, $\rho_{\mathrm{m}} = 7850$ kg/m^3), the speed of dilatational waves is calculated to be $\upsilon_e \cong 7745$ m/s. Using the results of the example of section 3.8 (see figure 3.4), the temperature field on surface 2, in the Hertzian zone of the contact, moves with a speed equal to the relative speed of the particle on the surface, which is 1 m/s (speed V_{p2} in figure 2.11). Of course, the strength of the field varies in time, but for the sake of this example, it can be assumed that the speed V_{p2} is a representative speed of the temperature field. Therefore, $\upsilon_\theta \cong 1$ m/s, which is significantly lower than υ_e ($\cong 7745$ m/s). Hence, ignoring the inertia effects is fully justified.

Following the previous explanations and clarifications, the analysis can now proceed with the solution of the 3-dimensional, uncoupled, quasi-static thermoelastic problem. The general, thermoelastic stress-strain equations are written as follows (Timoshenko and Goodier, 1970):

$$\left.\begin{aligned}
\varepsilon_x - \alpha \cdot T &= \frac{1}{E} \cdot \left[\sigma_x - \nu \cdot \left(\sigma_y + \sigma_z\right)\right] \\
\varepsilon_y - \alpha \cdot T &= \frac{1}{E} \cdot \left[\sigma_y - \nu \cdot \left(\sigma_z + \sigma_x\right)\right] \\
\varepsilon_z - \alpha \cdot T &= \frac{1}{E} \cdot \left[\sigma_z - \nu \cdot \left(\sigma_x + \sigma_y\right)\right]
\end{aligned}\right\} \tag{4.52}$$

$$\gamma_{xy} = \frac{\tau_{xy}}{G} \quad , \quad \gamma_{yz} = \frac{\tau_{yz}}{G} \quad , \quad \gamma_{zx} = \frac{\tau_{zx}}{G} \tag{4.53}$$

where σ stands for normal stress, τ for shear stress, ε for normal strain, and γ for shear strain. Moreover, E is the modulus of elasticity, G is the shear modulus, α is the coefficient of linear thermal expansion, and T is the temperature increase. The left parts of the thermoelastic stress-strain equations (4.52) refer to the total strains, which are made of two parts;

(1) A term ($\alpha{\cdot}T$), owing to the change of volume of the body following a temperature change. It is noted that for an isotropic body, this volume change results in normal strains only (no angular distortion).

(2) A term required to ensure the continuity of the body and to satisfy any external loads.

The thermoelastic displacements u, υ and w are related to the normal strains through the following equations:

$$\frac{\partial u}{\partial x} = \varepsilon_x \quad , \quad \frac{\partial \upsilon}{\partial y} = \varepsilon_y \quad , \quad \frac{\partial w}{\partial z} = \varepsilon_z \tag{4.54}$$

Goodier (1937) proposed a neat method to solve the thermoelastic problem, similar to the one used in elasticity through the application of the Airy stress functions. In a similar fashion of an Airy stress function, Goodier used what is known as "thermoelastic displacement potential", denoted by "ψ". Generally, ψ is a function of the spatial coordinates and time:

$$\psi = \psi(x, y, z, t) \tag{4.55}$$

By definition, the thermoelastic displacements are related to the thermoelastic displacement potential through the following equations:

$$u = \frac{\partial \psi}{\partial x} \quad , \upsilon = \frac{\partial \psi}{\partial y} \quad , \ w = \frac{\partial \psi}{\partial z} \tag{4.56}$$

Using equations (4.54) and (4.56), equations (4.52) give the following result:

$$(1-\nu)\cdot\frac{\partial(\nabla^2\psi)}{\partial h} = (1+\nu)\cdot\alpha\cdot\frac{\partial T}{\partial h} \quad , h \leftrightarrow x, y, z \tag{4.57}$$

where ∇^2 is the Laplacian operator

$$\nabla^2 \equiv \frac{\partial}{\partial x^2} + \frac{\partial}{\partial y^2} + \frac{\partial}{\partial z^2} \tag{4.58}$$

It can easily be shown that equations (4.57) are satisfied if ψ is taken to be the solution of the following equation:

$$\nabla^2\psi = \frac{1+\nu}{1-\nu}\cdot\alpha\cdot T \tag{4.59}$$

The heat-conduction equation is written as follows:

$$\nabla^2 T = \frac{1}{\lambda}\cdot\frac{\partial T}{\partial t} \tag{4.60}$$

where λ is thermal diffusivity. Differentiating equation (4.59) with respect to time and using equation (4.60), it is derived that

$$\nabla^2\left(\frac{\partial \psi}{\partial t} - \frac{1+\nu}{1-\nu}\cdot\alpha\cdot\lambda\cdot T\right) = 0 \tag{4.61}$$

which has a particular solution

$$\frac{\partial \psi}{\partial t} = \frac{1+\nu}{1-\nu} \cdot \alpha \cdot \lambda \cdot T \tag{4.62}$$

Integration of equation (4.62) yields

$$\psi(x, y, z, t) = \frac{1+\nu}{1-\nu} \cdot \alpha \cdot \lambda \cdot \int_0^t T(x, y, z, t') \cdot \mathrm{d}t' + c(x, y, z) \tag{4.63}$$

The integration function $c(x,y,z)$ in equation (4.63) must satisfy equation (4.59). Thus:

$$\nabla^2 c(x, y, z) = \frac{1+\nu}{1-\nu} \cdot \alpha \cdot T(x, y, z, 0) \tag{4.64}$$

which has a solution $c(x,y,z) = 0$ because $T(x,y,z,0) = 0$ (the flash temperature, or temperature increase above the bulk temperature, is initially zero). Finally:

$$\psi(x, y, z, t) = \frac{1+\nu}{1-\nu} \cdot \alpha \cdot \lambda \cdot \int_0^t T(x, y, z, t') \cdot \mathrm{d}t' \tag{4.65}$$

More information on the above method can be obtained from Goodier (1937), Boley and Weiner (1960, section 3.4), and Timoshenko and Goodier (1970, section 162).

It must be noted that the previous analysis gives a particular solution, which, in general, results in non-zero surface thermal stresses. This means that surface thermal-stress components $\overline{\sigma}^{(\psi)}_{z,\mathrm{thermal}}, \overline{\tau}^{(\psi)}_{zy,\mathrm{thermal}}$ and $\overline{\tau}^{(\psi)}_{zx,\mathrm{thermal}}$ are generally found to have non-zero values. Since the heated surfaces must be free of stresses (the problems of thermal and mechanical loading are initially solved independently, which means that for the thermal stress problem, the surfaces are free of stresses), an equal and opposite surface loading is artificially applied, in order to remove these non-zero thermal stress components (see step 5 below).

The whole procedure to solve the thermoelastic problem is summarized below. The procedure is of course applied in our particular case, that being the squashing of a soft particle in a line, elastohydrodynamic contact.

Step 0

The motion and behaviour of the particle are found by applying the preliminary part of the model, presented in chapter 2. This involves the calculation of solid pressure and traction between the particle and the counterfaces. Following that, the flash temperature fields of the counterfaces are calculated (chapter 3). The temperature calculations take place in 3-dimesional grids, covering the heated space in each counterface. (More on this follows in the next chapter.)

Step 1

For each node of the grids, the thermoelastic displacement potential is calculated from equation (4.65).

Step 2

For each node of the grids, the thermoelastic displacements are calculated from equations (4.56).

Step 3

For each node of the grids, the normal thermoelastic strains are calculated from equations (4.54), whereas the shear strains are calculated from the following equations:

$$\gamma_{xy} = \frac{\partial u}{\partial y} + \frac{\partial \upsilon}{\partial x} \quad , \gamma_{yz} = \frac{\partial \upsilon}{\partial z} + \frac{\partial w}{\partial y} \quad , \gamma_{zx} = \frac{\partial w}{\partial x} + \frac{\partial u}{\partial z} \tag{4.66}$$

Step 4

For each node of the grids, the thermoelastic stresses are calculated by the following equations:

$$\sigma_i = L \cdot \left(\varepsilon_x + \varepsilon_y + \varepsilon_z\right) + 2 \cdot G \cdot \varepsilon_i - \left(3 \cdot L + 2 \cdot G\right) \cdot \alpha \cdot T \qquad , i \leftrightarrow x, y, z \tag{4.67}$$

$$\tau_j = G \cdot \gamma_j \qquad , j \leftrightarrow xy, yz, zx \tag{4.68}$$

where the Lamé constant L is

$$L \equiv \frac{\nu \cdot E}{\left(1+\nu\right) \cdot \left(1 - 2 \cdot \nu\right)} \tag{4.69}$$

Step 5

Finally, a surface loading $\left\langle p, q_x, q_y \right\rangle$ is applied, such that

$$p = -\overline{\sigma}^{(\psi)}_{z,\mathrm{thermal}} \quad , \quad q_x = -\overline{\tau}^{(\psi)}_{zx,\mathrm{thermal}} \quad , \quad q_y = -\overline{\tau}^{(\psi)}_{zy,\mathrm{thermal}} \tag{4.70}$$

in order to remove any surface thermal stresses that are a byproduct of the current method. The subsurface stresses due to this surface loading are calculated according to the general method (Boussinesq-Cerruti equations) of section 4.2. After this step, the heated surfaces are guaranteed to be free of thermal stresses.

4.4 Overall-stress problem

The calculation of the overall stresses is a matter of an algebraic addition of the mechanical and thermal stresses, provided that both are below the elastic limit. This takes place at each node of the grids and can be accompanied by an appropriate yield check to test if there are any areas of plastic strains.

The set-up of a grid is such that a $z = constant$ layer (see figure 4.2) has as few nodes as is necessary for satisfactorily accurate results. However, this rule of thumb is applied only for the flash temperature and thermal-stress calculations, because these calculations are by far the most time-consuming, taking more than 50 % of the overall computational time for the complete solution of the problem. However, the solution of the Boussinesq-Cerruti equations (section 4.2) is done using vastly denser surface grids, in order to improve the accuracy of the necessary integrations (see equations (4.10)-(4.12)). Thus, for all mechanical-stress calculations, the surface grids used are constructed from the initial grids (used for temperature and thermal-stress calculations) with new nodes introduced among the old ones, as is shown in figure 4.3.

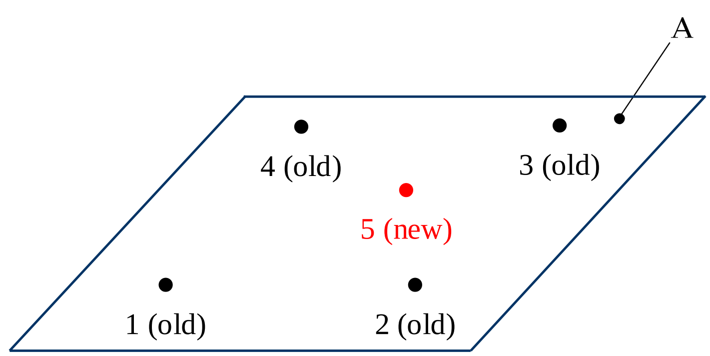

Figure 4.3 "Old" nodes (for temperature and thermal-stress calculations) and interpolation (new) nodes for increasing the mechanical-stress calculation accuracy.

There are 2500 new nodes for every set of four neighboring old nodes as in figure 4.3. The total number N of the surface nodes is given by the following equation:

$$N = 2500 \cdot \left(\frac{N_{\text{old}}}{2} - 1 \right) + N_{\text{old}} = 1251 \cdot N_{\text{old}} - 2500 \tag{4.71}$$

where N_{old} is the number of the old nodes. For example, if the initial surface grid contains 50×10 = 500 old nodes (used for temperature and thermal stress calculations), the total number of surface nodes (used for mechanical and overall stress calculations) is N = 1251·500 – 2500 = 623000.

The stresses at every new node are calculated by bilinear interpolation, using the stresses at the four surrounding old nodes. For example, using figure 4.3, the stress at the new node 5 is:

$$\sigma_5 = (1 - c_1) \cdot (1 - c_2) \cdot \sigma_1 + c_1 \cdot (1 - c_2) \cdot \sigma_2 + c_1 \cdot c_2 \cdot \sigma_3 + (1 - c_1) \cdot c_2 \cdot \sigma_4 \tag{4.72}$$

where

$$c_1 \equiv \frac{x_5 - x_1}{x_2 - x_1} \quad \text{and} \quad c_2 \equiv \frac{y_5 - y_1}{y_4 - y_1} \tag{4.73}$$

whereas (x,y) denote the coordinates of a node.

4.4.1 Boundary conditions for the overall-stress problem

The boundary conditions of the overall-stress problem are as follows.

(1) The solid pressure between the particle and the surfaces.

(2) The surface shear stresses due to particle’s motion relatively to a counterface.

(3) The elastohydrodynamic pressure between the counterfaces. This is satisfactorily approximated by a Hertzian pressure distribution in the Hertzian zone of the contact.

It is noted here that surface elastohydrodynamic tractions in the case of sliding contacts are neglected, as these are significantly lower than all the other surface stress components of the particular problem. In order to realize this, it suffices to say that a typical elastohydrodynamic traction coefficient is in the order of 0.06, whereas the friction coefficient between the particle and a counterface is in the order of 0.1-0.2, assuming that the lubrication between the particle and a counterface is boundary. Moreover, the particle occupies a significant area when being in the Hertzian zone of the contact, where the elastohydrodynamic tractions have (in the absence of the particle) their maximum strength. Thus, in the vicinity of the particle, the counterfaces sense (mainly) the effects of the presence of the particle rather than any elastohydrodynamic shearing effects.

The boundary conditions (1) and (2) are applicable in the area occupied by the particle at any time during particle's motion in the elastohydrodynamic gap. Condition (3) is applicable mainly in the Hertzian zone of the contact, excluding the area occupied by the particle. Therefore, a surface loading of the form $\langle p,0,0 \rangle$ is applied on each counterface, where

$$p = \begin{cases} \dfrac{2 \cdot W}{\pi \cdot b^2} \cdot \sqrt{b^2 - x^2} & \text{, if } -b < x < x_\mathrm{p} - R < b \ \text{ or } \ -b < x_\mathrm{p} + R < x < b \\ 0 & \text{, if } -b \le x_\mathrm{p} - R \le x \le x_\mathrm{p} + R \le b \end{cases} \tag{4.74}$$

whereas W is the load per unit length of the line contact, b is the Hertzian contact semi-width (equation (2.2)), x_p is the distance of the centre of the particle from the centre of the Hertzian zone of the contact, and R is the radius of the deformed (disk shaped) particle (equation 2.20)). However, this means that a generalized integration ($-\infty < y < +\infty$) along the y-axis must be performed. In order to avoid this computation, the following alternative method is applied; from Johnson (1985, pages

102-104), the stresses at a general point (x,z), produced by a Hertzian line loading as that of equation (4.74), are as follows:

$$\sigma_x^{(\text{Hertz})} = -\frac{2 \cdot W}{\pi \cdot b^2} \cdot \left(m \cdot \frac{m^2 + 2 \cdot n^2 + z^2}{m^2 + n^2} - 2 \cdot z \right) \tag{4.75}$$

$$\sigma_z^{(\text{Hertz})} = -\frac{2 \cdot W}{\pi \cdot b^2} \cdot m \cdot \frac{m^2 - z^2}{m^2 + n^2} \tag{4.76}$$

$$\tau_{zx}^{(\text{Hertz})} = -\frac{2 \cdot W}{\pi \cdot b^2} \cdot n \cdot \frac{m^2 - z^2}{m^2 + n^2} \tag{4.77}$$

where

$$m \equiv \operatorname{sgn}(z) \cdot \frac{1}{2} \cdot \left[\sqrt{\left(b^2 - x^2 + z^2\right)^2 + 4 \cdot (x \cdot z)^2} + b^2 - x^2 + z^2 \right] \tag{4.78}$$

$$n \equiv \operatorname{sgn}(x) \cdot \frac{1}{2} \cdot \left[\sqrt{\left(b^2 - x^2 + z^2\right)^2 + 4 \cdot (x \cdot z)^2} - b^2 + x^2 - z^2 \right] \tag{4.79}$$

The previous stress components can now be superimposed to those found by the mechanical loading (solely due to the presence of the particle) and the thermal loading of the counterfaces. Finally, the complete sub-surface stress field is obtained after accounting for the area occupied by the particle, which must be free of fluid (elastohydrodynamic pressure). The latter is achieved by applying a surface loading $\langle p,0,0 \rangle$, where

$$p = -\frac{2 \cdot W}{\pi \cdot b^2} \cdot \sqrt{b^2 - x^2} \quad , -b \le x_{\mathrm{p}} - R \le x \le x_{\mathrm{p}} + R \le b \tag{4.80}$$

(notice the minus sign on the right-hand side of equation (4.80)). What is done in essence is to apply an opposite Hertzian loading (tension instead of compression) over the area occupied by the particle.

Finally, the overall stresses are:

$$\left.\begin{aligned} \sigma_{\text{overall}} &= \sigma_{\text{mechanical}} + \sigma_{\text{thermal}} \\ \tau_{\text{overall}} &= \tau_{\text{mechanical}} + \tau_{\text{thermal}} \end{aligned}\right\} \tag{4.81}$$

4.4.2 Overall strains and displacements

Having calculated the overall stresses, the overall normal strains can now readily be calculated from the well-known Hookean equations of linear isothermal Elasticity:

$$\left.\begin{aligned} \varepsilon_{x,\text{overall}} &= \frac{1}{E}\cdot\left[\sigma_{x,\text{overall}} - \nu\cdot\left(\sigma_{y,\text{overall}} + \sigma_{z,\text{overall}}\right)\right] \\ \varepsilon_{y,\text{overall}} &= \frac{1}{E}\cdot\left[\sigma_{y,\text{overall}} - \nu\cdot\left(\sigma_{z,\text{overall}} + \sigma_{x,\text{overall}}\right)\right] \\ \varepsilon_{z,\text{overall}} &= \frac{1}{E}\cdot\left[\sigma_{z,\text{overall}} - \nu\cdot\left(\sigma_{x,\text{overall}} + \sigma_{y,\text{overall}}\right)\right] \end{aligned}\right\} \tag{4.82}$$

The overall displacements are calculated as follows:

$$\left.\begin{aligned} \varepsilon_{x,\text{overall}} &= \frac{\partial u}{\partial x} \Rightarrow \frac{u_{i+1} - u_{i-1}}{2\cdot\Delta x} \cong \varepsilon_{x_i,\text{overall}} \\ \varepsilon_{y,\text{overall}} &= \frac{\partial \upsilon}{\partial y} \Rightarrow \frac{\upsilon_{j+1} - \upsilon_{j-1}}{2\cdot\Delta y} \cong \varepsilon_{y_j,\text{overall}} \\ \varepsilon_{z,\text{overall}} &= \frac{\partial w}{\partial z} \Rightarrow \frac{w_{k+1} - w_{k-1}}{2\cdot\Delta z} \cong \varepsilon_{z_k,\text{overall}} \end{aligned}\right\} \tag{4.83}$$

where Δx, Δy and Δz are the spatial steps of the grid. The discretized equations (4.83) are rearranged to solve explicitly for the unknown displacements.

The dimensions of the grid are chosen such that the grid is larger than the practically heated space, which is considered as the space with a flash temperature of at least 1 °C. Moreover, the grid is large enough to ensure that the displacements at its boundaries (excluding the heated surface) are almost zero. More specifically, if N_x, N_y and N_z are the initial numbers of grid nodes along axes x, y and z, respectively, such that $1 \le i \le N_x$, $1 \le j \le N_y$ and $1 \le k \le N_z$, then the following boundary conditions are imposed:

$$u_{i=1} = u_{i=N_x} = \upsilon_{j=N_y} = w_{k=N_z} = 0 \qquad (4.82)$$

where $w_{k=N_z}$ is the *w*-displacement at the bottom of the heated space, away from the heated surface that lies at $z = 0$. Equations (4.82) apply the Saint-Venant's principle of stresses and strains becoming "exponentially" weaker away from the contact zone. In reality, and for mathematical consistency, the overall displacements calculated here are relative to the corresponding displacements at the boundaries of the grid (excluding the heated surface), which are taken as a suitable reference point.

4.5 Yield check

Having calculated the overall stresses throughout the solids, it is straightforward to check for plastic deformations. For this, the Maxwell-Huber-von Mises criterion, which is widely known as the "von Mises" criterion, is considered the most suitable choice. This criterion is expressed as follows:

$$\boxed{\text{If} \quad (\sigma_x - \sigma_y)^2 + (\sigma_y - \sigma_z)^2 + (\sigma_z - \sigma_x)^2 + 6 \cdot (\tau_{xy}^2 + \tau_{yz}^2 + \tau_{zx}^2) \ge 2 \cdot Y^2 \quad \text{then yield occurs.}}$$

where Y is the yield stress in uniaxial tension (or compression, depending on the loading situation, although for metals, there is no significant difference).

The von Mises criterion is better suited for ductile rather than brittle materials and experiments with metals have shown the slight superiority of the von Mises criterion over its usual contender – the Tresca criterion (see Khan and Huang, 1995, section 4.3.3). Therefore, the von Mises criterion is the best choice in our case (metals) and is always the preferred one in this Thesis.

CHAPTER 5

REFINEMENT OF THE MODEL AND GENERAL APPLICATION

5.1 Introduction

Chapters 2-4 of this Thesis are devoted to the development of a general model to study the thermo-elasto-plastic problem of the squashing of a soft and ductile particle in a line elastohydrodynamic contact. Chapter 2 deals with the particle's kinematics inside the contact gap and shows that, in the cases of contacts that involve sliding, the particle sticks to the counterface with the higher friction coefficient immediately after being pinched, thus sliding on the other counterface along the inlet and the Hertzian zone of the contact. The study is restricted to soft and ductile particles, which leaves space to consider the counterfaces as being rigid. In reality, the counterfaces are deformable, and their deformation causes some of the pressure between them and the particle to be released. Moreover, the elastohydrodynamic pressure in the contact affects the particle when the latter comes close to the Hertzian zone and the effect is transferred to the pressure and traction between the particle and the counterfaces. These effects have so far been neglected as the solid pressure model used until now is that presented in section 2.6, which omits counterface deformations and the effective elastohydrodynamic pressure on the particle.

In the present chapter, the pressure model of section 2.6 is replaced by a new and more detailed model to eliminate the previously mentioned inadequacies. The improvements reflect the effect of both mechanical and thermal stresses on the surface displacements, which are coupled in a non-linear relation to resolve the pressure between the particle and the counterfaces. The complete model is then presented in its full potential through a detailed example, which includes all the

3-dimensional temperature and stress/strain/displacement calculations. In summary, the model includes the following:

- Calculation of the motion of a trapped particle in a contact (chapter 2).
- Calculation of the heat produced due to friction between the particle and the counterfaces. Heat partitioning between the counterfaces (chapter 3).
- 3-dimensional heat conduction calculations in the counterfaces, assuming thermally anisotropic (orthotropic) solids (chapter 3).
- Calculation of the heat losses from the particle and the counterfaces to the lubricant (chapter 3).
- 3-dimensional mechanical and thermal stress/strain/displacement calculations for both counterfaces (chapter 4).
- Checking for plastic deformations in the counterfaces and, finally, assessing the risk of damage in the contact, due to the presence of the particle (chapter 4).

5.2 Solid pressure on the particle – an advanced model

In section 2.6, a simplified version of a model developed by Hamer *et al.* (1989b) to calculate the pressure on a soft particle being plastically compressed between two hard flat surfaces, was temporarily adopted. That model served as a neat tool to obtain quick results needed in further parts of the main model of this Thesis, but is not adequate (in its simplified form used by the present author) to give a satisfactorily accurate estimation of the pressure. There are three reasons for this inadequacy.

(1) The omission of surface displacements, normally imposed by the calculated pressure, which would release some of the pressure. This was done by the present author to simplify the early analysis and is not a feature of the original model of Hamer *et al.* (1989).

(2) The omission of thermal displacements, induced by the frictional heating and thermal stresses in the contact, as is shown in chapter 3.

(3) The omission of the effect of the elastohydrodynamic pressure along the periphery of the (disk shaped) particle.

The above are all removed in this section. Moreover, the local speeds and tractions at the interfaces of the particle with the counterfaces are more clearly and accurately defined, as is shown later. In general, the deformation of the particle is not axisymmetrical, because the tractions on both of its faces (when the particle is seen as a disk) and the lubricant pressure around it are variable with position. The result might be a slightly elongated particle, the elongation being in the direction of sliding of the counterfaces, if such a motion exists. In purely rolling contacts, this elongation is not present. This has indeed been experimentally shown by Wan and Spikes (1988) and Dwyer-Joyce (1993). However, even in the case of sliding contacts, the particle will be assumed to remain circular, and the reasons for this assumption are explained in section 2.4.

According to the model of section 2.4 (see figure 2.5), the particle is modelled as a cylinder, having its faces in contact with the counterfaces. At the last stage of its squashing (inside the Hertzian zone of the contact), the particle is thus transformed into a very thin circular disk. At any stage during its plastic deformation, the particle is partitioned in elemental orthogonal parallelepipeds, which, if projected on the xy plane as in figure 5.1, appear as squares. These parallelepipeds or squares are called “sectors” in the remaining of this study.

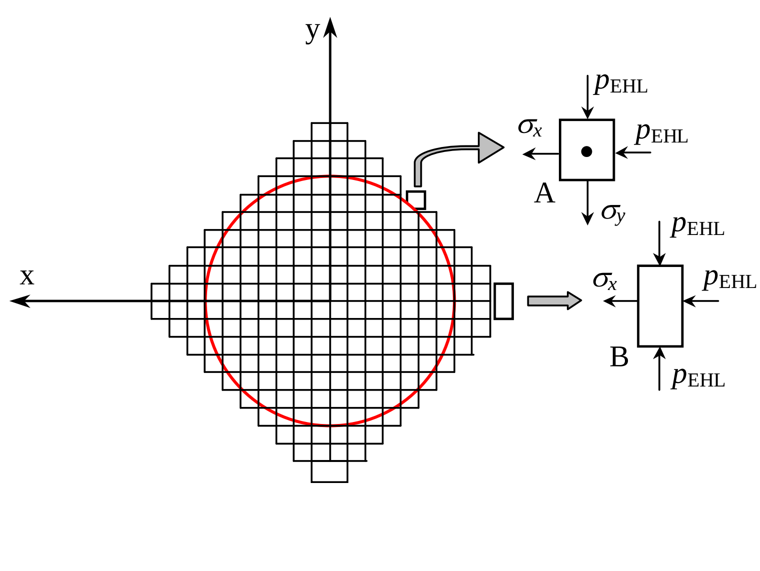

Figure 5.1 Particle (red circle) partitioned in sectors.

The peripheral sectors of the partitioned particle (figure 5.1) have either two or three wetted sides (like sectors A and B, respectively), which are under the action of the local elastohydrodynamic pressure p_{EHL}. The elastohydrodynamic pressure is calculated by solving the line EHL contact problem by any suitable method. Alternatively, it can be substituted by the relative Hertzian pressure distribution, which serves as a good approximation, especially in the Hertzian zone of the contact. Either way, pressure p_{EHL} is known at any position (x,y) in the contact.

Any sector of the particle is under the action of three normal stresses: the internal stresses σ_x, σ_y, and the externally applied solid pressure p (figure 5.2). Surface tractions τ_1 on surface 1 and τ_2 (not shown in figure 5.2) on surface 2 are also applied, caused by the friction between the particle and the counterfaces.

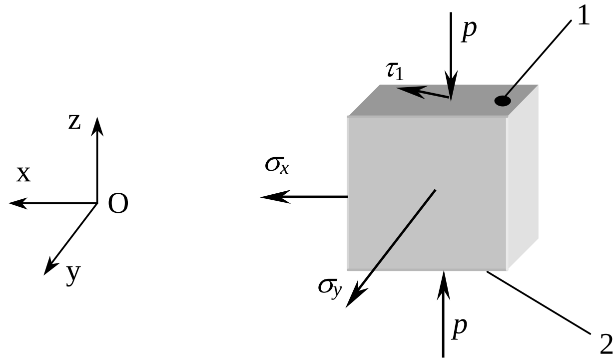

Figure 5.2 Forces on an elemental parallelepiped (sector) of the particle.

The directions of vectors $\underset{\sim}{\tau_1}$ and $\underset{\sim}{\tau_2}$ depend on the direction of the local velocity vectors. If V_{p1} and V_{p2} are the speeds of the particle as a rigid body relatively to counterfaces 1 and 2, respectively (see section 2.7, figure 2.7 and equations (2.45), (2.46)) and V_{extr} is the extrusion speed of the particle (see equation (2.52)), then the magnitudes of the x and y-components of the velocity vector of a sector (velocity relatively to a counterface) are given by the following equations:

$$\left.\begin{aligned} V_{1,x} &= -V_{\mathrm{p1}} - V_{\mathrm{extr}} \cdot \cos(\vartheta) \\ V_{2,x} &= V_{\mathrm{p2}} - V_{\mathrm{extr}} \cdot \cos(\vartheta) \\ V_{y} &= V_{\mathrm{extr}} \cdot \sin(\vartheta) \end{aligned}\right\} \quad ,(0 \le \vartheta \le \pi, \;\; V_{\mathrm{p1}} > 0, \;\; V_{\mathrm{p2}} > 0) \tag{5.1}$$

where angle ϑ can be viewed in figure 3.1 (it's the angle between axis x and the vector of the extrusion velocity). The resultant speeds V_1 and V_2 of a sector relatively to counterfaces 1 and 2 respectively, are as follows:

$$V_i = \sqrt{V_{i,x}^2 + V_y^2} \quad , (i = 1, 2) \tag{5.2}$$

The following angles φ_1 and φ_2 are defined:

$$\varphi_i \mathrel{\hat{=}} \angle\left(\underset{\sim}{V_i}, \mathrm{Ox}\right) = \arctan\left(\left|\frac{V_y}{V_{i,x}}\right|\right) \quad , (i = 1, 2, \;\; \varphi_i \le \pi / 2) \tag{5.3}$$

From the geometry of the problem and assuming (without loss of generality) that counterface 1 is moving with a higher tangential speed in comparison with counterface 2 ($u_1 > u_2$, see figure 2.1), it is proved that:

$$\text{If } V_i \ne 0 \Rightarrow \left\{\begin{aligned} \tau_i &= \mu_i \cdot p \\ \tau_{i,x} &= -\operatorname{sgn}(V_{i,x}) \cdot \tau_i \cdot \cos(\varphi_i) \\ \tau_{i,y} &= -\operatorname{sgn}(V_y) \cdot \tau_i \cdot \sin(\varphi_i) \end{aligned}\right\} \quad , (i = 1, 2) \tag{5.4}$$

$$\text{If } V_i = 0 \Rightarrow \left\{\begin{aligned} \tau_i &= \mu_j \cdot p \\ \tau_{i,x} &= \operatorname{sgn}(V_{j,x}) \cdot \tau_i \cdot \cos(\varphi_j) \\ \tau_{i,y} &= \operatorname{sgn}(V_y) \cdot \tau_i \cdot \sin(\varphi_j) \end{aligned}\right\} \quad , (i = 1, 2, \quad j = 1, 2, \quad i \ne j) \tag{5.5}$$

A typical sector has dimensions $\Delta s \times \Delta s \times H$ where H is the height of the sector along the z-axis:

$$H = h + \overline{w}_1 + \overline{w}_2 \tag{5.6}$$

where h is the elastohydrodynamic film thickness at the position of the sector (as if there were no particle present in the contact) and $\overline{w}_1, \overline{w}_2$, are the surface normal displacements of counterfaces 1 and 2, respectively, at the position of the sector. The surface displacements consist of two parts: a thermal part and a mechanical part.

$$\overline{w}_i = \overline{w}_{i,\text{thermal}} + \overline{w}_{i,\text{mechanical}} \quad ,(i = 1, 2) \tag{5.7}$$

Thermal normal surface displacements are calculated using the method of the "thermoelastic displacement potential" (see section 4.3). After calculating the thermal stresses, the surface thermal stresses $\overline{\sigma}^{(\psi)}_{z,\text{thermal}}$, $\overline{\tau}^{(\psi)}_{zx,\text{thermal}}$ and $\overline{\tau}^{(\psi)}_{zy,\text{thermal}}$, arising from the application of the method of the Potential (denoted by the symbol "ψ"), as explained in section 4.3, are suppressed by the application of an opposite surface loading $\left\langle -\overline{\sigma}^{(\psi)}_{z,\text{thermal}}, -\overline{\tau}^{(\psi)}_{zx,\text{thermal}}, -\overline{\tau}^{(\psi)}_{zy,\text{thermal}} \right\rangle$. The normal surface displacements due to the action of the suppressive surface loading are the sum of the displacements owing to the normal and the tangential surface stresses:

$$\overline{w}_i^{(\text{suppress})} = \overline{w}_{i,\text{normal}} + \overline{w}_{i,\text{tangential}} \quad ,(i = 1, 2) \tag{5.8}$$

From the Boussinesq-Cerruti equations (section 4.2), the following equations are extracted:

$$\overline{w}_{i,\text{normal}} = \frac{1-\nu_i^2}{\pi \cdot E_i} \cdot \iint\limits_{i\text{-counterface}} \frac{-\left[\overline{\sigma}^{(\psi)}_{z,\text{thermal}}\right]_{(\xi,\eta)}}{\sqrt{(\xi - x)^2 + (\eta - y)^2}} \cdot \mathrm{d}\xi \cdot \mathrm{d}\eta \tag{5.9}$$

$$\overline{w}_{i,\mathrm{tangential}} = \frac{2\cdot\nu_i - 1}{4\cdot\pi\cdot G_i}\cdot \iint\limits_{i\text{-counterface}} \frac{(\xi - \mathrm{x})\cdot\left\{-\left[\tau_{zx,\mathrm{thermal}}^{(\psi)}\right]_{(\xi,\eta)}\right\} + (\eta - \mathrm{y})\cdot\left\{-\left[\tau_{zy,\mathrm{thermal}}^{(\psi)}\right]_{(\xi,\eta)}\right\}}{(\xi - x)^2 + (\eta - y)^2}\cdot \mathrm{d}\xi\cdot\mathrm{d}\eta \qquad (5.10)$$

Finally,

$$\overline{w}_{i,\mathrm{thermal}} = \overline{w}_i^{(\psi)} + \overline{w}_i^{(\mathrm{suppress})} \quad ,(i = 1, 2) \qquad (5.11)$$

where the first part of the right-hand side of equation (5.11) is the surface displacement due to the application of the “thermoelastic displacement potential”.

On the other hand, the mechanical part of the overall surface normal displacement (see equation (5.7)) is calculated exactly as outlined in equations (5.8)-(5.10), where, instead of the suppressive surface loading, the mechanical loading imposed by the particle (pressure and tractions at the Hertzian contact circle between the particle and each counterface) $\langle p, \tau_{i,x}, \tau_{i,y} \rangle$ is used, where subscript i refers to a counterface (i = 1, 2). Of course, the calculation of the mechanical displacements requires the solid pressure between the particle and the counterfaces be known.

In order to calculate the solid pressure distribution on the particle, it is necessary to start from the peripheral sectors (figure 5.3), where the stress conditions are known (lubricant pressure p_{EHL}).

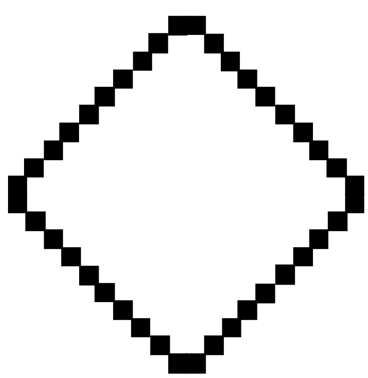

Figure 5.3 Peripheral sectors of the particle.

The force equilibrium of a sector along the axis x or y is written as follows:

$$\left(\sigma_q + \mathrm{d}\sigma_q\right)\cdot H \cdot \mathrm{d}y - \sigma_q \cdot H \cdot \mathrm{d}y + \tau_{1,q} \cdot \mathrm{d}x \cdot \mathrm{d}y + \tau_{2,q} \cdot \mathrm{d}x \cdot \mathrm{d}y = 0 \quad , q \leftrightarrow x, y \tag{5.12}$$

where dx = dy (= ds) because a sector is modelled as square on the xy-plane. Equation (5.12) finally gives:

$$-H \cdot \frac{\partial \sigma_q}{\partial q} = \tau_{1,q} + \tau_{2,q} \quad , q \leftrightarrow x, y \tag{5.13}$$

Discretizing equation (5.13), the following two equations are derived:

$$\sigma_x^{(i-1)} \cong \sigma_x^{(i)} + \frac{\Delta s}{H} \cdot \left[\tau_{1,x}^{(i)} + \tau_{2,x}^{(i)}\right] \tag{5.14}$$

$$\sigma_y^{(j-1)} \cong \sigma_y^{(j)} + \frac{\Delta s}{H} \cdot \left[\tau_{1,y}^{(j)} + \tau_{2,y}^{(j)}\right] \tag{5.15}$$

where sector (i–1,j–1) shares a common side with sector (i,j), the former being inner and the latter being outer. In equations (5.14) and (5.15), Δs denotes the length of an edge of the square base of a sector and is constant for all sectors:

$$\Delta s = \frac{R}{N_{\mathrm{y}}} \tag{5.16}$$

where R is the radius of the deformed (disk shaped) particle (equation (2.20)) and N_{y} is the number of sectors along the radius of the particle on axis y. The peripheral sectors are located as follows:

$$(i, j)_{\mathrm{peripheral}} \in \left\{ i = \pm\left[\frac{1}{2} + \sqrt{N_y^2 - \left(|j| - \frac{1}{2}\right)^2}\right] \;, -N_y \le j \le N_y \;, j \ne 0 \right\} \tag{5.17}$$

where the square brackets in equation (5.17) denote the "integer part" of the enclosed expression.

During its motion inside the elastohydrodynamic gap, the particle is under a full plastic state. Hence, the von Mises yield criterion can be applied at each sector of the particle. The von Mises equation is written as follows:

$$(\sigma_x - \sigma_y)^2 + (\sigma_y - \sigma_z)^2 + (\sigma_z - \sigma_x)^2 + 6 \cdot \left(\tau_{xy}^2 + \tau_{yz}^2 + \tau_{zx}^2\right) = 2 \cdot Y_{\mathrm{p}}^2 \tag{5.18}$$

where Y_{p} in our case is the yield stress in uniaxial compression of the particle's material (referring to the specific temperature of the sector). In our particular case, τ_{yz} and τ_{zx} are the tractions at the bases of the sector, whereas τ_{xy} is much less than the other shear stresses and can be ignored:

$$\tau_{zx} = \tau_{i,x} \quad , \quad \tau_{yz} = \tau_{zy} = \tau_{i,y} \quad , \quad \tau_{xy} << \min\{\tau_{yz}, \tau_{zx}\} \ , (i = 1, 2) \tag{5.19}$$

where $\tau_{i,x}$ and $\tau_{i,y}$ are given in equations (5.4) and (5.5). However, a complication arises because the tractions on the two bases of a sector are unequal ($\tau_1 \neq \tau_2$) when there is sliding <u>on both faces</u> of a sector, which is true (according to the model of the Thesis) when the particle is in the inlet zone of the contact, or in other words, during particle's extrusion. The inequality of tractions τ_1 and τ_2 is due to the unequal friction coefficients used for the counterfaces. In any case, the following effective friction coefficient is used in the von-Mises equation:

$$\mu \mathrel{\widehat{=}} \left\{ \begin{array}{l} \dfrac{\mu_1 + \mu_2}{2}, \text{ if } V_1 \neq 0 \text{ and } V_2 \neq 0 \\ \\ \mu_1 \text{ or } \mu_2 \text{ , if } V_1 = 0 \text{ or } V_2 = 0 \text{ , according to equations (5.4) and (5.5)} \end{array} \right\} \tag{5.20}$$

The von Mises equation (5.18) is finally written as follows (bearing in mind that $\sigma_z = -p$):

$$(\sigma_x - \sigma_y)^2 + (\sigma_x + p)^2 + (\sigma_y + p)^2 + 6 \cdot (\mu \cdot p)^2 = 2 \cdot Y_{\mathrm{p}}^2 \tag{5.21}$$

For a typical peripheral sector (like sector A of figure 5.1): $\sigma_x \cong \sigma_y \cong p_{\mathrm{EHL}}$. Thus, equation (5.21) can readily be solved to give the solid pressure on any peripheral sector.

The analysis can now proceed one step further to the first set of inner sectors, marked by red color in figure 5.4.

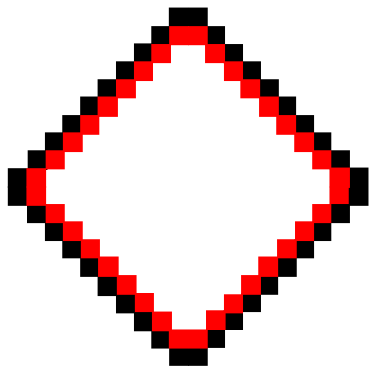

Figure 5.4 First set of inner sectors (red) and peripheral sectors (black).

The internal normal stresses σ_x and σ_y of any of these inner red sectors are calculated from equations (5.14) and (5.15), using equations (5.4) and (5.5). The pressure p is then calculated from the solution of equation (5.21).

Applying the same procedure to all remaining sets of inner sectors, the solid pressure distribution on the particle is found. Initially, the thickness of the particle disk is assumed equal to the film thickness at the position of the centre of the particle. After obtaining the pressure distribution, flash temperatures are recalculated following the method outlined in chapter 3. This is followed by surface-displacement calculations according to equations (5.7)-(5.11), and the variable thickness of the particle is established from equation (5.6). Between two successive steps of the iteration, the results for the pressure are checked for equality and, if found unacceptably unequal, a new pressure distribution is assembled through under-relaxation:

$$p_{\mathrm{new}} = p_{\mathrm{previous}} + \delta \cdot \left(p_{\mathrm{old}} - p_{\mathrm{previous}}\right) \tag{5.22}$$

where $p_{previous}$ and p_{old} are the pressures calculated one and two steps previously, respectively, and δ is the under-relaxation factor, suitably chosen as $\delta = 0.2$. The whole procedure is repeated until the results for the solid pressure distribution converge.

The effect of surface displacements on the shape of the cylindrical (deformed) particle is shown in figure 5.5.

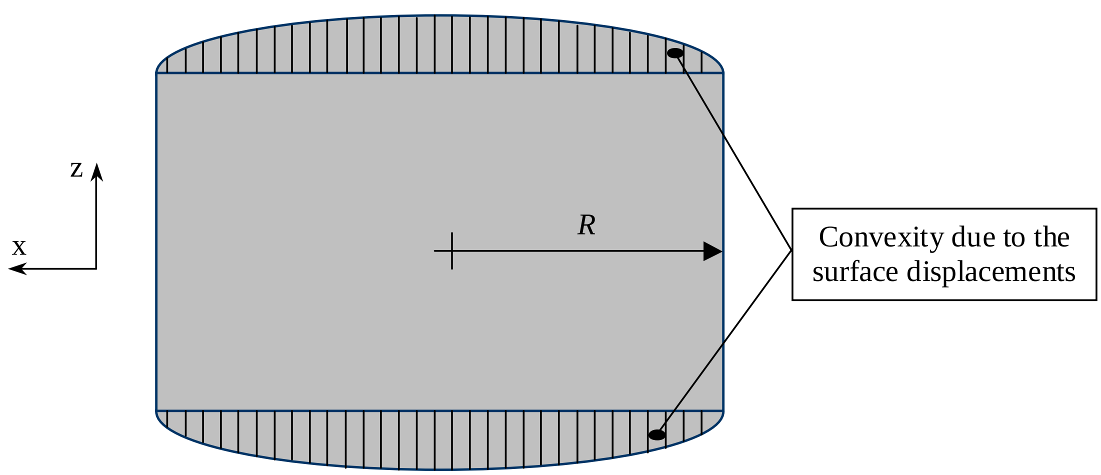

Figure 5.5 2-dimensional, lateral view of the deformed particle. The z-scale is greatly exaggerated for better viewing.

The elliptic-shaped upper and lower parts of the particle in figure 5.5 are the result of the counterface displacements. These displacements are much smaller in comparison with the radius R of the particle, shown in figure 5.5. In chapter 2, the radius of the deformed particle is calculated on the basis that the counterfaces are rigid. The latter assumption has been removed in the present chapter. Therefore, the shape of the deformed particle is no longer considered idealistically cylindrical, but allows for the base convexities shown in figure 5.5. This affects the way of calculation of particle's radius during deformation. The conservation of volume of the particle is easily derived from figure 5.5 and is written as follows:

$$\underbrace{V_\sigma}_{\text{inital volume}} = \underbrace{\pi \cdot R^2 \cdot \overset{\substack{\text{At the position of the centre of the particle.}\\ \uparrow}}{h} + \underbrace{\iint H \cdot dx \cdot dy}_{\substack{\text{Integration on the facial}\\ \text{surface of the particle}}}}_{\text{volume at an intermediate stage of deformation}} \tag{5.23}$$

where h is the lubricant film thickness at the position of the centre of the particle, as if the particle were absent from the contact. Using equation (5.23) and replacing the double integral to take into account particle's discretization into sectors, the radius of the deforming particle is given as follows:

$$R = \sqrt{\frac{V_\sigma - (\Delta s)^2 \cdot \sum_i \sum_j (H - h)}{\pi \cdot h}} \tag{5.24}$$

Equations (5.23) and (5.24) replace equations (2.18) and (2.20), respectively. It is worth noting that the author has verified the accuracy of equation (2.20) by plotting the results for radius R using both the simplified equation (2.20) and the "accurate" equation (5.24); the difference is indistinguishable. It must also be mentioned that surface thermal expansion partly counteracts the settling of the counterfaces due to the solid pressure applied by the particle. The results for radius R are presented later in this chapter.

5.3 Grids for the temperature and stress calculations

Because of the complexity of the complete model, the number of calculation nodes must be kept as low as possible, without sacrificing accuracy. However, the grids used for the calculations must cover the whole area affected by the frictional heat and the thermal and mechanical stresses. The latter causes problems when the particles studied are big (as for example larger than 20 μm) and the central film thickness relatively thin (as for example less than 0.5 μm), because the stressing conditions are more severe and the affected areas larger. Larger particles make their first contact with the counterfaces further away from the nominal point of contact (centre of the Hertzian zone – see figure 2.2) than smaller particles, which means that their travelling distance before reaching the outlet zone of the contact is longer in comparison with that for the smaller particles. Conclusively, larger particles require bigger grids, which require more nodes for adequate discretization.

The grids are part of the moving counterfaces and move in space with their tangential speeds (u_1, u_2), as is shown in figure 5.6.

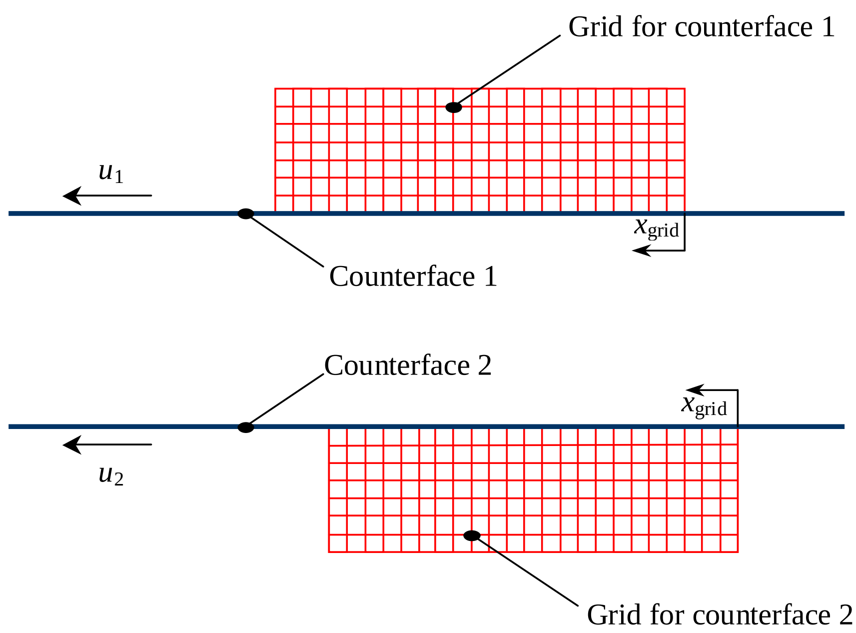

Figure 5.6 Grids for the temperature and stress calculations.

This means that the particle may move in relation to both grids (3-body problem) or in relation to just one grid (2-body problem). The boundary conditions of skin temperatures and pressures/tractions have to be continuously adjusted as the particle moves inside the elastohydrodynamic gap.

The boundaries of the grids are defined as follows:

$$\left.\begin{aligned}
&x_{\text{init}}^{(\text{t=0})} \mathrel{\hat{=}} x_{t=0} \quad , \quad x_{\text{fin}}^{(\text{t=0})} \mathrel{\hat{=}} 4 \cdot R_{\max} - x_{\text{init}} - \left(x_{t=0} + b\right) \cdot \frac{u_2}{u_1} \\
&y_{\text{init}} \mathrel{\hat{=}} 0 \quad , \quad y_{\text{fin}} \mathrel{\hat{=}} 2 \cdot R_{\max} \\
&z_{\text{init}} \mathrel{\hat{=}} 0 \quad , \quad z_{\text{fin}} \mathrel{\hat{=}} 2 \cdot R_{\max}
\end{aligned}\right\} \tag{5.25}$$

where $R_{\max}$ is the maximum possible radius of the disk-shaped (deformed) particle, which appears in the Hertzian zone of the contact:

$$R_{\max} = \sqrt{\frac{V_\sigma}{\pi \cdot h_{\text{c}}}} \tag{5.26}$$

The symmetry about plane $y = 0$ is fully taken into account in the calculations. The x-limits defined in equations (5.25) are relative about point $x = 0$ (the centre of the Hertzian zone of the contact) and refer to time $t = 0$, when the particle starts being elastically deformed. For $t > 0$, the x-position of the grids changes according to the motion of the counterfaces with their tangential speeds u_1 and u_2. If x_{grid} stands for the x-distance of a point inside the area of a grid and in the direction shown in figure 5.6 (in other words distance from the beginning of a grid), then, at any time $t \geq 0$, the distance of a surface point of a grid from the centre of the Hertzian zone ($x = 0$) is: $x_{\text{init}} + x_{\text{grid}} + u_i \cdot t$ ($i = 1, 2$). Thus, all nodes can be easily addressed in space at any time.

5.4 Application of the full model

At this point, the model has been completely addressed and outlined in its entirety. The next step is a general application, analyzing a case typical of the results the proposed model yields. A flowchart of the complete model is shown in figure 5.7.

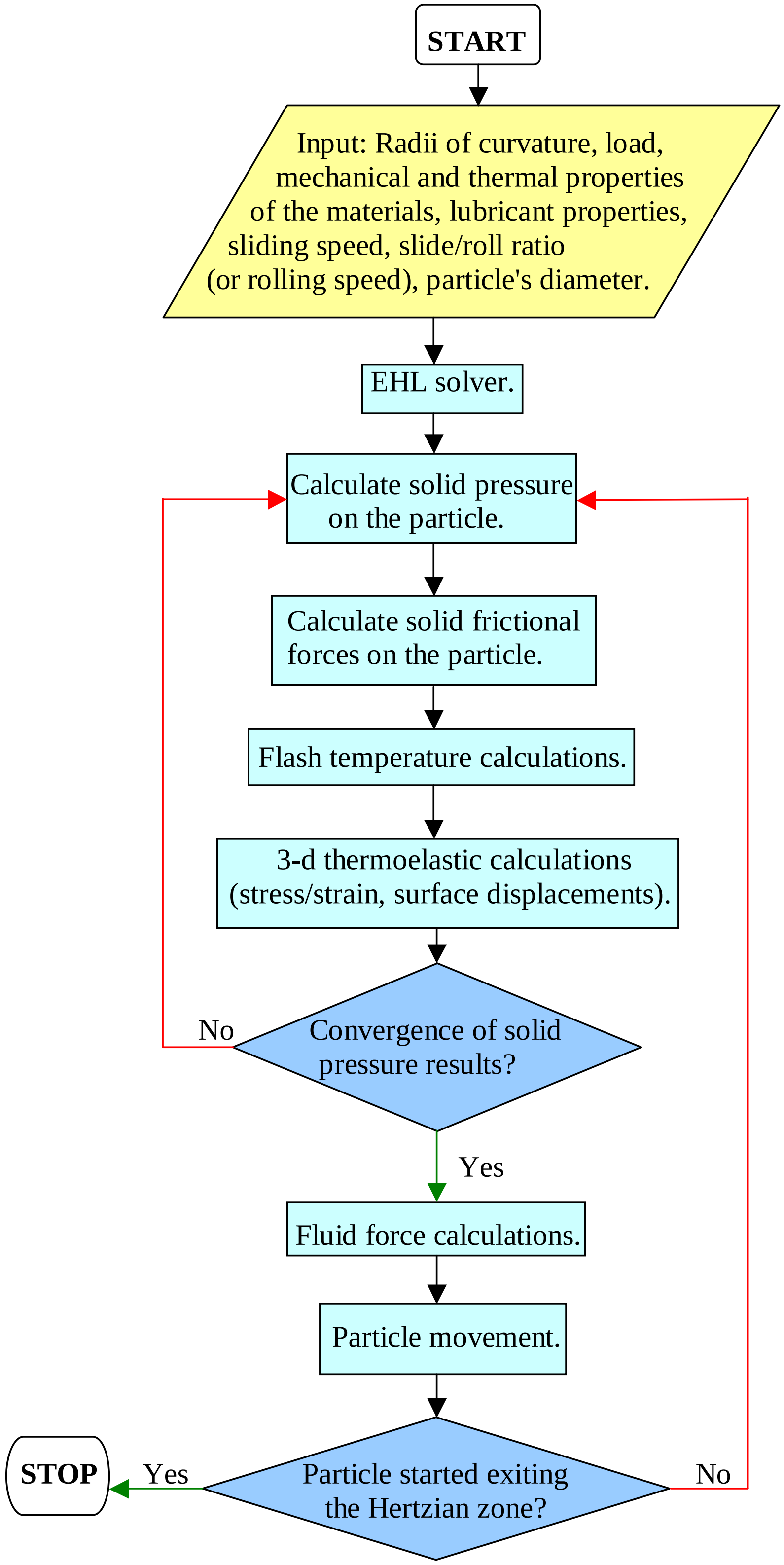

Figure 5.7 Flowchart of the full model.

In this example, all simplifying assumptions adopted in previous chapters (2-4) are removed. The only assumption kept is that the materials are mechanically (elastically) isotropic. All data for the example are quoted in tables 5.1-5.3.

Table 5.1

Particle data	
Diameter (sphere)	20 μm
Hardness at 0 °C	100 HV
Hardness at θ °C	$981 \cdot 10^6 - 122625 \cdot \theta$ Pa
Mass density	7850 kg/m^3
Specific heat at θ °C	$445 + 8073 \cdot 10^{-4} \cdot \theta - 1993 \cdot 10^{-6} \cdot \theta^2 + 2572 \cdot 10^{-9} \cdot \theta^3$ Joule/(kg·°C)
Thermal conductivity at θ °C	$59 - 2222 \cdot 10^{-5} \cdot \theta$ W/(m·°C)
Thermal diffusivity at θ °C	$= \dfrac{\text{thermal conductivity at } \theta\,°\text{C}}{(\text{specific heat at } \theta\,°\text{C}) \cdot (\text{mass density})}$
Yield stress in uniaxial tension at θ °C	$= \dfrac{\text{Hardness at } \theta\,°\text{C}}{2.8}$

The particle is initially spherical, with a diameter equal to 20 μm. At 60 °C (the initial temperature of the contact), the particle is approximately eight times softer than the counterfaces. The temperature dependency of the mechanical and thermal properties is clearly demonstrated in table 5.1. The values used are typical for steel and some of them (like those for the thermal properties) are more specifically typical for ferrite. The data for the counterfaces are quoted in table 5.2.

Table 5.2

Counterface data	
Radius of curvature	R_1 = 20 mm, R_2 = 28 mm
Hardness at 0 °C	800 HV
Hardness at θ °C	$7848 \cdot 10^6 - 981000 \cdot \theta$ Pa
Modulus of elasticity at θ °C	$207 \cdot 10^9 - 25875000 \cdot \theta$ Pa
Poisson ratio	0.3
Friction coefficient	$\mu_1 = 0.2$, $\mu_2 = 0.15$
Specific heat at θ °C	$445 + 8073 \cdot 10^{-4} \cdot \theta - 1993 \cdot 10^{-6} \cdot \theta^2 + 2572 \cdot 10^{-9} \cdot \theta^3$ Joule/(kg·°C)
Thermal conductivity in the x-direction at θ °C	$27.61 + 3.0558 \cdot 10^{-3} \cdot \theta$ W/(m·°C)
Thermal conductivity in the y-direction at θ °C	$27.61 + 3.0558 \cdot 10^{-3} \cdot \theta$ W/(m·°C)
Thermal conductivity in the z-direction at θ °C	$25.1 + 2.778 \cdot 10^{-3} \cdot \theta$ W/(m·°C)
Mass density	7850 kg/m^3
Thermal diffusivity at θ °C	$= \dfrac{\text{thermal conductivity at } \theta\,°\text{C}}{(\text{specific heat at } \theta\,°\text{C}) \cdot (\text{mass density})}$
Coefficient of linear thermal expansion	$11 \cdot 10^{-6}$ °C^{-1}
Yield stress in uniaxial tension at θ °C	$= \dfrac{\text{Hardness at } \theta\,°\text{C}}{2.8}$
Shear modulus at θ °C	$= \dfrac{\text{modulus of elasticity at } \theta\,°\text{C}}{2 \cdot (1 + \text{Poisson ratio})}$

The values used for the counterface properties are typical for steel and some of them (like those for the thermal properties) are more specifically typical for martensite.

Table 5.3

Lubricant, contact and other data	
Sliding speed of the contact	1 m/s
Slide/roll ratio	1
Load per unit length of the contact	100 N/mm
Viscosity-pressure coefficient (Z_1)	0.5
Dynamic viscosity at environmental conditions	0.1 Pa·s
Bulk (initial, environmental) temperature (θ_0)	60 °C
Density of the lubricant at ambient conditions	870 kg/m^3
Specific heat of the lubricant	2000 Joule/(kg·°C)
Thermal conductivity of the lubricant	0.14 W/(m·°C)
Flow perturbation parameter (ε, see equation (2.24))	0.8
Speed U (see equation (2.25))	0.5 m/s
Initially the particle is carried by counterface:	2
Number of sectors along the radius of the particle on axis y (N_y)	30
Along the trajectory of the particle, complete flash temperature and thermomechanical calculations are done at	317 points (every 2.4 μm)
Spatial steps for the thermomechanical stress calculations $\Delta x \times \Delta y \times \Delta z$	50 × 9 × 20
Boundaries of the grids: x_{init}, x_{fin}, y_{fin} (= z_{fin})	–700 μm, 1031 μm, 81 μm
Total number of surface nodes (old + new) for thermomechanical calculations (see equations (4.71))	560450
Number of grid nodes	9000 (= 50 × 9 × 20)

The values for the lubricant’s properties listed in table 5.3 are typical for unused engine oils (see Hamrock, 1994, chapter 4). Some interesting results are quoted in table 5.4.

Table 5.4

Some interesting results	
Central film thickness	$h_c \cong 0.7$ μm
Hertzian contact semi-width	$b \cong 114$ μm
Tangential speeds of the counterfaces	$u_1 = 1.5$ m/s, $u_2 = 0.5$ m/s
Point where the particle is first pinched	$x_{t=0} \cong -700$ μm
Maximum particle (cylinder – deformed) radius	$R_{max} \cong 43$ μm
Mass of the particle	$m \cong 0.03$ μgr
Time when the geometrical centre of the particle enters the Hertzian zone of the contact	0.39 ms
Particle pass time (from $x = x_{t=0}$ to $x = b$)	0.54 ms
Particle Reynolds number (equation (2.27)): - ignoring thermal effects due to internal shearing in the fluid - including thermal effects	 $\mathrm{Re}_p = O(10^{-3})$ $\mathrm{Re}_p = O(1)$
Maximum elastohydrodynamic pressure	0.55 GPa (figure 5.10)
Maximum flash temperature on counterface 1	1350 °C
Maximum flash temperature on counterface 2	846 °C

The particle sticks to the counterface with the higher friction coefficient, which is counterface 1. It then slides on counterface 2 all the way until it reaches the outlet zone of the contact. During its plastic deformation, the particle is transformed from a sphere (initially) to a thin disk (finally), with a final thickness at the order of the central film thickness of the contact. The final thickness of the particle is actually greater than the central film thickness of the contact since the counterfaces deform elastically and accommodate a part of the body of the particle. This counterface elastic displacement is shown graphically later in this chapter. The flattening of the particle is graphically demonstrated in figure 5.8. Figure 5.8 shows the change of the radius of the particle as it deforms plastically during its passage through the elastohydrodynamic gap. The particle, according to the model, is assumed to be a cylinder during its deformation (see figure 2.5).

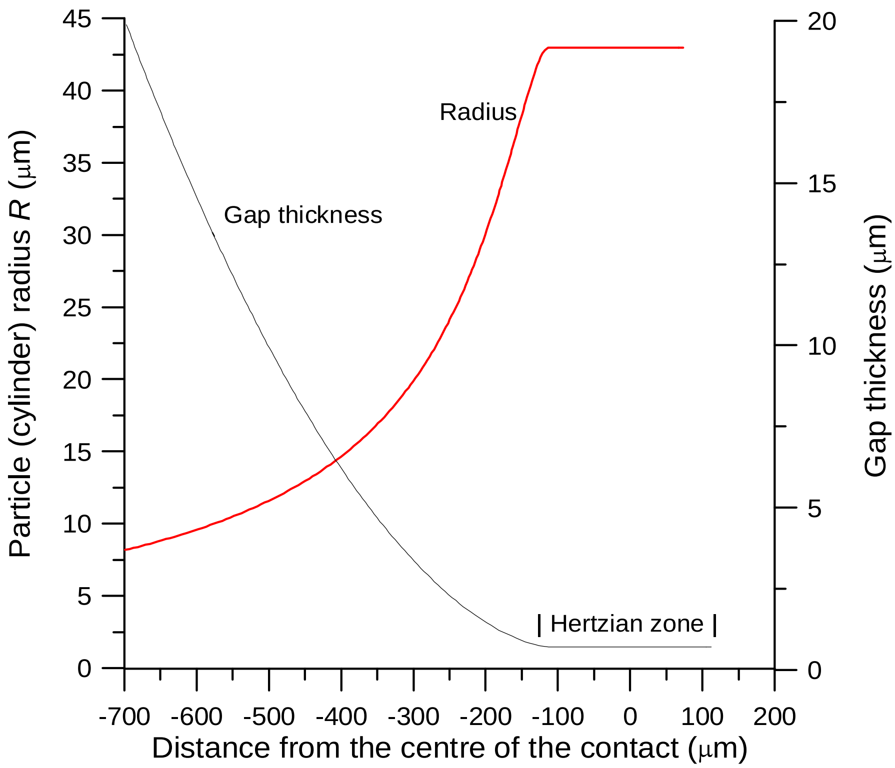

Figure 5.8 Calculated particle (cylinder) radius during plastic deformation of the particle in the elastohydrodynamic gap (equation (5.24)).

It is again noted here (like it was done in chapter 2, figure 2.8) that the initial radius shown in figure 5.8 is less than the radius of the spherical particle because it refers to the equivalent cylinder of volume equal to the volume of the initially spherical particle (i.e. it is not the radius of the sphere).

Immediately after being pinched, the particle starts being plastically deformed. Therefore, its radius changes continuously following the change of slope of the counterfaces in the inlet zone, until the particle reaches the flat Hertzian zone of the contact, where the radius remains approximately constant. Inside the Hertzian zone of the contact, the frictional heat produced between the particle and the counterfaces causes thermal expansion and alteration of the stress and temperature fields, which results in a slightly altered local geometry of the counterfaces. Nevertheless, this disturbance is very small to be noticed in the radius of the particle shown in figure 5.8, although it is clearly noted in the figures showing the normal and frictional forces on the particle following next.

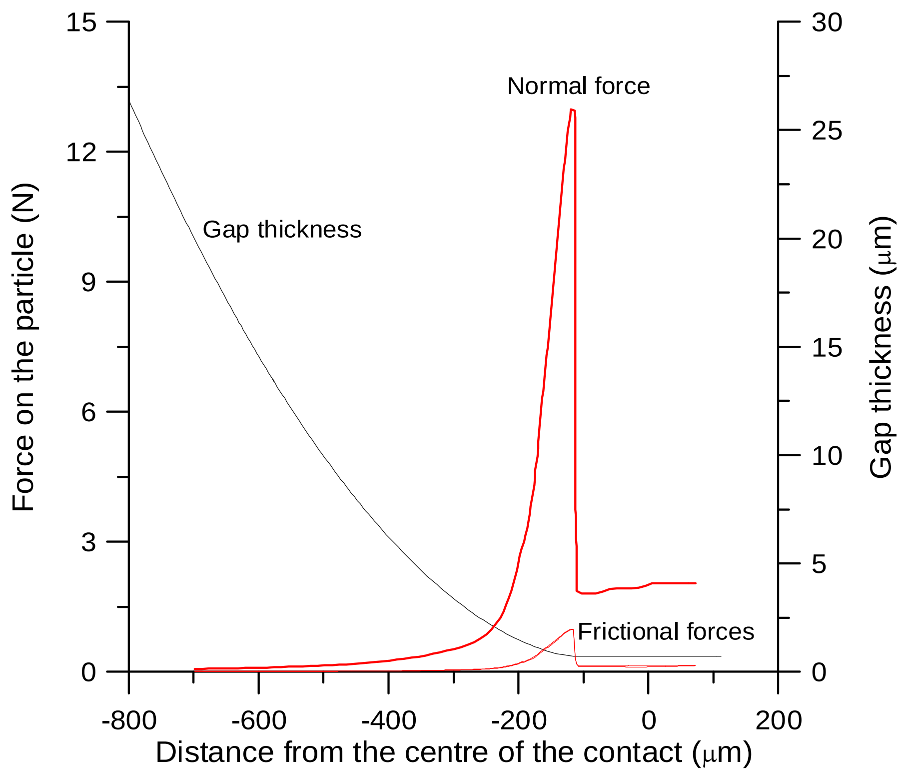

Figure 5.9 Normal force and frictional forces on the particle during its passage through the contact.

Figure 5.9 shows the normal force on the particle (due to its plastic compression in the contact) as well as the two frictional forces (which are essentially indistinguishable in this particular figure due to the vertical-axis scaling necessary for plotting the normal force). Comparing figure 5.9 with figure 2.9, the latter created with the simplified model of chapter 2, it is immediately noticeable a change in the morphology of the curves. The curves in figure 2.9 are monotonically increasing until the entrance to the Hertzian zone, whereas the curves in figure 5.9 exhibit a sudden drop just before the entrance to the Hertzian zone. It is vital to realize that the simplified model represented by figure 2.9 omits the effect of the elastohydrodynamic pressure on the particle as well as the instantaneous counterface displacements due to the pressure applied by the particle. The simplified model also omits the frictional force components on the particle applied in the direction of sliding of the particle (axis x). The traction map on the particle surface changes drastically as the particle enters the Hertzian zone of the contact, because at that point, its lateral expansion suddenly stops and the only remaining tractions are those due to its continuing sliding (and thus friction) on counterface 2. It is easily understood that when the extrusion of the particle ceases at the entrance of the Hertzian zone, the solid pressure on the particle is substantially released. However, the sudden drop observed in figure 5.9 is actually a mathematical idealization, since, in reality, the particle enters gradually (and not instantly) the flat Hertzian zone. In reality, the average solid pressure on the particle is expected to exhibit a more gradual reduction, compared with the reduction shown in figure 5.9, as the particle enters the Hertzian zone at a finite speed. Nevertheless, the amount of reduction should be the same, regardless of the model used in the study, and, thus, being equal to that shown in figure 5.9.

All the previously named simplifications have been removed from the refined model of the present chapter. Apparently, the effect of the elastohydrodynamic pressure and of the variable tractions is quite significant in the calculation of the pressure on the particle, and this has been fully taken into account in the advanced model outlined in section 5.2. The elastohydrodynamic pressure distribution for the presented example (neglecting any effects from the presence of the particle) is shown in figure 5.10. The pressure distribution of figure 5.10 resembles the Hertzian pressure distribution, the major deviation being in the inlet zone of the contact. It must be realized that the sudden rise of the elastohydrodynamic pressure at the entrance and the first half of the Hertzian zone is “sensed” by the particle relatively long before the centre of the particle disk enters the Hertzian zone because at that point, the leading front particle semi-disk has already entered deep enough inside the Hertzian zone.

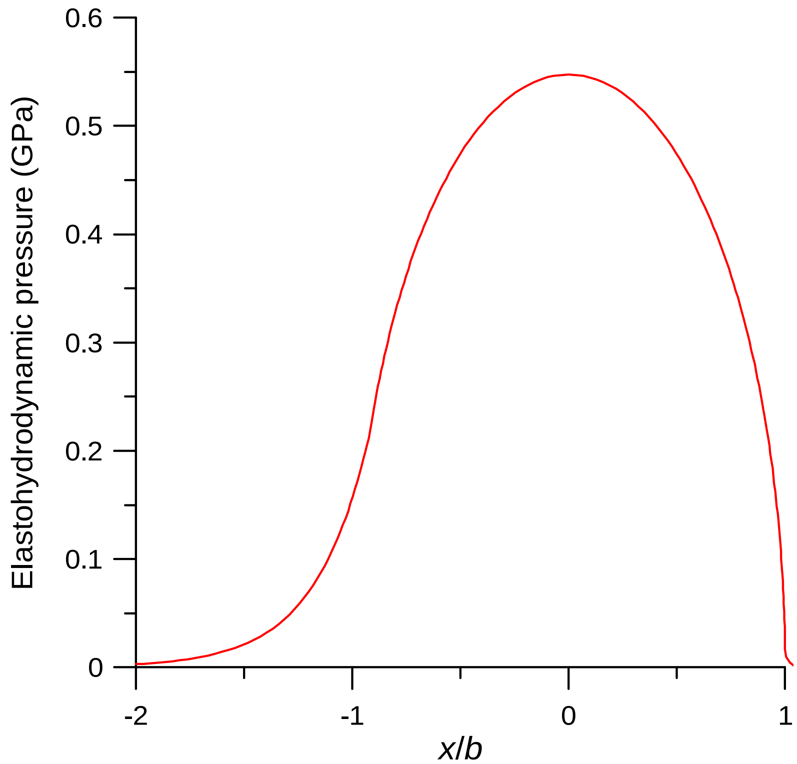

Figure 5.10 Approximate elastohydrodynamic pressure distribution of the line contact, neglecting the presence of the particle.

More specifically, in our particular example, at the time when the centre of the particle crosses the imaginary line of the entrance to the Hertzian zone, the leading edge (sector) of the particle is at a distance $-b - R_{max} = -114\ \mu m + 43\ \mu m = -71\ \mu m$ from the centre of the contact (see table 5.4). At that distance, $\frac{x}{b} = \frac{-71}{114} \cong -0.623$, and the corresponding elastohydrodynamic pressure is 78 % of the maximum elastohydrodynamic pressure in the contact, which is quite significant.

Figure 5.11 compares the solid frictional forces T_1 and T_2 with the lubricant forces on the particle (F_{stat}, F_{dyn}), similarly to figure 2.10 in chapter 2.

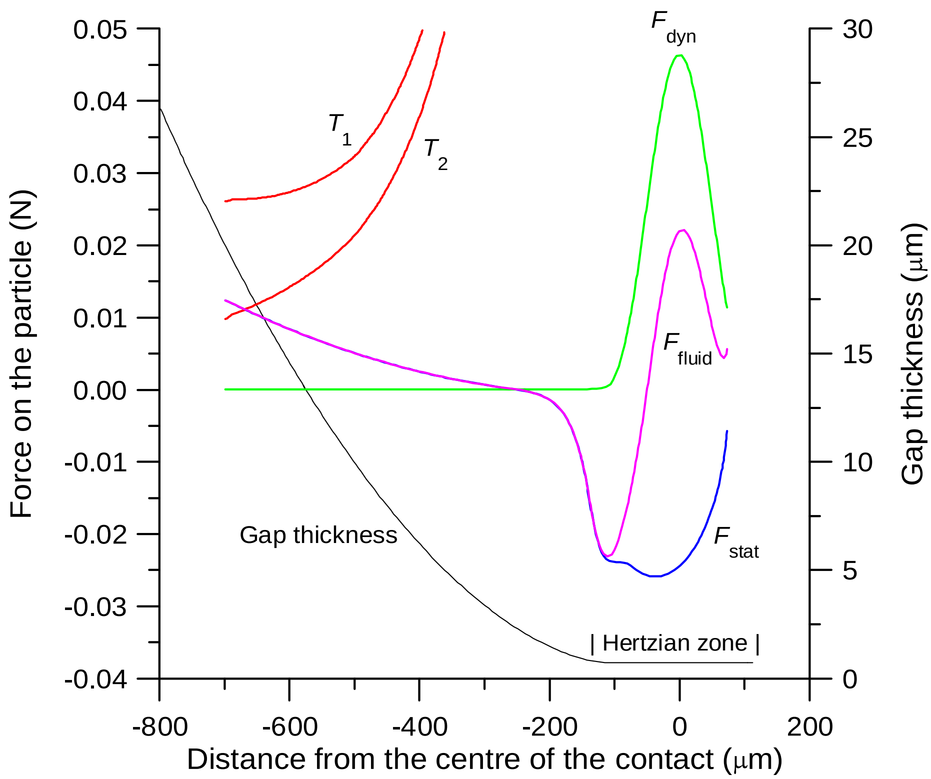

Figure 5.11 Solid frictional and fluid forces on the particle during its passage through the elastohydrodynamic gap.

Figure 5.11 shows that the solid frictional forces are much higher than the lubricant force components and the overall fluid force ($F_{\text{fluid}} = F_{\text{stat}} + F_{\text{dyn}}$) on the particle, as had been confirmed with the simpler model in chapter 2. As can be seen, the static-pressure fluid force on the particle becomes negative for $x < -250$ μm. This means that although the elastohydrodynamic pressure initially pushes the particle out of the contact, it finally acts in favor of particle entrapment and drags the particle inside the contact gap. Of course, as already mentioned, this is by no means a decisive force in the particle's motion and direction as it is much weaker than the solid frictional forces, which, essentially, govern the motion of the particle inside the gap.

In chapter 2, it is shown that the particle sticks to the counterface with the higher friction coefficient, immediately after being trapped (see figure 2.11). This is also the case with the advanced model of the present chapter, as is clearly shown in figure 5.12.

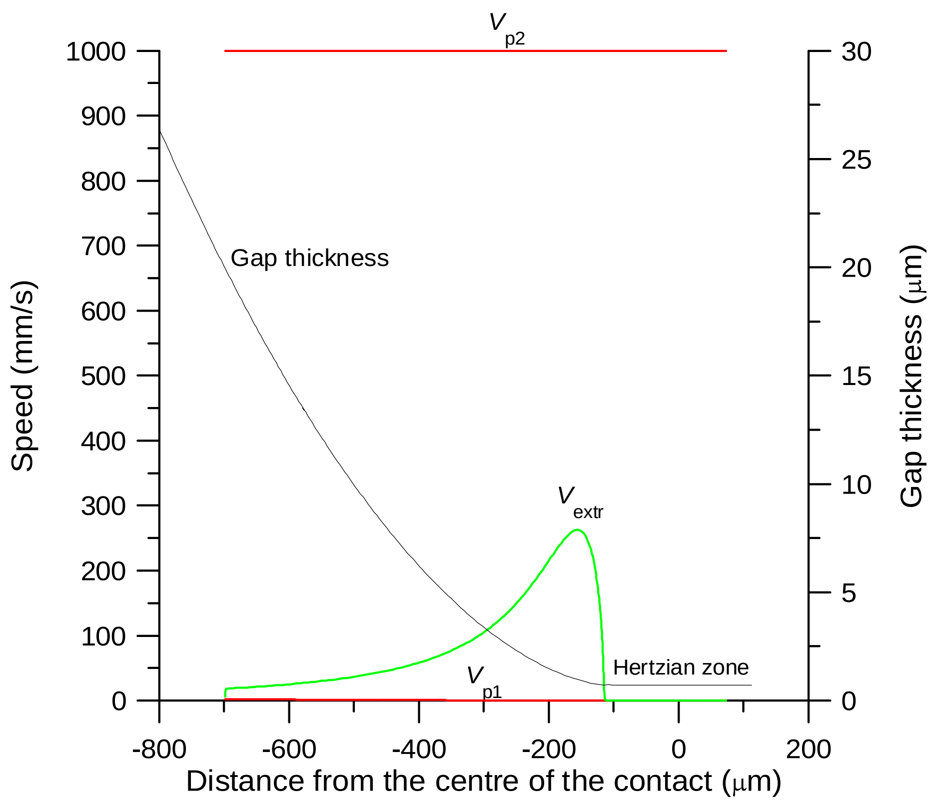

Figure 5.12 Relative sliding speeds and extrusion speed of the particle during its motion inside the elastohydrodynamic gap.

V_{p1} is the sliding speed of the particle relatively to counterface 1. Similarly, V_{p2} is the sliding speed of the particle relatively to counterface 2. From figure 5.12, it is infered that the particle sticks to counterface 1 (because $V_{p1} = 0$) and slides on counterface 2 ($V_{p2} \neq 0$). The same comments accompanying figure 2.11 hold here as well.

The plastic compression and sliding of the particle inside the elastohydrodynamic gap results in friction, which produces heat. According to the analysis of chapter 3, this heat can be very high for large and/or hard particles. In the example of section 3.8, it is shown (despite the simplifications made there) that the frictional heat is also very high even for large but relatively *soft* particles. In the present chapter, after removing the simplifications of chapter 3, it is actually shown that the frictional heating is indeed more severe than one might expect. This is clearly demonstrated in figure 5.13.

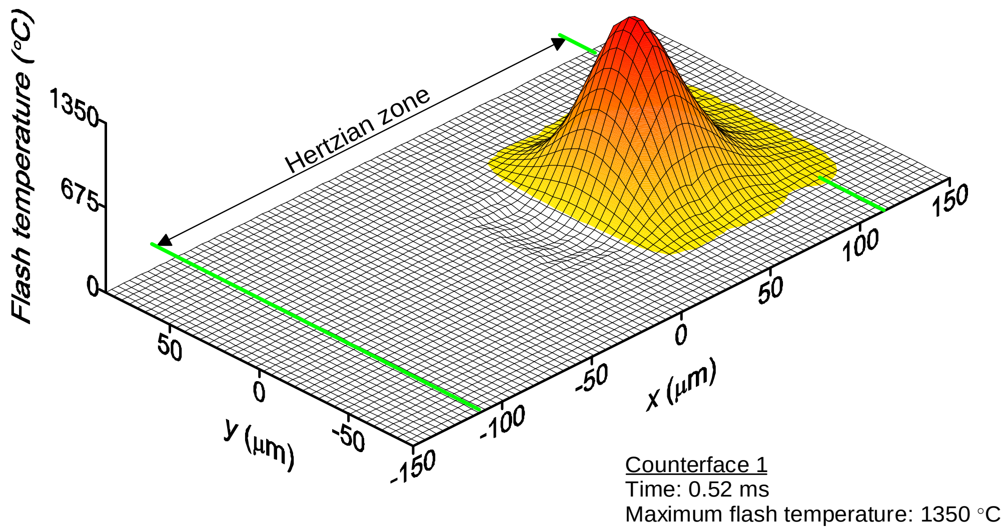

Figure 5.13 Flash temperature distribution on counterface 1 as the particle starts exiting the Hertzian zone of the contact ($t \cong 0.52$ ms). The particle sticks to this counterface.

Figure 5.13 shows the distribution of the flash temperature (temperature increase above the bulk-initial temperature) on surface 1 as the particle (its leading sector) starts exiting the Hertzian zone of the contact. The flash-temperature field is completely enveloped in the Hertzian zone because the particle at this stage has a diameter equal to $2{\cdot}R_{max} = 2{\cdot}43 = 86$ μm (see table 5.4), which is much smaller than the width of the Hertzian zone ($2{\cdot}b = 2{\cdot}114 = 228$ μm). The maximum flash temperature on counterface 1 is 1350 °C, which is quite high thinking that the particle is eight times softer than the counterfaces. However, the particle is also rather large (20 μm). The latter means that, when compressed in order to pass through the elastohydrodynamic gap (which is around 0.7 μm), the particle becomes a disk with a diameter equal to 86 μm. Moreover, the particle sticks to the surface shown in figure 5.13, which means that all of the frictional heat that goes to the aforementioned surface is concentrated to a relatively small area. Due to the previous two reasons and the fact that the solid pressure on the particle is sufficiently high, the magnitude of the flash temperature reaches such a high value.

For the other counterface (2) on which the particle slides all the way from its entrapment to its rejection in the outlet zone of the contact, the frictional heating is less severe, because heat is spread over a larger area. Figure 5.14 shows the flash-temperature distribution on counterface 2 at the same time as for counterface 1 (compare with figure 5.13).

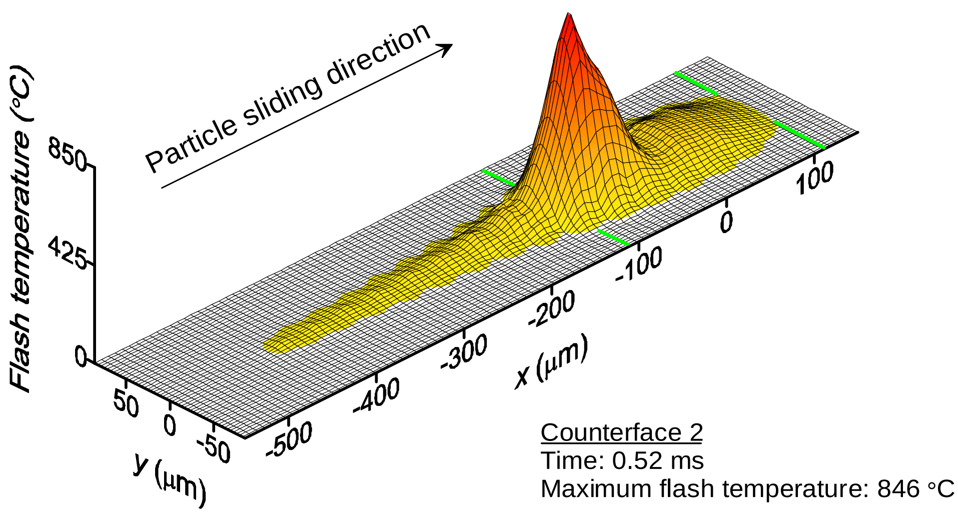

Figure 5.14 Flash temperature distribution on counterface 2 as the particle starts exiting the Hertzian zone of the contact ($t \cong 0.52$ ms). The green lines indicate the boundaries of the Hertzian zone.

Because of the sliding of the particle on counterface 2 along the x-direction, the flash-temperature field extends over a wide area in the x-axis. The magnitude of the flash temperature follows closely the variation of the normal force on the particle, as can be realized by comparing figures 5.9 and 5.14.

Compared with the temperature distribution on counterface 1, the temperature distribution on counterface 2 exhibits a displacement towards the inlet zone of the contact. This is due to the lower tangential speed of counterface 2 in comparison with that of counterface 1.

The maximum flash temperatures calculated in this example are encountered only 0.5 ms after the particle is entrapped. This is the time needed for the particle to travel from the point it is pinched to the point where its leading edge starts entering the outlet zone of the contact. There is a travelling distance omitted in the calculations, and this is the distance between the centre of the particle disk and the leading edge of the particle, as the leading edge (or sector) starts entering the outlet zone (or, equivalently, starts exiting the Hertzian zone). At the aforementioned travelling path, the part of the particle standing in the outlet zone will be under no solid pressure from the counterfaces. In fact, the solid pressure distribution on the particle will change, but this change is difficult to calculate with a simple analysis. It rather requires an elastoplastic analysis with a Finite Element method. However, this change has very little effect on the maximum temperature encountered in the contact and this can be realized by observing figure 5.14, where it is obvious that the major heating has already occurred before the particle starts exiting the Hertzian zone of the contact. Another perspective of the flash-temperature fields is obtained from the two contour maps shown in figures 5.15 and 5.16.

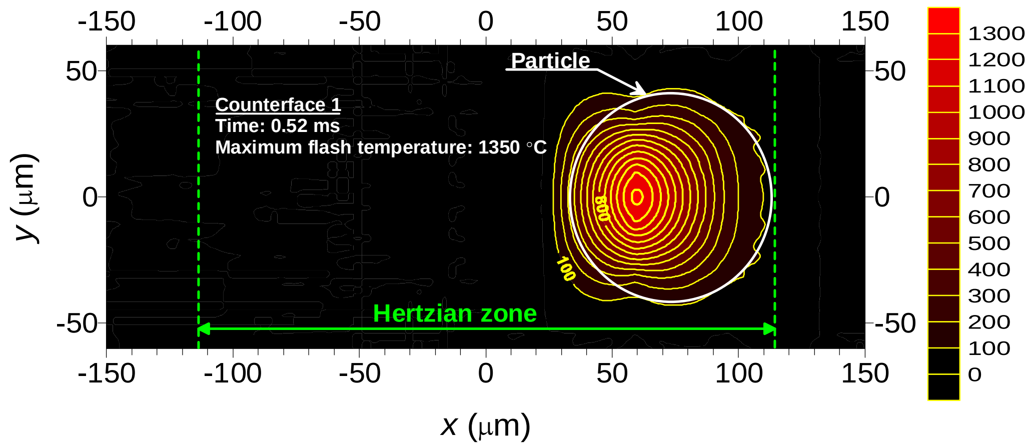

Figure 5.15 Contour map of the temperature distribution on counterface 1 as the particle starts exiting the Hertzian zone of the contact. The particle stays stationary on this counterface. Temperatures shown are in degrees C.

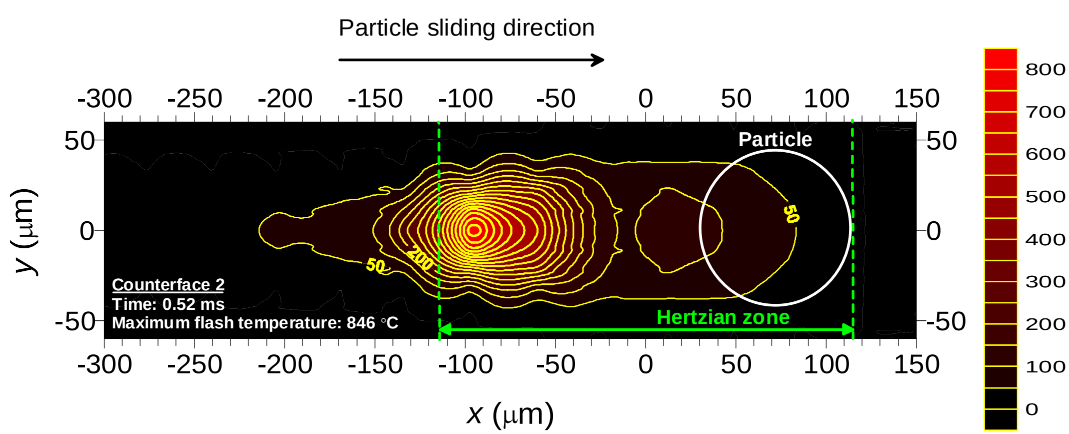

Figure 5.16 Contour map of the temperature distribution on counterface 2 as the particle starts exiting the Hertzian zone of the contact. The particle slides from left to right on this counterface. Temperatures shown are in degrees C.

Figure 5.16 shows that the particle has left a very hot spot on counterface 2, where the maximum temperature is 906 °C (60 + 846). This hot area is located behind the particle and in the first half of the Hertzian zone. The lubricant covering this area is obviously affected by this thermal shock. The effect is expected to be more widespread when not only one but also more particles are squashed at the same time. The latter was speculated by Chandrasekaran *et al.* (1985) when attempting to explain experimental results on the scuffing of bearings lubricated with contaminated oils. However, as is shown later, the heat convection from the counterfaces to the lubricant is very weak. Therefore, despite the high surface temperatures, the lubricant is not affected significantly by the heat wave.

It is interesting to see how rapid the heat accumulation is, by ploting the flash-temperature fields on the counterfaces before the particle enters the Hertzian zone. Figure 5.17 shows the flash-temperature distribution on counterface 1 at the time the particle starts entering the Hertzian zone ($t \cong 0.36$ ms).

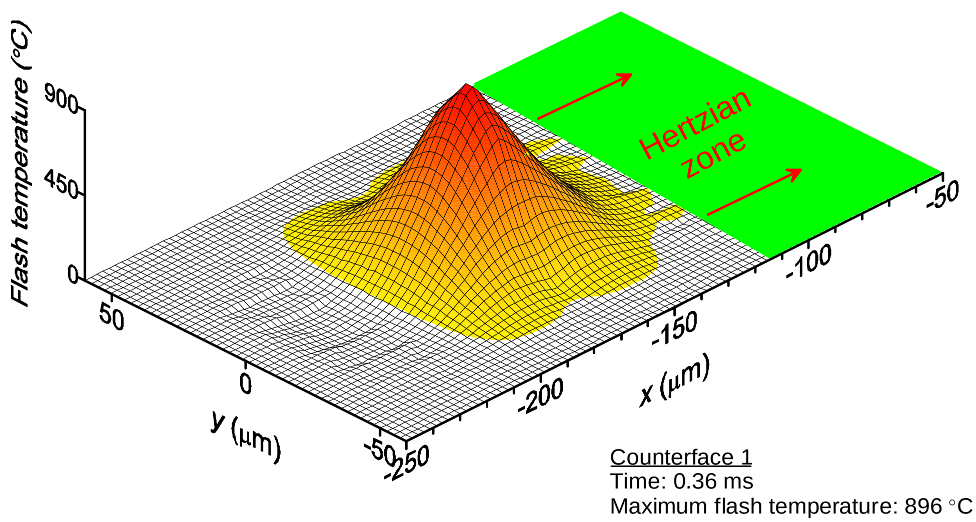

Figure 5.17 Flash temperature distribution on counterface 1 as the particle starts entering the Hertzian zone of the contact ($t \cong 0.36$ ms). The particle sticks to this counterface. Compare with figure 5.13.

At that time, the maximum flash temperature on counterface 1 is “only” 896 °C (instead of 1350 °C at the time when the particle starts exiting the Hertzian zone). Similarly for counterface 2, the maximum flash temperature at the time when the particle starts entering the Hertzian zone is 646 °C (instead of 846 °C when the particle starts exiting the Hertzian zone, a 200 °C difference). The corresponding flash-temperature distribution is presented in figure 5.18.

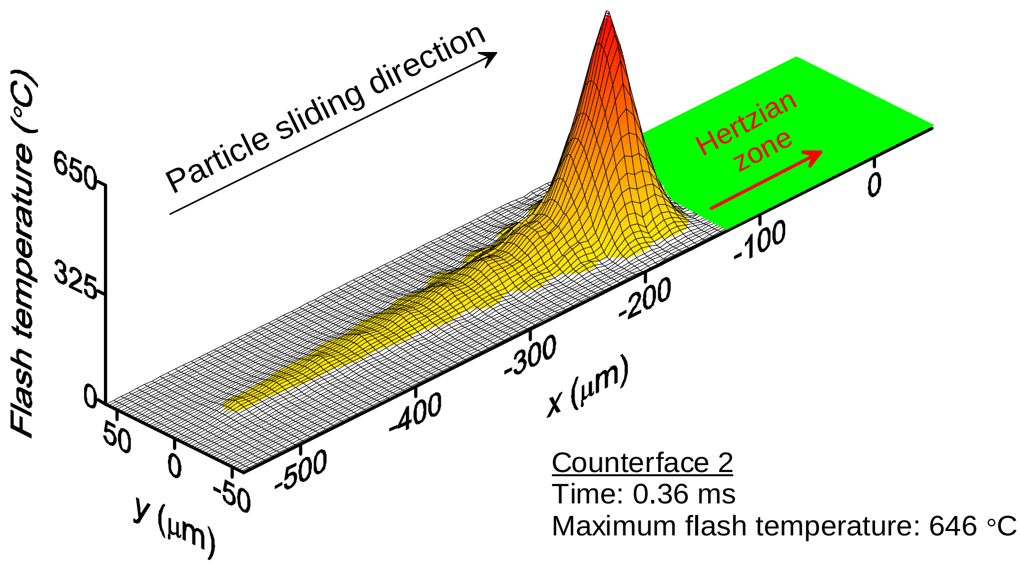

Figure 5.18 Flash temperature distribution on counterface 2 as the particle starts entering the Hertzian zone of the contact ($t \cong 0.36$ ms). The particle sticks to this counterface. Compare with figure 5.14.

Therefore, inside the Hertzian zone of the contact (width: $2 \cdot b = 2 \cdot 114 = 228$ μm), the produced frictional heat results in a 454 °C and 200 °C temperature increase for surfaces 1 and 2, respectively. These increments represent 34 % and 24 % of the maximum flash temperatures encountered on counterfaces 1 and 2, respectively. The percentages are significant and show that the wider the Hertzian zone of the contact, the more time the particle spends sliding and, hence, heating the counterfaces. On the other hand, it is obvious that larger particles travel longer sliding distances before reaching the outlet zone as compared with smaller particles, because larger particles start sliding further away from the Hertzian zone in comparison with smaller ones.

The isothermal lines for the flash-temperature fields are shown in figures 5.19 and 5.20, for the time when the particle starts entering the Hertzian zone.

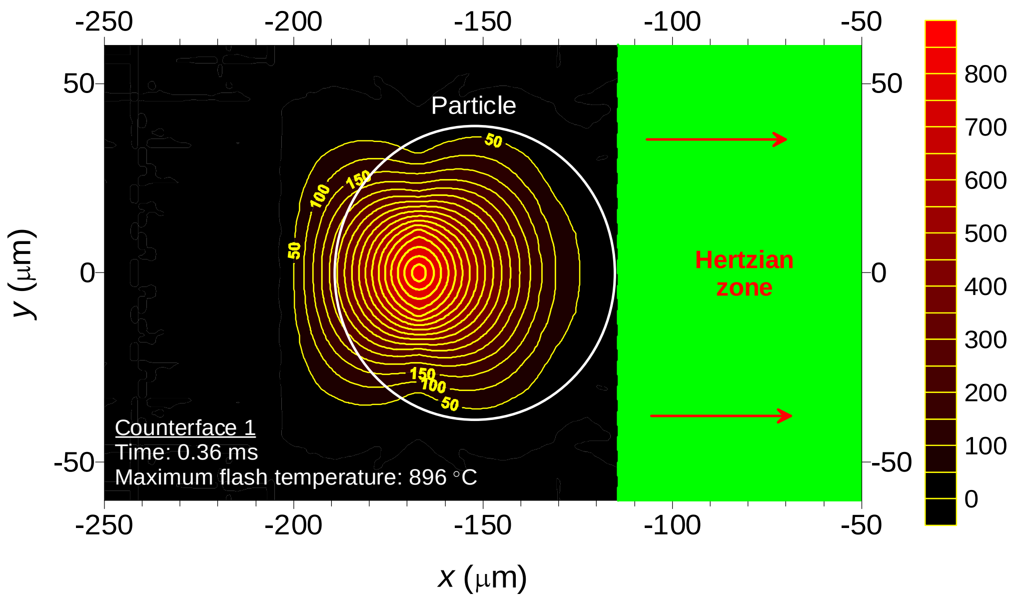

Figure 5.19 Contour map of the flash-temperature distribution on counterface 1 as the particle starts entering the Hertzian zone of the contact. The particle sticks to this counterface. Temperatures shown are in degrees C.

Figure 5.19 shows that the thermally affected area of counterface 1 is concentrated in the vicinity of the deforming particle. This is so because the particle is stationary on counterface 1. However, the sliding of the particle on the other surface (counterface 2) produces a strikingly different result. As figure 5.20 demonstrates, even with the particle outside the Hertzian zone, the thermally affected area on counterface 2 extends well beyond the boundaries of the particle in the direction of its trailing edge.

This leaves a hot path on surface 2 and affects the lubricant in the inlet zone of the contact.

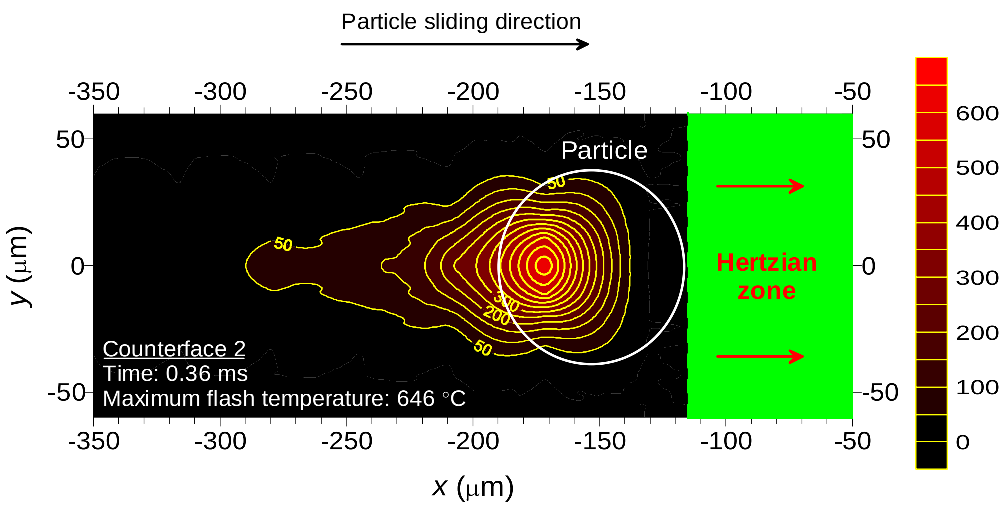

Figure 5.20 Contour map of the flash-temperature distribution on counterface 2 as the particle starts entering the Hertzian zone of the contact. The particle stays stationary on this counterface. Temperatures shown are in degrees C.

Figure 5.20 shows that just behind the trailing edge of the particle (in the inlet zone of the contact), counterface 2 has a temperature of around 460 °C (60 + 400). Even at a distance of around 100 μm behind the trailing edge, the overall temperature is still around 100 °C.

The previous results demonstrate in a dramatic way that soft-ductile particles are anything but harmless when squashed in an elastohydrodynamic sliding contact. For the particular (typical) example, a 100 HV, 20 μm particle is capable of producing such immence frictional heat that maximum temperature increase in the contact reaches 1350 °C. The mechanism of the event is based on the fact that the particle is ductile and will expand substantially, until its thickness is reduced to the order of the central film thickness, in order for the particle to pass through the narrow elastohydrodynamic gap (which is usually less than 1 μm). On the other hand, the particle has a tendency to stick to one counterface and, thus, slide against the other.

Therefore, an object of large contact area will eventually slide on a surface under relatively high solid pressures. The end effect is the build-up of heat, which is transferred mainly to the counterfaces.

The softness of the particle would imply that the solid pressures between it and the counterfaces will be lower than in the case of a hard particle. This is indeed the case as is shown in figure 5.21.

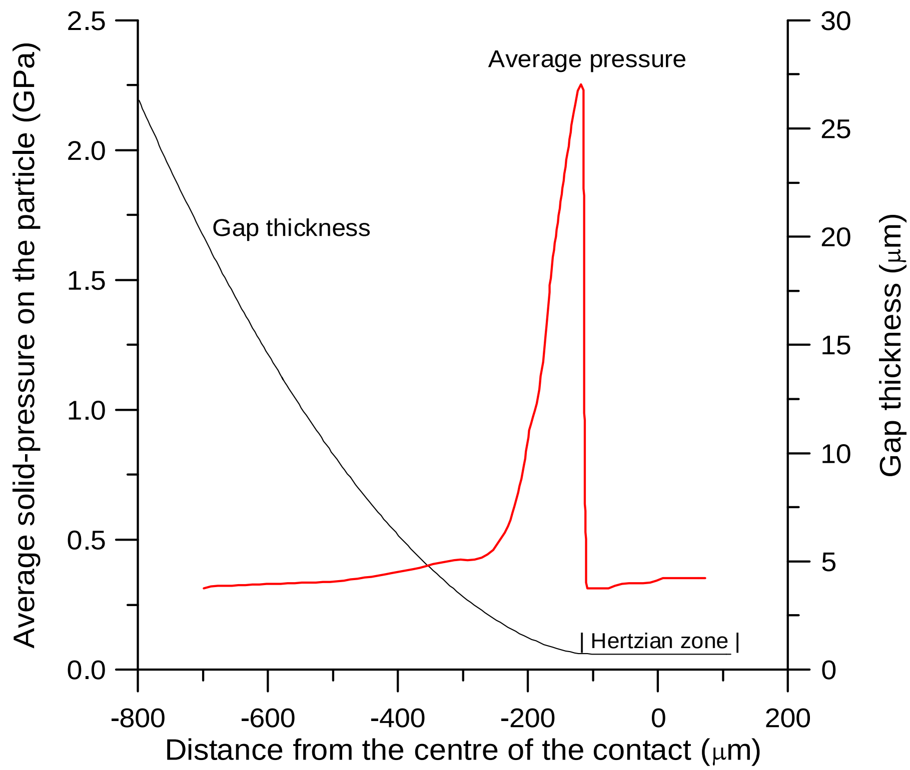

Figure 5.21 Average pressure on the particle during its plastic compression in the elastohydrodynamic gap.

However, although the calculated solid pressure may be lower than in the case of a much harder particle (but still significantly high), a soft-ductile particle is flattened in the contact in contrast to a hard particle, which will more-or-less retain its initial shape. In other words, a hard particle will provide much less surface for friction, compared with a soft-ductile particle.

It is interesting to discuss at this point the possibility of particle melting due to the severe heating. As was shown, the particle sticks to counterface 1, where the maximum overall temperature is 1350 + 60 = 1410 °C. Depending on particle's material, the particle might soften and even partially melt, although the flash heat incident lasts only about 0.6 ms. The possible softening of the particle (or melting) could explain some occasions where it appears that the particle sticks to the faster moving surface, even when the faster moving surface has, apparently, a lower friction coefficient in comparison with the slower moving surface. As is also discussed in chapter 2 (see the last paragraph of section 2.8), semi-solid substances (like grease) are known to adhere to the faster moving surface in sliding contacts. Therefore, if the particle behaves as a semi-solid substance, it is logical to assume that it will stick to the faster moving surface at some point during its deformation, and that point is when the particle will start to melt. However, such behaviour is not universal and material can stick to the slower moving surface, too, or to both surfaces (see for example Zantopoulos (1998), page 429, who observed such behaviour during scuffing tests in tapered roller bearings). From the point of view of this Thesis, a possible melting of the particle marks the end of the temperature and stress analysis because the particle is unable to cause serious damage when being in a semi-liquid state.

Before assessing further the damage risks involved in the entrapment of soft particles in concentrated contacts, the complete series of thermal and overall stress-components distributions in the contact are presented in the following pages. All diagrams refer to the time when the particle starts exiting the Hertzian zone. At that time, the flash temperatures have reached magnitudes close to their absolute maximum.

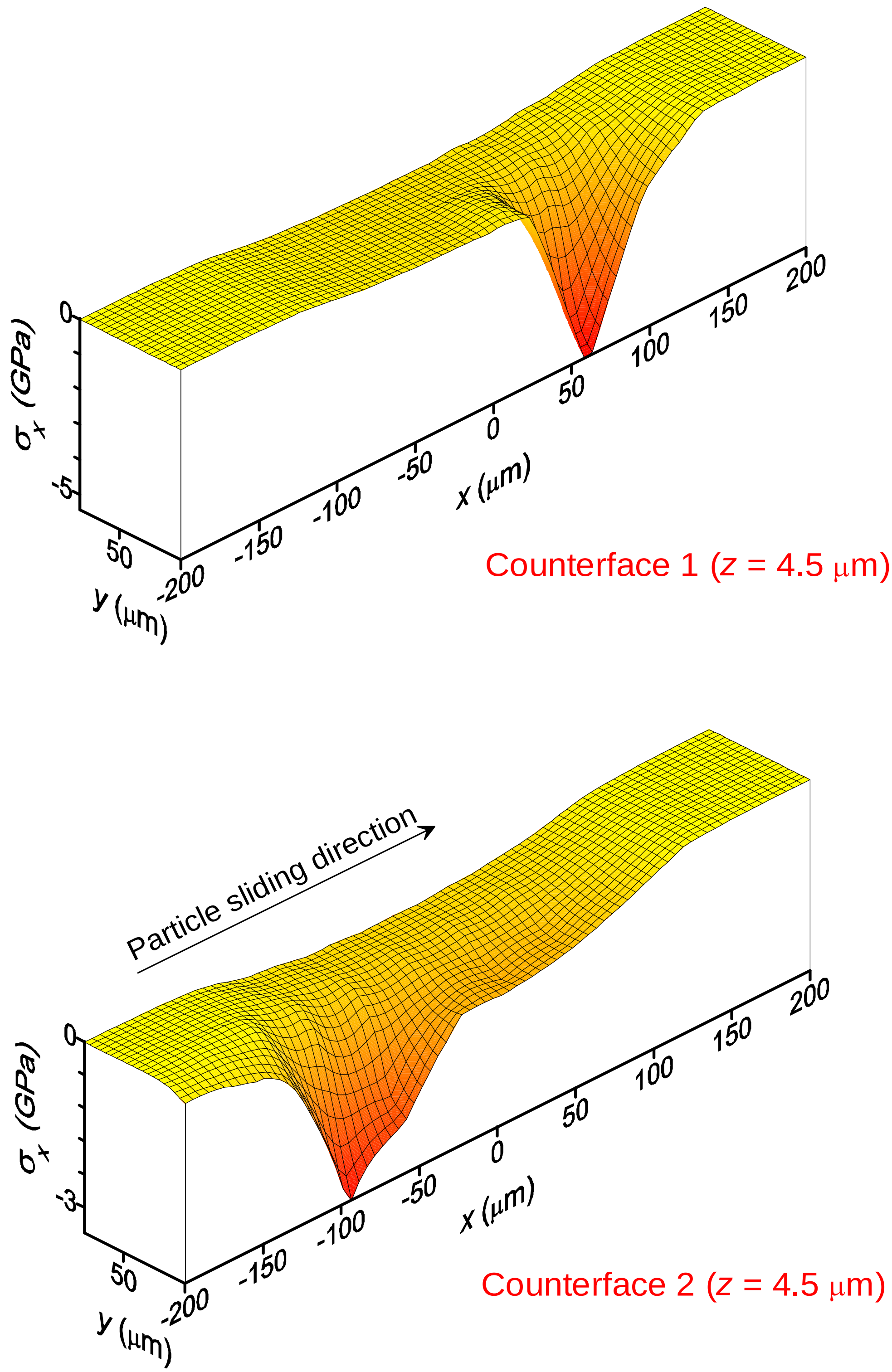

Figure 5.22 Overall stress distribution σ_x on the counterfaces at the time when the particle starts exiting the Hertzian zone (t = 0.52 ms).

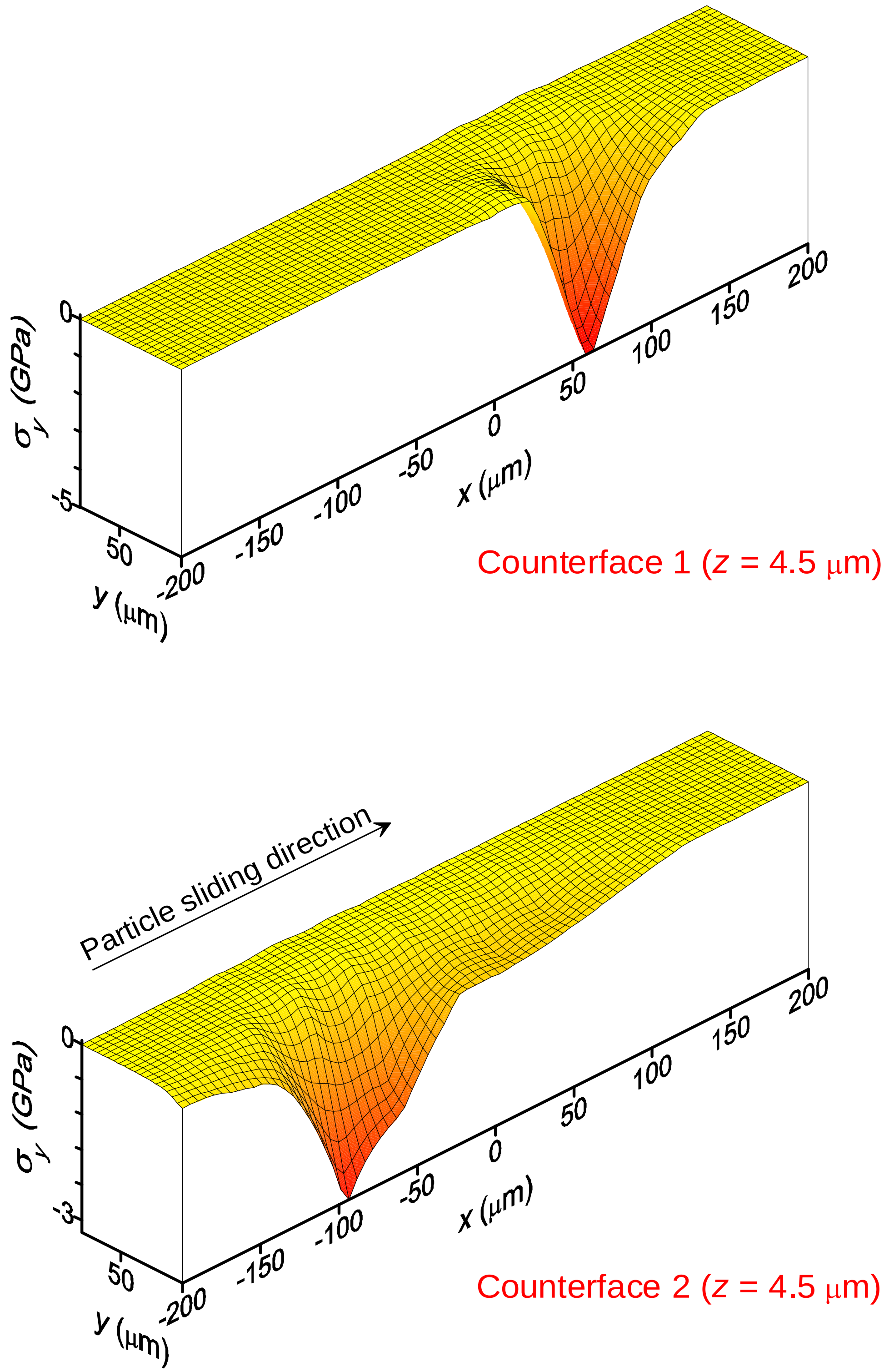

Figure 5.23 Overall stress distribution σ_y on the counterfaces at the time when the particle starts exiting the Hertzian zone (t = 0.52 ms).

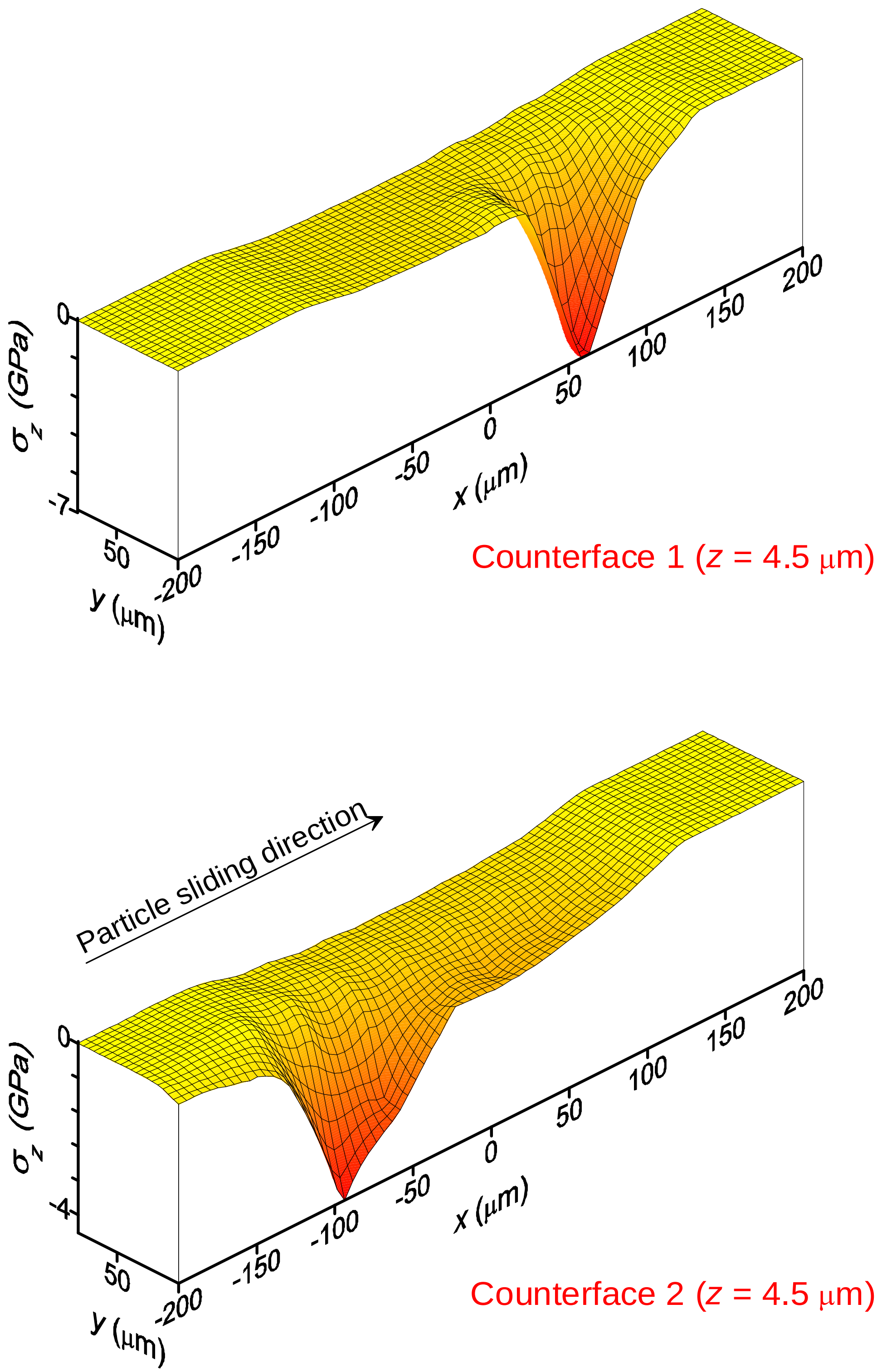

Figure 5.24 Overall stress distribution σ_z on the counterfaces at the time when the particle starts exiting the Hertzian zone (t = 0.52 ms).

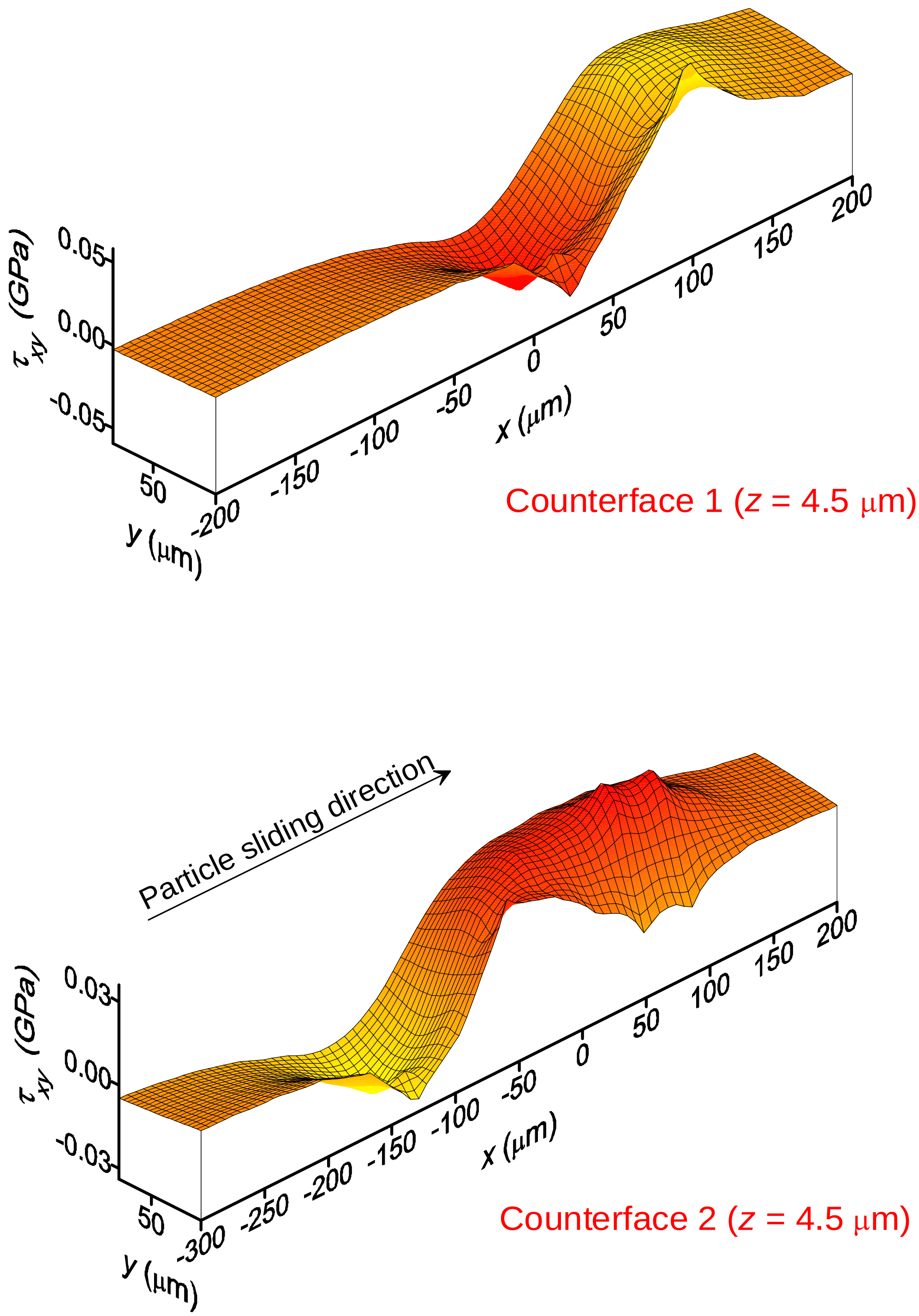

Figure 5.25 Overall stress distribution τ_{xy} on the counterfaces at the time when the particle starts exiting the Hertzian zone (t = 0.52 ms).

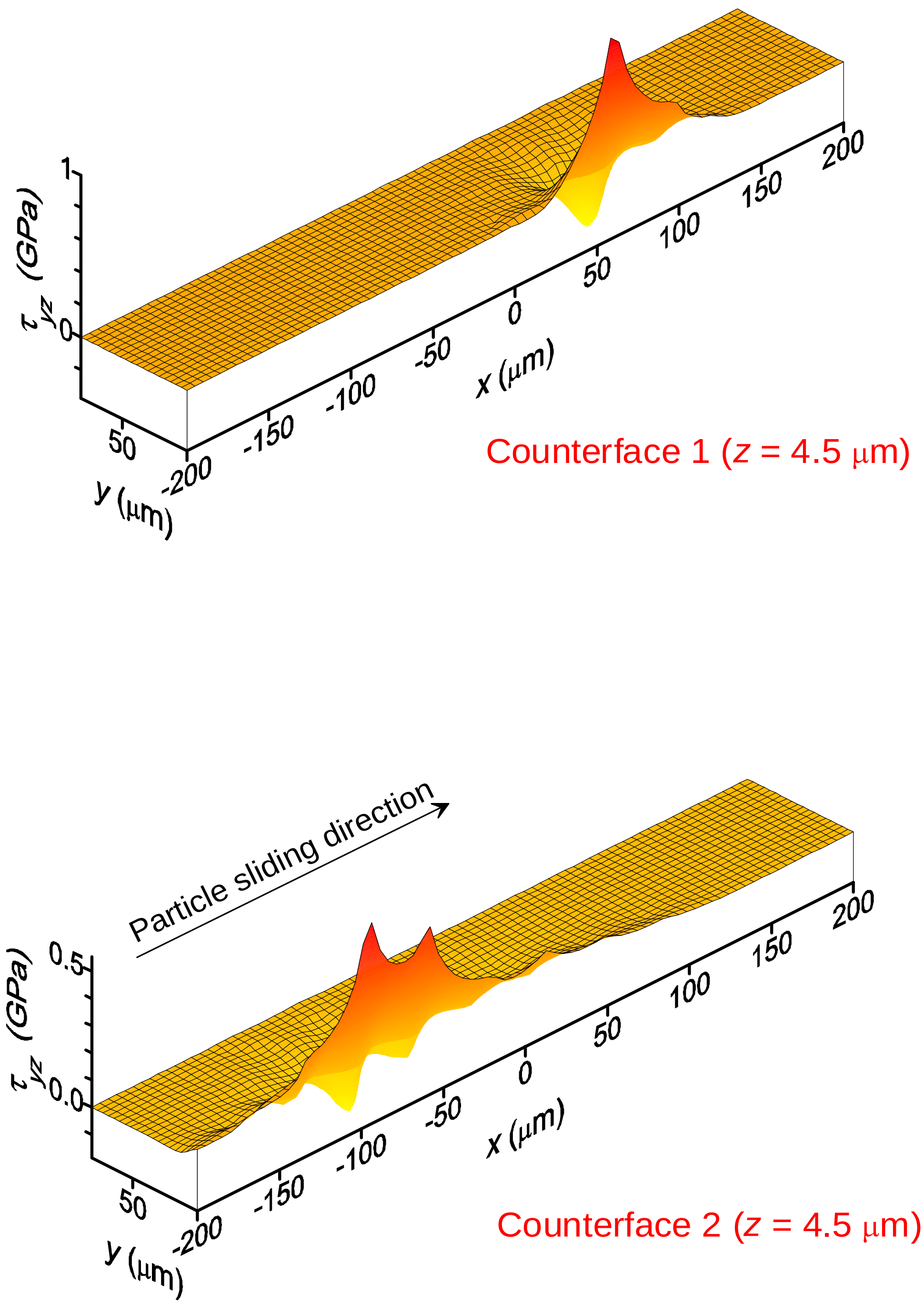

Figure 5.26 Overall stress distribution τ_{yz} on the counterfaces at the time when the particle starts exiting the Hertzian zone (t = 0.52 ms).

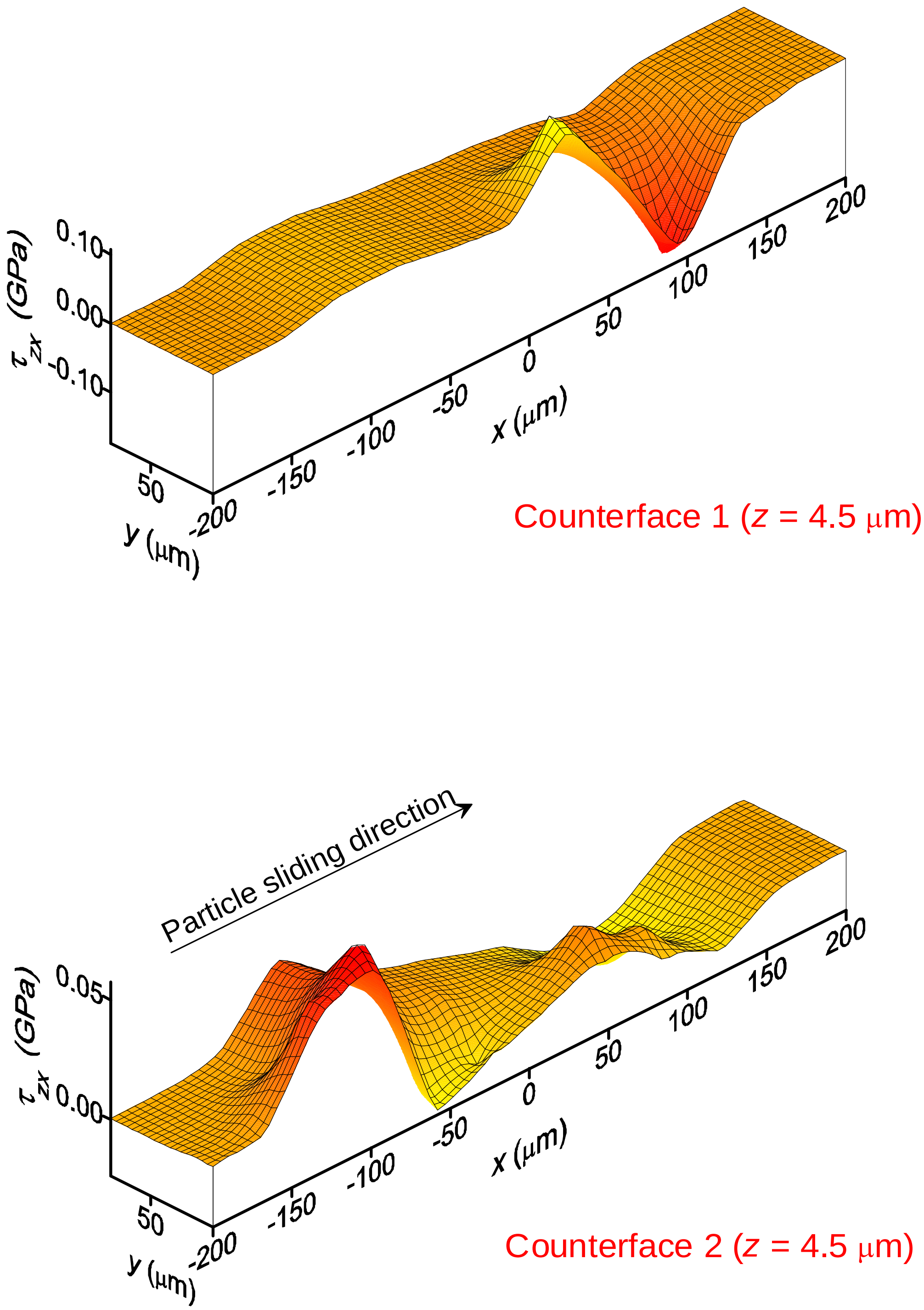

Figure 5.27 Overall stress distribution τ_{zx} on the counterfaces at the time when the particle starts exiting the Hertzian zone (t = 0.52 ms).

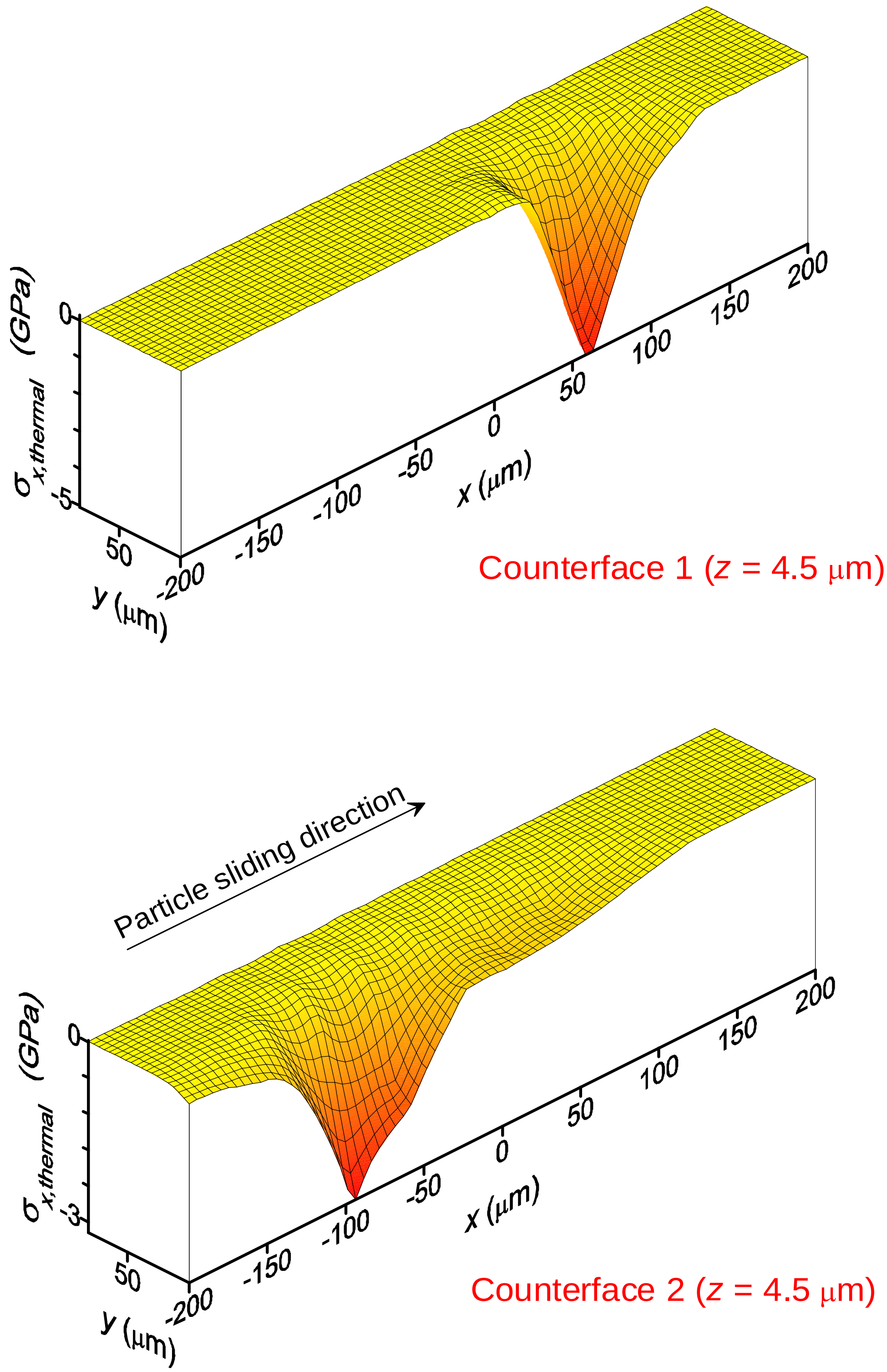

Figure 5.28 Thermal stress distribution $\sigma_{x,\text{thermal}}$ on the counterfaces at the time when the particle starts exiting the Hertzian zone (t = 0.52 ms).

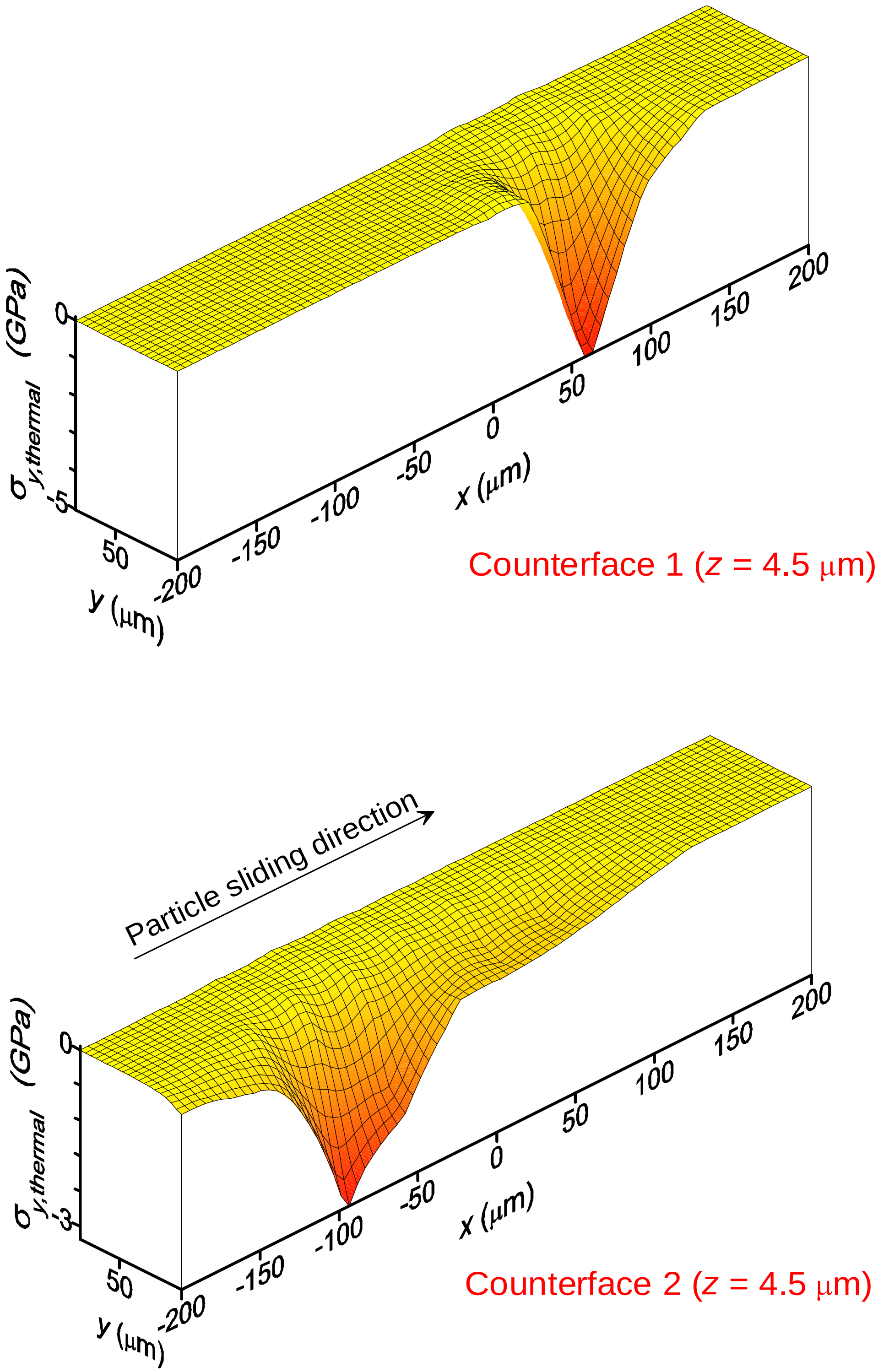

Figure 5.29 Thermal stress distribution $\sigma_{y,\mathrm{thermal}}$ on the counterfaces at the time when the particle starts exiting the Hertzian zone (t = 0.52 ms).

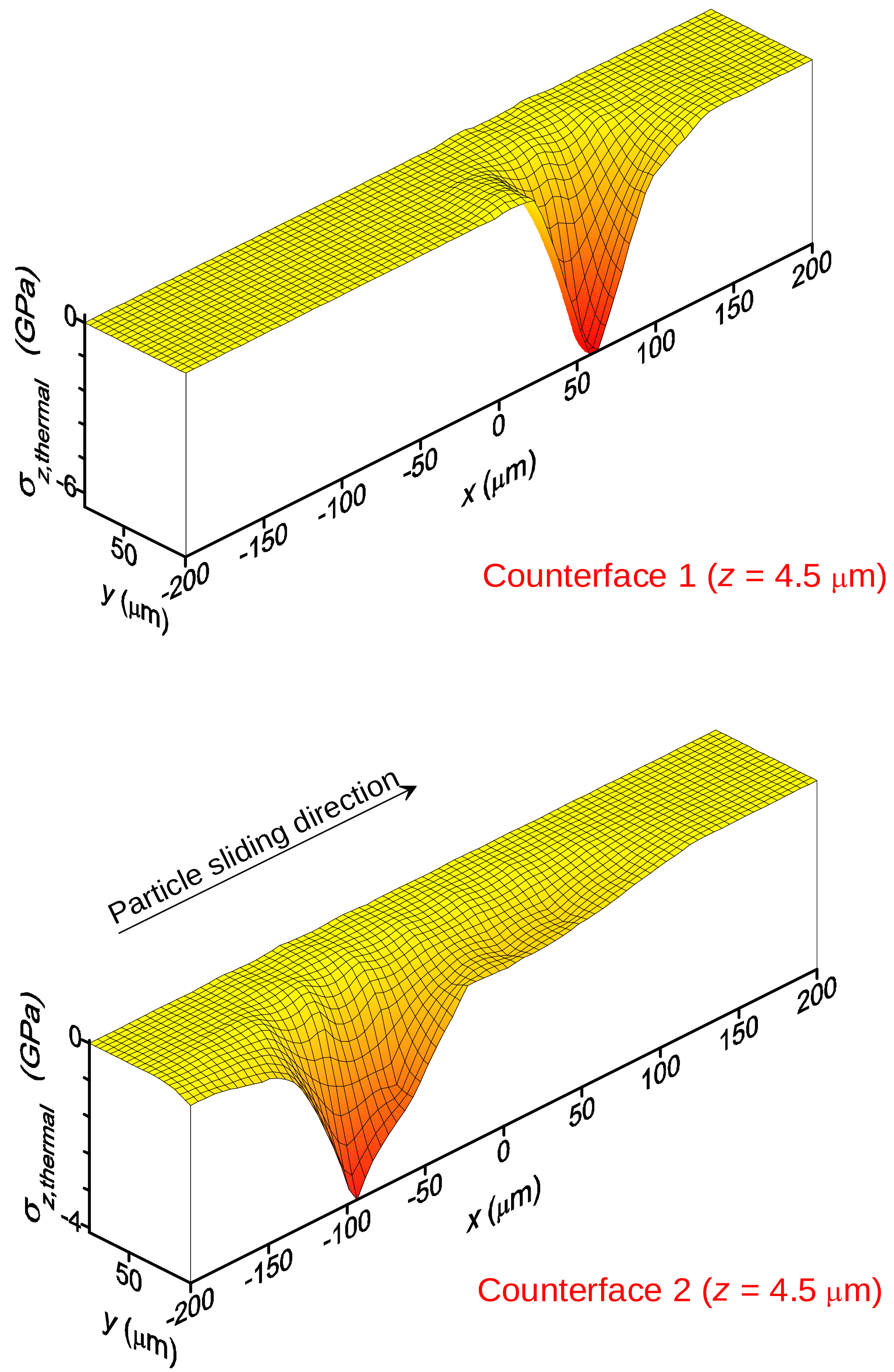

Figure 5.30 Thermal stress distribution $\sigma_{z,\mathrm{thermal}}$ on the counterfaces at the time when the particle starts exiting the Hertzian zone (t = 0.52 ms).

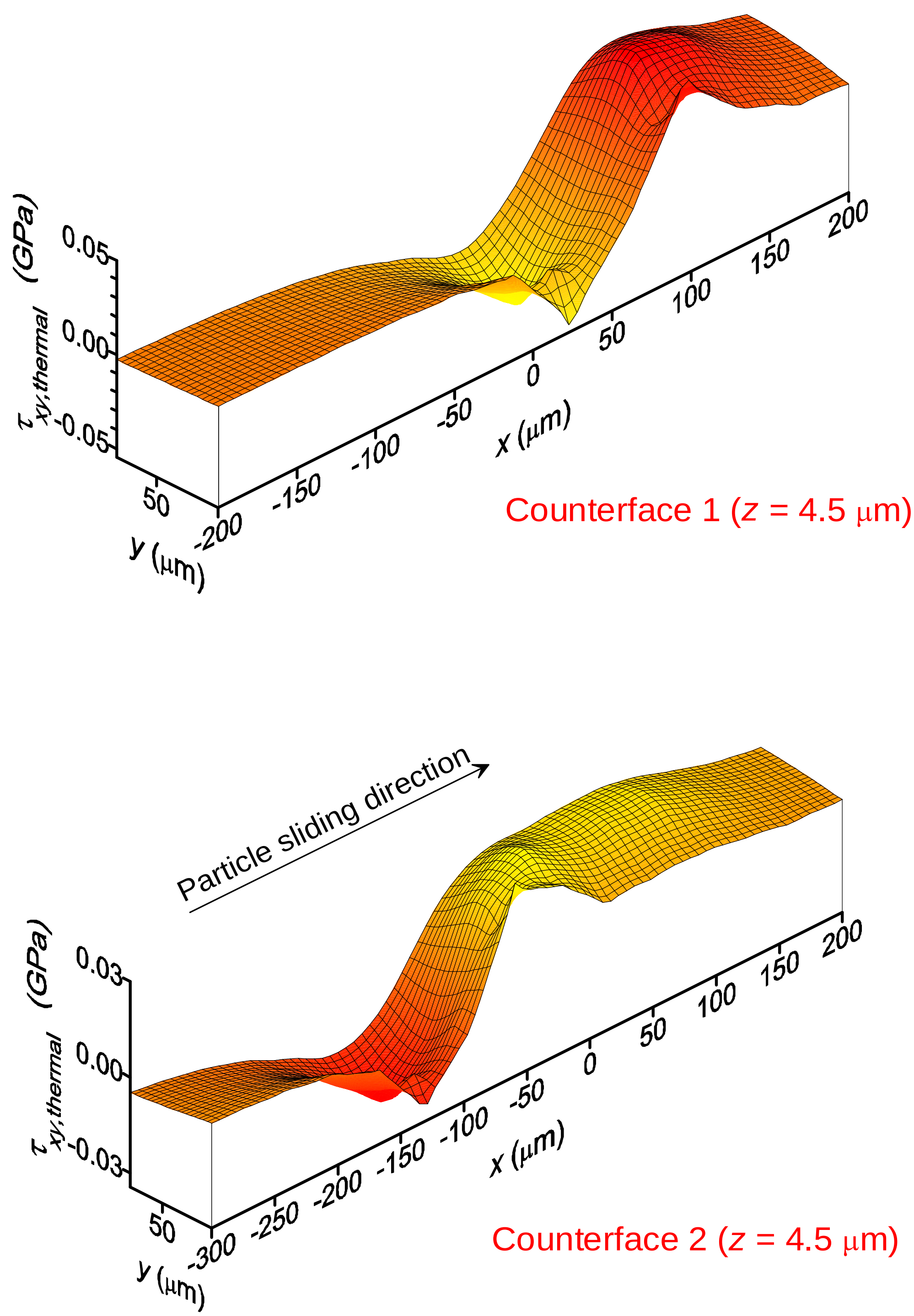

Figure 5.31 Thermal stress distribution $\tau_{xy,\mathrm{thermal}}$ on the counterfaces at the time when the particle starts exiting the Hertzian zone (t = 0.52 ms).

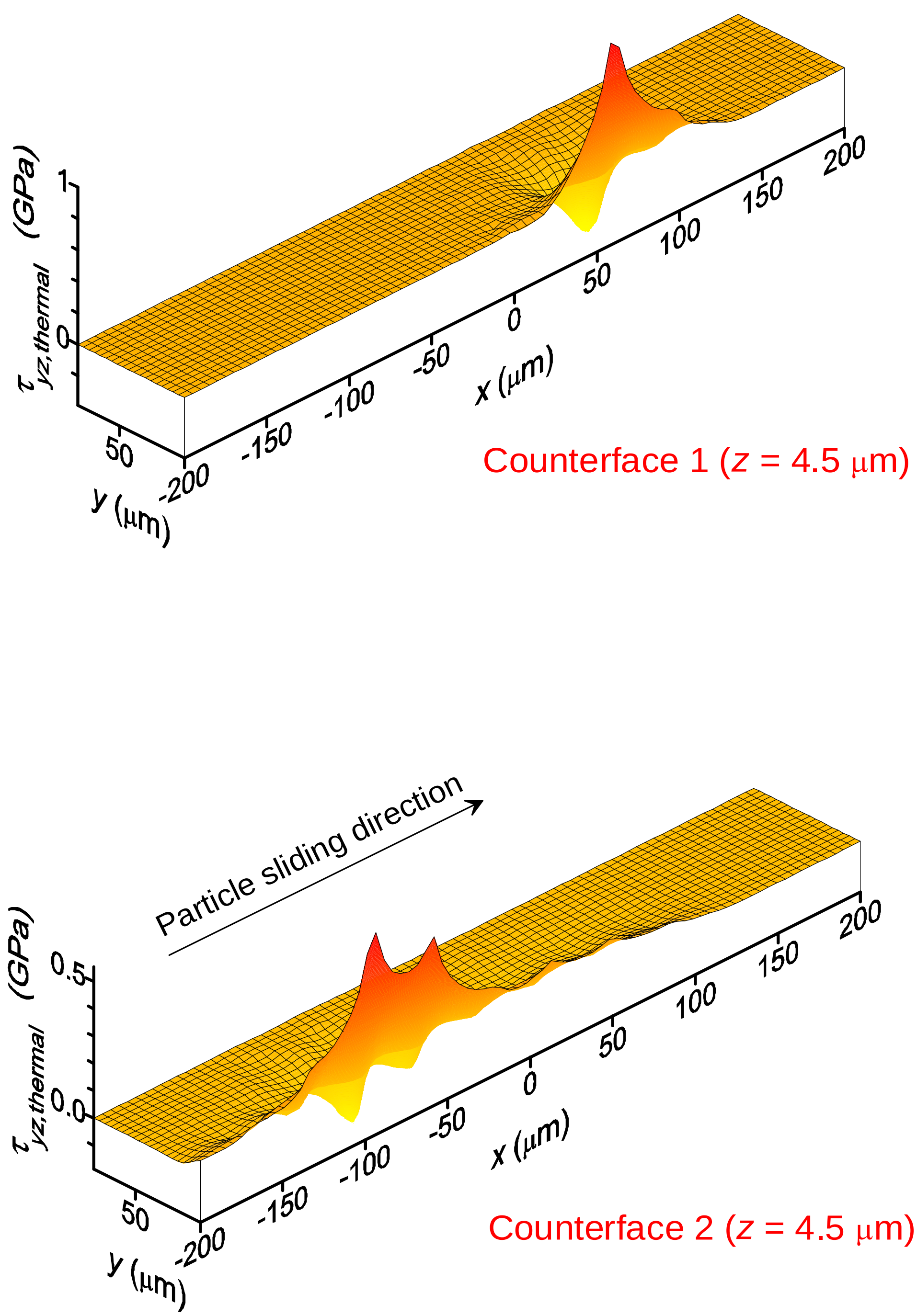

Figure 5.32 Thermal stress distribution $\tau_{yz,\mathrm{thermal}}$ on the counterfaces at the time when the particle starts exiting the Hertzian zone (t = 0.52 ms).

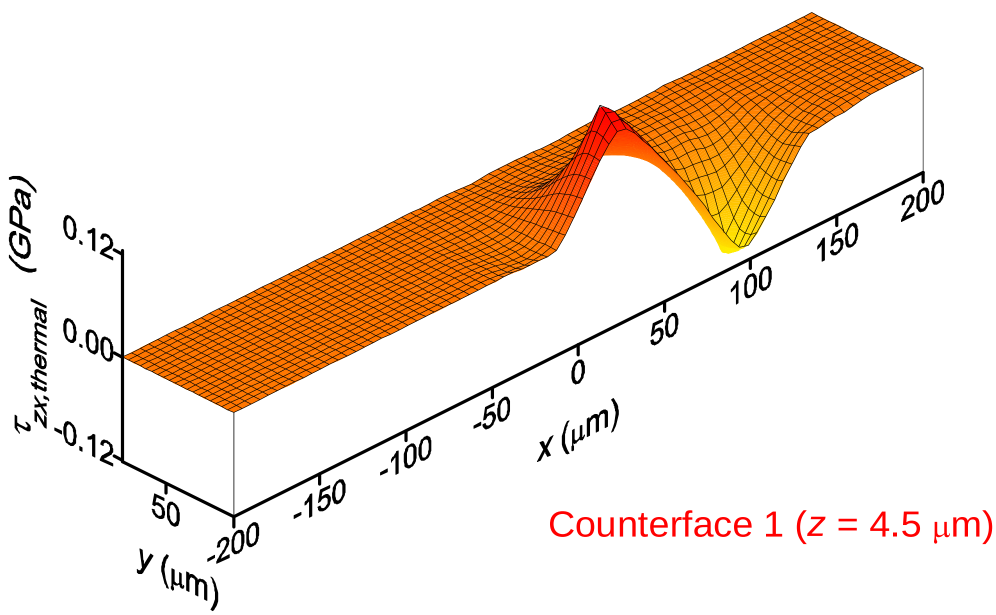

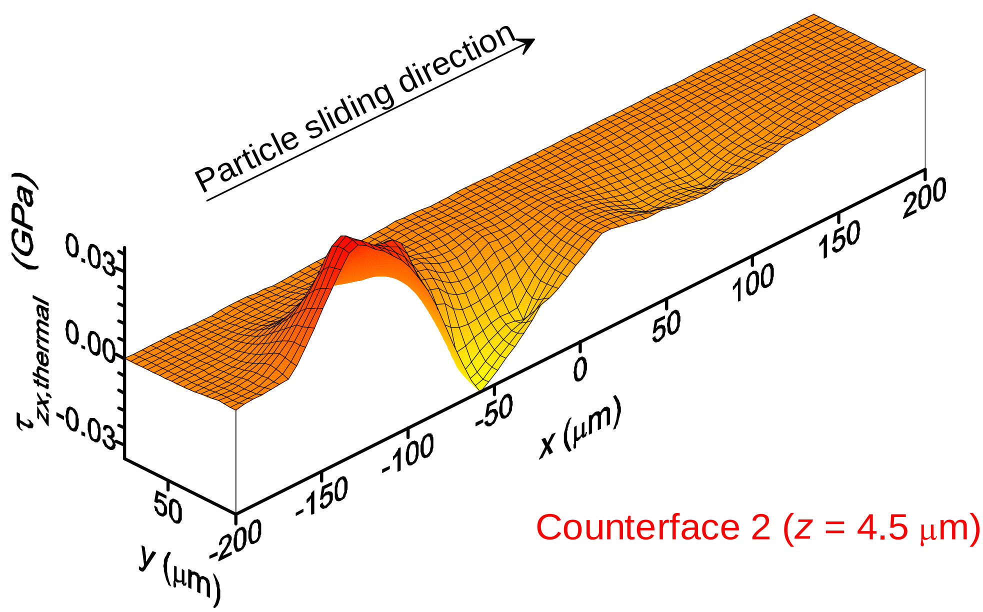

Figure 5.33 Thermal stress distribution $\tau_{zx,\mathrm{thermal}}$ on the counterfaces at the time when the particle starts exiting the Hertzian zone (t = 0.52 ms).

Small irregularities in some of the stress distributions shown in figures 5.22-5.33 are easily explained through the scale used in the figures (magnified), the number of nodes used (not very high because of CPU time constraints), and the large number of competing factors (temperature-dependent mechanical and thermal material-properties, thermal anisotropy, mechanical, thermal and Hertzian stresses, artificial surface loading to remove parasitic surface thermal stresses produced by the method of the "Thermoelastic Displacement Potential" (see the explanations above equation (5.8))).

The maximum values of all stress components at the time when the particle starts exiting the Hertzian zone (t = 0.52 ms) are summarized in table 5.5. Overall and thermal stress values of the same stress component do not necessarily refer to the same location in the bodies.

Table 5.5

Maximum values of the overall and thermal stresses at the time when the particle starts exiting the Hertzian zone ($t \cong$ 0.52 ms)				
Stress	Overall stress (GPa)		Thermal stress (GPa)	
	Body 1	Body 2	Body 1	Body 2
σ_x	–5.75	–3.30	–5.29	–3.28
σ_y	–5.23	–3.32	–5.27	–3.32
σ_z	–7.22	–4.24	–6.74	–4.24
τ_{xy}	–0.07	+0.04	+0.07	–0.04
τ_{yz}	+1.00	+0.61	+1.04	+0.61
τ_{zx}	+0.29	–0.14	+0.25	+0.12

As is evident from table 5.5 and from figures 5.22-5.33, the frictional heating between the particle and the counterfaces results in high thermal normal stresses, which actually account for the largest part of the overall normal stresses, with surface 1 being the more overly stressed due to the higher flash temperatures there.

However, the loading map shown in table 5.5 might not be representative of the worst loading of the contact. This can be realized from figure 5.21, where the average solid pressure on the particle is plotted. In the latter figure, it is evident that at the time when the particle starts exiting the Hertzian zone ($t \cong 0.52$ ms), the average solid pressure between the particle and the counterfaces is quite small compared with the maximum pressure encountered when the particle enters the Hertzian zone, which is at a time around $t = 0.39$ ms. Consequently, the mechanical stresses at time $t = 0.52$ ms are not very high, as opposed to the thermal stresses, which at the same time have their maximum strength. The "contest" between mechanical and thermal stresses starts as soon as the particle gets trapped. After that, the contest is continuous until the particle enters the Hertzian zone, where the thermal stresses prevail. The area of high risk for surface damage (plastic deformation) is located somewhere near the entrance to the Hertzian zone, where both mechanical and thermal stresses have high magnitudes. The exact location can be found by studying the stress history of the counterfaces during the motion of the particle, as is done for the flash temperatures. Due to the excessive CPU (Central Processing Unit) times for a complete solution of the problem, the author reports here an approximate time, equal to 0.36 ms, when the worst loading is expected to take place. At that time, the particle's geometrical centre is about to enter the Hertzian zone. The maximum flash temperatures are 896 °C on counterface 1 and 646 °C on counterface 2, which are 66 % and 76 % of the absolute maxima (encountered at $t \cong 0.52$ ms), respectively, as is shown in figures 5.17-5.20. Damage is indeed predicted to initiate on surface 1 (where the particle is stationary). This would mark the end of the present analysis, because after the creation of a plasticity zone on one counterface, any *elastic* results from the model of this Thesis are, obviously, invalid.

The omission of the thermal stresses from the stress calculations would have given false predictions of the risk of damage in the contact. This is made clearer when checking for yielding at each node of the grids. For example, applying the simpler model of chapter 3 in a case of a 30 μm particle (with all other properties as in the main example of this section) it was found that for a $20 \times 15 \times 40$ node grid, counterface 2 would encounter plastic deformations as follows:

- 0 nodes, considering only thermal stresses,
- 26 nodes, considering only mechanical stresses,
- 351 nodes, considering mechanical *and* thermal stresses.

This means that the omission of thermal stresses from the calculations would have resulted in about 90 % underestimation of the risk of plastic deformation and damage on counterface 2 (let alone the damage on counterface 1).

There are two important observations at this stage:

(1) Thermal stresses increase significantly the risk of damage in the contact. This is immediately noticeable in table 5.5. Although *mechanical* stress maxima do not usually coincide with *thermal* stress maxima, it can be seen that in some areas on the counterfaces, thermal stresses account for the highest part of the overall loading. This has been confirmed by numerous authors in the past. For example, Ju and Huang (1982) showed analytically that the thermal stress is compressive and at a much higher level than that resulting from mechanical loading, when modelling the friction of a moving asperity on the surface of a bearing seal (check the conclusion of their paper). Marcher (1982b) showed analytically that "*…the thermal stresses were greater than the mechanical stresses during the majority of the rub event*.", during his study of thermal versus mechanical effects in high speed sliding. He speculated that this high surface thermal (compressive) loading could explain the occurrence of surface "mud-flat" cracks, which could promote and accelerate wear. Similar effects from thermomechanical cracking were mentioned in Ju and Huang (1982). The analytical paper of Tseng and Burton (1982) (on the thermal stress in a two-dimensional half-space for a moving heat input) is even more spectacular in that it shows that "*…the thermal compressive stress is found to be* ***ten*** *times the normal load for the assumed contact conditions and hence it is this stress rather than simple load concentration which causes the trouble*.". The importance of thermal stresses was also raised by Roylance *et al*. (1986), who showed that by omitting them and treating their problem as isothermal, significant damage would not have been predicted.

(2) The role of the thermal stresses, apart from increasing the risk of failure in the contact, is to bring the high-risk strain zone much closer to the surface, than in the case where thermal loading is absent. This has also been shown analytically in, for example, Roylance *et al*. (1986), and Ting and Winer (1989). The effect of introducing thermal stresses is qualitatively similar to the effect of increasing the friction coefficient; both increase the overall level of stresses and bring the high-risk strain zone closer to the surface, with the thermal-stress maximum occurring

on the surface. The latter explains the initiation and propagation of surface thermo-cracks and the material melting and detachment from scuffed components. It is also important to mention here that the rapid decrease of flash temperature below the surface, as is shown in figure 3.3, results in a corresponding fast weakening of the thermal stresses with depth. This has been confirmed by, for example, Roylance *et al.* (1986, see the discussion section and figure 5 of their paper). Kulkarni *et al.* (1991) performed an elastoplastic FEM analysis of a rolling-sliding contact with a translating heat source and found that thermal gradients were negligible below a depth equal to the contact half-width. This is exactly the result of the present model as can be seen in table 3.3 where it is quoted that in a depth of 100 μm (with the contact half-width equal to 114 μm), the maximum overall temperature is 62 °C, which is only 2 °C (or 3 %) above the bulk temperature of 60 °C. At the higher depth of 114 μm, the temperature is almost equal to the bulk temperature and the thermal gradients are negligible (see also figure 3.3).

Since thermal stresses are so important in the development of cracks and high-stress zones, it is interesting to seek information on the contribution of the particle's internal heating and particle and surface cooling in the final level of flash temperatures in the contact.

For the particular example studied in this section, the omission of the particle's internal heating results in maximum flash temperatures reduced by 10 °C for both counterfaces. This means that the maximum flash temperatures would be 1340 °C (instead of 1350 °C) and 836 °C (instead of 846 °C) for counterfaces 1 and 2, respectively, which is only 0.7 % and 1.2 % less than the calculated flash temperatures, correspondingly. Similar results have been obtained in other examples tested by the author, which suggests that the contribution of the heat generated inside the particle due to its plastic deformation is too small to make a real difference in the level of temperatures in the contact.

On the other hand, the contribution of particle and surface cooling due to heat convection to the lubricant is much less influential and can be neglected completely. In absolute terms, the cooling effect is extremely weak (< $O(10^{-6})$ as compared with the amount of frictional heat produced in the contact). This weakness is attributed mainly to the value of the heat convection coefficient, which is extremely small. The lubricant film is indeed too thin to act as a heat sink for the absorption of the frictional heat, which is almost completely dissipated by conduction to the counterfaces. In an analytical work with some similarities (thermal stresses from a moving band heat source on the surface of a semi-infinite solid, using FEM analysis), Mercier *et al*. (1978) reached the same conclusion: "*…For flood cooling such as found in sliding and machining processes, H* (author's quote: *H* is the heat convection coefficient) *is not sufficiently large to significantly reduce the thermal stresses*.". It should be noted that the work of the previous authors (Mercier *et al*.) is not dealing with the even more extreme case of elastohydrodynamic films, which would induce even weaker cooling effects, as the present author invokes here. The interested reader is advised to study also the paper of DesRuisseaux and Zerkle (1970) which includes surface cooling effects in a theoretical analysis.

It is now clear that the squashed particle is able to cause severe frictional heating, which affects directly the counterfaces, the particle and the lubricant, increasing dramatically the risk of surface thermal failure from the predominant thermal stresses. It appears that the primary failure mode is thermal rather than mechanical. Even if the initial damage is local, the possibility of tempering reactions induced by the high temperatures (for example: martensite-to-austenite transformations at around 700-800 °C) followed by rapid cooling that introduces residual stresses, and the risk of microscopic surface thermo-cracks that could later propagate under the influence of elastohydrodynamic pressures to result in pitting (as in gears) are both precursors of extended damage. From this point of view, it is instructive to assess the risk of damage by just looking at the level of temperatures in the contaminated contact, rather than studying the stress results, which might not indicate direct damage. Table 5.6 shows a parametric study for the maximum flash temperatures for various operational conditions. The parameters of the study are the particle's size (diameter) and hardness, assuming all other data are the same as shown in tables 5.1-5.3. The results presented in table 5.6 are typical results of the full model of this Thesis and not specially selected. The magnitude difference in the temperature results (for surface 2 only) of table 5.6 (full model) and those of table 3.4 (preliminary model) is basically explained by the fact that the preliminary model neglects the heat directed from the particle to surface 2. The latter heat comes from:

(a) the interface of the particle with surface 1,

(b) the interior of the particle, and

(c) the interface of the particle with counterface 2, (temporarily transferred to the particle and partly redirected back to surface 2, according to the model of section 3.4).

Table 5.6

Parametric study – Theoretical maximum flash temperatures (full model)
(conditions other than those listed below are the same as in tables 5.1-5.3)
The particle sticks to surface 1.

Particle diameter [μm]	Particle hardness [HV]	Maximum flash temperature [°C]		T_2/T_1 [%]
		Surface 1 (T_1)	Surface 2 (T_2)	
5	100	93	17	18
5	200	185	34	18
5	400	350	68	19
10	100	211	103	49
10	200	415	182	44
10	400	760	318	42
20	100	1350	846	63
20	200	1560	962	62
20	400	1830	1120	61

According to table 5.6, a 20 μm, 400 HV spherical particle (half the hardness of the counterfaces) is capable of raising the local temperature in the elastohydrodynamic contact by 1830 °C! Larger particles, like 30 μm ones, result in theoretical temperatures in excess of 2,000 °C, which cannot be accepted in practice because they are expected to cause particle and/or counterface melting and this is shown through the full model of this Thesis, which applies the von-Mises yield criterion and detects *if*, *where* and *when* plastic deformation would occur.

Table 5.6 shows also that small and soft particles (like 5 μm and eight times softer than the counterfaces or less) do not cause severe frictional heating, as was also shown in chapter 3. For so small particles, the highest risk for damage comes from the fact that they may accumulate in the inlet zone of the contact and cause fluid starvation, as is shown in chapter 1.

The analysis of the example in this section is completed with the presentation of the elastic surface-distortions in figures 5.34 and 5.35.

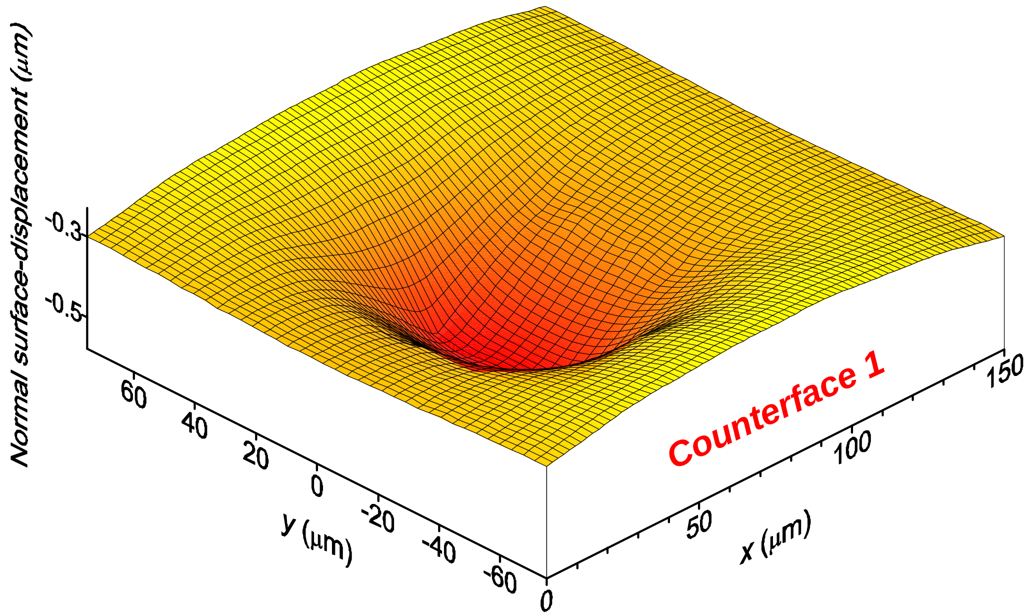

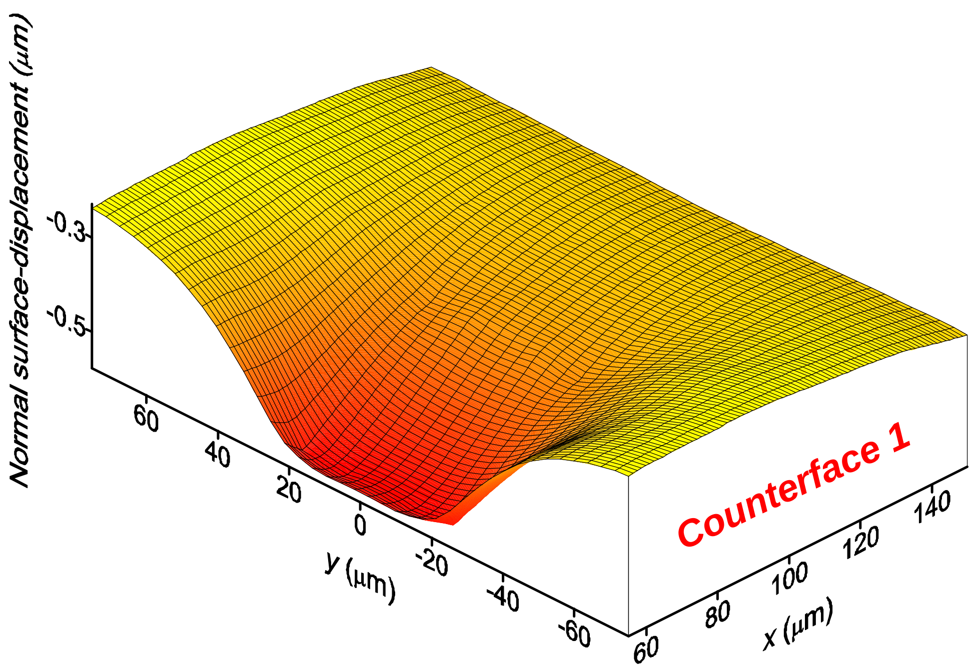

Figure 5.34 Elastic distortion of counterface 1 as the particle starts exiting the Hertzian zone (t = 0.52 ms). Full view on the upper graph and partial view on the lower graph.

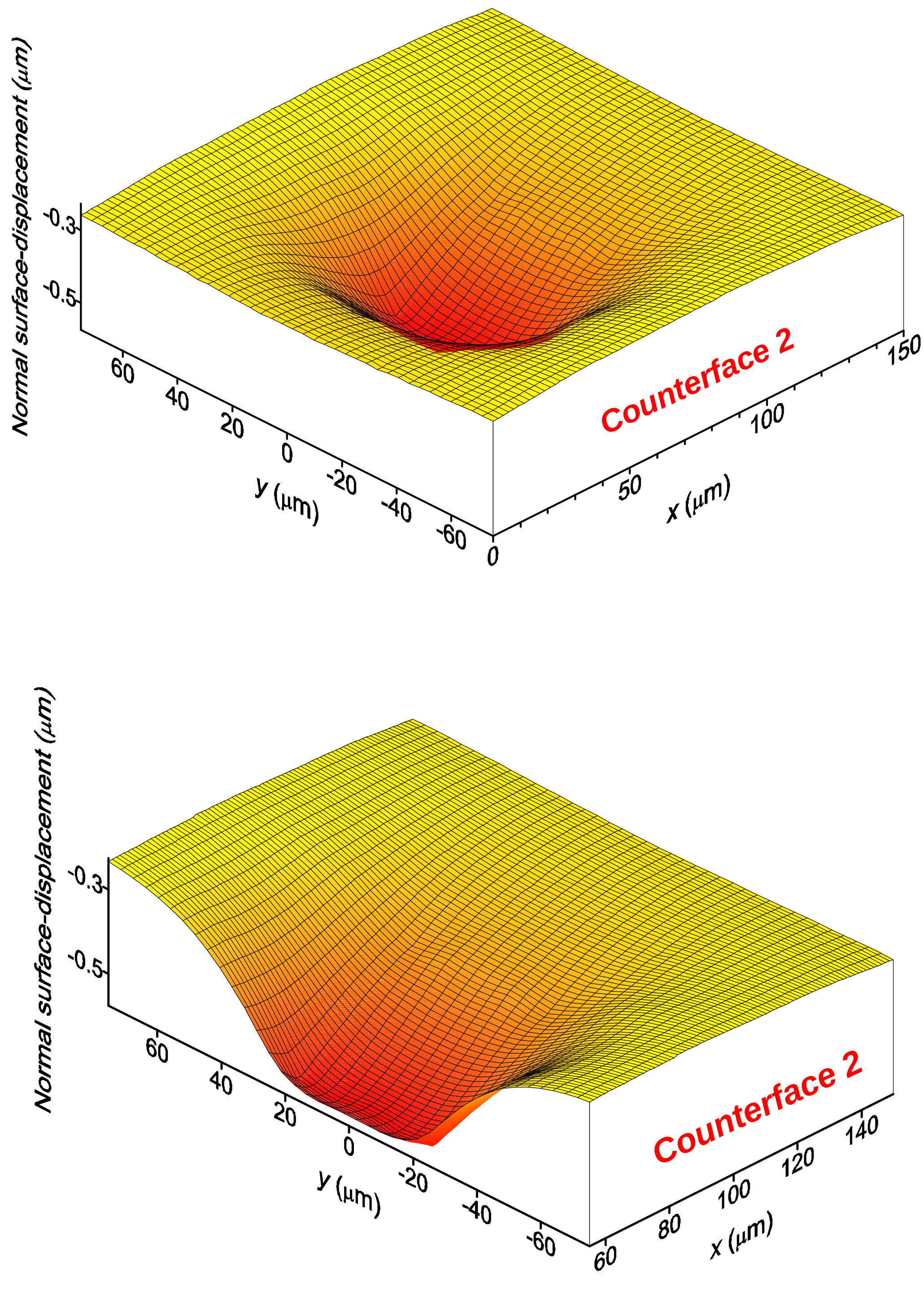

Figure 5.35 Elastic distortion of counterface 2 as the particle starts exiting the Hertzian zone (t = 0.52 ms). Full view on the upper graph and partial view on the lower graph.

Figures 5.34 and 5.35 show the real elastic distortion of the counterfaces, as they would be observed with a naked eye, if it were possible to be frozen in time and have the particle removed. The maximum elastic displacements are quoted in table 5.7.

Table 5.7

Maximum elastic displacements at the time when the particle starts exiting the Hertzian zone ($t \cong 0.52$ ms)		
Displacement	Displacement on surface 1 [μm]	Displacement surface 2 [μm]
u	–0.95	–0.86
υ	+0.22	+0.13
w	+0.57*	+0.24*

* A positive value for *w* indicates a cavity, according to the notation of figure 4.2, where the z-axis is directed towards the interior of the bodies. This rule is not followed in figures 5.34 and 5.35 where the *w*-values shown have the opposite sign (negative).

As figures 5.34 and 5.35 show, the elastic distortions of both counterfaces are very smooth. Although the displacements are elastic, it is worth mentioning here that, as is well known (see Tallian (1992), section 12.4), the dents caused by soft particles have a smooth appearance, in contrast to dents caused by hard particles, which appear irregular with sharp edges. According to the exhaustively detailed book of Tallian (1992) (see section 12.4, page 214, cases 1 and 3 of his book), "…*Soft particle dents show rounded or drop shapes and rounded edges.*", whereas "…*Debris (hard particle) dents are sharp-edged depressions corresponding to the shape of the indenting particle, originally with raised edges,…*". Additional information can be found in the work of Sayles and Dwyer-Joyce (see for example Sayles (1995) and Dwyer-Joyce *et al.* (1992)).

As is also extensively explained in section 3.8 with the comments about Zantopoulos' (1998) paper, such soft-particle dents have usually the appearance of a drop (named "teardrop" in Zantopoulos' paper, although not directly referring to contamination particles). The results of this Thesis and especially figures 5.34 and

5.35 confirm the experimental findings and, moreover, "suggest" that there may be further evidence of the presence of soft debris right at the bottom of soft-rounded dents: at that area we might expect to see a secondary small dent, or cavity, caused by the increased softening of the material due to the high local heating, *if* and *when* the operating conditions permit the development of high temperatures. The lower graphs in figures 5.34 and 5.35 show very small bumps, which, although elastic and thus recoverable, are expected to possibly leave a trace of their existence when the deformation is irrecoverable (plastic). If such small secondary cavities exist indeed inside macro-dents, then the deformed ductile particles responsible for their creation should also exhibit a complementary bump, which should fit in those micro-cavities. In fact, Ville and Nelias (1997) discovered experimentally such secondary-dents (small holes) in indentation tests with ductile, spherical steel particles, which were of equal hardness to the counterfaces in rolling-sliding contacts. However, their tests revealed such formations even under pure rolling conditions (no sliding) and it is not evident to the present author that the mechanism of their creation can be explained solely or partially by the thermo-plastic softening factor put forward in this Thesis. It would be more interesting to perform an FEM analysis using the thermomechanical stress results at the area of maximum loading or at the area where the first yield is predicted to occur, before reaching more solid conclusions.

5.5 Construction of a safe map

It would be very interesting and instructive to apply the model of the Thesis in order to predict which combinations of particles and operating conditions involve high (or low) risk of damage in a rolling-sliding contaminated contact. This study can neatly take the form of a map showing safe and unsafe regions of operation. Such maps were presented by Hamer *et al*. (1989b), and Hamer and Hutchinson (1992), but are confined to one-dimensional compression, squashing a particle between two slowly approaching flat surfaces.

A similar map is constructed for the needs of this Thesis. For reasons of usefulness and clarity, a 2-dimensional map with axes D/h_c (particle diameter/central film thickness) and V_s (sliding speed of the contact) has been chosen as the best option. The diameter D of the particle is the diameter of the particle before its plastic deformation, visualizing the particle as a sphere. The counterfaces are considered to be of equal hardness (800 HV). The friction coefficients between the particle and the counterfaces are chosen to lie in the boundary lubrication regime ($\mu_1 = 0.20$ and $\mu_2 = 0.15$). The particle is taken to be ductile and much softer than the counterfaces, as is the main objective of this Thesis. The particle's hardness is 80 HV, which means that the particle is ten times softer than the counterfaces. Finally, the slide/roll ratio (sliding velocity divided by the arithmetic mean of the tangential speeds of the counterfaces) is chosen to be equal to 1. The "safe map" is shown in figure 5.36 and has been produced by applying the preliminary model of the Thesis, developed in chapters 2, 3 and 4, with the assumptions shown in table 3.2.

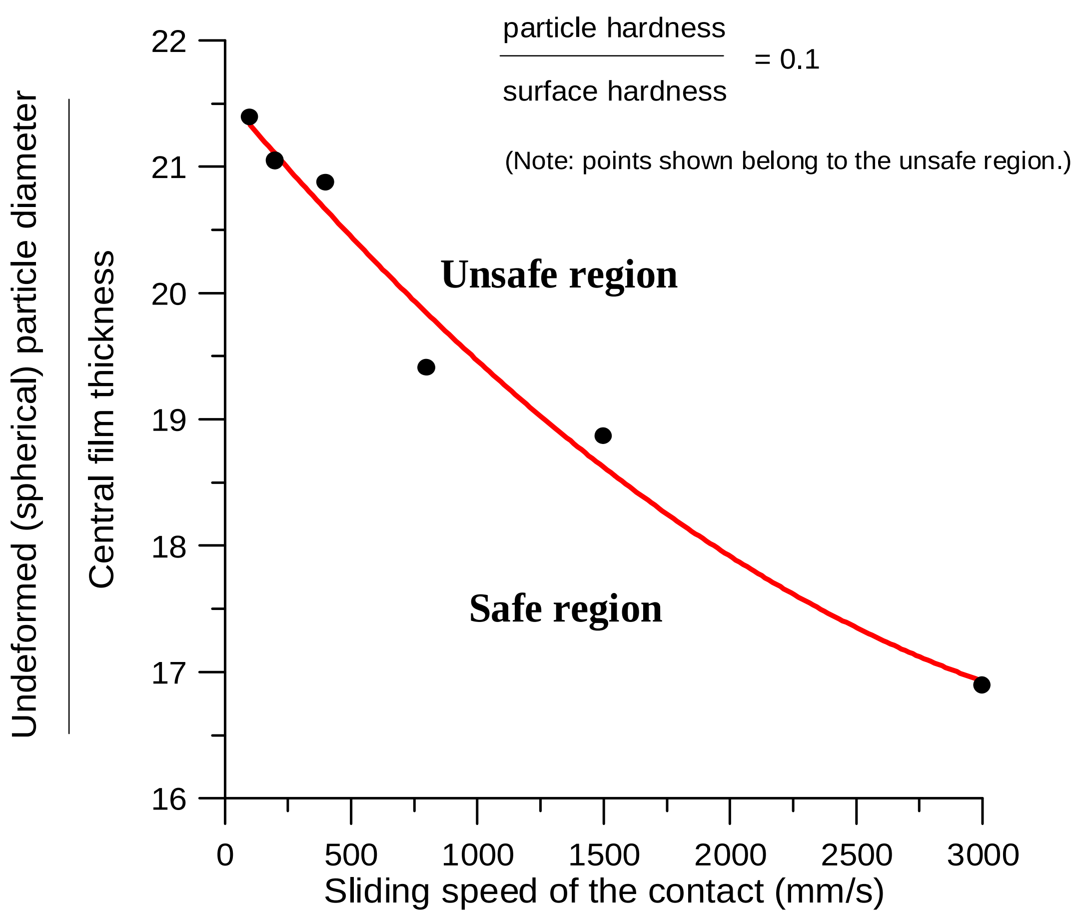

Figure 5.36 Safe map (based on the preliminary model of chapters 2, 3 and 4).

These assumptions result in calculating significantly lower flash temperatures, but, on the other hand, the pressure between the particle and the counterfaces is significantly higher due to the assumption of rigid counterfaces. The preliminary model was preferred to the more accurate full model of the Thesis because of time constraints: the full model is significantly slower in CPU times because of the added computational tasks involved. For the reader to get an idea of the difficulties, it suffices to say that a single run of the main computer program of the Thesis with the full model requires approximately two weeks of time in a Personal Computer with a 266 MHz INTEL Pentium-II processor for a sufficiently accurate analysis. This computing power is equivalent, if not superior, to the power of large Workstations and Mini computers ten years ago! The six points shown in the safe map (figure 5.36) require several program runs <u>each</u>, in order to locate them on the map. Even with the preliminary model, the total computational (CPU) time for the construction of the map of figure 5.36 was no less than 3 months, using a 166 MHz processor, excluding the time lost in correcting minor bags and inefficiencies of the code, which raised the overall running time to well over one year! Although the use of a fast Workstation or even Mainframe computer was not prohibited, such an option was not convenient due to the large number of tests and runs required for the development of the computer program, which took more than four years and more than twenty releases before reaching its final form of over 2,000 lines of FORTRAN 90 optimized code.

Returning to the safe map, a satisfactory data fit (red line on the map) is given by the following quadratic model:

$$D_{\mathrm{critical}} = \left(21.565034 - 0.002378 \cdot V_{\mathrm{s}} + 2.771 \cdot 10^{-7} \cdot V_{\mathrm{s}}^{2}\right) \cdot h_{\mathrm{c}} \tag{5.27}$$

which has a correlation coefficient equal to 0.990. For harder particles (or softer counterfaces), the red line shown in the map will move towards the safe region. Note that $h_{\mathrm{c}} \sim V_{\mathrm{s}}^{0.69}$ since $S_r = \dfrac{V_s}{\text{rolling velocity}} = 1$ and h_{c} is proportional to (rolling velocity)$^{0.69}$, according to the central film thickness formula used in this study (as in Pan and Hamrock (1989)).

Increasing the sliding speed of the contact has two effects:

(1) For typical working conditions, the central film thickness is increased. This results in lower mechanical stressing from the particle, especially in the Hertzian zone of the contact. Thus, the likelihood of yielding is decreased.

(2) More frictional heat is produced, which results in higher thermal loading. Thus, the likelihood of yielding is increased.

Clearly, (1) and (2) above are in conflict. The outcome of their competition depends on the relation of the central film thickness to the sliding speed of the contact. Using $h_c \sim V_s^{0.69}$, as mentioned previously, the critical particle diameter is monotonically increasing with increasing sliding speed of the contact. This result is derived from equation (5.27), setting $h_c = c \cdot V_s^{0.69}$, where c is a constant, and plotting the result, as in figure 5.37.

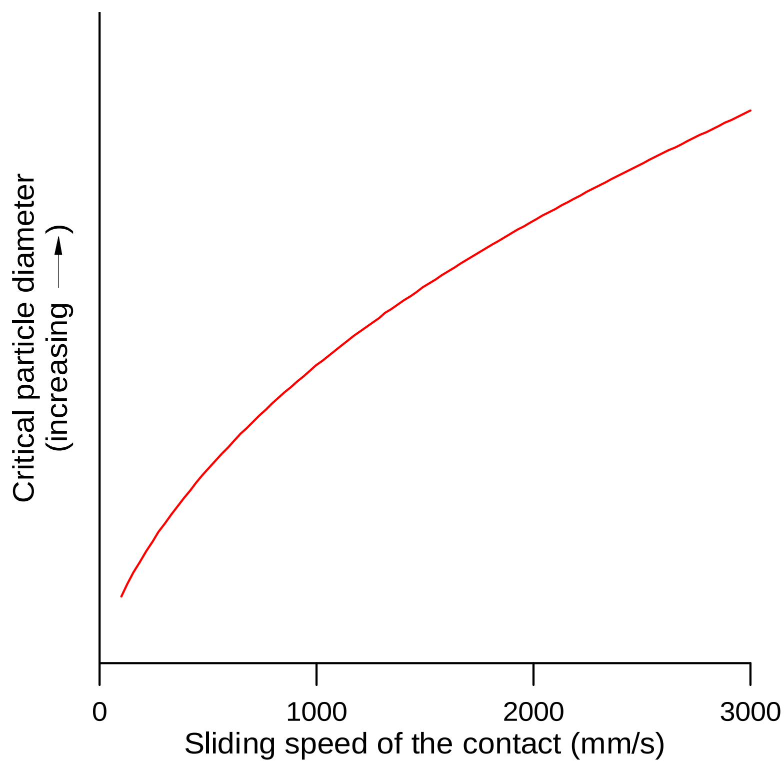

Figure 5.37 Critical particle diameter (qualitative view) to cause damage; from equation (5.27), with $h_c = c \cdot V_s^{0.69}$, where c is a constant.

The safe map shown in this section is associated with the particular operational conditions in the contact, namely the slide/roll ratio, specific mechanical and thermal material-properties, specific ratio of particle hardness over counterface hardness, etc. If any of these were to change, a new safe map should be constructed. The data chosen for the map of figure 5.36 are typical and average, in order to give a representative view of what should be expected in most applications. However, particular applications cannot rely on figure 5.36 and need their own damage-risk analysis.

5.6 Conclusions

The basic model to study particle compression and shearing between two rolling-sliding surfaces in an elastohydrodynamic contact was re-established in this chapter, in order to achieve a more accurate calculation of the stresses and temperatures expected to affect the lubricated contact. A flowchart of the complete model is presented in figure 5.7. Moreover, the simplifying assumptions adopted in previous chapters (see table 3.2), regarding the sharing of heat among the various elements (counterfaces, particle and lubricant) were all removed and the resulting full model was applied in a typical case of a ductile, spherical 20 μm particle being trapped between two rolling-sliding counterfaces, which were eight times harder than the particle.

The results of the full model are in line with the results of the simplified model, and are briefly summarized as follows.

(1) The particle flattens in the inlet zone of the contact and becomes a thin disk as it passes through the flat Hertzian zone (figure 5.8).

(2) The solid frictional forces on the particle are much higher than the overall fluid force and the individual fluid-force components (figure 5.11). As a result, the motion of the particle when compressed between the counterfaces is basically governed by the solid frictional forces.

(3) The particle sticks to the counterface with the higher friction coefficient immediately after its entrapment in the contact (figure 5.12). This sticking is due

to the much higher solid-frictional forces on the particle as compared with the fluid forces, as was explained in (2) previously.

(4) The lateral expansion (extrusion) and shearing of the particle during its plastic compression in a rolling-sliding lubricated contact results in frictional heating of the counterfaces, the particle and the lubricant. The heating can be very high (see table 5.6) for relatively large and moderately hard particles (but still much softer than the counterfaces), and the flash temperatures encountered in the contact can reach hundreds of degrees C. The maximum flash temperature is reached in times of the order of 1 ms for typical applications, depending on the rolling and sliding speeds of the contact. For bigger and/or harder (ductile) particles, the maximum flash temperature can easily exceed the melting point of the materials of the counterfaces and/or the particle. Figures 5.13-5.20 demonstrate the development of high flash temperatures in a contact, caused by the entrapment of a spherical 20 μm particle, which is eight times softer than the counterfaces.

(5) The distributions of the flash temperatures on the counterfaces follow the variation of the average solid pressure on the particle (figure 5.21), which is affected by the elastohydrodynamic pressure in the contact. The average solid pressure on the particle exhibits a maximum at the entrance to the Hertzian zone of the contact (figure 5.21), and this affects significantly the level and location of the maximum flash temperature, as can be realized by comparing figure 5.21 with figures 5.16 and 5.18.

(6) The partition of the frictional heat between the particle and the counterfaces is ruled by the thermal properties of the bodies in question, but the greatest amount of heat goes to the surface which is stationary to the particle, for obvious reasons. This is obvious in table 5.6, where the last column gives an idea of the temperature difference between the hotter and the cooler surface. It is seen that, generally, the bigger and/or harder the particle, the smaller is (as a percentage) the temperature difference between the two surfaces. However, the biggest impact on the level of the flash temperature is the size of the particle. From table 5.6, the absolute difference of the maximum flash temperatures for a 5 μm and for a 20 μm particle is quite substantial.

(7) The particle is expected to have an average temperature distribution closer to that of the counterface to which it is stationary, which turns out to be the hotter.

(8) Due to its plastic compression, the particle is a heat generator itself. The heat is generated in its interior due to internal shearing, but this is relatively small compared with the frictional heat produced at the interfaces of the particle with the counterfaces. For the example studied in section 5.4, this internal heat accounts for only around 1 % of the maximum flash temperatures. It can therefore be disregarded.

(9) The heat convected by the particle and the counterfaces to the lubricant is negligible and can be omitted without any consequence in the results. The reason for this is the extremely small heat-convection coefficient for the typical elastohydrodynamic-lubrication case analyzed in this study. Consequently, the counterfaces are essentially transferring all of the frictional heat by conduction.

(10) For typical thermal properties of materials studied (engineering steels), the frictional heat transferred to the counterfaces is dissipated in a short range inside the counterfaces and is very weak at a depth equal to the Hertzian contact semi-width below the surfaces (see figure 3.3 and table 3.3). Therefore, the thermally affected areas are those that are immediately below the surfaces, at a depth of a few microns.

(11) Because of the frictional heating in the contact, thermal stresses develop in those areas that are mostly heated. The thermal stresses are quite high as compared with the mechanical stresses in the contact (arising from the compression of the particle) and, in some areas of the counterfaces, account for the highest part of the overall loading (see table 5.5 and figures 5.22-5.33). Following this, the risk of surface damage is significantly increased. Thermal stresses also displace the high-risk zone for plastic deformations much closer to (or on) the surface. The omission of thermal-stress calculations would significantly underestimate the true risk of damage in the contact.

(12) The frictional heating following the particle's presence in the contact, results in the creation of a hot spot in the Hertzian zone, at the time when the particle is rejected to the outlet zone (see figures 5.15 and 5.16). The elastic distortion of the counterfaces (seen in the example of figures 5.34 and 5.35) has a smooth appearance, representative of soft and ductile debris dents. Due to the high temperatures in the aforementioned "hot spots", it is expected that these areas, if undergone plastic deformation, would appear as smooth and shiny indentations. The shiny or white-color appearance is because of possible tempering reactions

due to the high temperatures, as for example martensite-to-austenite transformations at 700-800 °C, followed by fast cooling to a much lower temperature.

(13) It appears that soft and ductile particles are more likely to produce high frictional heating conditions in a sliding contact as compared with hard particles, because the area they occupy when plastically compressed is much bigger than the area occupied by same-size hard particles. This is because soft/ductile particles are fully flattened in the inlet zone, whereas hard particles resist their extrusion and retain their initial shape, embedding the counterfaces that try to squash them. Therefore, the soft particles offer a much bigger interface for friction with the counterfaces as opposed to hard particles and, thus, cause higher thermal stressing. Consequently, and because of the usual prevalence of the thermal stresses over the mechanical stresses, it might not be surprising that soft/ductile particles are sometimes equivalently destructive (as far as direct surface defects are concerned) than hard particles of equal size!

(14) The creation of hot spots from the frictional heating caused by soft/ductile debris could explain some failures and resembles closely the damage characterized as “local scuffing”. Although the author is not implying that the mechanism of local scuffing is solely wear-particle related, the theoretical predictions of this Thesis suggest strongly that debris particles have their own unique contribution in thermomechanical failures of contacts in a significant proportion of reported cases.

(15) Because of the high heat zone at the core of the hot spots, it is sometimes expected to observe a secondary (micro) cavity inside a surface dent and a corresponding bump around the centre of the faces of the soft/ductile deformed particle, which was responsible for the damage.

CHAPTER 6

SUMMARY OF CONCLUSIONS OF THE THESIS

The main objective of this Thesis was the theoretical modelling of the behaviour of soft/ductile debris particles in rolling-sliding elastohydrodynamic contacts. In pursuit of this target, two models were developed. The first model (chapter 1) deals with the entrainment of solid particles in elastohydrodynamic point contacts and is aimed to predict the behaviour of the particles in the inlet zone and assess the risks of lubricant starvation and surface indentation due to the accumulation, agglomeration and entrapment of the particles in the contact. The second model (chapters 2-5) deals with the entrapment and squashing of solid particles in line elastohydrodynamic contacts and is used to study subjects like the thermomechanical loading of both the particle and the counterfaces of the contact, and to assess the risk of damage of the contact in various forms (indentation, abrasion, thermal failure, etc.).

Detailed discussions and explanations are scattered throughout chapters 1-5 and main conclusions are analyzed in the relevant sections at the end of each of chapters 1, 2, 3 and 5. Analytical and experimental verification of the predictions of this Thesis are drawn from the literature and referenced wherever necessary, and wherever it is possible, in all previous chapters. The present chapter serves as a brief summary of the main conclusions only, quoted without repeating the lengthy discussions and literature references found in other chapters of the Thesis. Therefore, this chapter is only a quick guide of main results.

The important conclusions are briefly as follows.

1. Depending on the operational conditions, debris particles tend to, sometimes, accumulate in the inlet zone of lubricated contacts (verified for point contacts in chapter 1), and, by blocking the inlet and preventing the replenishment of the contact with lubricant, can cause lubricant starvation, film collapse and even scuffing. Particle accumulation is usually promoted by high sliding conditions in the contact (high slide/roll ratios). Specific combinations of particle size – oil bath thickness that would give higher risk of particle accumulation and lubricant starvation are shown in figure 1.53.

- More information: chapter 1 (section 1.3, 1.4, figure 1.53).

2. Similarly to conclusion 1 previously, some operational conditions in lubricated point contacts promote the *entrapment* of debris particles, with a consequent risk of surface indentation and abrasion. This is more evident for large particles (like 20 μm ones) in elastohydrodynamic contacts, but other combinations of particle size – oil bath thickness are also of risk, as can be seen in figure 1.53.

- More information: chapter 1 (section 1.3, 1.4, figure 1.53).

3. Very large particles (as for example larger than 100 μm), which are much bigger than the film thickness in lubricated contacts, are more difficult to become entrapped, especially in contacts that involve sliding. Therefore, very large particles can be harmless.

- More information: chapter 1 (section 1.3, 1.4), chapter 2 (sub-section 2.3.3).

4. In a line elastohydrodynamic contact, the forces applied by the lubricant on a particle are much weaker than the forces due to friction between the particle and the counterfaces. Therefore, and in view of its infinitesimal inertia, the motion of the particle is ruled by the solid frictional forces.

- More information: chapter 2 (section 2.5, 2.6, 2.8, 2.9, figure 2.10, table 2.5), chapter 5 (figure 5.11).

5. In a line elastohydrodynamic contact, a *soft/ductile* particle becomes flattened in the inlet zone as it gets squashed between the counterfaces, and becomes a platelet with a thickness at the order of the central film thickness of the contact. The platelet might be circular (rolling contacts) or slightly elliptical (sliding contacts).

- More information: chapter 2 (sections 2.4, 2.9).

6. In a line elastohydrodynamic contact, a *soft/ductile* particle, if entrapped, usually *sticks* to the counterface with the higher friction coefficient (provided the two counterfaces are of almost equal hardness) *immediately* after being pinched. For counterfaces with unequal hardness, the particle sticks to the softer surface. The sticking involves only the inlet and central zones of the contact. "Sticking" of the particle to a counterface when entering the outlet zone and sticking to the faster surface (reported in the literature) are given separate special explanation.

- More information: chapter 2 (sections 2.7-2.9, figure 2.11), chapter 5 (section 5.4, figure 5.12).

7. In concentrated lubricated contacts, debris particles generate heat due to friction with the counterfaces in the contact, especially when there is sliding in the contact and the particles are relatively large (usually larger than 5-10 μm). The heating can be very high (see table 5.6) even for particles that are 10 times softer than the counterfaces. Maximum temperature increase in the contact, owing to this frictional heating, is achieved rapidly (in the order of 1 ms, depending on the sliding/rolling speed of the contact) and the maximum flash temperature can even exceed the melting point of the materials involved in the process (particle and counterfaces). Temperatures between 1000-2000 °C are not uncommon for larger particles (table 5.6). In the case of soft particles, particle size is more important than its hardness from the point of view of the maximum flash temperature (table 5.6). Rolling contacts suffer much less from this kind of frictional heating than sliding contacts.

- More information: chapter 3 (section 3.2, 3.8, 3.9), chapter 5 (section 5.4, figures 5.13-5.16, table 5.6).

8. Following conclusion 7, the distribution of flash temperature on the counterfaces follows closely the variation of the average solid pressure on the particle (figure 5.21), which is affected by the elastohydrodynamic pressure.

- More information: chapter 5 (section 5.4, figure 5.16, 5.18, 5.21).

9. Following conclusion 7, the partition of the frictional heat between the particle and the counterfaces is ruled by the thermal properties of the bodies in question, but the greatest amount of heat goes to the surface that is stationary to the particle, for obvious reasons (table 5.6). Generally, the bigger and/or harder the particle is, the smaller is (as a percentage) the temperature difference between the two counterfaces.

- More information: chapter 5 (section 5.4, table 5.6, figures 5.13-5.20).

10. Following conclusion 7, the amount of heat generated inside the particle due to its plastic compression is much smaller compared with the amount of frictional heat generated at the interfaces of the particle with the counterfaces (at the order of 1 % for the example of section 5.4). Moreover, the heat lost due to convection from the hot particle and the counterfaces to the lubricant is infinitesimal (under typical elastohydrodynamic conditions). Therefore, almost all of the frictional heat is transferred to the counterfaces by conduction.

- More information: chapter 3 (sections 3.3-3.5), chapter 5 (section 5.4).

11. Following conclusion 7, the frictional heat transferred to the counterfaces is dissipated in a short range and is barely detectable at a depth equal to the Hertzian contact semi-width of the contact below the counterfaces. Consequently, the thermally affected areas are those immediately below the surfaces, at a depth of a few microns.

- More information: chapter 3 (figure 3.3, table 3.3), chapter 5 (section 5.4).

12. Following conclusion 7, the frictional heating in the contact results in thermal stresses. These stresses are often quite high in comparison with the mechanical stresses in the contact and, in some areas, account for the highest proportion of the overall stress. Thermal stresses increase significantly the risk of surface damage and bring the high-risk zone for plastic deformation closer to the surface.

- More information: chapter 5 (section 5.4, figure 5.22-5.33, table 5.5).

13. Following conclusion 7, the frictional heating from the particle results in the creation of a hot spot on the counterfaces. Due to the (often) high temperatures developed in the aforementioned hot spots, it is expected that these areas, if having undergone plastic deformation, would eventually appear as “shiny” indentations. The shiny or white-color appearance is because of possible tempering reactions due to the high temperatures, as for example martensite-to-austenite transformations at 700-800 °C, followed by fast cooling to a much lower temperature. The indentations are expected to have a smooth appearance due to the softness of the particles, as the surface elastic displacements suggest (figures 5.34, 5.35).

- More information: chapter 5 (section 5.4, figure 5.15, 5.16, 5.34, 5.35).

14. Following conclusion 7, soft and ductile particles are more likely to result in high frictional heating conditions in a sliding contact as compared with hard particles because the area they occupy when plastically compressed is much bigger than the area occupied by same-size hard particles. This is because soft/ductile particles are fully flattened in the inlet zone, whereas hard particles resist their extrusion and retain their initial shape, embedding the counterfaces that try to squash them. Therefore, the soft particles offer a much bigger interface for friction with the counterfaces as opposed to hard particles and, thus, cause higher thermal stressing. Consequently, and because of the usual prevalence of the thermal stresses over the mechanical stresses, it may not be surprising that soft/ductile particles are sometimes equivalently destructive (as far as direct surface defects are concerned) as hard particles of equal size!

- More information: chapter 2 (section 2.4), chapter 5 (section 5.4).

15. Following conclusions 7 and 13, the creation of hot spots from debris particles in concentrated contacts could explain some failures and can be characterized as *local scuffing*.

- More information: chapter 5 (section 5.4, figure 5.15, 5.16).

16. Following conclusions 7 and 13, it is sometimes expected to observe a secondary (micro) cavity inside a (past) hot spot (present surface dent) and a corresponding bump around the centre of the faces of the (now flattened) soft particle responsible for that damage. The cavity is due to softening of the material, following a high local heating.

- More information: chapter 5 (section 5.4, figure 5.15, 5.16, 5.35, 5.36).

REFERENCES

Ai, X., Cheng, H. S., and **Zheng, L.,** 1993, "A Transient Model for Micro-Elastohydrodynamic Lubrication with Three-Dimensional Irregularities", Transactions of the ASME, Journal of Tribology, vol. 115, pages 102-110.

Ai, X., and **Haiqing, Y.,** 1988, "A Full Numerical Solution for General Transient Elastohydrodynamic Line Contacts and its Application", Wear, vol. 121, pages 143-159.

Anaya-Dufresne, M., and **Sinclair, G. B.,** 1995, "Some Exact Solutions of Reynolds Equation", Transactions of the ASME, Journal of Tribology, vol. 117, pages 560-562.

Aramaki, H., Cheng, H. S., and **Zhu, D.,** 1992, "Film Thickness, Friction, and Scuffing Failure of Rib/Roller End Contacts in Cylindrical Roller Bearings", Transactions of the ASME, Journal of Tribology, vol. 114, pages 311-316.

Archard, J. F., 1958, "The Temperature of Rubbing Surfaces", Wear, vol. 2, pages 438-455.

Archard, J. F., 1973, "Elastohydrodynamic Lubrication of Real Surfaces", Tribology, (February 1973), pages 8-14.

Bailey, D. M., and **Sayles, R. S.,** 1991, "Effect of Roughness and Sliding Friction on Contact Stresses", Transactions of the ASME, Journal of Tribology, vol. 113, pages 729-738.

Barber, J. R., 1967, "The Influence of Thermal Expansion on the Friction and Wear Process", Wear, vol. 10, pages 155-159.

Barber, J. R., 1970, “The Conduction of Heat from Sliding Solids”, International Journal of Heat and Mass Transfer, vol. 13, pages 857-868.

Barber, J. R., 1972, “Distortion of the Semi-Infinite Solid due to Transient Surface Heating”, International Journal of Mechanical Sciences, vol. 14, pages 377-393.

Barber, J. R., 1980a, “The Transient Thermoelastic Contact of a Sphere Sliding on a Plane”, Wear, vol. 59, pages 21-29.

Barber, J. R., 1980b, “Some Implications of Dundur’s Theorem for Thermoelastic Contact and Crack Problems”, Proceedings of the IMechE, Journal of Mechanical Engineering Science, vol. 22, No. 5, pages 229-232.

Barber, J. R., and **Martin-Moran, C. J.,** 1982, “Green’s Functions for Transient Thermoelastic Contact Problems for the Half-Plane”, Wear, vol. 79, pages 11-19.

Barwell, F. T., 1984, “The Role of Particle Analysis - a Review of Ferrography”, Developments in Numerical and Experimental Methods Applied to Tribology, Proceedings of the 10th Leeds-Lyon Symposium on Tribology (6-9 September 1983), Butterworths, pages 3-10.

Bell, J.C., and **Willemse, P. J.,** 1998, “Mid-life Scuffing Failure in Automotive Cam-Follower Contacts”, Proceedings of the IMechE, Part J: Journal of Engineering Tribology, vol. 212, pages 259-269.

Benedict, G. H., and **Kelley, B. W.,** 1961, “Instantaneous Coefficients of Gear Tooth Friction”, ASLE Transactions, vol. 4, pages 59-70.

Berry, G. A., and **Barber, J. R.,** 1984, “The Division of Frictional Heat – a Guide to the Nature of Sliding Contact”, Transactions of the ASME, Journal of Tribology, vol. 106, pages 405-415.

Bissett, E. J., and **Glander, D. W.,** 1988, "A Highly Accurate Approach that Resolves the Pressure Spike of Elastohydrodynamic Lubrication", Transactions of the ASME, Journal of Tribology, vol. 110, pages 241-246.

Blok, H., 1937a, "Theoretical Study of Temperature Rise at Surfaces of Actual Contact under Oiliness Lubricating Conditions", Proceedings of the IMechE, General Discussion on Lubrication (Group IV: Properties and Testing), vol. 2, pages 222-235.

Blok, H., 1937b, "Measurement of Temperature Flashes on Gear Teeth under Extreme Pressure Conditions", Proceedings of the IMechE, General Discussion on Lubrication (Group III: Industrial Applications), vol. 2, pages 14-20.

Boley, B. A., and **Weiner, J. H.,** 1960, *Theory of Thermal Stresses*, Wiley.

Bos, J., and **Moes, H.,** 1994, "Frictional Heating of Tribological Contacts", Transactions of the ASME, Journal of Tribology, paper No. 94-Trib-29.

Bowden, F. P., and **Tabor, D.,** 1986 (reprint), *The Friction and Lubrication of Solids*, Clarendon Press, Oxford.

Bretherton, F. P., 1962, "The Motion of Rigid Particles in a Shear Flow at Low Reynolds Number", Journal of Fluid Mechanics, vol. 14, pages 284-304.

Brunn, P., 1976a, "The Slow Motion of a Sphere in a Second-order Fluid", Rheologica Acta, vol. 15, No. 3/4, pages 163-171.

Brunn, P., 1976b, "The Behavior of a Sphere in Non-homogeneous Flows of a Viscoelastic Fluid", Rheologica Acta, vol. 15, No. 11/12, pages 589-611.

Brunn, P., 1977, "Interaction of Spheres in a Viscoelastic Fluid", Rheologica Acta, vol. 16, No. 5, pages 461-475.

Burton, R. A., 1980, "Thermal Deformation in Frictionally Heated Contact", Wear, vol. 59, pages 1-20.

Cameron, A., 1966, *The Principles of Lubrication*, Longmans, London.

Cameron, A., 1986, "On a Generalized Theory of Scuffing", Mechanisms and Surface Distress, Proceedings of the 12th Leeds-Lyon Symposium on Tribology (3-6 September 1985), Butterworths, pages 3-9.

Cameron, A., Gordon, A. N., and **Symm, G. T.,** 1964, "Contact Temperatures in Rolling/Sliding Surfaces", Proceedings of the Royal Society, A286, pages 45-61.

Carslaw, H. S., and **Jaeger, J. C.,** 1959, *Conduction of Heat in Solids*, second edition, reprint 1993, Clarendon Press, Oxford, England.

Chandrasekaran, S., Khemchandani, M. V., and **Sharma, J. P.,** 1985, "Effect of Abrasive Contaminants on Scuffing", Tribology International, vol. 18, No. 4, pages 219-222.

Chao, K. K., Saba, C. S., and **Centers, P. W.,** 1996, "Effects of Lubricant Borne Solid Debris in Rolling Surface Contacts", STLE Tribology Transactions, vol. 39, No. 1, pages 13-22.

Chapman, A. J., 1987, *Fundamentals of Heat Transfer*, Macmillan.

Chu, W. H., and **Abramson, H. N.,** 1960, "Transient Heat Conduction in a Rod of Finite Length, With Variable Thermal Properties", Transactions of the ASME, Journal of Applied Mechanics, pages 617-622.

Cole, S. J., and **Sayles, R. S.,** 1991, "A Numerical Model for the Contact of Layered Elastic Bodies with Real Rough Surfaces", Transactions of the ASME, paper No. 91-Trib-11.

Cook, N. H., and **Bhushan, B.,** 1973, "Sliding Surface Interface Temperatures", Transactions of the ASME, Journal of Lubrication Technology, pages 59-64.

Cusano, C., and **Sliney, H. E.,** 1982, “Dynamics of Solid Dispersions in Oil During the Lubrication of Point Contacts, Part I – Graphite”, ASLE Transactions, vol. 25, No. 2, pages 183-189.

Dai, F., and **Khonsari, M. M.,** 1993, “A Continuum Theory of a Lubrication Problem With Solid Particles”, Transactions of the ASME, Journal of Applied Mechanics, vol. 60, pages 48-58.

Dawson, P. H., and **Coyle, M. B.,** 1969, “Metal Transfer During Rolling With Sliding – A Challenge”, Wear, vol. 14, pages 385-386.

DesRuisseaux, N. R., and **Zerkle, R. D.,** 1970, “Temperature in Semi-infinite and Cylindrical Bodies Subjected to Moving Heat Sources and Surface Cooling”, Transactions of the ASME, Journal of Heat Transfer, pages 456-464.

Dow, T. A., and **Burton, R. A.,** 1972, “Thermoelastic Instability of Sliding Contact in the Absence of Wear”, Wear, vol. 19, pages 315-328.

Dow, T. A., and **Burton, R. A.,** 1973, “The Role of Wear in the Initiation of Thermoelastic Instabilities of Rubbing Contact”, Transactions of the ASME, Journal of Lubrication Technology, pages 71-75.

Dowson, D., and **Higginson, G. R.,** 1966, *Elasto-hydrodynamic Lubrication, The Fundamentals of Roller and Gear Lubrication*, Pergamon Press, Oxford.

Drew, D. A., 1978, “The Force on a Small Sphere in Slow Viscous Flow”, Journal of Fluid Mechanics, vol. 88, part 2, pages 393-400.

Dundurs, J., 1974, “Distortion of a Body Caused by Free Thermal Expansion”, Mechanics Research Communication, vol. 1, No. 3, pages 121-124.

Dwyer-Joyce, R. S., 1993, “The Effects of Lubricant Contamination on Rolling Bearing Performance”, Ph.D. Thesis, Imperial College of Science, Technology and

Medicine, Mechanical Engineering Department, Tribology Section, London, England.

Dwyer-Joyce, R. S., Hamer, J. C., and **Ioannides, E.,** 1992, “Lubricant Screening for Debris Effects to Improve Fatigue and Wear Life”, Proceedings of the 18th Leeds-Lyon Symposium on Tribology (3-6 September 1991), Tribology Series 21, Elsevier, pages 57-63.

Dwyer-Joyce, R. S., and **Heymer, J.,** 1996, “The Entrainment of Solid Particles into Rolling Elastohydrodynamic Contacts”, Proceedings of the 22nd Leeds-Lyon Symposium on Tribology, September 1995, Tribology Series 31, Elsevier, pages 135-140.

Dwyer-Joyce, R. S., Sayles, R. S., and **Ioannides, E.,** 1994, “An Investigation into the Mechanisms of Closed Three-body Abrasive Wear”, Wear, vol. 175, pages 133-142.

Earles, S. W. E., and **Powell, D. G.,** 1967, “Surface Temperature and its Relation to Periodic Changes in Sliding Conditions between Unlubricated Steel Surfaces”, ASLE paper No. 67-LC-3.

Enthoven, J. C., and **Spikes, H. A.,** 1995, “Visual Observation of the Process of Scuffing”, Proceedings of the 21st Leeds-Lyon Symposium on Tribology (6-9 September 1994), Tribology Series 30, Elsevier, pages 487-494.

Evans, H. P., and **Snidle, R. W.,** 1981, “Inverse Solution of Reynolds’ Equation of Lubrication under Point-contact Elastohydrodynamic Conditions”, Transactions of the ASME, Journal of Lubrication Technology, vol. 103, pages 539-546.

Glander, D. W., and **Bissett, E. J.,** 1988, “On the Stability and Uniqueness of Elastohydrodynamic Lubrication Solutions”, Transactions of the ASME, Journal of Tribology, vol. 110, pages 628-631.

Godet, M., 1984, “The Third-body Approach: a Mechanical View of Wear”, Wear, vol. 100, pages 437-452.

Goodier, J. N., 1937, “On the Integration of the Thermo-Elastic Equations”, Philosophical Magazine, Series 7, vol. 23, pages 1017-1032.

Greenstein, T., 1980, “Interaction and Wall Corrections for the Slow Motion of Two Fluid or Solid Particles Parallel to the Axis of a Circular Cylinder Through a Viscous Fluid”, Journal of Mechanical and Engineering Science, (IMechE), vol. 22, No. 5, pages 243-249.

Greenwood, J. A., 1991, “An Interpolation Formula for Flash Temperatures”, Wear, vol. 150, pages 153-158.

Greenwood, J. A., 1996, “Flash Temperatures for Bodies Moving at Equal High Speeds in Opposite Directions”, Transactions of the ASME, Journal of Tribology, vol. 118, pages 255-257.

Greenwood, J. A., and **Kauzlarich, J. J.,** 1973, “Inlet Shear Heating in Elastohydrodynamic Lubrication”, Transactions of the ASME, Journal of Lubrication Technology, pages 417-426.

Griffioen, J. A., Bair, S., and **Winer, W. O.,** 1986, “Infrared Surface Temperature Measurements in a Sliding Ceramic-Ceramic Contact”, Mechanisms and Surface Distress, Proceedings of the 12th Leeds-Lyon Symposium on Tribology (3-6 September 1985), Butterworths, pages 238-245.

Hamer, J. C., and **Hutchinson, J.,** 1992, “Denting of Rolling Element Bearings by Third Body Particles”, Report No. 33/92, Issue Number 2, PCS – The Technology Transfer Centre, Imperial College of Science, Technology and Medicine, London, England.

Hamer, J. C., Lubrecht, A. A., Ioannides, E., and **Sayles, R. S.,** 1989a, “Surface Damage on Rolling Elements and its Subsequent Effects on Performance and Life”, Proceedings of the 15th Leeds-Lyon Symposium on Tribology (6-9 September 1988), Tribology Series 14, Elsevier, pages 189-197.

Hamer, J. C., Sayles, R. S., and **Ioannides, E.,** 1987, “Deformation Mechanisms and Stresses Created by 3rd Body Debris Contacts and their Effects on Rolling Bearing Fatigue”, Proceedings of the 14th Leeds-Lyon Symposium on Tribology (8-11 September 1987), Tribology series 12, Elsevier, pages 201-208.

Hamer, J. C., Sayles, R. S., and **Ioannides, E.,** 1989b, “Particle Deformation and Counterface Damage When Relatively Soft Particles are Squashed Between Hard Anvils”, STLE Tribology Transactions, vol. 32, No. 3, pages 281-288.

Hamilton, R. W., Sayles, R. S., and **Ioannides, E.,** 1998, “Wear Due to Debris Particles in Rolling Bearing Contacts”, Proceedings of the 24th Leeds-Lyon Symposium on Tribology (4-6 September 1997), Tribology Series 34, Elsevier, pages 87-93.

Hamrock, B. J., 1994, *Fundamentals of Fluid Film Lubrication*, McGraw-Hill.

Hamrock, B. J., Pan, P., and **Lee, R.-T.,** 1988, “Pressure Spikes in Elastohydrodynamically Lubricated Conjunctions”, Transactions of the ASME, Journal of Tribology, vol. 110, pages 279-284.

Heckmann, S. R., and **Burton, R. A.,** 1980, “Surface Displacements for High Speed Rubs”, Wear, vol. 59, pages 61-77.

Hooke, C. J., 1986, “The Elasto-hydrodynamic Lubrication of Soft, Highly Deformed Contacts under Conditions of Nonuniform Motion”, Transactions of the ASME, Journal of Tribology, vol. 108, pages 545-550.

Horng, J. H., Lin, J. F., and **Li, K. Y.,** 1996, “Scuffing as Evaluated from the Viewpoint of Surface Roughness and Friction Energy”, Transactions of the ASME, Journal of Tribology, vol. 118, pages 669-675.

Houpert, L. G., and **Hamrock, B. J.,** 1986, “Fast Approach for Calculating Film Thicknesses and Pressures in Elastohydrodynamically Lubricated Contacts at High Loads”, Transactions of the ASME, Journal of Tribology, vol. 108, pages 411-420.

Hua, D. Y., and **Khonsari, M. M.,** 1996, “Elastohydrodynamic Lubrication by Powder Slurries”, Transactions of the ASME, Journal of Tribology, vol. 118, pages 67-73.

Ioannides, E., and **Harris, T. A.,** 1985, “A New Fatigue Life Model for Rolling Bearings”, Transactions of the ASME, Journal of Tribology, vol. 107, pages 367-377.

Jacobson, B., Ioannides, E., and **Tripp, J. H.,** 1987, “Redistribution of Solidified Films in Rough Hertzian Contacts. Part I: Theory”, Proceedings of the 14^{th} Leeds-Lyon Symposium on Tribology (8-11 September 1987), Tribology series 12, Elsevier, pages 51-57.

Jaeger, J. C., 1942, “Moving Sources of Heat and the Temperature at Sliding Contacts”, Proceedings of the Royal Society of New South Wales, vol. 76, pages 203-224.

Jeffery, G. B., 1922, “The Motion of Ellipsoidal Particles Immersed in a Viscous Fluid”, Proceedings of the Royal Society of London, Series A, vol. 102, pages 161-179.

Johnson, K. L., 1985, *Contact Mechanics*, (reprint 1994), Cambridge University Press.

Johnson, R.R., Dow, T. A., and **Zhang, Y. Y.,** 1988, “Thermoelastic Instability in Elliptic Contact Between Two Sliding Surfaces”, Transactions of the ASME, Journal of Tribology, vol. 110, pages 80-86.

Ju, F. D., and **Huang, J. H.,** 1982, “Heat Checking in the Contact Zone of a Bearing Seal (a Two-dimensional Model of a Single Moving Asperity)”, Wear, vol. 79, pages 107-118.

Katayama, K., Saito, A., and **Kobayashi, N.,** 1974, “Transient Heat Conduction in Anisotropic Solids”, Proceedings of the 5th International Conference on Heat Transfer, Tokyo, Japan, pages 137-141.

Kennedy, F. E. Jr., 1984, “Thermal and Thermomechanical Effects in Dry Sliding”, Wear, vol. 100, pages 453-476.

Kennedy, F. E. Jr., and **Ling, F. F.,** 1974, “A Thermal, Thermoelastic, and Wear Simulation of a High-Energy Sliding Contact Problem”, Transactions of the ASME, Journal of Lubrication Technology, pages 497-507.

Khan, A. S., and **Huang, S.,** 1995, *Continuum Theory of Plasticity*, Wiley.

Khonsari, M. M., and **Hua, D. Y.,** 1993, “Generalized Non-Newtonian Elastohydrodynamic Lubrication”, Tribology International, vol. 26, No. 6, pages 405-411.

Khonsari, M. M., Pascovici, M. D., and **Kucinschi, B. V.,** 1999, “On the Scuffing Failure of Hydrodynamic Bearings in the Presence of an Abrasive Contaminant”, Transactions of the ASME, Journal of Tribology, vol. 121, pages 90-96.

Khonsari, M. M., and **Wang, S. H.,** 1990, “On the Role of Particulate Contamination in Scuffing Failure”, Wear, vol. 137, pages 51-62.

Kjer, T., 1981, “Particles in New Motor Oils”, Wear, vol. 69, pages 395-396.

Ko, C. N., and **Ioannides, E.,** 1989, “Debris Denting – The Associated Residual Stresses and Their Effect on the Fatigue Life of Rolling Bearing: An FEM Analysis”, Tribological Design of Machine Elements, Elsevier, Amsterdam, The Netherlands, pages 199-207.

Korovchinski, M. V., 1965, “Plane-Contact Problem of Thermoelasticity During Quasi-Stationary Heat Generation on the Contact Surfaces”, Transactions of the ASME, Journal of Basic Engineering, pages 811-817.

Kulkarni, S. M., Rubin, C. A., and **Hahn, G. T.,** 1991, “Elasto-Plastic Coupled Temperature-Displacement Finite Element Analysis of Two-Dimensional Rolling-Sliding Contact with a Translating Heat Source”, Transactions of the ASME, Journal of Tribology, vol. 113, pages 93-101.

Kumar, A., Schmid, S. R., and **Wilson, W. R. D.,** 1997, “Particle Behavior in Two-Phased Lubrication”, Wear, vol. 206, pages 130-135.

Lai, W. T., and **Cheng, H. S.,** 1985, “Temperature Analysis in Lubricated Simple Sliding Rough Contacts”, ASLE Transactions, vol. 28, No. 3, pages 303-312.

Landau, H. G., and **Zwicky, E. E. Jr.,** 1960, “Transient and Residual Thermal Stresses in an Elastic-Plastic Cylinder”, Transactions of the ASME, Journal of Applied Mechanics, pages 481-488.

Languirand, M. T., and **Tichy, J. A.,** 1983, “The Effect of a Translating High Aspect Ratio Particle in a Plane Slider Bearing”, Transactions of the ASME, Journal of Lubrication Technology, vol. 105, pages 396-405.

Larsen-Badse, J., 1968a, “Influence of Grit Size on the Groove Formation During Sliding Abrasion”, Wear, vol. 11, pages 213-222.

Larsen-Badse, J., 1968b, “Influence of Grit Diameter and Specimen Size on Wear During Sliding Abrasion”, Wear, vol. 12, pages 35-53.

Leal, L. G., 1979, “The Motion of Small Particles in Non-Newtonian Fluids”, Journal of Non-Newtonian Fluid Mechanics, vol. 5, pages 33-78.

Leal, L. G., 1980, “Particle Motions in a Viscous Fluid”, Annual Review on Fluid Mechanics, vol. 12, pages 435-476.

Lee, K., and **Barber, J. R.,** 1993, “Frictionally Excited Thermoelastic Instability in Automotive Disk Brakes”, Transactions of the ASME, Journal of Tribology, vol. 115, pages 607-614.

Lee, R.-T., and **Hamrock, B. J.,** 1990, “A Circular Non-Newtonian Fluid Model: Part I – Used in Elastohydrodynamic Lubrication”, Transactions of the ASME, Journal of Tribology, vol. 112, pages 486-496.

Lee, S. C., and **Cheng, H. S.,** 1991, “Scuffing Theory Modeling and Experimental Correlations”, Transactions of the ASME, Journal of Tribology, vol. 113, pages 327-334.

Leng, J. A., and **Davies, J. E.,** 1988, “Ferrographic Examination of Unused Lubricants for Diesel Engines”, Wear, vol. 122, pages 115-119.

Lessen, M., 1956, “Thermoelasticity and Thermal Shock”, Journal of the Mechanics and Physics of Solids, vol. 5, pages 57-61.

Lin, J. F., and **Chu, H. Y.,** 1991, “A Numerical Solution for Calculating Elastic Deformation in Elliptical-Contact EHL of Rough Surface”, Transactions of the ASME, Journal of Tribology, vol. 113, pages 12-21.

Lin, J. F., and **Horng, J. H.,** 1992, “Analyses of Thermal Hydrodynamic Lubrication in High-Speed Rolling. Part II: the Effect of Non-Newtonian Viscosity Models”, Tribology International, vol. 25, No. 5, pages 341-349.

Lin, T.-R., and **Lin, J.-F.,** 1991, “Thermal Effects in Elastohydrodynamic Lubrication of Line Contacts Using a Non-Newtonian Lubricant”, Tribology International, vol. 24, No. 6, pages 365-372.

Ling, F. F., 1969, “On Temperature Transients at Sliding Interface”, Transactions of the ASME, Journal of Lubrication Technology, pages 397-405.

Ling, F. F., and **Rice, J. S.,** 1966, “Surface Temperature with Temperature-Dependent Thermal Properties”, ASLE Transactions, vol. 9, page 195-201.

Lo, S. W., 1994, “Die-Workpiece Interfacial Behaviors in Axisymmetric Forging Processes with Flat Dies”, STLE Transactions, paper No. 94-TC-6C-1.

Love, A. E. H., 1944 (reprint), *A Treatise on the Mathematical Theory of Elasticity*, 4th edition, Dover Publications, New York.

Lowen, E. G., and **Shaw, M. C.,** 1954, “On the Analysis of Cutting Tool Temperatures”, Transactions of the ASME, vol. 76, page 217-251.

Lu, C.-J., and **Bogy, D. B.,** 1992, “The Influence of Thermal Deformation on the Contact Temperature of Sliding Asperities”, Transactions of the ASME, Journal of Applied Mechanics, vol. 59, pages S102-S106.

Lubrecht, A. A, Dwyer-Joyce, R. S., and **Ioannides, E.,** 1992, “Analysis of the influence of Indentations on Contact Life”, Proceedings of the 18th Leeds-Lyon Symposium on Tribology (3-6 September 1991), Tribology Series 21, Elsevier, pages 173-181.

Lubrecht, A. A., ten Napel, W. E., and **Bosma, R.,** 1986, “Multigrid, an Alternative Method for Calculating Film Thickness and Pressure Profiles in Elastohydrodynamically Lubricated Line Contacts”, Transactions of the ASME, Journal of Tribology, vol. 108, pages 551-556.

Maksimov, I. L., 1988, “Thermal Instability of Sliding and Oscillations due to Frictional Heating Effect”, Transactions of the ASME, Journal of Tribology, vol. 110, pages 69-72.

Marscher, W. D., 1982a, “A Critical Evaluation of the Flash-Temperature Concept”, ASLE Transactions, vol. 25, No. 2, pages 157-174.

Marscher, W. D., 1982b, “Thermal Versus Mechanical Effects in High Speed Sliding”, Wear, vol. 79, pages 129-143.

Martin, K. F., 1978, “A Review of Friction Predictions in Gear Teeth”, Wear, vol. 49, pages 201-238.

McLean, D., 1962, *Mechanical Properties of Metals*, Wiley.

Mercier, R. J., Malkin, S., and **Mollendorf, J. C.,** 1978, “Thermal Stresses from a Moving Band Source of Heat on the Surface of a Semi-Infinite Solid”, Transactions of the ASME, Journal of Engineering for Industry, vol. 100, pages 43-48.

Mokhtar, M. O. A., Abdel-Ghany, A. A., 1985, “Elastohydrodynamic Behavior of Rolling Elliptical Contacts: Part I: Pressure and Temperatures Distributions”, Transactions of the ASME, Journal of Tribology, vol. 107, pages 343-351.

Mokhtar, M. O. A., Abdel-Ghany, A. A., 1985, “Elastohydrodynamic Behavior of Rolling Elliptical Contacts: Part II: Oil Film Thickness and Contact Profile”, Transactions of the ASME, Journal of Tribology, vol. 107, pages 352-358.

Montmitonnet, P., 1991, “Lubrication of Forging under Thick Film Conditions with Thermal Effects”, Lubrication Science, vol. 3, No. 4, pages 223-231.

Moore, A. J, 1997, “The Behaviour of Lubricants in Elastohydrodynamic Contacts”, Proceedings of the IMechE, Part J: Journal of Engineering Tribology, vol. 211, pages 91-106.

Mostofi, A., and **Gohar, R.,** 1983, “Elastohydrodynamic Lubrication of Finite Line Contacts”, Transactions of the ASME, Journal of Lubrication Technology, vol. 105, pages 598-604.

Motosh, N., and **Saman, W. Y.,** 1986, “A Method for Estimating the Effect of Normal Approach on Film Thickness in Elastohydrodynamic Line Contacts”, Proceedings of the 13th Leeds-Lyon Symposium on Tribology (8-12 September 1986), Tribology Series 11, Elsevier, pages 285-290.

Munson, B. R., Young, D. F., and **Okiishi, T. H.,** 1990, *Fundamentals of Fluid Mechanics*, Wiley.

Myllerup, C. M., 1993, “Perturbation Approach to Fluid Film Lubrication Theory”, Ph.D. Thesis, The Technical University of Denmark, Department of Machine Design, Denmark.

Nadano, H., and **Terauchi, Y.,** 1987, “The Mechanism of Seizure in Two-Roller Tests”, JSME International Journal, vol. 30, No. 265, pages 1152-1158.

Nelias, D., Sainsot, P., and **Flamand, L.,** 1992, “Deformation of a Particular Metallic Contaminant and Role on Surface Damage in High Speed Ball Bearings”, Proceedings of the 18th Leeds-Lyon Symposium on Tribology (3-6 September 1991), Tribology Series 21, Elsevier, pages 145-151.

Nicolson, D. M., 1996, “Scuffing at High Temperature and Speed”, Ph.D. Thesis, Imperial College of Science Technology and Medicine, Mechanical Engineering Department, Tribology Section, London, England.

Nivatvongs, K., Cheng, H. S., Ovaert, T. C., and **Wilson, W. R. D.,** 1991, “Influence of Surface Topography on Low-Speed Asperity Lubrication Breakdown and Scuffing”, Wear, vol. 143, pages 137-148.

Nowacki, W., 1986, *Thermoelasticity*, second edition, Pergamon Press.

Odi-Owei, S., and **Roylance, B. J.,** 1986, “The Effect of Solid Contamination on the Wear and Critical Failure Load in a Sliding Lubricated Contact”, Wear, vol. 107, pages 239-255.

Oktay, S. T., and **Suh, N. P.,** 1992, “Wear Debris Agglomeration in Dry and Boundary Lubrication Sliding”, Proceedings of the 18th Leeds-Lyon Symposium on Tribology (3-6 September 1991), Tribology Series 21, Elsevier, pages 347-356.

Olver, A. V., 1991, “Testing Transmission Lubricants: the Importance of Thermal Response”, Proceedings of the IMechE, Part G: Journal of Aerospace Engineering, vol. 205, pages 35-44.

Osborn, K. F., and **Sadeghi, F.,** 1992, “Time Dependent Line EHD Lubrication Using the Multigrid/Multilevel Technique”, Transactions of the ASME, Journal of Tribology, vol. 114, pages 68-74.

Özisik, M. N., 1993, *Heat Conduction*, 2nd edition, Wiley.

Pan, P., and **Hamrock, B. J.,** 1989, “Simple Formulae for Performance Parameters Used in Elastohydrodynamically Lubricated Line Contacts”, Transactions of the ASME, Journal of Tribology, vol. 111, pages 246-251.

Pearsall, G. W., and **Backofen, W. A.,** 1963, “Frictional Boundary Conditions in Plastic Compression”, Transactions of the ASME, Journal of Engineering for Industry, pages 68-76.

Peterson, M. B., Florek, J. J., and **Lee, R. E.,** 1960, “Sliding Characteristics of Metals at High Temperatures”, ASLE Transactions, vol. 3, pages 101-109.

Press, W. H., Teukolsky, S. A., Vetterling, W. T., and **Flannery, B. P.,** 1992, *Numerical Recipes in FORTRAN*, second edition, Cambridge University Press.

Protasov, B. V., and **Kragelskii, I. V.,** 1982, “On Heat Generation in External Friction”, Soviet Journal of Friction and Wear, vol. 2, pages 1-6.

Quinn, T. F. J., 1978, “The Division of Heat and Surface Temperatures at Sliding Steel Interfaces and Their Relation to Oxidational Wear”, ASLE Transactions, vol. 21, No. 1, pages 78-86.

Quinn, T. F. J., and **Winer, W. O.,** 1985, “The Thermal Aspects of Oxidational Wear”, Wear, vol. 102, pages 67-80.

Rabinowicz, E., and **Mutis, A.,** 1965, “Effect of Abrasive Particle Size on Wear”, Wear, vol. 8, pages 381-390.

Rhatigan, J. L., Johnson, R. R., and **Dow, T. A.,** 1989, “An Experimental Study of Thermoelastic Effects in Scuffing Failure of Sliding Lubricated Contacts”, Transactions of the ASME, Journal of Tribology, vol. 111, pages 23-28.

Richardson, R. C. D., 1968, “The Wear of Metals by Relatively Soft Abrasives”, Wear, vol. 11, No. 4, pages 245-275.

Rigney, D. A., and **Hirth, J. P.,** 1979, “Plastic Deformation and Sliding Friction of Metals”, Wear, vol. 53, pages 345-370.

Roelands, C. J. A., Vlugter, J. C., and **Waterman, H. I.,** 1963, “The Viscosity-Temperature-Pressure Relationship of Lubricating Oils and Its Correlation With Chemical Constitution”, Transactions of the ASME, Journal of Basic Engineering, vol. 85, pages 601-607.

Roelands, C. J. A., 1966, “Correlation Aspects of the Viscosity-Temperature-Pressure Relationship of Lubricating Oils”, Ph.D. Thesis, Technische Hogeschool, Delft, The Netherlands.

Rohde, S. M., Whicker, D., and **Booker, J. F.,** 1979, “Elastohydrodynamic Squeeze Films: Effects of Viscoelasticity and Fluctuating Load”, Transactions of the ASME, Journal of Lubrication Technology, vol. 101, pages 74-80.

Rohde, S. M., Whicker, D., and **Browne, A. L.,** 1976, “Dynamic Analysis of Elastohydrodynamic Squeeze Films”, Transactions of the ASME, Journal of Lubrication Technology, pages 401-408.

Ronen, A., Malkin, S., and **Loewy, K.,** 1980, “Wear of Dynamically Loaded Hydrodynamic Bearings by Contaminant Particles”, Transactions of the ASME, Journal of Lubrication Technology, vol. 102, pages 452-458.

Roylance, B. J., Siu, S. W., and **Vaughan, D. A.,** 1986, “Thermally-Related Stress Behaviour in Concentrated Contacts and the Implications for Scuffing Failure”, Mechanisms and Surface Distress, Proceedings of the 12th Leeds-Lyon Symposium on Tribology (3-6 September 1985), Butterworths, pages 117-127.

Rozeanu, L., and **Pnueli, D.,** 1980, “Hardness Controlled Thermal Failures”, Transactions of the ASME, Journal of Lubrication Technology, vol. 102, pages 545-551.

Rubinow, S. I., and **Keller, J. B.,** 1961, “The Transverse Force on a Spinning Sphere Moving in a Viscous Fluid”, Journal of Fluid Mechanics, vol. 11, pages 447-459.

Russell, J. A., Campbell, W. E., Burton, R. A., and **Ku, P. M.,** 1965, “Boundary Lubrication Behavior of Organic Films at Low Temperatures”, ASLE Transactions, vol. 8, pages 48-58.

Ryhming, I. L., 1979, “On Temperature and Heat Source Distributions in Sliding Contact Problems”, Acta Mechanica, vol. 32, pages 261-274.

Sadeghi, F., and **Sui, P. C.,** 1990, “Thermal Elastohydrodynamic Lubrication of Rough Surfaces”, Transactions of the ASME, Journal of Tribology, vol. 112, pages 341-346.

Saffman, P. G., 1965, “The Lift on a Small Sphere in a Slow Shear Flow”, Journal of Fluid Mechanics, vol. 22, part 2, pages 385-400.

Saville, D. A., 1977, “Electrokinetic Effects With Small Particles”, Annual Review on Fluid Mechanics, vol. 9, pages 321-337.

Sayles, R. S., 1995, “Debris and Roughness in Machine Element Contacts: Some Current and Future Engineering Implications”, Ninth BP-IMechE Tribology Lecture, Proceedings of the IMechE, Part J: Journal of Engineering Tribology, vol. 209, pages 149-172.

Sayles, R. S., 1996, “Basic Principles of Rough Surface Contact Analysis Using Numerical Methods”, Tribology International, vol. 29, No. 8, pages 639-650.

Sayles, R. S., Hamer, J. C., and **Ioannides, E.,** 1990, “The Effects of Particulate Contamination in Rolling Bearings – a State of The Art Review”, Proceedings of the IMechE, Part G: Journal of Aerospace Engineering, vol. 204, pages 29-36.

Sayles, R. S., and **Ioannides, E.,** 1988, “Debris Damage in Rolling Bearings and its Effects on Fatigue Life”, Transactions of the ASME, Journal of Tribology, vol. 110, pages 26-31.

Shieh, J., and **Hamrock, B. J.,** 1991, “Film Collapse in EHL and Micro-EHL”, Transactions of the ASME, Journal of Tribology, vol. 113, pages 372-377.

Shukor, A., 1994, “Debris Entrainment in Rolling Element Bearings”, Third-Year-Project Report (supervisor: Dr R.S. Sayles), Imperial College of Science, Technology and Medicine, Mechanical Engineering Department, Tribology Section, London, England.

Stachowiak, G. W., Kirk, T. B., and **Stachowiak, G. B.,** 1991, “Ferrography and Fractal Analysis of Contamination Particles in Unused Lubricating Oils”, Tribology International, vol. 24, No. 6, pages 329-333.

Storm, M. L, 1951, “Heat Conduction in Simple Metals”, Journal of Applied Physics, vol. 22, No. 7, pages 940-951.

Sugihara-Seki, M., 1993, “The Motion of an Elliptical Cylinder in Channel Flow at Low Reynolds Numbers”, Journal of Fluid Mechanics, vol. 257, pages 575-596.

Sui, P. C., and **Sadeghi, F.,** 1991, "Thermoelastic Effects in Lubricated Rolling/Sliding Line Contacts", Transactions of the ASME, Journal of Tribology, vol. 113, pages 174-181.

Tallian, T. E., 1992, *Failure Atlas for Hertz Contact Machine Elements*, ASME Press, New York.

Tian, X., and **Kennedy, F. E. Jr.,** 1993, "Contact Surface Temperature Models for Finite Bodies in Dry and Boundary Lubricated Sliding", Transactions of the ASME, Journal of Tribology, vol. 115, pages 411-418.

Tieu, A. K., and **Worden, J.,** 1987, "Transient Oil Film Thickness in Gear Contacts under Dynamic Loads", Proceedings of the 13th Leeds-Lyon Symposium on Tribology (8-12 September 1986), Tribology Series 11, Elsevier, pages 285-290.

Timoshenko, S. P., and **Goodier, J. N.,** 1970, *Theory of Elasticity*, third edition, McGraw-Hill.

Ting, B.-Y., Winer, W. O., 1989, "Friction-Induced Thermal Influences in Elastic Contact Between Spherical Asperities", Transactions of the ASME, Journal of Tribology, vol. 111, pages 315-322.

Tseng, M.-L., and **Burton, R.,** 1982, "Thermal Stress in a Two-Dimensional (Plane Stress) Half-Space for a Moving Heat Input", Wear, vol. 79, pages 1-9.

Uetz, H., and **Föhl, J.,** 1978, "Wear as an Energy Transformation Process", Wear, vol. 49, pages 253-264.

Venner, C. H., 1991, "Multilevel Solution of the EHL Line and Point Contact Problems", Ph.D. Thesis, University of Twente, The Netherlands.

Venner, C. H., and **Lubrecht, A. A.,** 1994, "Transient Analysis of Surface Features in an EHL Line Contact in the Case of Sliding", Transactions of the ASME, Journal of Tribology, vol. 116, pages 186-193.

Venner, C. H., ten Napel, W. E., and **Bosma, R.,** 1990, “Advanced Multilevel Solution of the EHL Line Contact Problem”, Transactions of the ASME, Journal of Tribology, vol. 112, pages 426-432.

Vichard, J. P., 1971, “Transient Effects in the Lubrication of Hertzian Contacts”, Journal of Mechanical Engineering Science, vol. 13, No. 3, pages 173-189.

Ville, F., and **Nelias, D.,** 1997, “An Experimental Study on the Concentration and Shape of Dents Caused by Spherical Metallic Particles in EHL Contacts”, presented at the 52nd STLE Annual Meeting, 18-22 May 1997, Kansas City, USA.

Ville, F., and **Nelias, D.,** 1998, “Influence of the Nature and Size of Solid Particles on the Indentation Features in EHL Contacts”, Proceedings of the 24th Leeds-Lyon Symposium on Tribology (4-6 September 1997), Tribology Series 34, Elsevier, pages 399-409.

Wan, G. T. Y., and **Spikes, H. A.,** 1986, “Two Phase Lubricants in Elastohydrodynamic Contacts - Graphite in Oil Dispersions”, Mechanisms and Surface Distress, Proceedings of the 12th Leeds-Lyon Symposium on Tribology (3-6 September 1985), Butterworths, pages 249-257.

Wan, G. T. Y., and **Spikes, H. A.,** 1988, “The Behavior of Suspended Solid Particles in Rolling and Sliding Elastohydrodynamic Contacts”, STLE Transactions, vol. 31, No. 1, pages 12-21.

Wang, Q., and **Cheng, H. S.,** 1994, “A Mixed Lubrication Model for Journal Bearings with a Thin Soft Coating – Part II: Flash Temperature Analysis and its Application to Tin Coated Al-Si Bearings”, STLE paper No. 94-TC-4B-2.

Wang, S., Cusano, C., and **Conry, T. F.,** 1991, “Thermal Analysis of Elastohydrodynamic Lubrication of Line Contacts Using the Ree-Eyring Fluid Model”, Transactions of the ASME, Journal of Tribology, vol. 113, pages 232-244.

Wang, S., and **Komvopoulos, K.,** 1994, “A Fractal Theory of the Temperature Distribution at Elastic Contacts of Fast Sliding Surfaces”, Transactions of the ASME, Journal of Tribology, paper No. 94-Trib-16.

Webster, M. N., Ioannides, E., and **Sayles, R. S.,** 1986, “The Effect of Topographical Defects on the Contact Stress and Fatigue Life in Rolling Element Bearings”, Mechanisms and Surface Distress, Proceedings of the 12th Leeds-Lyon Symposium on Tribology (3-6 September 1985), Butterworths, pages 207-221.

West, M. A., and **Sayles, R. S.,** 1987, “A 3-Dimensional Method of Studying 3-Body Contact Geometry and Stress on Real Rough Surfaces”, Proceedings of the 14th Leeds-Lyon Symposium on Tribology (8-11 September 1987), Tribology series 12, Elsevier, pages 195-200.

Williams, J. A., and **Hyncica, A. M.,** 1992, “Abrasive Wear in Lubricated Contacts”, Journal of Physics, Part D: Applied Physics, vol. 25, pages A81-A90.

Wilson, E. A., 1969, “Compression of a Thin Plastic Mass Between Two Elastic Cylinders”, Transactions of the ASME, Journal of Lubrication Technology, pages 342-350.

Wilson, W. R. D., and **Wong, C. J.,** 1974, “Analysis of the Lubricant Film Formation Process in Plane Strain Forging”, Transactions of the ASME, Journal of Lubrication Technology, pages 605-616.

Wolf, R., 1991, “The Influence of Surface Roughness Texture on the Temperature and Scuffing in Sliding Contact”, Wear, vol. 143, pages 99-118.

Wong, P. L., Wang, R., and **Lingard, S.,** 1996, “Pressure and Temperature Dependence of the Density of Liquid Lubricants”, Wear, vol. 201, pages 58-63.

Wu, Y.-W., and **Yan, S.-M.,** 1987, “A Full Numerical Solution for the Non-Steady State Elastohydrodynamic Problem in Nominal Line Contacts”, Proceedings of the

13th Leeds-Lyon Symposium on Tribology (8-12 September 1986), Tribology Series 11, Elsevier, pages 285-290.

Xu, G., Sadeghi, F., and **Hoeprich, M.,** 1997, “Residual Stresses Due to Debris Effects in EHL Contacts”, STLE Tribology Transactions, vol. 40, No. 4, pages 613-620.

Xuan, J. L., Hong, I. T., and **Fitch, E. C.,** 1989, “Hardness Effect on Three-Body Abrasive Wear under Fluid Film Lubrication”, Transactions of the ASME, Journal of Tribology, vol. 111, pages 35-40.

Yang, C. C., 1971, “Incipient Plastic Yielding of an Elastoplastic Half-Space under an Arbitrarily Distributed Moving Heat Source”, International Journal of Engineering Science, vol. 9, pages 507-519.

Yang, P., and **Wen, S.,** 1990a, “A Forward Iterative Numerical Method for Steady-State Elastohydrodynamically Lubricated Contacts”, Tribology International, vol. 23, No. 1, pages 17-22.

Yang, P., and **Wen, S.,** 1990b, “A Generalized Reynolds Equation for Non-Newtonian Thermal Elastohydrodynamic Lubrication”, Transactions of the ASME, Journal of Tribology, vol. 112, pages 631-636.

Yang, P., and **Wen, S.,** 1992, “The Behavior of Non-Newtonian Thermal EHL Film in Line Contacts at Dynamic Loads”, Transactions of the ASME, Journal of Tribology, vol. 114, pages 81-85.

Yang, P., and **Wen, S.,** 1993, “A Fast, Robust, Straightforward Algorithm for Thermal Elastohydrodynamic Lubrication”, Tribology International, vol. 26, No. 1, pages 17-23.

Young-Ze, L., and **Ludema, K. C.,** 1990, “The Shared-Load Wear Model in Lubricated Sliding: Scuffing Criteria and Wear Coefficients”, Wear, vol. 138, pages 13-22.

Zantopoulos, H., 1998, "Some Observations on Scuffing in Tapered Roller Bearings", Transactions of the ASME, Journal of Tribology, vol. 120, pages 427-435.

Zhu, D., and **Cheng, H. S.,** 1988, "Effect of Surface Roughness on the Point Contact EHL", Transactions of the ASME, Journal of tribology, vol. 110, pages 32-37.

RELEVANT PUBLICATIONS OF THE AUTHOR

At the time of writing this Thesis (March 1999), there were four publications based on this research. Other papers based on this Thesis are under preparation. The four relevant publications are as follows.

- **Nikas, G. K., Sayles, R. S.,** and **Ioannides, E.,** 1997, “Effects of Debris Particles in Sliding/Rolling EHD Contacts”, Proceedings of the 1st World Tribology Congress (8-12 September 1997, London, England), IMechE, page 271.

- **Nikas, G. K., Sayles, R. S.,** and **Ioannides, E.,** 1998, “Effects of Debris Particles in Sliding/Rolling Elastohydrodynamic Contacts”, Proceedings of the IMechE, Journal of Engineering Tribology, vol. 212, No. J5, pages 333-343.

- **Nikas, G. K., Ioannides, E.,** and **Sayles, R. S.,** 1999, “Thermal Modeling and Effects From Debris Particles in Sliding/Rolling EHD Line Contacts – A Possible Local Scuffing Mode”, Transactions of the ASME, Journal of Tribology, vol. 121, No. 2 (April), pages 272-281.

- **Nikas, G. K., Sayles, R. S.,** and **Ioannides, E.,** 1999, “Thermoelastic Distortion of EHD Line Contacts During the Passage of Soft Debris Particles”, Transactions of the ASME, Journal of Tribology, vol. 121, No. 2 (April), pages 265-271.